energies

Advances in Supercapacitor Technology and Applications II

Edited by
Alon Kuperman and Alessandro Lampasi

Printed Edition of the Special Issue Published in *Energies*

www.mdpi.com/journal/energies

MDPI

Advances in Supercapacitor Technology and Applications II

Advances in Supercapacitor Technology and Applications II

Editors

Alon Kuperman
Alessandro Lampasi

MDPI • Basel • Beijing • Wuhan • Barcelona • Belgrade • Manchester • Tokyo • Cluj • Tianjin

Editors

Alon Kuperman
Ben-Gurion University of the Negev
Israel

Alessandro Lampasi
National Agency for New Technologies, Energy and Sustainable Economic Development (ENEA)
Italy

Editorial Office
MDPI
St. Alban-Anlage 66
4052 Basel, Switzerland

This is a reprint of articles from the Special Issue published online in the open access journal *Energies* (ISSN 1996-1073) (available at: https://www.mdpi.com/journal/energies/special_issues/supercapacitor_ii).

For citation purposes, cite each article independently as indicated on the article page online and as indicated below:

LastName, A.A.; LastName, B.B.; LastName, C.C. Article Title. *Journal Name* **Year**, *Volume Number*, Page Range.

ISBN 978-3-0365-4301-7 (Hbk)
ISBN 978-3-0365-4302-4 (PDF)

Contents

About the Editors

Alon Kuperman

Alon Kuperman received the Ph.D. degree in electrical and computer engineering from the Ben-Gurion University of the Negev, Beersheba, Israel, in 2006. He was a Marie Curie Training Site Member with Imperial College London, London, U.K, in 2003–2006. He was an Honorary Research Fellow with the University of Liverpool, Liverpool, U.K., in 2008–2009. He is currently with the School of Electrical and Computer Engineering, Ben-Gurion University, Israel, where he is heading the Power and Energy Systems track and directing the Applied Energy Laboratory. His research interests include all aspects of energy conversion and applied control.

Alessandro Lampasi

Alessandro Lampasi received the M.Sc. degree in electronic engineering and the Ph.D. degree in electrical engineering from the University of Rome Sapienza, Rome, Italy, in 2002 and 2006, respectively. He is currently with the Italian National Agency for New Technologies, Energy and Sustainable Economic Development (ENEA), Frascati, Italy, where he is in charge for several international projects concerning nuclear fusion and power systems. His current research interests include modeling and measurement techniques in the fields of nuclear fusion, power electronics, energy storage, and applied electromagnetics.

energies

MDPI

Article

Influence of the Perovskite $La_{0.8}Sr_{0.2}Mn_{0.5}Co_{0.5}O_{3-\delta}$ on the Electrochemical Performance of the Graphene-Based Supercapacitor

Bo-Min Kim [1], Hyo-Young Kim [2], Young-Wan Ju [2,3,*] and Jeeyoung Shin [1,4,*]

1 Department of Mechanical Systems Engineering, Sookmyung Women's University, Seoul 04310, Korea; bomin12@sookmyung.ac.kr
2 Department of Chemical Engineering, College of Engineering, Wonkwang University, Iksan, Jeonbuk 54538, Korea; gydud4070@naver.com
3 Nanoscale Sciences and Technology Institute, Wonkwang University, Iksan, Jeonbuk 570-749, Korea
4 Institute of Advanced Materials and Systems, Sookmyung Women's University, Seoul 04310, Korea
* Correspondence: ywju1978@wku.ac.kr (Y.-W.J.); jshin@sookmyung.ac.kr (J.S.)

Received: 30 April 2020; Accepted: 8 June 2020; Published: 12 June 2020

Abstract: A supercapacitor is a potential energy system that will be a part of an efficient storage device of renewable energy, such as a small battery and a large energy storage system (ESS), etc. However, a lot of efforts have been devoted to improving stability. Generally, ABO_3-type perovskite structure has been studied as an electrode and/or an oxide ion-conducting electrolyte for solid oxide fuel cells with stable structural stability at high temperatures. In this study, perovskite material ($La_{0.8}Sr_{0.2}Mn_{0.5}Co_{0.5}O_{3-\delta}$. LSMCO) was added as a component of the supercapacitor electrode for enhanced stability. According to electrochemical measurements, at 5 mV/s, the specific capacitance of the graphene-based electrode (G95) is 68 F/g, and the electrode mixed with perovskite (G70L25) is 55 F/g. Nonetheless, the standard deviation of the capacitance value of G70L25 is smaller than that of G95. Alongside this, the G70L25 electrode showed that specific capacitance decreased in the cycling test, but, for the G95 electrode, the specific capacitance after the 4990th cycle increased or decreased, resulting in unpredictable results. Therefore, perovskite added electrode (G70L25) shows higher stability compared to the graphene nanoplatelets electrode (G95) in both initial and cycling performance, albeit a lower specific capacitance.

Keywords: perovskite; supercapacitors; stability

1. Introduction

A supercapacitor is a promising energy storage device that has been an essential component in most fields, ranging from portable electronics to hybrid electric vehicles and large industrial equipment [1]. A supercapacitor can also be used in various applications such as power electronics, energy storage at intermittent generators including windmills, and smart grid applications because it has a high power density, high rate of charge/discharge, long life, etc. [2].

The energy storage method of the supercapacitor can be divided into two types: electrical double-layer capacitors (EDLC) and pseudocapacitors [3]. EDLC, made of materials with a high surface area, has a high power density but a lower volumetric energy density than traditional batteries. In contrast, the pseudocapacitor has an energy density higher than EDLC because it stores electrons through a redox reaction on the surface of the electrode. In this regard, metal-based pseudocapacitors can take the intermediate role of conventional electrostatic capacitors and batteries. Electric double-layer capacitors (EDLC) and commercial devices can store between 3 and 6 Wh [3].

The pseudocapacitor has a very fast charge/discharge rate compared to lithium-ion batteries but has the disadvantage of a somewhat low energy density. In this regard, there have been a number of

efforts to increase energy density through the selection of new materials or the improvement of the electrode structure, current-collecting method, etc. For example, metal oxides have the potential to improve energy density significantly due to reversible faradaic surface reactions [4].

There are three methods of charge storage for pseudocapacitor electrodes [3]: The first is the adsorption of electrolyte ions on the metal surface with monolayers. This adsorption can be revealed through partial charge transfer between the metal center of the electrode and the electrolyte anion, and underpotential deposition of the so-called electrosorption valence [5,6]. The second method, pseudocapacitance, includes redox reactions on the surface of the electrode. These redox reactions are chemical reactions on the surface that result in a charge transfer with strong bonds [7]. The third is the reversibly rapid insertion of ions into the bulk of the material. As the ions are inserted into the crystalline material, the intercalation pseudocapacitance is observed and eventually behaves like a capacitor [8,9]. All of these can be described as pseudocapacitive because of the change of the oxidation state of the transition metal.

Established electrode materials include activated carbon (AC), carbon nanotube (CNT), polymers, graphene, etc. [10–12]. Among them, graphene is widely studied because of its high specific surface area, aspect ratio, and conductivity [13]. Additionally, graphene has high charge mobility (>200,000 $cm^2/V{\cdot}S$), zero effective mass, and ballistic transport even at room temperature [14]. Graphene nanoplatelets are composed of several graphene layers and have similar properties to single graphene and are much easier to produce and handle [15,16]. When AC was used as an electrode at a current density of 0.5 A/g, specific capacitance values at 1 V (voltage window) were maintained at 242 F/g initially to 204 F/g after 7000 cycles, which was 84% of the initial value [17]. Yan et al. reported that the capacitance of PANI (polyaniline)-based graphene electrodes was 1046 F/g at a scan rate of 1 mV/s among the graphene electrodes. However, the graphene and PANI composite electrodes showed a linear decrease after the 1000th cycle, with the capacitance dropping to 50% of the initial value [18].

In this respect, perovskite has got attention to improve the cyclic stability of the graphene-based electrode. $La_{0.8}Sr_{0.2}Mn_{0.5}Co_{0.5}O_{3-\delta}$ perovskites (LSMCO) are known to be good catalysts for total oxidation due to a large amount of oxygen in the perovskite structure and the redox behavior of the Mn- and Co-ions. Their catalytic activity is comparable with some noble metal catalysts. ABO_3-type perovskite structure has been studied as an electrode for solid oxide fuel cells and an oxide ion-conducting electrolyte with stable structural stability at high temperatures [19–21]. A is the lanthanum group or the alkali earth element, and B is the transition metal [22]. The adjustment of the site of A and B can control the electrical properties of the material, which induces the role of anion vacancy as a charge storage site for pseudocapacitance [23]. For example, $SrRuO_3$ exhibits metallic conductivity and is stable in alkaline electrolytes [24]. In addition, the microemulsion technique can enhance electrochemical performance by generating perovskite nanostructure [25].

Mefford et al. presented an anion-based mechanism through a supercapacitor using $LaMnO_3$ perovskite, which is the first example of anion-based intercalation pseudocapacitance and the first oxygen insertion method used for fast energy storage [23]. The composite electrode was fabricated by growing Ag nanoparticles on a $La_{0.7}Sr_{0.3}CoO_3$ (LSCO) substrate by Liu et al. The Ag/LSCO electrode maintained 81% capacitance after 3000 cycles at the current density of 50 mA/cm^2. Liu and coworkers have released anion-intercalation type electrodes. When the cycling performance of $SrCoO_3$ (SCO) was measured with an activated carbon electrode at 1 A/g current density, the specific capacitance of approximately 80% was maintained after the 2000th cycle [26]. Previous research using perovskite $LaSrMnO_3$ shows the capacitive behavior (102 F/g) and charge storage performance for supercapacitors through the anion-intercalation mechanism [27–32].

Structurally stable perovskite is expected to help maintain the stability of the supercapacitor electrode. Our goal is to maintain the initial capacitance of the pseudo-supercapacitor and to improve the capacitance stability after 4990 cycles using a perovskite-mixed electrode. In our experiment, we compared the electrochemical characteristics, including cyclic voltammetry, galvanostatic

charge-discharge, etc. with an electrode G95 (graphene nanoplatelets 95 wt%) and electrode G70L25 (graphene nanoplatelets 70 wt%, LSMCO 25 wt%).

2. Materials and Methods

2.1. Preparation of Perovskite ($La_{0.8}Sr_{0.2}Mn_{0.5}Co_{0.5}O_{3-\delta}$. LSMCO)

Stoichiometrically calculated amounts of lanthanum(III) nitrate hydrate ($La(NO_3)_3{\cdot}6H_2O$, 99.9%, Sigma Aldrich, St.Louis, MO, USA), strontium nitrate ($Sr(NO_3)_2$, 98%, Samchun), manganese(II) nitrate tetrahydrate ($Mn(NO_3)_2{\cdot}4H_2O$, 97%, Sigma Aldrich, St.Louis, MO, USA) and cobalt(II) nitrate hexahydrate ($Co(NO_3)_2{\cdot}6H_2O$, 97%, Samchun, Seoul, Korea) were used to prepare $La_{0.8}Sr_{0.2}Mn_{0.5}Co_{0.5}O_{3-\delta}$ perovskites (LSMCO). The citric acid ($HOC(COOH)(CH_2COOH)_2$ and 99.5%, Samchun, Seoul, Korea) and ethylenediaminetetraacetic acid (EDTA, 99.5%, Sigma Aldrich, St. Louis, MO, USA) were used as the chelating agent. The obtained powder was calcined at 1273 K for 5 h.

2.2. Preparation of Electrodes (G95 and G70L25)

To evaluate the electrochemical properties of the graphene nanoplatelets/LSMCO composites, electrodes were fabricated as follows: 5 wt% of polyvinylidene fluoride (PVDF, MTI corporation, California, CA, USA) was mixed with enough dimethyl sulfoxide (DMSO, Sigma-Aldrich, St. Louis, MO, USA) to dissolve the powder. Graphene nanoplatelets (GN, Alfa Aesar, Haverhill, MA, USA) used in the experiment have a specific surface area of 500 m^2/g, and a particle diameter of smaller than 2 microns and a typical particle size of a few nanometers, depending on the surface area. For the G70L25 electrode, the graphene nanoplatelets and perovskite were mixed to a 70%:25% weight ratio for 30 min. For the G95 electrode, 95 wt% graphene nanoplatelets were used. Mixed active material was applied on a carbon paper substrate and baked in an oven at 150 °C for 15 min. The two-dimensional size of the electrode was 10 mm × 10 mm. The mass of active material in the working electrode was 1.0–2.0 mg.

2.3. Characterizations

The morphology and principle of the products were characterized by field-emission scanning electron microscopy (FE-SEM) and energy-dispersive X-ray spectroscopy (EDX) on a JEOL (JSM-7600F) and Oxford instrominis (X-Max). The crystalline phase compositions of the samples were characterized by X-ray diffraction (XRD) on a D8 Advance (TRIO/TWIN) X-ray diffractometer. The specific surface area, pore diameter, and volume were obtained using Brunauer, Emmett, Teller (BET, BELSORPmini II) involving N_2 gas adsorption/desorption isotherms analysis. The properties of the interface were analyzed by X-ray photoelectron spectroscopy (XPS) on the Thermo ESCALAB 250.

2.4. Electrochemical Measurements

Cyclic voltammetry (CV), galvanostatic charge-discharge (GCD), and electrochemical impedance spectroscopy (EIS) of single electrodes were performed using a potentiostat (VSP, Bio-Logic). The electrolyte is a 1 M H_2SO_4 aqueous solution that purged N_2 gas for 20 min. Measurements are conducted through a three-electrode system. A reference electrode was a saturated calomel electrode (SCE), and a counter electrode was a platinum wire. For voltammetry measurements, the cell potential was scanned at 5 mV/s and 20 mV/s. When the scan rate was 5 mV/s, it was measured for 5 cycles, and when it was 20 mV/s, it was measured for 4990 cycles. Galvanostatic charge-discharge behavior was measured in current density, from 0.5 to 20 A/g. EIS was measured from 100 kHz to 100 mHz.

3. Results and Discussion

3.1. SEM and EDX

Figure 1a–d shows SEM images of the G95 electrode and G70L25 electrode before and after cyclic voltammetry measurements. In Figure 1a, it can be seen that layers of graphene nanoplatelets are randomly stacked. Figure 1c shows that LSMCO is randomly contained between graphene nanoplatelets layers in the G70L25 the electrode. After cyclic voltammetry, both the G95 and G70L25 electrodes have white granules, as in Figure 1b,e. EDX analysis confirmed that carbon, platinum, and sulfur were found in the overall area, which are the primary materials of working and counter electrodes and electrolytes (H_2SO_4). In addition, white granules appear to be sulfur and Pt of counter electrodes as a result of the analysis. In reference [33], it is reported that, after the CV experiment, Pt particles generated on the working electrode surface and weight loss of the Pt electrode occurred in the H_2SO_4 electrolyte.

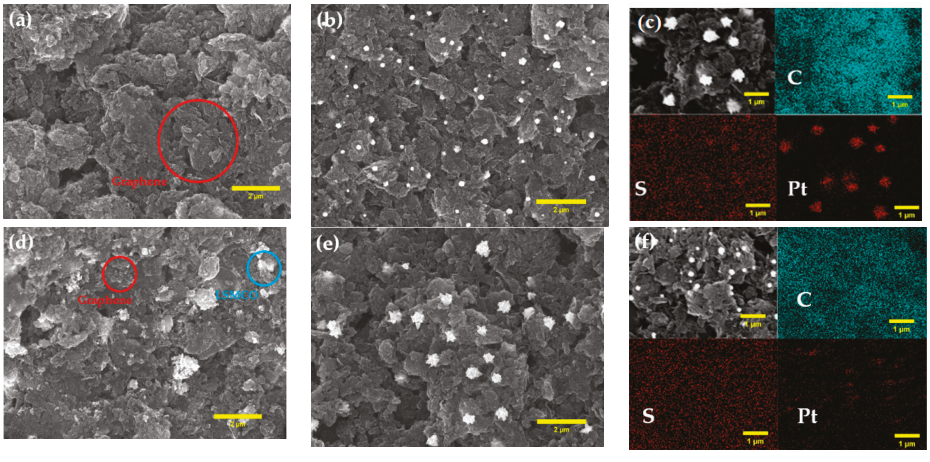

Figure 1. SEM images of as-prepared (**a**) electrode of G95 before cyclic voltammetry; (**b**) after cyclic voltammetry 5000 cycles; (**c**) SEM image of G95 with EDX mapping of C, S, and Pt; (**d**) electrode of G70L25 before cyclic voltammetry and (**e**) after cyclic voltammetry 5000 cycles; (**f**) SEM image of G70L25 with EDX mapping of C, S, and Pt.

3.2. XRD

The XRD patterns of pure graphene nanoplatelets, pure LSMCO, G70L25, and G95 electrode active materials are shown in Figure 2. In the patterns of the G70L25 electrodes, we can see that the major diffraction peaks of the LSMCO are maintained as the same as those of the as-synthesized LSMCO material. It demonstrates that LSMCO was successfully anchored on the graphene sheets without a secondary reaction.

3.3. BET

BET nitrogen adsorption/desorption isotherm measurements were used to determine the surface area, pore diameter, and pore volume. Figure 3 corresponds to type II with unrestricted mono-multilayer characteristics in the classification of adsorption isotherms. The specific surface area has 441.83 and 317.17 m^2/g for G95 and G70L25, respectively. The average pore diameter was around 8.5 nm for both G95 and G70L25. The total pore volume is 0.9483 and 0.6935 cm^3/g, respectively, for G95 and G70L25.

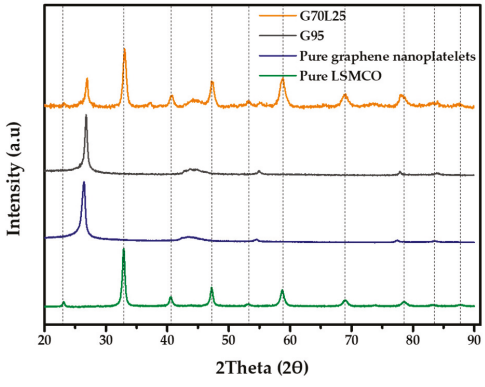

Figure 2. XRD pattern of comparing G70L25, G95, pure graphene nanoplatelets, and pure LSMCO; The DIFFRAC.EVA program was used to identify the data.

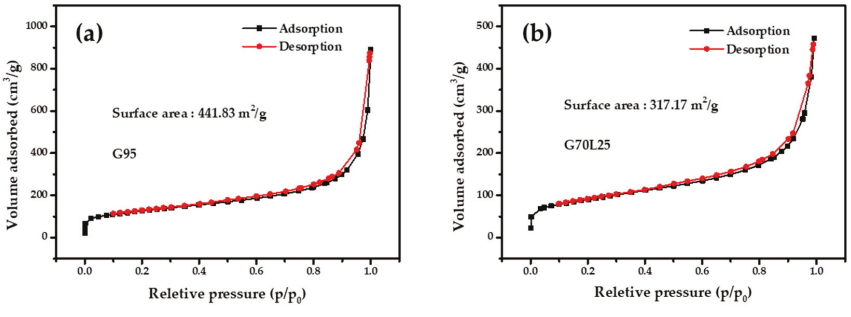

Figure 3. Nitrogen adsorption and desorption isotherms for (**a**) G95 and (**b**) G70L25.

3.4. XPS

The chemical composition of samples was analyzed by using X-ray photoelectron spectroscopy (XPS). The full XPS spectrum of G95 reveals the presence of C elements along with a small quantity of O elements. The G7025 electrode includes the perovskite LSMCO elements along with the above-mentioned elements. Figure 4b–f shows an XPS spectrum of core levels of C1s and O1s from the G95 and G70L25 electrodes, each of which can be decomposed into three peaks. Binding energy values were analyzed by reference to previous literature [34,35]. The detailed analysis of the C1s spectrum is as follows: sp2 carbon at 248.6 eV (C_a), alcohol and ether groups at ~286.4 eV (C_b), and ester and carboxyl groups at ~289.04 eV (C_c) both for G70L25 and G95 electrodes. The deconvoluted spectrum of G70L25's O1s was shown to be three peaks: a carbon-oxygen double bond at ~531.95 eV (O_b), carbon-oxygen single-bonds in hydroxyl groups at ~533.68eV (O_d), and quinine or pyridone groups at ~530.16 eV (O_a). However, for G95, single bonds such as carbon-oxygen ether at 532.33 eV (O_c) or absorbed water or oxygen at 535.23 eV (O_e) appears. The same combination type appears in the G70L25 for two measurements, but different combination types appear in the G95. Additionally, the oxygen content of G70L25 is higher than G95.

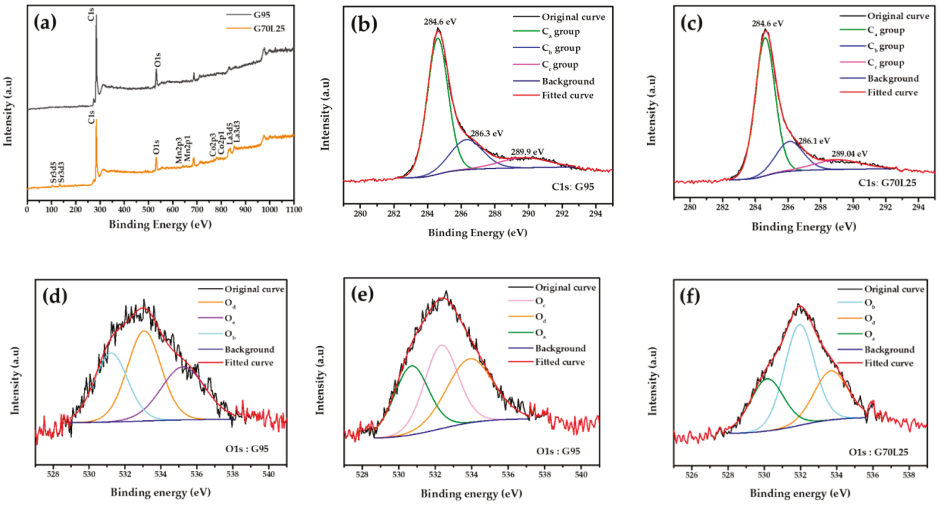

Figure 4. (**a**) XPS fully scanned spectrum of G95 and G70L25; fitted results of XPS C1s spectra of (**b**) G95 and (**c**) G70L25; fitted results of XPS O1s spectra of (**d**,**e**) G95 and (**f**) G70L25.

3.5. Cyclic Voltammetry (CV)

In the CV curve, the specific capacity of the electrode can be obtained through the following equation:

$$C_s = \frac{1}{s \cdot m \cdot \Delta V} \int_{V_1}^{V_2} idV \quad (1)$$

Here, C_S is a specific capacitance (F/g), s is a scan rate (V/s), m is a mass of active material, ΔV is a voltage window (0 V–0.8 V), I is a current (A), V_1 is a lower voltage limit (V), and V_2 is an upper voltage limit (V) [36].

In Figures 5 and 6, the CV curve has a nearly rectangular shape and represents the capacitive behavior of the EDLC. Figure 5 shows the CV curves of the G95 electrode and G70L25 electrode at a scan rate of 5 mV/s in 1 M H_2SO_4 after 5 cycles. The specific capacitance of the G95 electrode is 69.34 F/g, and the standard deviation is 6.961. The specific capacitance of the G70L25 electrode is 52.31 F/g, and the standard deviation is 2.576. The specific capacitance of the G95 electrode is about 10% higher than that of G70L25. The higher specific surface area of G95 can explain the higher initial specific capacitance values of G95 in CV measurements. However, the standard deviations of the results for G95 are quite high compared to those of G70L25. It might mean that producing supercapacitors with the expected design values in the mass production phase can be difficult.

Figure 6 shows a CV curve measured for 4990 cycles by increasing the scan rate to 20 mV/s. Figure 6a,b is the CV curve of the G95 electrode. The specific capacitance is 62.23 F/g at 11 cycles and 61.38 F/g at 4990 cycles. The reduction of 1.38% can be seen in Figure 6a. On the other hand, specific capacitance is 57.07 F/g at 11 cycles and 59.81 F/g at 4990 cycles, which means an increase of the specific capacitance (Figure 6b). However, Figure 6c,d shows a CV curve of the G70L25 electrode. In Figure 6c, the specific capacitance was 47.37 F/g at 11 cycles and 45.94 F/g at 4990 cycles, so it decreased by 3.01%. In Figure 6d, specific capacitance is 50.98 F/g at 11 cycles and 48.41 F/g at 4990 cycles. For the G70L25 electrode, after 4990 cycles, the performance of the G70L25 electrode is consistent for several data sets, and up to 7% reduction can be expected.

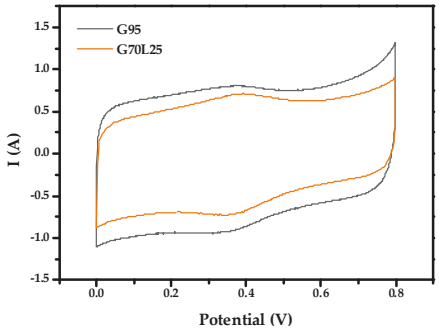

Figure 5. Cyclic voltammetry at 5 mV/s of G95 electrode and G70L25 electrode in 1 M H_2SO_4.

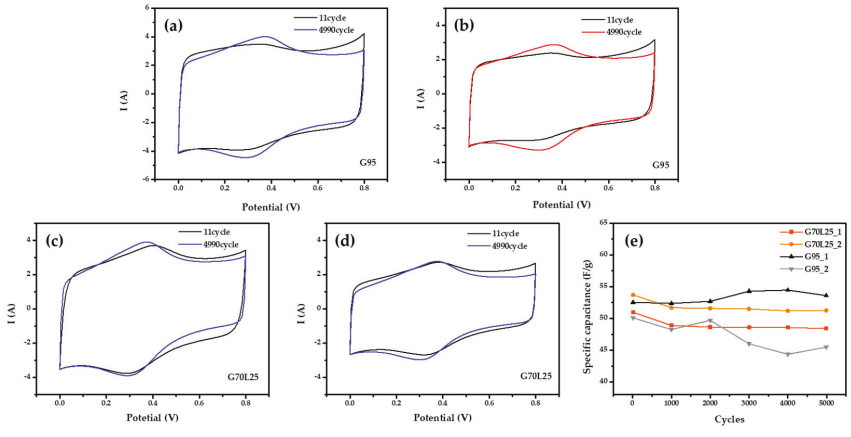

Figure 6. Cyclic voltammetry at 20 mV/s (**a**) specific capacitance decreased after 4990 cycles for the electrode of G95 in 1M H_2SO_4; (**b**) specific capacitance increased after 4990 cycles for the electrode of G95 in 1 M H_2SO_4; (**c**,**d**) specific capacitance decreased after 4990 cycles for the electrodes of G70L25 in 1 M H_2SO_4; (**e**) the plot of specific capacitance verse cycle at 20 mV/s in H_2SO_4.

The results of the G95 electrode, however, show that it is difficult to expect a reproducibility of the experiments because specific capacitance tends to both increase or decrease, which means that we cannot guarantee some level of the supercapacitor capacity after long term operation. However, all of the G70L25 electrodes tend to decrease. Therefore, even though the specific capacitance of the electrode G70L25 with the perovskite LSMCO added onto graphene nanoplatelets is lower than that of the G95 electrode, the stability seems to be superior.

3.6. Galvanostatic Charge–Discharge (GCD)

The specific capacitance of the electrodes obtained from GCD curves is calculated at various current densities by the following equation [37]:

$$C = \frac{I \cdot t_d}{m \cdot \Delta V} \tag{2}$$

I is a discharge current (A), t_d is a discharge time (s), m is an active material mass, and ΔV is a potential drop during discharge.

Specific capacitance values of G95 and G70L25 for each current density are shown in Table 1. The specific capacitances of both the G95 and G70L25 electrodes were similar to those of the CV

experiments. When the current density increased from 0.5 to 20 A/g, specific ion diffusion rates tended to reduce specific capacities of the G95 and G70L25 electrodes at a high current density [38]. As a result, the variation of the specific capacitance of the G95 and G70L25 electrodes over current density shows the typical behavior of a supercapacitor. The low value of capacitance at a high current density is due to the low ion penetration on the electrode surface [39]. The Ragone plot of G95 and G70L25 is shown in Figure 7d. For the G95 and G70L25 electrodes, the energy density is 21.80–16.24 Wh/kg and 17.10–15.12 Wh/kg at the same range of current density, respectively. The G70L25 electrode shows a 22% decrease in energy density at 0.5 A/g, but only a 7% decrease at 20 A/g compared to G95, which means catalytic effects of the perovskite enhances at a higher current density. In addition, we fabricated composite electrodes of LSMCO and graphene nanoplatelets by mixing and dispersing using magnetic bars and ultrasonic. In this process, we believe that structural stability increases because graphene nanoplatelets wrap around LSMCO [40].

Table 1. The specific capacitance of G95 and G70L25 according to current density.

Electrodes	G95	G70L25
Current Density [A/g]	**Specific Capacitance [F/g]**	**Specific Capacitance [F/g]**
0.5	68.13	53.44
1.0	64.63	51.25
1.5	62.81	50.63
2.0	61.50	49.75
3.0	57.00	49.13
5.0	57.38	48.31
7.0	55.83	47.86
9.0	54.68	47.48
10	54.13	47.25
20	50.75	47.25

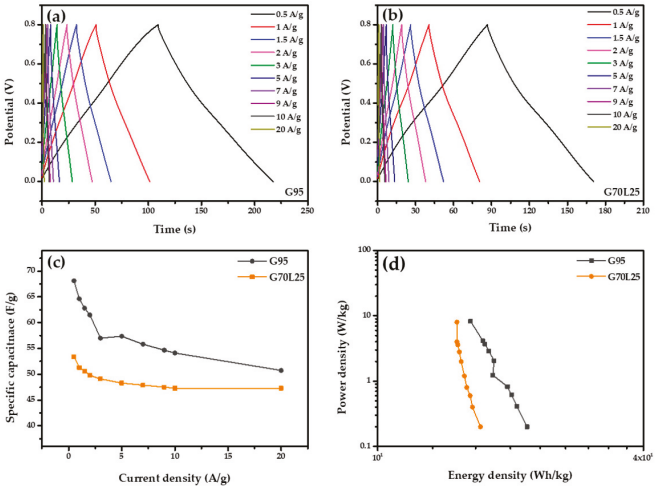

Figure 7. Galvanostatic charge-discharge graph of (**a**) G95 electrode and (**b**) G70L25 electrode; (**c**) specific capacitance variation of G95 and G70L25 with current density; (**d**) comparative Ragone plots of the G95 and G70L25 electrodes.

3.7. Electrochemical Impedance Spectroscopy (EIS)

EIS is an excellent technique to investigate the electrochemical behaviors of electrodes. Figure 8 shows the replotted typical Nyquist diagram of the G95 and G70L25 electrodes. The Nyquist plot is generally composed of three parts: the first part in the high-frequency region is x-interference at the semicircle start point, which is considered as an effective ohmic resistance; the second part is a semicircular shape in the mid-frequency region, which is assumed to be a charged transfer resistance (R_{ct}) and is equal to the diameter of the semicircle; the last part is a vertical line at the low-frequency region, which is assumed to be ion transport of diffusion resistance at the electrode/electrolyte interface [41]. In both electrodes, diffusion resistance is similar due to the same electrolyte being used. However, R_{ct} of two electrodes is slightly different. The G70L25 electrode showed slightly larger R_{ct} due to the additional 25 wt% LSMCO causing a decrease of the diffusion pathway accompanied by the reduction in surface area, as shown in Figure 3. The steeper slope of the G95 can explain the higher initial specific capacitance in the CV experiment because it means a faster diffusion.

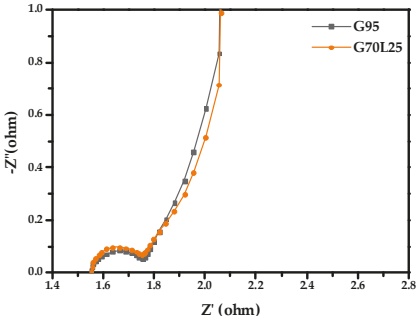

Figure 8. Impedance spectra of the G95 and G70L25 electrodes, measured at an AC amplitude of 10 mV, in H_2SO_4 electrolyte.

The G70L25 electrode exhibits increasing ohmic resistance, which may originate from the low electrical conductivity of LSMCO perovskite oxide.

4. Conclusions

In summary, the supercapacitor electrode was prepared by the synthesis of graphene and perovskite material (LSMCO). XRD showed that it was well mixed without a secondary reaction. According to electrochemical analyses, for the G95 electrode, the specific capacitance ranges from 53 to 68 F/g, and the standard deviation is about 6. For the G70L25 electrode, the specific capacitance ranges from 49 to 55 F/g, and the standard deviation ranges from 1 to 2.5. The initial specific capacity of the G70L25 electrode of 49 to 55 F/g is about 10%–20% smaller than that of the G95 but has a small standard deviation. The cycling test showed that the specific capacitance of G70L25 was reduced (~5%) at all times, indicating that the cycling stability was improved compared to the unpredictable (both cases increasing or decreasing) results of G95. Therefore, the supercapacitor using LSMCO and graphene electrode is better for commercialization considering the repeatable performance and seems to be an excellent material for improving cycling stability in other electrochemical applications.

Author Contributions: Conceptualization, Y.-W.J. and J.S.; data curation, B.-M.K. and H.-Y.K.; investigation, B.-M.K. and H.-Y.K.; methodology, J.S.; supervision, Y.-W.J. and J.S.; validation, B.-M.K., H.-Y.K., Y.-W.J., and J.S.; visualization, B.-M.K. and H.-Y.K.; writing – original draft, B.-M.K.; writing – review and editing, Y.-W.J. and J.S. All authors have read and agreed to the published version of the manuscript.

Funding: This research was supported by the Basic Science Research Program through the National Research Foundation of Korea (NRF), funded by the Ministry of Education (No. NRF-2018R1D1A1A02085324). This research was supported by the Mid-Career Researcher Program (No. NRF-2020R1A2C1007847) through the National Research Foundation of Korea, funded by the Korean government's Ministry of Education.

Conflicts of Interest: The authors declare no conflicts of interest.

References

1. Simon, P.; Gogotsi, Y. Materials for electrochemical capacitors. *Nat. Mater.* **2008**, *7*, 845–854. [CrossRef]
2. Obreja, V.V.N. On the performance of supercapacitors with electrodes based on carbon nanotubes and carbon activated material—A review. *Phys. E Low Dimens. Syst. Nanostruct.* **2008**, *40*, 2596–2605. [CrossRef]
3. Conway, B.E. *Electrochemical Supercapacitors: Scientific Fundamentals and Technological Applications*; Springer Science & Business Media, LLC: New York, NY, USA, 2013.
4. Augustyn, V.; Simon, P.; Dunn, B. Pseudocapacitive oxide materials for high-rate electrochemical energy storage. *Energ. Environ. Sci.* **2014**, *5*. [CrossRef]
5. Guidelli, R.; Schmickler, W. Electrosorption valency and partial charge transfer. *Mod. Asp. Electrochem.* **2005**, *38*, 303–371.
6. Herrero, E.; Buller, L.J.; Abruña, H.D. Underpotential deposition at single crystal surfaces of Au, Pt, Ag and other materials. *Chem. Rev.* **2001**, *101*, 1897–1930. [CrossRef] [PubMed]
7. Zheng, J.P. A new charge storage mechanism for electrochemical capacitors. *J. Electrochem. Soc.* **1995**, *142*, L6. [CrossRef]
8. Augustyn, V.; Come, J.; Lowe, M.A.; Kim, J.W.; Taberna, P.L.; Tolbert, S.H.; Abruña, H.D.; Simon, P.; Dunn, B. High-rate electrochemical energy storage through Li + intercalation pseudocapacitance. *Nat. Mater.* **2013**, *12*, 518–522. [CrossRef]
9. Brezesinski, T.; Wang, J.; Tolbert, S.H.; Dunn, B. Ordered mesoporous α-MoO3 with iso-oriented nanocrystalline walls for thin-film pseudocapacitors. *Nat. Mater.* **2010**, *9*, 146–151. [CrossRef]
10. Bai, L.; Ge, Y.; Bai, L. Boron and Nitrogen co-doped porous carbons synthesized from polybenzoxazines for high-performance supercapacitors. *Coatings* **2019**, *9*, 657. [CrossRef]
11. Heydari Gharahcheshmeh, M.; Gleason, K.K. Device fabrication based on oxidative chemical vapor deposition (CVD) synthesis of conducting polymers and related conjugated organic materials. *Adv. Mater. Interfaces* **2019**, *6*, 1801564. [CrossRef]
12. Feng, N.; Meng, R.; Zu, L.; Feng, Y.; Peng, C.; Huang, J.; Liu, G.; Chen, B.; Yang, J. A polymer-direct-intercalation strategy for MoS $_2$/carbon-derived heteroaerogels with ultrahigh pseudocapacitance. *Nat. Commun.* **2019**, *10*, 1–11. [CrossRef]
13. Cao, M.S.; Wang, X.X.; Cao, W.Q.; Yuan, J. Ultrathin graphene: Electrical properties and highly efficient electromagnetic interference shielding. *J. Mater. Chem. C* **2015**, *3*, 6589–6599. [CrossRef]
14. Ji, X.; Xu, Y.; Zhang, W.; Cui, L.; Liu, J. Review of functionalization, structure and properties of graphene/polymer composite fibers. *Compos. Part A Appl. Sci. Manuf.* **2016**, *87*, 29–45. [CrossRef]
15. Wang, J.; Li, Z.; Fan, G.; Pan, H.; Chen, Z.; Zhang, D. Reinforcement with graphene nanosheets in aluminum matrix composites. *Scr. Mater.* **2012**, *66*, 594–597. [CrossRef]
16. Zhai, W.; Shi, X.; Wang, M.; Xu, Z.; Yao, J.; Song, S.; Wang, Y.; Zhang, Q. Effect of graphene nanoplate addition on the tribological performance of Ni3Al matrix composites. *J. Comp. Mater.* **2013**, *48*, 3727–3733. [CrossRef]
17. Ruiz, V.; Santamaría, R.; Granda, M.; Blanco, C. Long-term cycling of carbon-based supercapacitors in aqueous media. *Electrochim. Acta* **2009**, *54*, 4481–4486. [CrossRef]
18. Yan, J.; Wei, T.; Fan, Z.; Qian, W.; Zhang, M.; Shen, X.; Wei, F. Preparation of graphene nanosheet/carbon nanotube/polyaniline composite as electrode material for supercapacitors. *J. Power Sources* **2010**, *195*, 3041–3045. [CrossRef]
19. Sengodan, S.; Choi, S.; Jun, A.; Shin, T.H.; Ju, Y.W.; Jeong, H.Y.; Shin, J.; Irvine, J.T.S.; Kim, G. Layered oxygen-deficient double perovskite as an efficient and stable anode for direct hydrocarbon solid oxide fuel cells. *Nat. Mater.* **2015**, *14*, 205–209. [CrossRef]
20. Kim, S.; Kwon, O.; Kim, C.; Gwon, O.; Jeong, H.Y.; Kim, K.H.; Shin, J.; Kim, G. Strategy for enhancing interfacial effect of bifunctional electrocatalyst: Infiltration of cobalt nanooxide on perovskite. *Adv. Mater. Interfaces* **2018**, *5*, 1800123. [CrossRef]
21. Gwon, O.; Kim, C.; Kwon, O.; Jeong, H.Y.; Park, H.-K.; Shin, J.; Ju, Y.-W.; Kim, G. An efficient oxygen evolution catalyst for hybrid lithium air batteries: Almond stick type composite of perovskite and cobalt oxide. *J. Electrochem. Soc.* **2016**, *163*, A1893–A1897. [CrossRef]
22. Ishihara, T. *Perovskite Oxide for Solid Oxide Fuel Cells*; Springer Science & Business Media: Berlin, Germany, 2009.

23. Mefford, J.T.; Hardin, W.G.; Dai, S.; Johnston, K.P.; Stevenson, K.J. Anion charge storage through oxygen intercalation in LaMnO $_3$ perovskite pseudocapacitor electrodes. *Nat. Mater.* **2014**, *13*, 726–732. [CrossRef] [PubMed]
24. Wohlfahrt-Mehrens, M.; Schenk, J.; Wilde, P.M.; Abdelmula, E.; Axmann, P.; Garche, J. New materials for supercapacitors. *J. Power Sources* **2002**, *105*, 182–188. [CrossRef]
25. Lim, C.; Kim, C.; Gwon, O.; Jeong, H.Y.; Song, H.K.; Ju, Y.W.; Shin, J.; Kim, G. Nano-perovskite oxide prepared via inverse microemulsion mediated synthesis for catalyst of lithium-air batteries. *Electrochim. Acta* **2018**, *275*, 248–255. [CrossRef]
26. Liu, Y.; Dinh, J.; Tade, M.O.; Shao, Z. Design of perovskite oxides as anion-intercalation-type electrodes for supercapacitors: Cation leaching effect. *ACS Appl. Mater. Interfaces* **2016**, *8*, 23774–23783. [CrossRef] [PubMed]
27. Saranya, P.; Selladurai, S. Facile synthesis of NiSnO $_3$/graphene nanocomposite for high-performance electrode towards asymmetric supercapacitor device. *J. Mater. Sci.* **2018**, *53*, 16022–16046. [CrossRef]
28. He, L.; Shu, Y.; Li, W.; Liu, M. Preparation of La $_{0.7}$ Sr $_{0.3}$ CoO $_{3-\delta}$ (LSC)@ MnO $_2$ core/shell nanorods as high-performance electrode materials for supercapacitors. *J. Mater. Sci. Mater. Electron.* **2019**, *30*, 17–25. [CrossRef]
29. Yin, S.; Wu, Y.; Chen, J.; Chen, Z.; Hou, H.; Liu, Q.; Wang, Y.; Zhang, W. Facile hydrothermal synthesis of BiFeO3 nanoplates for enhanced supercapacitor properties. *Funct. Mater. Lett.* **2018**, *11*, 1850013. [CrossRef]
30. George, G.; Jackson, S.L.; Luo, C.Q.; Fang, D.; Luo, D.; Hu, D.; Wen, J.; Luo, Z. Effect of doping on the performance of high-crystalline SrMnO3 perovskite nanofibers as a supercapacitor electrode. *Ceramics Int.* **2018**, *44*, 21982–21992. [CrossRef]
31. Kim, H.-Y.; Shin, J.; Jang, I.-C.; Ju, Y.-W. Hydrothermal synthesis of three-dimensional perovskite $NiMnO_3$ oxide and application in supercapacitor electrode. *Energies* **2020**, *13*, 36. [CrossRef]
32. Lang, X.; Mo, H.; Hu, X.; Tian, H. Supercapacitor performance of perovskite $La_{1-x}Sr_xMnO_3$. *Dalton Trans.* **2017**, *46*, 13720–13730. [CrossRef]
33. Wei, R.; Fang, M.; Dong, G.; Ho, J.C. Is platinum a suitable counter electrode material for electrochemical hydrogen evolution reaction? *Sci. Bull.* **2017**, *62*, 971–973. [CrossRef]
34. Gardner, S.D.; Singamsetty, C.S.K.; Booth, G.L.; He, G.R.; Pittman, C.U. Surface characterization of carbon fibers using angle-resolved XPS and ISS. *Carbon* **1995**, *33*, 587–595. [CrossRef]
35. Arrigo, R.; Hävecker, M.; Wrabetz, S.; Blume, R.; Lerch, M.; McGregor, J.; Parrott, E.P.J.; Zeitler, J.A.; Gladden, L.F.; Knop-Gericke, A.; et al. Tuning the acid/base properties of nanocarbons by functionalization via amination. *J. Am. Chem. Soc.* **2010**, *132*, 9616–9630. [CrossRef] [PubMed]
36. Liu, W.W.; Yan, X.B.; Xue, Q.J. Multilayer hybrid films consisting of alternating graphene and titanium dioxide for high-performance supercapacitors. *J. Mater. Chem. C* **2013**, *1*, 1413–1422. [CrossRef]
37. Dezfuli, A.S.; Ganjali, M.R.; Naderi, H.R.; Norouzi, P. A high performance supercapacitor based on a ceria/graphene nanocomposite synthesized by a facile sonochemical method. *RSC Adv.* **2015**, *5*, 46050–46058. [CrossRef]
38. Zhang, C.; Lei, C.; Cen, C.; Tang, S.; Deng, M.; Li, Y.; Du, Y. Interface polarization matters: Enhancing supercapacitor performance of spinel NiCo2O4 nanowires by reduced graphene oxide coating. *Electrochim. Acta* **2018**, *260*, 814–822. [CrossRef]
39. Szunerits, S.; Boukherroub, R. Electrochemistry of graphene: The current state of the art. *Electrochemistry* **2013**, *12*, 211–242.
40. Kim, C.; Gwon, O.; Jeon, I.-Y.; Kim, Y.; Shin, J.; Ju, Y.-W.; Baek, J.-B.; Kim, G. Cloud-like graphene nanoplatelets on Nd $_{0.5}$ Sr $_{0.5}$ CoO $_{3-\delta}$ nanorods as an efficient bifunctional electrocatalyst for hybrid Li–air batteries. *J. Mater. Chem. A* **2016**, *4*, 2122–2127. [CrossRef]
41. Mei, B.A.; Munteshari, O.; Lau, J.; Dunn, B.; Pilon, L. Physical interpretations of Nyquist plots for EDLC Electrodes and Devices. *J. Phys. Chem. C* **2018**, *122*, 194–206. [CrossRef]

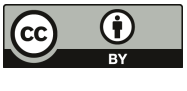

energies

MDPI

Article

Natural Polymers for Green Supercapacitors

Giovanni Emanuele Spina †, Federico Poli †, Alessandro Brilloni, Daniele Marchese and Francesca Soavi *

Department of Chemistry "Giacomo Ciamician", Alma Mater Studiorum Universita' di Bologna, Via Selmi 2, 40126 Bologna, Italy; giovanni.spina3@unibo.it (G.E.S.); federico.poli8@unibo.it (F.P.); alessandro.brilloni2@unibo.it (A.B.); daniele.marchese@studio.unibo.it (D.M.)

* Correspondence: francesca.soavi@unibo.it

† These authors contributed equally.

Received: 11 May 2020; Accepted: 10 June 2020; Published: 16 June 2020

Abstract: Water-processable natural polymers represent a valuable alternative for the sustainable manufacturing of electrical double layer capacitors (EDLCs). Here, we demonstrate for the first time the feasibility of the use of pullulan to produce high mass loading electrodes (>10 mg cm^{-2}) at low binder content (10%) for ionic-liquid based EDLCs. Pullulan has also been processed as a porous separator by electrospinning. Its ionic resistance and thermal stability have been evaluated in different electrolytes and were found to be superior compared to those of a cellulose triacetate electrospun separator. Pullulan-ionic liquid EDLCs were, thus, assembled and charged up to 3.2 V. The EDLCs delivered specific energy and power of 7.2 Wh kg^{-1} and 3.7 kW kg^{-1} and featured good cycling stability over 5000 cycles.

Keywords: green supercapacitor; water processable polymer; pullulan; ionic liquid; electrospinning

1. Introduction

Today one of the biggest challenges our society is facing is how to replace the use of fossil energy sources (coal, oil, gas) with renewable ones (solar and wind). The inherent intermittence of the latter sources requires the development of efficient energy storage systems. Among all the possibilities, electrochemical energy storage by secondary batteries and electrical double layer capacitors (EDLCs) is one of the most efficient approach [1–4]. EDLCs are receiving great attention for their unique characteristics of outstanding power and cycle life, that are related to their electrostatic operating mechanism. However specific energies of EDLCs are one order of magnitude lower than that of batteries.

Commercial EDLCs feature activated carbon (AC) electrodes, a porous polymer separator, and an organic electrolyte, typically a solution of alkylammonium salts in acetonitrile or propylene carbonate. The use of the organic electrolyte enables cell voltages as high as 2.5 V [5].

The energy density of EDLCs can be improved by increasing: (i) the operating voltage window, (ii) electrodes specific capacitance, and (iii) the mass loading of the electrodes.

High operating voltage can be achieved by using an electrolyte with a wide electrochemical stability window, like ionic liquids (ILs) or highly concentrated aqueous electrolytes [6–9]. Electrode specific capacitance can be improved by tailoring carbon porosity to the electrolyte, in order to enhance ion access to the carbon surface. An alternative strategy is represented by the use of redox (pseudocapacitive) electrode materials, like metal oxides or electronically conductive polymers, in asymmetric or hybrid supercapacitors. Regarding the third approach, literature provides a very limited number of publications. Achieving mass loading higher than 5–10 mg cm^{-2} is considered a great challenge. Indeed, thick electrodes might delaminate from the current collector that is detrimental

for cycling stability. Furthermore, high mass loading may lead to worse ionic and electronic connection between the carbon particles, leading to higher internal resistance [10–12].

Ionic liquids, thanks to their low flammability, represent an even safer alternative to the more volatile acetonitrile solutions. In addition, ILs are known for their high thermal stability, good conductivity and wide electrochemical stability window (>3 V). Despite these interesting properties, they cannot be considered as totally green and strategies to recover them after use are needed. The most investigated ILs for EDLCs are based on the bis(trifluoromethanesulfonyl)imide (TFSI) anion [13–15]. ILs feature bulky ions, therefore in order to promote a high and efficient exploitation of the electron carbon surface of the double layer, the porosity of the carbon has to be properly designed [16,17]. Furthermore, it has been demonstrated that the chemistry of ILs affects the double layer thickness and permittivity, and hence, the electrode capacitance. Indeed, in Ref. [1,2], the capacitive response of different carbon electrodes in *N*-butyl-*N*-methylpyrrolidinium bis(trifluoromethane-sulfonyl)imide ($PYR_{14}TFSI$), 1-ethyl-3-methylimidazolium bis(trifluoromethanesulfonyl)imide (EmimTFSI) and $PYR_{(2O1)}TFSI$ was compared. In EmimTFSI, all the tested electrodes featured a specific capacitance that was double than that exhibited in the other ILs.

In EDLCs the biggest share of the cost is related to electrodes (28%) and electrolytes (27%). Electrodes are processed by casting slurries made of AC, conductive carbon, binder, and suitable solvents on metal current collectors. The binder material itself does not contribute significantly to the overall cost. However, its chemistry drives the selection of the solvent used for electrode processing, that has a great economic and environmental impact on EDLCs manufacturing [18]. Indeed, nowadays, commercial AC electrodes are mostly fabricated with F-based polymers as binders, such as poly (vinylidene difluoride) (PVdF) which needs N-methyl-2-pyrrolidone (NMP) as solvent/dispersant, both very toxic for humans and environment. This process requires expensive atmosphere-controlled environments [19].

In light of that and to meet the requirements of sustainable and cheaper production processes, much effort is being devoted to the substitution of F-based components with alternative ones. Transition to aqueous electrode preparation by non-toxic binders is expected to provide a great step forward towards an ideally sustainable and environmentally friendly technology for energy storage systems [20,21].

Carboxymethyl cellulose (CMC) represents the state of the art of water-soluble binders [10,21–24]. One of the first attempts of substituting F-based compounds with CMC, was reported by Bonnefoi et al. in 1999 [25]. Two of the major drawbacks in the use of CMC, are: (i) the relatively low achievable electrode mass loading, and (ii) the brittleness shown after the drying step. Winter et al. [23], first proposed Natural Cellulose (NC). While NC is cheaper (0.5–1.5 EUR kg^{-1} vs. 1–2 EUR kg^{-1}) and more abundant than CMC, it cannot be dissolved in water nor in almost all organic solvents while being soluble in certain ionic liquids [26–29]. Varzi et al. dissolved NC in 1-ethyl-3-methylimidazolium acetate (EmimAc) and demonstrated that NC has enhanced stability at high voltages. An EDLC assembled with electrodes featuring 10% NC binder and a mass loading of ca. 3 mg cm^{-2} and $PYR_{14}TFSI$ ionic liquid electrolyte, exhibited a specific capacitance of ca. 13 F g^{-1} at 10 mA cm^{-2}, and a capacitance retention of 52%, after cycling for 750 h at 3.7 V [30]. Pursuing the research of even more eco-friendly binders, potato starch, a highly abundant polysaccharide that can be extracted from non-edible potatoes, was also proposed. By the use of this polysaccharide, the production of thick electrodes (240 μm, 9.3 mg cm^{-2}) was demonstrated [18]. These electrodes were used to assemble a 2.5 V-EDLC with 1 M Et_4NBF_4 in propylene carbonate (PC) electrolyte, that delivered 0.36 F cm^{-2} at 10 mA cm^{-2}.

Recently, we demonstrated the use of the biodegradable biopolymer pullulan (Pu) as a water processable separator and binder for EDLCs. Specifically, the separator was obtained by electrospinning and the EDLCs featured EmimTFSI electrolyte and pepper seed derived biochar carbon. The EDLC was able to operate at 3.2 V and delivered up to 5 kW kg^{-1} specific power and 27.8 Wh kg^{-1} specific energy. Its performances were compared with that of conventional electrical double-layer capacitor, with the added value of being eco-friendly and cheap.

Furthermore, the smart combination of the water-soluble, biodegradable Pu with the hydrophobic ionic liquid EmimTFSI, enabled a novel and easy approach for the recovery of EDLC components at the end-of-life. Indeed, the IL and carbon easily separate when immersed in water. The expensive IL can therefore be recollected for a second use [31].

Following these preliminary results, here we report the challenging study that aims to demonstrate the feasibility of the use of Pu to process electrodes at low binder content (10%) and high mass loading (>10 mg cm^{-2}). In the first part of our work we compare the electrochemical response and thermal stability of Pu and cellulose triacetate (CTA) in different electrolytes, namely EmimTFSI, 0.5 m LiTFSI TEGDME, PYR_{14}TFSI. The two natural polymers have been processed by electrospinning and their contribution to ionic resistance of the electrolyte has been investigated by Electrochemical Impedance Spectroscopy (EIS) at different temperatures. On the basis of this investigation, Pu and EmimTFSI were selected to assemble two different EDLCs, one with low electrode mass loading and high binder content (HBLME) and a second one with high mass loading and low binder content (LBHME). The EDLCs have been tested by cyclic voltammetry, EIS and galvanostatic charge/discharge cycles. A deep analysis of the EDLCs performance is reported and discussed to demonstrate that natural polymers and, specifically Pu, may pave the way towards a new approach for a green manufacturing of EDLCs.

2. Materials and Methods

2.1. Materials

N-butyl-*N*-methylpyrrolidinium bis(trifluoromethanesulfonyl)imide (PYR_{14}TFSI, purity >99.9%) was purchased from Solvionic (Toulouse, France). 1-Ethyl-3-methylimidazolium bis(trifluoromethanesulfonyl) imide (EmimTFSI, purity >99%) was purchased from Solvent Innovation (Köln, Germany). Lithium bis(trifluoromethanesulfonyl)imide and tetraethylene glycol dimethyl ether (TEGDME) (purity >99%) were both purchased from Sigma-Aldrich (St. Louis, MO, USA). Activated carbon PICACTIF was purchased from PICA (Basiano, Italy). Conductive carbon additive (SUPER C45) was purchased from TIMCAL (Bodio, Switzerland). Pullulan (P0978, η = 15.0 ÷ 180.0 mPa s, 10% in H_2O at 30 °C) was purchased from TCI Europe (Zwijndrecht, Belgium). Cellulose triacetate (CTA, Mw = 74,000 g/mol, DS 3.0) was purchased from Honeywell Fluka (Charlotte, NC, USA). Glycerol (purity >99%) was purchased from Sigma-Aldrich. Nickel foam was purchased from Alantum (Munich, Germany).

2.2. Preparation of the Electrospun Separator

Electrospinning was used to prepare the non-woven separator. In particular an home-made electrospinning apparatus has been used, this consisted of a high-voltage power supply (SL 50 P 10/CE/230, Spellman, West Sussex, UK), a syringe pump (200 series, KD Scientific, Holliston, MA, USA), a glass syringe containing the polymer solution and connected to a stainless-steel blunt-ended needle (inner diameter = 0.51 mm) through a polytetrafluoroethylene (PTFE) tube. The Pu membrane was electrospun starting from a 23% *w/v* solution of pullulan in Milli-Q water. The solution was spun at 18 kV at 20 cm from the collector with a flow rate of 1 mL h^{-1}. The cellulose triacetate (CTA) separator has been electrospun starting from a 6% *w/v*. solution in DCM/EtOH 80/20 solution. The solution was spun at 15 kV and at a 15 cm distance from the collector with a flowrate of 2 mL/h, at room temperature (RT) with a relative humidity of 40–50%. After electrospinning the mat has been soaked into a 0.1 M solution of sodium hydroxide in a mixture of Ethanol and water 4:1 *v/v* for 24 h. In the end the electrospun separator was washed in MilliQ water twice for fifteen minutes each.

2.3. Membrane Characterization

Electrospun membranes have been characterized at first by scanning electron microscopy (SEM) using an EVO 50 apparatus (Zeiss, Oberkochen, Germany). The feasibility of the use of the electrospun mats as separators was evaluated by EIS. Swagelok-type cells with two stainless steel blocking electrodes (0.9 cm diameter), separated by the membranes (dried overnight before use at RT) soaked in

the different investigated electrolytes, were used. The EIS spectra were collected by a VSP multichannel potentiostat/galvanostat/FRA (BioLogic, Seyssinet-Pariset, France) within 500 kHz–100 mHz frequency range and 5 mV AC perturbation, acquiring 10 points per decade. The cells were thermostated at 30, 40 and 60 °C by a thermostatic oven. The bulk conductivity of the electrolytes without membranes were measured by a CDM 210 Conductivity Meter (MeterLab, Milano, Italy) with an Amel standard cell (platinum electrodes). The temperature was controlled by a DC50 K40 thermocryostat (Haake, Thermo Fisher Scientific, Karlsruhe, Germany) with an accuracy of 0.1 °C. Samples were thermostated for 1 h before every measurement.

2.4. Preparation of the Electrodes

Electrodes were prepared using the mesoporous carbon PICACTIF from PICA (BP10) as reported in [8] and described in Figure S1a. BP10 featured a Brunauer, Emmett and Teller (BET) specific surface >2000 m^2 g^{-1} and a pores size distribution centered at 2.7 nm [8]. Two water processable formulations have been studied. A first one with 70% BP10, 10% Carbon black, 20% pullulan-glycerol (1:1 wt) and low mass loading (3.6–4.6 mg cm^{-2}) is referred in the following text as high binder low mass electrode (HBLME). A second one with 85% BP10, 5% Carbon black, 10% pullulan-glycerol and higher mass loading is labelled as low binder high mass electrode (LBHME). Electrodes have been obtained by casting on pre-cut nickel foams (diameter 0.9 cm) a slurry containing 23.5 mg of BP10, 3.5 mg of carbon black (as conducting additive), 6.7 mg of pullulan (P0978, TCI) and glycerol in 0.8 g of MilliQ water for HBLME. For LBHME the ink was composed of 40.2 mg of BP10, 2.3 mg of carbon black (as conducting additive), 4.7 mg of pullulan and glycerol in 0.57 g of MilliQ water. The electrodes were then dried in an oven (under vacuum) overnight at room temperature (Büchi glass oven B-585). The composite electrode loadings (excluding the nickel foam mass) are reported in Table 1.

Table 1. Composition and mass loading of High Binder Low Mass Electrode (HBLME) and Low Binder High Mass Electrode (LBHME).

Name	Composition	Mass Loading Range *
HBLME	70% BP10/10% CB/20% binder	3.6–4.6 mg cm^{-2}
LBHME	85% BP10/5% CB/10% binder	6.3–7.5 mg cm^{-2}

* single electrodes mass loading.

2.5. Supercapacitor Assembly

A T Swagelok-type cell assembly (BOLA Cell made from Teflon, BOLA GmbH, Grünsfeld, Germany) with a silver quasi-reference electrode disk and stainless-steel current collectors was used. Cells were assembled in a dry box (Labmaster 130, H_2O, and O_2 <0.1 ppm MBraun, Garching, Germany). The separator (12 mm diameter) and the electrodes (9 mm diameter) were soaked under vacuum together with the IL before the assembly. The ratio of the positive to negative electrode composite loading was >1 to achieve cell voltages higher than 3 V [32]. EDLCs were assembled with two carbon based composite electrodes alienated by a circular sheet of electrospun pullulan separator, with 1-ethyl-3-methylimidazolium bis(trifluoro-methylsulfonyl) imide IL (EmimTFSI) as the electrolyte, as described in Figure S1b.

2.6. Supercapacitor Characterization

The electrochemical tests consisted in EIS, cyclic voltammetry (CV) and galvanostatic (GCPL) tests and were performed in a thermostatic oven at 30 °C using a BioLogic VSP multichannel potentiostat/galvanostat/FRA. EIS was performed with a 100 kHz–100 mHz frequency range and 5 mV AC perturbation, acquiring 10 points per decade. To evaluate the impedance of each of the EDLC electrodes, three electrode measurements, have been done. A silver disk has been used as pseudo reference. Here, the working electrode was the tested one and counter the other. To evaluate the

complete cell impedance, two electrode measurement have been done. For two electrode measurements, the silver disk was disconnected, the EDLC positive electrode was the working, and the EDLC negative electrode was connected to the counter and reference instrument plugs.

CV discharge curves were analyzed to get a first evaluation of the EDLC specific capacitance (C_{EDLC}). Specifically, C_{EDLC} was calculated from the slope of the voltammetric plots of the discharge capacity vs. cell voltage. The capacity was calculated by the integral of the CV current over time. The slope values were divided by the total composite mass of the two electrodes (m_{tot}).

The GCPL curves were analyzed to quantify the equivalent series resistance (ESR) and the C_{EDLC}, the specific energy and power of the devices at different discharge currents. ESR was calculated according to Equation (1), where ΔV_{ohmic} is the ohmic voltage drop at the beginning of discharge, and i is the current density (A cm^{-2}):

$$ESR = \Delta V_{ohmic}/(2 \times i) \quad (1)$$

C_{EDLC} was calculated from the reciprocal of the slope of the GCPL voltage profile during the discharge (dt/dV) by Equation (2):

$$C_{EDLC} = i \times dt/dV/m_{tot} \quad (2)$$

The single electrode specific capacitance ($C_{electrode}$) was therefore calculated from the EDLC's one by Equation (3)

$$C_{electrode} = 4 \times C_{EDLC} \quad (3)$$

The EDLCs specific energy (E) and power (P) were calculated from the GCPL discharge curves through Equations (4) and (5):

$$E = i \int V \times dt/(3600 \times m_{tot}) \quad (4)$$

$$P = 3600 \times E/\Delta t \quad (5)$$

where Δt is the discharge time in seconds.

3. Results

3.1. Electrospun Separator and Electrolyte Selection

Figure 1a,b report the SEM images of the electrospun Pu and CTA membranes, respectively. They feature interconnected fibers, randomly deposited, with a low number of defects. The Pu mat thickness was 55 μm and the mean fiber diameter was around 0.3 μm. The CTA mat thickness was 22 μm and the mean fiber diameter was around 0.6 μm. The fiber thickness of the two mats is in line with the value already reported for electrospun separators obtained with different polymers [33]. Furthermore, the PU and CTA mat thicknesses were adequate for an easy handling and assembly of the EDLCs. In addition to the difference in fiber diameter, the two polymers differ in terms of fiber diameter distribution, the CTA fibers being less homogeneous with a broader distribution.

Before the evaluation of the ionic conductivity response of the membranes, at first bulk conductivity of the electrolytes was measured. The values at different temperatures are reported in Table 2. The ionic conductivity of all the tested electrolytes grows with temperature. Among the considered electrolytes, the most conductive one is the EmimTFSI. Specifically, at 30 °C EmimTFSI features 12.6 mS cm^{-1}, which is 5-fold higher than the conductivity of 0.5 m LiTFSI in TEGDME (2.05 mS cm^{-1}) and PYR_{14}TFSI (3.01 mS cm^{-1}).

The separators of the EDLCs should be designed in order to achieve low ESR. This can be obtained by minimizing their hindrance to the ion flow during the charge/discharge, while guaranteeing the electronic separation of the two electrodes.

In order to evaluate the contribution of the investigated separators and electrolytes to ESR, EIS measurements were performed. The tests were carried out using cells with stainless steel blocking electrodes separated by the separator soaked with the electrolyte. EIS was carried out at constant

interval of time (24 h) and at different temperature (30 °C, 40 °C and 60 °C) to check the chemical and electrochemical stability of the different membranes in the tested electrolytes.

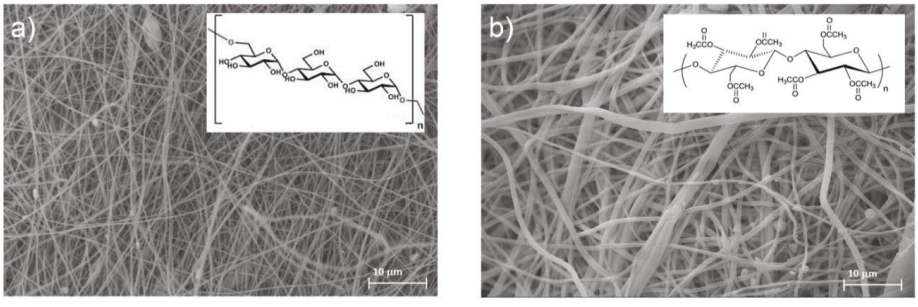

Figure 1. SEM images of electrospun membrane of (**a**) pullulan and (**b**) cellulose triacetate with their molecular structures.

Table 2. Ionic conductivity of the tested electrolytes at different temperatures.

Conductivity (mS cm^{-1})	σ (30°)	σ (40°)	σ (60°)
EmimTFSI	12.60	15.10	25.70
0.5 m LiTFSI in TEGDME	2.05	2.63	4.82
PYR_{14} TFSI	3.01	3.90	6.30

As an example, Figure 2 reports the Nyquist plots of the electrospun pullulan separator in EmimTFSI over time at the different tested temperatures. The Nyquist plots for all the combination of Pu and CTA membranes with the different electrolytes are reported in Figure S2.

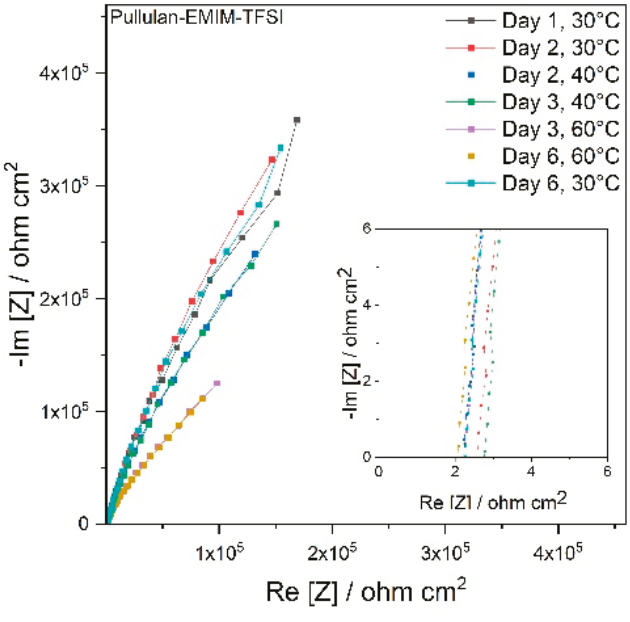

Figure 2. Nyquist plot of Pullulan electrospun membrane in EmimTFSI electrolyte.

In Figure 2, the impedance spectra of the Pullulan membrane resemble a straight line. This response can be modelled with a resistance (R) in series with a constant phase element (Q), therefore the resulting impedance is given by the following equation:

$$Z = R - 1/(j\ \omega\ Q)^n \quad (6)$$

In Equation (6), R is the equivalent resistance of the separator soaked in the electrolyte and can be evaluated from the intercept with the real axis in the 150–300 kHz frequencies region. It includes the electronic resistance of the current collectors and the ionic resistance of the cell which reasonably dominates the response. When n = 1, the plot is a line parallel to the imaginary axis and Q represents the capacitive response of the cell. When n = 0.5, the plot is a line with a slope of 45° and Q corresponds to the Warburg element that is representative of diffusion-controlled processes.

Figure 2 shows that the temperature increase leads to the decrease of the resistance of the cell that is related to the increase of the electrolyte conductivity (cf. Table 2). In parallel, it is noticeable that the slope of the Nyquist plot decreases, unveiling that ion diffusion through the membrane becomes more sluggish.

This behaviour could be explained with the swelling of the membrane at the highest temperature that, in turn, brings about thickening of the fibres and narrowing of the inter-fibre voids. This might result in a more tortuous path for ion conduction.

Tables S1 and S2 and Figure 3a,b report the values of resistance of Pu and CTA membrane respectively, at different temperatures over time, in the different electrolytes. The values are in the same order of magnitude and span between ca. 2 and 5 ohm cm^2. The first day at 30 °C, Pu features 2, 3 and 3.5 Ohm cm^2 when soaked with EmimTFSI, 0.5 m LiTFSI TEGDME and $PYR_{14}TFSI$, respectively. CTA exhibits 2, 3 and 3.5 Ohm cm^2 with EmimTFSI, 0.5 m LiTFSI TEGDME and $PYR_{14}TFSI$. Therefore, resistance values are similar for both membranes in the same electrolytes, with EmimTFSI accounting for the smallest values. A more straightforward comparison must consider the mat thickness of both separators and can be carried out referring to the effective resistivity (ϱ_{eff}) of the membrane-electrolyte system. The value of ϱ_{eff} can be obtained by Equation (7):

$$\varrho_{eff} = S \times R/L \quad (7)$$

where R is the resistance (in Ohm), L is the membrane thickness (cm), and S is the current collector area (cm^2).

As commented above, Pu separator features a thickness of 55 μm that is almost 2.5 times larger than the CTA's that is 22 μm. Therefore, ϱ_{eff} of Pu at 30 °C in EmimTFSI results 450 Ohm cm and is almost half than CTA's (over 1000 Ohm cm). This can be related to the thinner fibres of the former membrane (0.3 μm) vs. the latter (0.6 μm). Thinner fibres provide a greater surface area and a greater density of free volume that can be exploited by ions to achieve higher conductivity. Noticeably, the resistance values of Pu at the different temperatures keep almost constant during time. At the contrary, those of CTA membrane gradually increase achieving 5 Ohm cm^2 at 60 °C, after 5 days, a value that doubles the Pu ones. Furthermore, after six day, the temperature was lowered to 30 °C. The resistance of Pu-EmimTFSI went back to its initial value while the CTA-EmimTFSI ones doubled (4 Ohm cm^2). This indicates that the swelling process promoted by the increase of temperature is reversible for Pu but not for CTA. Overall, the data of Figure 2 suggest that Pu membrane is more stable than CTA.

In order to get further insight into the contribution of the separator to the ESR, the Mac Mullin number (N_M) has been calculated for all the tested systems. Indeed, N_M quantifies the increase of resistivity of the separator soaked in the electrolyte (ϱ_{eff}) with respect to the bulk resistivity of the electrolyte solution (ϱ_0), and it is calculated after Equation (8):

$$N_M = \varrho_{eff}/\varrho_0 \quad (8)$$

where ϱ_{eff} has been evaluated by Equation (6) using the resistance values listed in Tables S3 and S4. In turn, ϱ_0 is the reciprocal of the electrolyte conductivity (σ_0) and is calculated by Equation (9):

$$\varrho_0 = 1/\sigma_0 \quad (9)$$

The N_M values for the different separator/electrolyte combinations at the different temperatures are reported in Tables S5 and S6 and in Figure 3c,d as comparative histograms.

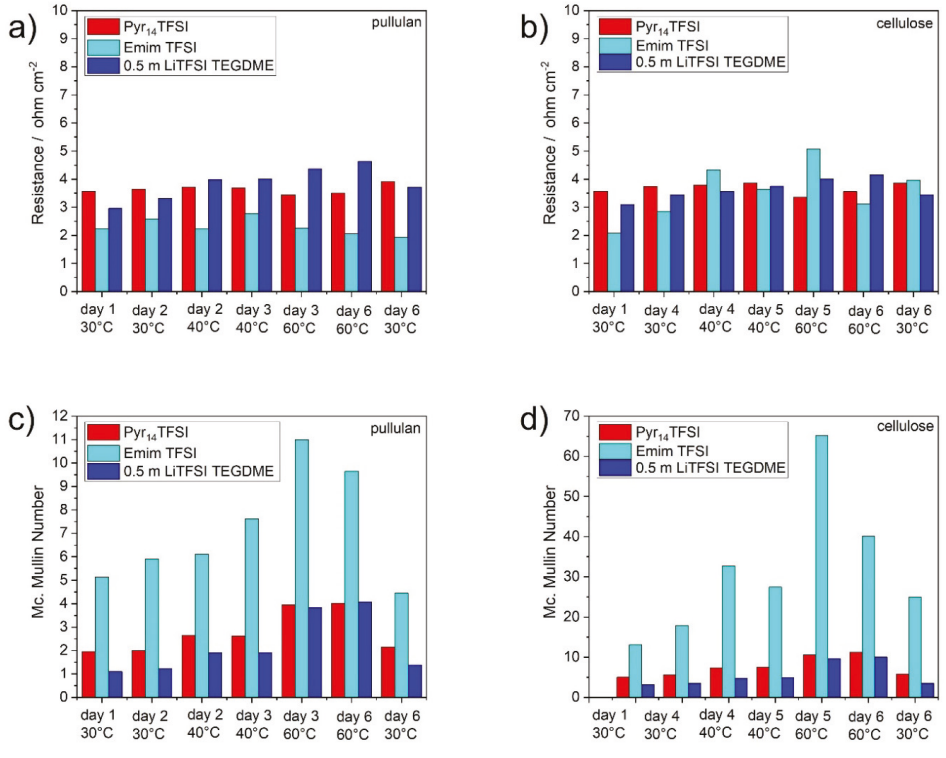

Figure 3. Resistance normalized by the plain area and MacMullin number of (**a**,**c**) Pullulan and (**b**,**d**) Cellulose triacetate electrospun separators in different tested electrolytes.

The values of the Pu are always smaller than those of the CTA in all the tested condition. For both membranes, in all the tested conditions, EmimTFSI holds the greater values of N_M, while the smaller ones are exhibited by 0.5 m LiTFSi in TEGDME. The first day at 30 °C, Pu features N_M of 5, 1 and 2 when soaked with EmimTFSI, 0.5 m LiTFSI TEGDME and $Pyr_{14}TFSI$, respectively. For CTA, N_M is 13, 3 and 5 with EmimTFSI, 0.5 m LiTFSI and $PYR_{14}TFSI$. These trends indicate that EmimTFSI is the electrolyte that has a conductivity that is more affected by the presence of the membranes. In turn, this can be explained taking into account the protic behaviour of EmimTFSI. Indeed, unlike the other electrolytes, EmimTFSI features an acidic proton in alpha position in the imidazolium ring, that contributes to its bulk ionic conductivity. When EmimTFSI is in contact with the membranes this proton drives specific acid-base interactions that decrease its activity. Specifically, it can be claimed that hydrogen bond with the carboxyl functionalities of the membranes are formed (Figure 1).

For both separators soaked with EmimTFSI, N_M increases with temperature. In case of Pu, it reaches a maximum of 11 on the day 3 at 60 °C. For CTA N_M is 65 during the day 5 at the same

temperature. Once cooled at 30 °C (day 6), Pu-EmimTFSI's N_M reversibly reduces to 4 that is even smaller than its initial value, in agreement with the resistance trend (Figure 3a). At the contrary CTA-EmimTFSI's N_M does not recover its initial value and doubles (25).

To conclude this section, EmimTFSI-Pu featured a resistance considerably smaller than the one obtained with the other electrolytes. Pu ehibited a lower McMullin number than CTA along with a better thermal behaviour. Therefore, the pullulan based electrospun membrane and EmimTFSI were selected to assemble and test EDLCs as described in the next section below.

3.2. Supercapacitor Testing

The EDLCs featured the commercial high surface area carbon BP10 and the conductive additive Super C45. We already demonstrated the good binding properties of the pullulan: glycerol mixtures, that was therefore selected for the aqueous processing of the carbon composite electrodes [31].

The following sections report the electrochemical characterization of EDLCs assembled with 20% binder and low composite electrode mass loading (3.6–4.6 mg cm^{-2}), referred as high binder low mass electrode (HBLME, Section 3.2.1), and with 10% binder and higher mass loading, labelled as low binder high mass electrode (LBHME, Section 3.2.2). The first composition was meant to verify the feasibility of the use of Pu binder and Pu membrane in the tested electrolyte while the second is meant to reach a formulation closer to that exploited commercial EDLCs. Section 3.2.3 compares the performances of HBLME and LBHME based EDLCs.

The electrochemical tests at first included EIS measurements of both the individual electrodes and of the full cell. These tests enable the evaluation of the EDLCs ESR that accounts for the contributions of (i) the contact resistance between composite material and current collector and (ii) the ionic resistance of the separator/electrolyte. Two electrodes cyclic voltammetry (CV) experiments have been carried out between 0 V and 3.2 V to evaluate the electrochemical stability and the capacitance of the EDLC as function of the scan rate. Galvanostatic (GCPL) charge/discharge measurements between 0 and 3.2 V (GLV) at different specific currents were subsequently performed to evaluate the specific energy and power. Finally, GCPL cycling has carried out at 1 A g^{-1} in order to evaluate the stability of the proposed EDLCs.

3.2.1. High Binder Low Mass Loading Electrodes (HBLME)

In this section, the results of the electrochemical characterization of the HBLME-EDLCs are reported. Figure 4a shows the Nyquist plots of the HBLME-EDLC single electrodes and the full cell. The three Nyquist plots share all the same shape. They can be divided into three components: (i) a high frequencies semicircle, (ii) a middle frequencies line with a slope of ca. 45°, and (iii) a low frequency line that approaches a slope of 90°. The intercepts at the highest frequencies of the semicircles represents the ohmic resistances (electronic and ionic) of the electrodes and electrolyte-separator system. Values of 1.4, 1.5 and 3.3 Ohm cm^2 have been measured, respectively for the negative, the positive electrode and the full cell. The small semicircle has been attributed to (i) the ion transport at the electrolyte-carbon interface and (ii) the contact between the electrode and the current collector [34]. For the full cell the semicircle diameter is 0.3 Ohm cm^2. The middle frequency line with 45° slope is representative of diffusion limited phenomenon. Specifically, it refers to diffusion of ions required to charge inner pores of the carbon electrodes. The low frequency line represents the capacitive behavior of the electrodes and the EDLC. For an ideal EDLC, a vertical line is expected. In Figure 4a the lines deviate from this ideal behavior because of the presence of different class of pores [35]. The real axis intercept of the linear fit of the cell low frequency line gives the ESR that was quantified in 6.4 ohm cm^2.

Figure 4b reports the CVs of the full HBLME-EDLC cell at different scan rate, between 0 and 3.2 V. The voltammogram are symmetric and box shaped, which indicates the absence of faradic secondary process and an electrical double layer driven process. The maximum current of 3 A g^{-1} (25 mA cm^{-2}) is reached with a scan rate of 200 mV s^{-1}, this value is comparable with the ILs based EDLC already reported in literature [8]. Figure 4c reports the trend of C_{EDLC} versus the scan rate. The highest specific

capacitance of HBLME-EDLC is 18 F g^{-1} at 5 mV s^{-1} and decreases to 14 F g^{-1} at 200 mV s^{-1}. This trend has been widely discussed in literature and is attributed to the ionic diffusion limitation upon the double layer formation in the smallest pores at fast scan rates [36]. Indeed, micropores with an internal area less exposed to the electrolytes need more time for the creation of the electrical double layer than bigger pores. At low scan rate, the polarization is slow and ions have enough time to access the internal area of micro-pores. Increasing the scan rate, only the external surface of the pores becomes easily accessible. This process also explains the 45° Warburg line of the Nyquist plot of Figure 4a.

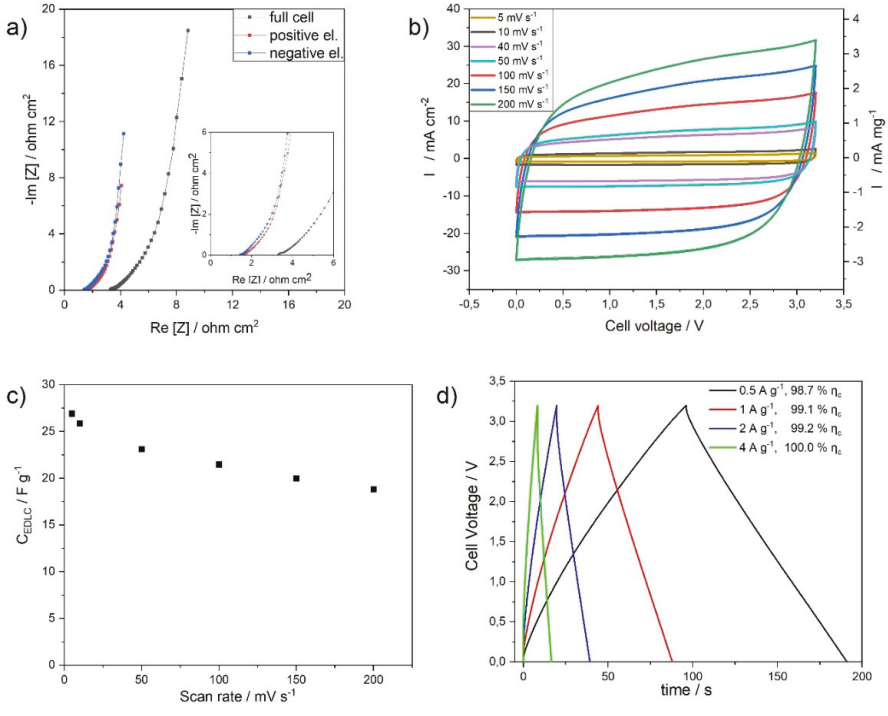

Figure 4. Electrochemical characterization of HBLME-EDLC (**a**) Nyquist plots of the (black) full cell, (red) positive and (blue) negative electrodes (500 kHz and 100 mHz), (**b**) 2-electrode CVs at different scan rate from 5 mV s^{-1} to 200 mV s^{-1}, between 0 V and 3.2 V, (**c**) Capacitance of the EDLC evaluated by CV reported as function of the scan rate; and (**d**) selected galvanostatic charge/discharge cycles between 0 V and 3.2 V at different current densities from 0.5 A g^{-1} to 4 A g^{-1}.

Figure 4d reports selected voltage profiles of the HBLME-EDLC under galvanostatic charge/discharge cycles at different current density, between 0 and 3.2 V. The voltage profile of the cell has a symmetric, triangular shape which is characteristic of electrical double layer driven process. Increasing the current from 0.5 to 4 A g^{-1} leads, as expected, to the decrease of the charge/discharge time. Coulombic efficiency (η_c), i.e., the ratio between the charge released during discharge and the charge stored during charge, is reported as inset in Figure 3d. This quantity is always greater than 98% and reaches the highest value of 100% at 4 A g^{-1}. The GCPL ohmic drops were analyzed to quantify ESR of the device and resulted in 5.9 Ohm cm^2, that well compares with the value obtained by EIS. EDLC. Specific capacitance C_{EDLC} has been calculated from the slope of the GCPL discharge profile and for HBLM-EDLC resulted in 15.9, 15.4, 14.6 and 13.7 F g^{-1} at 0.5, 1, 2 and 4 A g^{-1}, respectively. The corresponding single electrode specific capacitances ($C_{electrode}$) are 63, 61, 58 and 54.8 F g^{-1}. These values well compare with those of electrodes featuring the same electrolyte and carbon but employing

a fluorinated binder [8]. Table 3 reports the ESR and C_{EDLC} at 0.5 A g^{-1} of the HBLME-EDLC along with the EDLC areal capacitance.

Table 3. Gravimetric and surface quantities of HBLME-EDLC and LBHME-EDLC.

Electrode Label	HBLME-EDLC	LBHME-EDLC
Mass loading (mg cm^{-2})	9.3	13.8
ESR (ohm)	5.9	7.9
Capacitance * (F g^{-1})	15.9	6.2
Areal capacitance (mF cm^{-2})	148.0	85.5
Specific energy ** (Wh kg^{-1})	19.6	7.2
Specific power *** (kW kg^{-1})	4.6	3.7
Areal energy density (μWh cm^{-2})	182.3	99.4
Areal power density (mW cm^{-2})	42.8	51.1

* Capacitance has been calculated from the CV at 50 mV s^{-1}, ** Specific energy has been calculated from GCPL at minimum current (0.5 A g^{-1}), *** Specific power has been calculated at maximum current (4 and 5 A g^{-1}).

3.2.2. Lower Binder High Mass Loading Electrodes (LBHME)

In this section, the results of the electrochemical characterization of the LBHME-EDLCs are reported. Figure 5a shows the Nyquist plots of the LBHME-EDLC single electrodes and full cell.

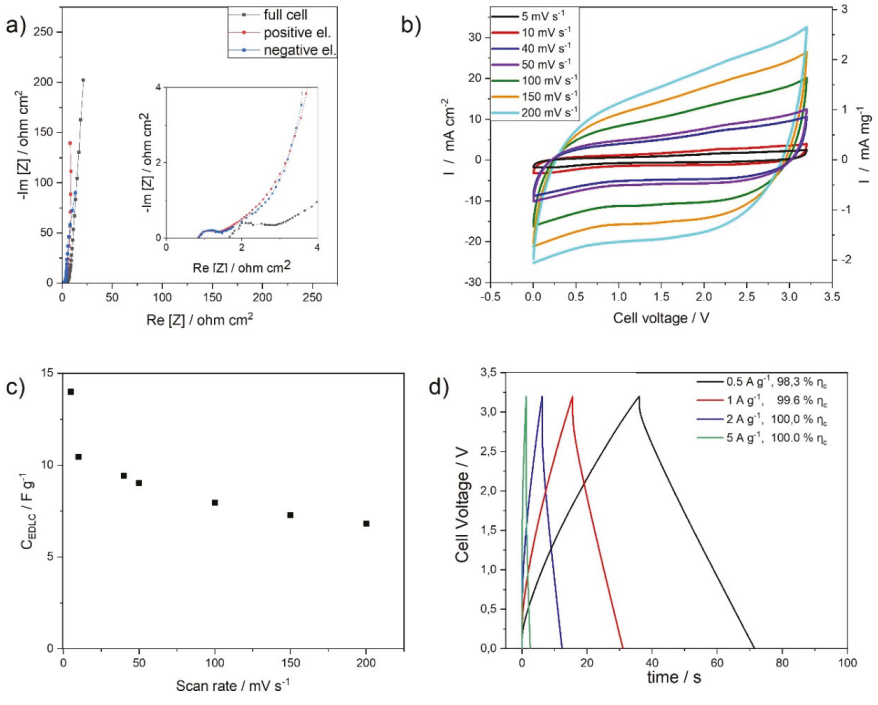

Figure 5. Electrochemical characterization of LBHME-EDLC (**a**) Nyquist plots of the (black) full cell, (red) positive and (blue) negative electrodes (500 kHz and 100 mHz), (**b**) 2-electrode CVs at different scan rate from 5 mV s^{-1} to 200 mV s^{-1}, between 0 V and 3.2 V, (**c**) Capacitance of the EDLC evaluated by CV reported as function of the scan rate; and (**d**) selected galvanostatic charge/discharge cycles between 0 V and 3.2 V at different current densities from 0.5 A g^{-1} to 5 A g^{-1}.

Like for HBLME, the three Nyquist plots share all the same shape. For the physical interpretation of the Nyquist plots, the considerations that have been drawn in the previous section are still valid. The high frequency intercepts with the real axis of the semicircles are 0.8, 0.9 and 1.7 Ohm cm^2 for the positive and negative electrodes and full cell, respectively. Noticeably these values are halved with respect to those of the HBLME electrodes and EDLC (cf. Figure 4a). In LBHME formulation, the quantity of binder and conductive carbon are halved compared to the HBLME one. Therefore, the decrease of the high frequency impedance achieved by LBHME can be explained with the decrease of the insulating component of the electrode, i.e., the binder. Comparing the high frequency semicircles in Figures 4a and 5a, it is possible to notice that the LBHME's is wider than HBLME's. Indeed, the LBHME-EDLC semicircle diameter is 1.3 Ohm cm^2 while the HBLME's is 0.3 Ohm cm^2. This difference is due to the high mass loading of LBHME with respect to HBLME (1.5-fold), that brings about a worse ionic and electronic connection between the carbon particles [10]. The LBHME-EDLC middle frequency line (45° slope) span across the same range of resistance with respect to the HBLME-EDLC. The ESR of the LBHME-EDLC was evaluated from the real axis intercept of the low frequency line and resulted in 7.6 Ohm cm^2.

Figure 5b reports the CVs of the full LBHME-EDLC cell at different scan rate, between 0 and 3.2 V. From these measurements, voltammetric specific capacitance values have been calculated and are reported as function of the scan rate in Figure 5c. The highest specific capacitance is 14 F g^{-1} at 5 mV s^{-1} and decreases to 7 F g^{-1} at 200 mV s^{-1}. Therefore, from 5 mV s^{-1} to 200 mV s^{-1} there is a 50% specific capacitance reduction, that is higher than what observed for HBLME-EDLC (22%). This can be related to a not optimized electronic and ionic connection of the electrodes carbon particles that has been highlighted by the Nyquist plot analysis reported above (Figure 5a).

The LBHME-EDLC galvanostatic charge/discharge profiles at different current are reported in Figure 5d. The coulombic efficiency was 98.3%, 99.6%, 100%, 100% at 0.5, 1, 2, 5 A g^{-1}, respectively. These values are slightly higher than those that have been observed for the HBLME. The ESR was 7.9 Ohm cm^2 in agreement with the EIS value. The C_{EDCL} was 6.2, 5.8, 5.3 and 4.2 F g^{-1} at 0.5, 1, 2 and 5 A g^{-1}. These values are lower than those featured by HBLME-EDLC and this can be explained with the not optimized ionic and electronic connection highlighted by Table 3 that reports the ESR and C_{EDLC} at 0.5 A g^{-1} of LBHME-EDLC. The EDLC areal capacitance is also reported in the Table 3.

3.2.3. Cycling Stability, Energy and Power of HBLME- and LBHME-EDLCs

Figure 6a reports the trends of the specific capacitance of the two EDLCs over cycling at 1 A g^{-1}. The values are normalized by the value of the specific capacitance of the first cycle. Both devices show a good stability with capacitance retention of 90% at the 2000th cycle. This result demonstrates the feasibility of the use of pullulan as alternative separator and binder for green supercapacitors.

Note that the cycling stability of LBHME-EDLC at low binder content was further evaluated even over 5000 cycles (Figure S3). The test indicated that also over prolonged cycling, a capacitance retention of 77% can be obtained.

The specific energy and power values of the two EDLCs, calculated through Equations (4) and (5) are compared in the Ragone plot reported in Figure 6b. Both devices deliver the maximum specific energy at the lowest current, and the maximum power is delivered at the highest current.

Indeed, at 0.5 A g^{-1}, the specific energy is 19.6 Wh kg^{-1} and 7.2 Wh kg^{-1} for HBLME-EDLC and LBHME-EDLC, respectively. At 4 A g^{-1}, the specific power is 4.7 kW kg^{-1} for the HBLME EDLC and 3.8 kW kg^{-1} for the LBHME-EDLC. These values are reported in Table 3. If energy and power are normalized by the electrode area, they become 182 μWh cm^{-2} and 42.8 mW cm^{-2} for the HBLME-EDLC, and 99.4 μWh cm^{-2} and 51 mW cm^{-2} for the LBHME-EDLC (Table 3). These results clearly demonstrate that increasing electrode thickness is detrimental for energy and power performance. Indeed, specific energy of LBHME-EDLC is lower than HBLME-EDLC and this is mainly related to an inefficient exploitation of the electrode carbon surface. This is highlighted by the comparison of the area capacitance of HBLME-EDLC (148 mF cm^{-2}) and LBHME-EDLC (85.5 mF cm^{-2}).

Therefore, in LBHME-EDLC, the increase of the electrode mass is not enough to offset such specific energy decrease, and the areal energy density keeps lower than that of HBME-EDLC. However, power performance of the two EDLCs are comparable, suggesting that the decrease of the binder content has a positive effect.

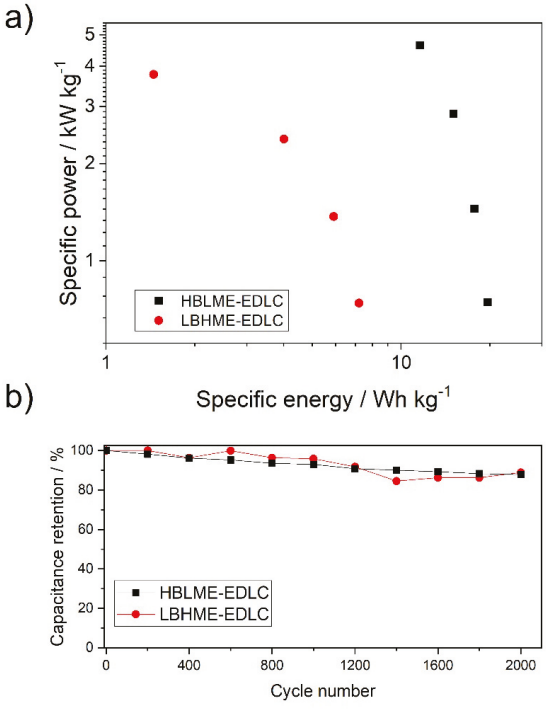

Figure 6. EDLC comparison by galvanostatic tests. (**a**) Trend of the capacitance percentage normalized by the value at first cycle the as function of the cycle number (at 1 A g^{-1}, cell voltage cut-off: 0 V–3.2 V) and (**b**) Ragone plots of HBLME-EDLC and LBHME-EDLC.

4. Discussion

Today many efforts are being devoted to increasing the specific energy of supercapacitors by different strategies. Among them promises are held by the use of ionic liquids, thick electrodes and pseudocapacitive active materials [2,6,12]. Ionic liquids enable high practical voltage (>3 V) and therefore energy density, but their major drawbacks are the greater ESR respect to commercial electrolytes and high cost. The use of thick electrodes (>10 mg cm^{-2}) may seem the simpler solution, but the achieving high performance ith thick electrodes is still an unsolved problem [10,11]. Indeed, thick electrodes suffer of poor electronic and ionic connection between the particles, and only the external portion of the electrodes take part in the charge/discharge processes.

The increasing market for supercapacitors requires that sustainable manufacturing processes and materials are exploited to manufacture green supercapacitors. Aqueous processable bio-derived polymers represent a valuable alternative to today's fluorinated separators and binders. Furthermore, we have already demonstrated that the smart combination of a water processable binder and separator (like pullulan) and a hydrophobic ionic liquid electrolyte (EmimTFSI) enables an easy recovery of the expensive ionic liquid [31]. Indeed, the pullulan-IL-based EDLC can be readily separated into each of its components by immersion in water. After these very interesting but preliminary results, in this

paper we have carried out a study to get further insight into the impact of the use of natural polymer in supercapacitors performance. We have investigated the use of cellulose, which is the most widely studied bio-based polymer for green supercapacitors, and pullulan, that we have proposed for the first time in [31]. CTA and Pu separators were processed as self-standing mats by electrospinning. Their permeability to different electrolytes (EmimTFSI, 0.5 m LiTFSI TEGDME, $PYR_{14}TFSI$), which is critical in the formation of the electrical double layer, has been evaluated by EIS and quantified referring to the Mac Mullin number. This characterization has been done at different temperatures over one week, in order to get insight on the thermal and chemical stability of the tested bio-polymer in the selected electrolytes. Both membranes at 30 °C featured the lower resistance (Pu 2 Ohm cm^2 CTA 2 Ohm cm^2) when soaked with EmimTFSI. However, given that the thickness of Pu (55 μm) was higher than that of CTA (22 μm), the resistivity of the Pu-EmimTFSI system was considerably smaller (0.407 kOhm cm vs. 1.041 kOhm cm). Furthermore, Pu-EmimTFSI exhibited a better thermal stability respect to the CTA-EmimTFSI. Notably, the N_M for the Pu is always smaller than that of CTA, in particular, in EmimTFSI values of 5 and 12 were found, respectively. Overall, this study highlighted the presence of different and specific interactions between the tested electrolytes and the membranes that affect the ionic permeability and stability. It also indicated Pu-EmimTFSI as the best system. Indeed, Pu-EmimTFSI was the combination capable to minimize the ESR and avoid performance degradation due to temperature changes.

On the basis of these results, Pu was selected as separator and binder for EmimTFSI-based EDLCs. The big challenge we faced in this study was to reach high electrode mass loading at low binder content.

Two EDLCs have been assembled featuring two different formulations, one with lower mass loading and high binder content (HBLME) and a second one with higher mass loading and lower binder content (LBHME). These have been characterized electrochemically to evaluate how binder decrease and mass loading increase affect performance. In particular, these devices have been characterized at first by EIS. Analysis of the Nyquist plots highlighted an increase of the ESR moving from the HBLME-EDLC to the LBHME-EDLC, (5.9 Ohm cm^2 vs. 7.6 Ohm cm^2). This trend was mainly related to the increase of the ionic and electronic contact resistances between carbon particles with the increase of electrode mass loading (1.5-fold from HBLME-EDLC to LBHME-EDLC).

For both devices' CVs have shown the absence of faradaic parasitic reactions within the cell voltage range 0 to 3.2 V. This wide range is feasible thanks to the good electrochemical stability of Pu-EmimTFSI. Specific capacitances have been calculated for both EDLCs. The highest specific capacitance was featured at the lowest scan rate of 5 mV s^{-1} for both devices and was 18 F g^{-1} and 14 F g^{-1} for HBLME-EDLC and LBHME-EDLC, respectively. Both supercapacitors featured a good capacitance retention with the increase of the scan rate that however was higher for HBLME-EDLC (22%) than LBHME-EDLC (50%).

GLV cycling with high coulombic efficiency (higher than 98%) was demonstrated for both devices at the high cell voltage of 3.2 V. Noticeably, the EDLC featured a very good cycling behaviour demonstrated over more than 2000 cycles even at low binder content, confirming the stability of the Pu-polymer in EmimTFSI.

The high cell voltage and good specific capacitance provided specific energy of 19.6 Wh kg^{-1} and 7.2 Wh kg^{-1} at 0.5 A g^{-1} that well compare with those of EDLCs featuring the same electrolyte and active carbon but employing a fluorinated binder and fiber glass separators [16]. The highest specific power was 4.6 kW kg^{-1} and 3.7 kW kg^{-1} at 4–5 A g^{-1} respectively for HBLME-EDLC and for the LBHME-EDLC

The gravimetric performance of the HBLME-EDLC is superior respect to that of the LBHME-EDLC. This is due to the lower specific capacitance of the latter vs. the former. In turn, this is due to an inefficient ionic electronic contact between electrode carbon particles that leads to a partial exploitation of the electrodes surface.

5. Conclusions

This work demonstrates that aqueous processable biodegradable polymers such as pullulan can be effectively exploited for the development of the major components (separator and binder) of ionic-liquid-based green EDLCs. After studying different combinations of biopolymer and organic electrolyte, pullulan-EmimTFSI was found to be the best system in terms of resistivity and thermal behavior. Therefore, we assembled Pu-based EDLCs with EmimTFSI as electrolyte. Our study demonstrates for the first time the feasibility of the use of pullulan to produce high mass loading electrodes at low binder content for high voltage EDLCs. We prepared electrodes with mass loadings up to 13.84 mg cm^{-2} with 10% binder content. Pullulan-EmimTFSI EDLCs were charged up to 3.2 V with good cycling stability over 5000 cycles. Pullulan-EmimTFSI EDLCs featured specific energy and power comparable with those of supercapacitors based on the same activated carbon and ionic liquid, but with fluorinated binder and fiberglass separator.

Further work is in progress to improve the specific capacitance of these thick electrodes by using high surface area carbons with tailored porosity, different conductive carbon additives, and by exploring different electrolytes.

Supplementary Materials: The following are available online at http://www.mdpi.com/1996-1073/13/12/3115/s1, Figure S1. Schemes of the casting preparation of the pullulan-based electrodes and of the supercapacitor assembly, Figure S2. Nyquist plot of Pullulan electrospun membrane soaked with (a) $PYR_{14}TFSI$, (c) EmimTFSI, (e) 0.5 m LiTFSI TEGDME and Cellulose triacetate electrospun membrane soaked with (b) $PYR_{14}TFSI$, (d) EmimTFSI, (f) 0.5 m LiTFSI TEGDME, Figure S3. Trend of the capacitance percentage normalized by the value at first cycle the as function of the cycle number (at 1 A g^{-1}, cell voltage cut-off: 0 V–3.2 V), Table S1. Resistance normalized by the plain area of Pullulan electrospun separator in different tested electrolytes, Table S2. Resistance normalized by the plain area of Cellulose triacetate electrospun separator in different tested electrolytes, Table S3. Resistivity of Pullulan electrospun separator in different tested electrolytes, Table S4. Resistivity of Cellulose triacetate electrospun separator in different tested electrolytes, Table S5. Mac Mullin number of Pullulan electrospun separator in different tested electrolytes, Table S6. Mac Mullin number of Cellulose triacetate electrospun separator in different tested electrolytes.

Author Contributions: Conceptualization: F.S. Data curation: G.E.S., F.P. Formal analysis: G.E.S., F.P., Funding acquisition: F.S. Investigation: G.E.S., F.P. Project administration: F.S. Supervision: F.S., Writing–original draft: G.E.S., F.P., A.B., D.M., F.S. Writing—review & editing: G.E.S., F.P., A.B., D.M, F.S. All authors have read and agreed to the published version of the manuscript.

Funding: This research was funded by the Italy-South Africa joint Research Programme 2018–2020 (Italian Ministers of Foreign Affairs and of the Environments) and "Piano Triennale di Realizzazione 2019–2021, Accordo di Programma Ministero dello Sviluppo Economico"—ENEA.

Acknowledgments: Maria Letizia Focarete (University of Bologna) and her research group are acknowledged for their precious contribution and support on electrospinning of natural polymers.

Conflicts of Interest: All The authors declare no conflict of interest for this manuscript.

References

1. Dunn, B.; Kamath, H.; Tarascon, J.M. Electrical energy storage for the grid: A battery of choices. *Science* **2011**, *334*, 928–935. [CrossRef] [PubMed]
2. Yang, Z.; Zhang, J.; Kintner-Meyer, M.C.W.; Lu, X.; Choi, D.; Lemmon, J.P.; Liu, J. Electrochemical energy storage for green grid. *Chem. Rev.* **2011**, *111*, 3577–3613. [CrossRef] [PubMed]
3. Chen, G.Z. Supercapacitor and supercapattery as emerging electrochemical energy stores. *Int. Mater. Rev.* **2017**, *62*, 173–202. [CrossRef]
4. Siwach, P.; Sharma, K.; Arora, A.; Tripathi, S.K. Review of supercapacitors: Materials and devices. *J. Energy Storage* **2019**, *21*, 801–825. [CrossRef]
5. Schütter, C.; Pohlmann, S.; Balducci, A. Industrial Requirements of Materials for Electrical Double Layer Capacitors: Impact on Current and Future Applications. *Adv. Energy Mater.* **2019**, *9*, 1900334. [CrossRef]
6. DeVos, N.; Maton, C.; Stevens, C.v. Electrochemical Stability of Ionic Liquids: General Influences and Degradation Mechanisms. *ChemElectroChem* **2014**, *1*, 1258–1270. [CrossRef]
7. González, A.; Goikolea, E.; Barrena, J.A.; Mysyk, R. Review on supercapacitors: Technologies and materials. *Renew. Sustain. Energy Rev.* **2016**, *58*, 1189–1206. [CrossRef]

8. Lazzari, M.; Mastragostino, M.; Soavi, F. Capacitance response of carbons in solvent-free ionic liquid electrolytes. *Electrochem. Commun.* **2007**, *9*, 1567–1572. [CrossRef]
9. Mauger, A.; Julien, C.M.; Paolella, A.; Armand, M.; Zaghib, M. A comprehensive review of lithium salts and beyond for rechargeable batteries: Progress and perspectives. *Mater. Sci. Eng. R Rep.* **2018**, *134*, 1–2110. [CrossRef]
10. Ruschhaupt, P.; Varzi, A.; Passerini, S. Natural Polymers as Green Binders for High-Loading Supercapacitor Electrodes. *ChemSusChem* **2020**, *13*, 763–770. [CrossRef]
11. Arbizzani, C.; Yu, Y.; Li, J.; Xiao, J.; Xia, Y.; Yang, Y.; Santato, C.; Raccichini, R.; Passerini, S. Good practice guide for papers on supercapacitors and related hybrid capacitors for the Journal of Power Sources. *J. Power Sources* **2020**, *450*, 227636. [CrossRef]
12. Stojanovska, E.; Kilic, A. Carbon nanofibers as thick electrodes for aqueous supercapacitors. *J. Energy Storage* **2019**, *26*, 100981. [CrossRef]
13. Krause, A.; Balducci, A. High voltage electrochemical double layer capacitor containing mixtures of ionic liquids and organic carbonate as electrolytes. *Electrochem. Commun.* **2011**, *13*, 814–817. [CrossRef]
14. Krummacher, J.; Balducci, A. Al(TFSI)3 as a Conducting Salt for High-Voltage Electrochemical Double-Layer Capacitors. *Chem. Mater.* **2018**, *30*, 4857–4863. [CrossRef]
15. Krummacher, J.; Hess, L.H.; Balducci, A. Al(TFSI) 3 in Acetonitrile as Electrolytes for Electrochemical Double Layer Capacitors. *J. Electrochem. Soc.* **2019**, *166*, A1763–A1768. [CrossRef]
16. Lazzari, M.; Soavi, F.; Mastragostino, M. Mesoporous carbon design for ionic liquid-based, double-layer supercapacitors. *Fuel Cells* **2010**, *10*, 840–847. [CrossRef]
17. Chmiola, J.; Largeot, C.; Taberna, P.L.; Simon, P.; Gogotsi, Y. Desolvation of ions in subnanometer pores and its effect on capacitance and double-layer theory. *Angew. Chem. Int. Ed.* **2008**, *47*, 3392–3395. [CrossRef]
18. Varzi, A.; Passerini, S. Enabling high areal capacitance in electrochemical double layer capacitors by means of the environmentally friendly starch binder. *J. Power Sources* **2015**, *300*, 216–222. [CrossRef]
19. Ahmed, S.; Nelson, P.A.; Gallagher, K.G.; Dees, D.W. Energy impact of cathode drying and solvent recovery during lithium-ion battery manufacturing. *J. Power Sources* **2016**, *322*, 169–178. [CrossRef]
20. Mauger, A.; Julien, C.; Paolella, A.; Armand, M.; Zaghib, K. Recent Progress on Organic Electrodes Materials for Rechargeable Batteries and Supercapacitors. *Materials* **2019**, *12*, 1770. [CrossRef] [PubMed]
21. Bresser, D.; Buchholz, D.; Moretti, A.; Varzi, A.; Passerini, S. Alternative binders for sustainable electrochemical energy storage-the transition to aqueous electrode processing and bio-derived polymers. *Energy Environ. Sci.* **2018**, *11*, 3096–3127. [CrossRef]
22. Yamagata, M.; Ikebe, S.; Soeda, K.; Ishikawa, M. Ultrahigh-performance nonaqueous electric double-layer capacitors using an activated carbon composite electrode with alginate. *RSC Adv.* **2013**, *3*, 1037–1040. [CrossRef]
23. Böckenfeld, N.; Jeong, S.S.; Winter, M.; Passerini, S.; Balducci, A. Natural, cheap and environmentally friendly binder for supercapacitors. *J. Power Sources* **2013**, *221*, 14–20. [CrossRef]
24. Dühnen, S.; Betz, J.; Kolek, M.; Schmuch, R.; Winter, M.; Placket, T. Toward Green Battery Cells: Perspective on Materials and Technologies. *Small Methods* **2020**, 2000039. [CrossRef]
25. Bonnefoi, L.; Simon, P.; Fauvarque, J.F.; Sarrazin, C.; Sarrau, J.F.; Dugast, A. Electrode compositions for carbon power supercapacitors. *J. Power Sources* **1999**, *80*, 149–155. [CrossRef]
26. Phillips, D.M.; Drummy, L.F.; Conrady, D.G.; Fox, D.M.; Naik, R.R.; Stone, M.O.; Trulove, P.C.; de Long, H.C.; Mantz, R.A. Dissolution and regeneration of Bombyx mori silk fibroin using ionic liquids. *J. Am. Chem. Soc.* **2004**, *126*, 14350–14351. [CrossRef]
27. Swatloski, R.P.; Spear, S.K.; Holbrey, J.D.; Rogers, R.D. Dissolution of Cellose with Ionic Liquids. *J. Am. Chem. Soc* **2002**, *124*, 4974–4975. [CrossRef]
28. Recham, N.; Armand, M.; Tarascon, J.M. Novel low temperature approaches for the eco-efficient synthesis of electrode materials for secondary Li-ion batteries. *Comptes Rendus Chim.* **2010**, *13*, 106–116. [CrossRef]
29. Heinze, T.; Dorn, S.; Schöbitz, M.; Liebert, T.; Köhler, S.; Meister, F. Interactions of Ionic Liquids with Polysaccharides—2: Cellulose. *Macromol. Symp.* **2008**, *262*, 8–22. [CrossRef]
30. Varzi, A.; Balducci, A.; Passerini, S. Natural Cellulose: A Green Alternative Binder for High Voltage Electrochemical Double Layer Capacitors Containing Ionic Liquid-Based Electrolytes. *J. Electrochem. Soc.* **2014**, *161*, A368–A375. [CrossRef]

31. Poli, F.; Momodu, D.; Spina, G.E.; Terella, A.; Mutuma, B.K.; Focarete, M.L.; Manyala, N.; Soavi, F. Pullulan-ionic liquid-based supercapacitor: A novel, smart combination of components for an easy-to-dispose device. *Electrochim. Acta* **2020**, *338*, 135872. [CrossRef]
32. Arbizzani, C.; Lazzari, M.; Soavi, F.; Mastragostino, M.; Conte, M. ILHYPOS Ionic Liquid-Based Supercapacitors. *ECS Trans.* **2010**, *25*, 25–30.
33. Li, Y.; Li, Q.; Tan, Z. A review of electrospun nanofiber-based separators for rechargeable lithium-ion batteries. *J. Power Sources* **2019**, *443*, 227262. [CrossRef]
34. Yoo, H.D.; Jang, J.H.; Ryu, J.H.; Park, Y.; Oh, S.M. Impedance analysis of porous carbon electrodes to predict rate capability of electric double-layer capacitors. *J. Power Sources* **2014**, *267*, 411–420. [CrossRef]
35. Conway, B.E. *Electrochemical Supercapacitors: Scientific Fundamentals and Technological*; Springer Science & Business Media: Berlin, Germany, 2013.
36. Kötz, R.; Carlen, M. Principles and applications of electrochemical capacitors. *Electrochim. Acta* **2000**, *45*, 2483–2498. [CrossRef]

energies

MDPI

Article

Studies on Dynamic Properties of Ultracapacitors Using Infinite r–C Chain Equivalent Circuit and Reverse Fourier Transform

Shailendra Rajput [1], Alon Kuperman [2], Asher Yahalom [1] and Moshe Averbukh [1,*]

[1] Department of Electrical/Electronic Engineering, Ariel University, Ariel 40700, Israel; shailendrara@ariel.ac.il (S.R.); asya@ariel.ac.il (A.Y.)

[2] School of Electrical & Computer Engineering, Ben-Gurion University of the Negev, Beer-Sheva 8410501, Israel; alonk@bgu.ac.il

* Correspondence: mosheav@ariel.ac.il; Tel.: +972-528-814-120

Received: 29 July 2020; Accepted: 3 September 2020; Published: 4 September 2020

Abstract: The specific power storage capabilities of double-layer ultracapacitors are receiving significant attention from engineers and scientific researchers. Nevertheless, their dynamic behavior should be studied to improve the performance and for efficient applications in electrical devices. This article presents an infinite resistor–capacitor (r–C) chain-based mathematical model for the analysis of double layer ultracapacitors. The internal resistance and capacitance were measured for repetitive charging and discharging cycles. The magnitudes of internal resistance and capacitance showed approximately ±10% changes for charge-discharge processes. Electrochemical impedance spectroscopy investigations revealed that the impedance of a double-layer ultracapacitor does not change significantly in the temperature range of (−30 °C to +30 °C) and voltage range of (0.3376–2.736 V). The analysis of impedance data using the proposed mathematical model showed good agreement between the experimental and theoretical data. The dynamic behavior of the ultracapacitor was successfully represented by utilizing the proposed infinite r–C chains equivalent circuit, and the reverse Fourier transform analysis. The r–C electrical equivalent circuit was also analyzed using the PSIM simulation software to study the dynamic behavior of ultracapacitor parameters. The simulation study yields an excellent agreement between the experimental and calculated voltage characteristics for repetitive charging-discharging processes.

Keywords: ultracapacitor; equivalent circuit; Fourier transform; internal resistance

1. Introduction

Modern technologies such as portable electronic devices, electrical transportation, communication systems, and smart medical equipment need efficient energy storage systems [1,2]. Electrical energy storage devices are also used for smart grid control, grid stability, and peak-power saving as well as for frequency and voltage regulation [3–5]. Electricity generated from renewable sources (e.g., solar power, wind energy) can hardly deliver an immediate response to demand because of fluctuating power supply [6–8]. Hence, it has been suggested to preserve the harvested electrical energy for future requirements. The present status of electrical energy storage technologies is quite far away from the needed demand. These circumstances motivate us to continue scientific research for the improvement in the parameters of existing storage devices and to develop new storage machinery.

Currently, ultracapacitors (UCs) are considered as an efficient energy storage system for electrical devices [9]. Electric double-layer capacitors (EDLCs) or symmetric double-layer UCs have attracted attention as plausible electrical energy storage devices [10–14]. EDLCs are a complex of two identical porous electrodes, electrolytic solution, and a separator, which is used as an ion conductor. The negative

electrode attracts the cations during the charging process, and the anions are collected at the pores of the positive plate. The EDLCs are characterized by longer life cycle due to the absence of chemical reactions, efficient charge-discharge cycles, ability to discharge at higher current density, fast charging-discharging ability, and the lack of heavy metals, which make the device environmentally friendly [11,14]. The increasing popularity of UCs has been directed toward a better understanding of dynamic behavior and ultimately improved performance. The parameters responsible for the dynamic behavior of UCs have not been studied for the applicable range. In very recent work, we studied the dynamic behavior of a double-layer UC [13]. The capacitance remained nearly constant for a wide range of temperatures (+25 °C to −40 °C), but the internal resistance increased ~1.5 times as the temperature decreased to −40 °C [13]. The equivalent electrical circuit models are required to simulate the device parameters for the development and design of electrical appliances. Previously, different types of equivalent circuit models have been proposed in order to understand the dynamic characteristics of UCs [13,15–20]. Importantly, the electrochemical analysis-based modeling approaches have also been employed to study the performance of UCs [21–24].

A mathematical model should demonstrate model precision, robustness, and ease of application in the well-known software platforms (e.g., MATLAB and others). The functionality of UCs is defined by the movement of charged particles (ions) from positive to negative electrodes in the electrolyte. Hence, the correct description of UCs should be based on partial differential equations (PDE). These equations have to describe the continuum flow of ions, which determine the internal resistance and the capacitance of UC. In the electrolyte, the particle movement is related to the diffusion of ions, which is linearly dependent on the concentration difference in adjacent points of a space. The electrical potential describes the charge distributions in the electrolyte, and electrical resistance defines the diffusion movement of ions. Thus, this information should be used to fix the constraints of the equivalent electrical circuit and to characterize the internal resistance and capacitance. In previous studies, this principle is employed to design an equivalent circuit using a finite number of resistors and capacitors [15]. However, the application of a finite number of resistances and capacitances cannot describe UC parameters with high precision. The requirement to simplify the equivalent circuit prevents the use of a significant number of elements. Moreover, the complicated equivalent circuits create substantial mathematical difficulties to determine the magnitudes of equivalent electrical components correctly. Several artificial mathematical operators (fractional impedance [16], Warburg impedance [25], and constant phase element [26]) have been employed to analyze the equivalent circuit. Previous studies did not describe the precise physical phenomena responsible for the electrical properties of UCs. As a result, these equivalent circuits require permanent matching of circuit parameters depending on applied voltage and current. These methods could not explain exact changes in the UC parameters during their functionality since equivalent circuits do not have a rigorous physical base. In a previous article, we proposed that the infinite r–C chains-based equivalent circuit model could describe the behavior of double layer UCs [13]. The multibranch r–C circuit modeling approach was also studied by other researchers [27–33]. The frequency-domain models comprise the best overall performance in terms of complexity, correctness, and robustness [31–33]. Logerais et al. proposed the multibranch r–C circuit model for the analysis of UC [28], but the proposed model did not provide rigorous closed-form analytical solutions and did not consider the inductance of connecting cables and electrodes. Navarro et al. considered the inductance of connecting cables and an infinite number of r–C chains. However, the reverse Fourier transform can be difficult to apply for the prediction of voltage alterations during charge-discharge due to the lack of a closed-form analytical solution.

This work aimed to study the dynamic behavior of symmetric double layer UC and develop an adequate equivalent circuit model. The novelty of the proposed work was the application of the reverse Fourier transforms to get a time-domain response of UC parameters such as voltage and current. The reverse Fourier transforms analysis was based on the rigorous analytical solution for the frequency-domain impedance spectroscopy. The rest of this paper is organized as follows.

First, the internal resistance and capacitance are measured for repetitive charge-discharge cycles. Second, the impedance, which includes reactance and resistance, is measured at different applied voltage and temperatures using electrochemical impedance spectroscopy (EIS). Third, the impedance data are analyzed using an infinite r–C chain equivalent circuit model. Fourth, dynamic parameters of UC are represented using the reverse Fourier transform analysis. Finally, the proposed equivalent circuit model is simulated using the PSIM simulating package.

2. Experimental Studies

2.1. Experimental Setup

The dynamic behavior of symmetric double-layer UC (BCAP3400: 3400 F, 2.85 V [34]) was investigated using the electrochemical impedance spectroscopy (EIS), and repetitive charge-discharge cycles. Figure 1a,b demonstrate the experimental setups, and detailed descriptions of experimental setups were discussed in our previous article [13]. For charge-discharge cycle experiments, a charge/discharge system controller [35], regulated DC power supply [36], electronic load [37], and midi-logger GL900 [38] were used. A constant repetitive pulsed current (50 A) was applied for both charge-discharge cycles. The constant current was applied for two seconds, with an interval of two seconds. The internal resistance and capacitance were calculated using the typical voltage vs. time curve for the discharging process [13]. The EIS investigations were performed using the EchemLab XM potentiostat-galvanostat analyzer [39] and Tenney temperature test chamber [40]. The EIS experiments were performed with an AC current of 1 A (rms) and frequencies of 1 Hz–1 kHz.

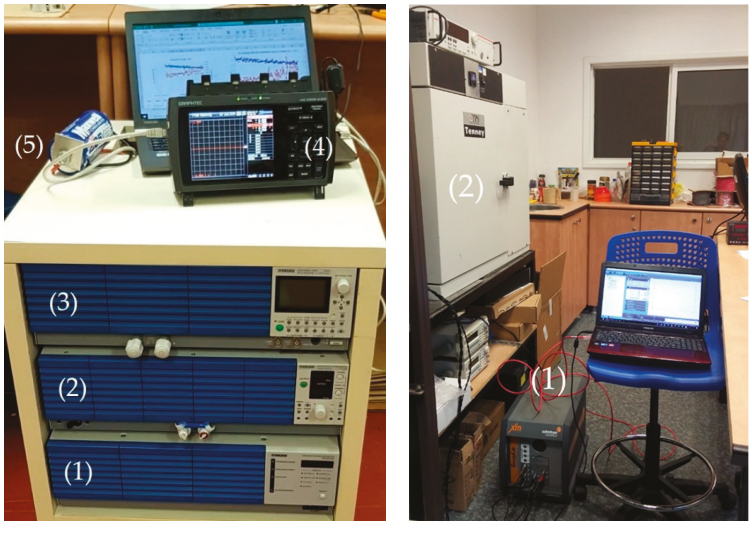

(**a**) (**b**)

Figure 1. (**a**) Experimental setup for the charge-discharge cycles (1-charge/discharge system controller, 2-regulated DC power supply, 3-electronic load unit, 4-midi-logger, and 5-capacitor). (**b**) Experimental setup for the EIS measurement (1-Potentiostat-galvanostat, and 2-Tenneytemperature test chamber).

2.2. Results

Figure 2 demonstrates the internal resistance (R_{int}) and capacitance (C) as a function of voltage at a constant current of 50 A. Both the parameters showed approximately ±10% changes for charge/discharge cycles. Similar outcomes were also observed for an applied current of 20 A and 75 A [13]. It was also noticed that both parameters slightly upsurged as the capacitor voltage enhanced from minimum to

maximum. Importantly, the tendency of UC capacitance during charge/discharge cycles was identical to the internal resistance.

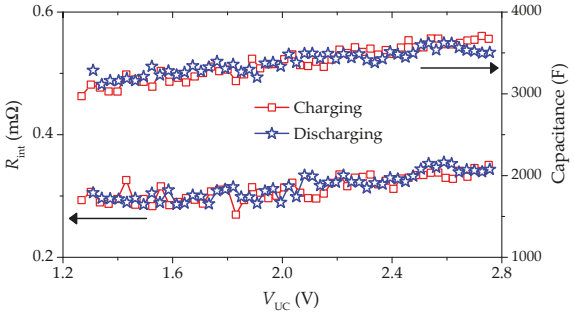

Figure 2. Internal resistance and capacitance of symmetric double-layer UC measured at a constant current of 50 A for charge-discharge cycles.

Figure 3a demonstrates the impedance (|Z|) of the double layer UC at different temperatures for constant voltage of ~2.5 V and frequency range of 1 Hz–100 kHz. Figure 3b shows the impedance (|Z|) for different voltages (0.3376–2.736 V) and frequencies of 1 Hz–100 kHz at constant temperature (15 °C). The phase impedance of the double-layer UC is shown in Figure 4. The impedance and phase values remained almost constant for different working temperatures (−30 °C to +30 °C). These parameters also remain unchanged for different voltage magnitudes of 0.3376–2.736 V.

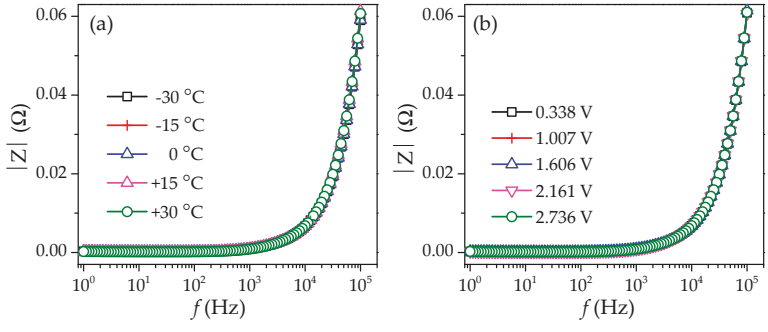

Figure 3. Module impedance (|Z|) as a function of frequency (**a**) at different temperatures for constant voltage (~2.5 V), and (**b**) at different voltages for a constant temperature of 15 °C.

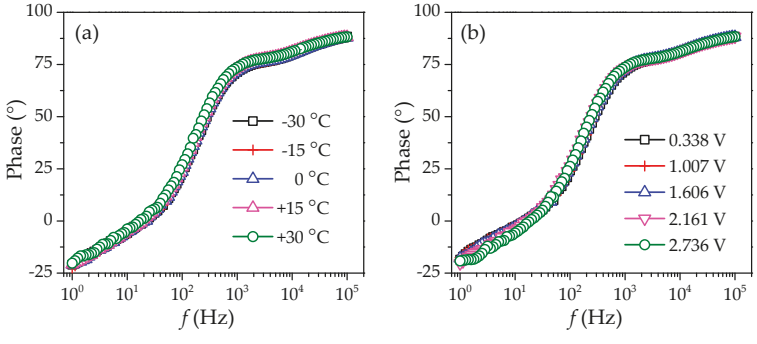

Figure 4. Phase (θ) of Z as a function of frequency (**a**) at different temperatures for constant voltage (~2.5 V) and (**b**) at different voltages for a constant temperature of 15 °C.

3. Equivalent Circuit Development

3.1. Mathematical Model

The equivalent electrical circuit for the analysis of UC was developed by employing a ladder of infinite r–C chains. This approach takes into account the real physical nature of charge movement in the electrolyte. Additionally, it provides high precision of the output UC parameters, however, without the application of PDE. Figure 5 shows the schematic of the proposed infinite r–C chains based equivalent circuit model. The resistor (r) models the resistance of diffusion movement, and consequently, the ohmic loss, which is termed as a real part of equivalent impedance. The element 'C' simulates the distribution of space charge in the electrolyte and thus the capacitance of UC. For the mathematical analysis, it was assumed that the r–C chains exhibit similar impedance (Z) as the input one.

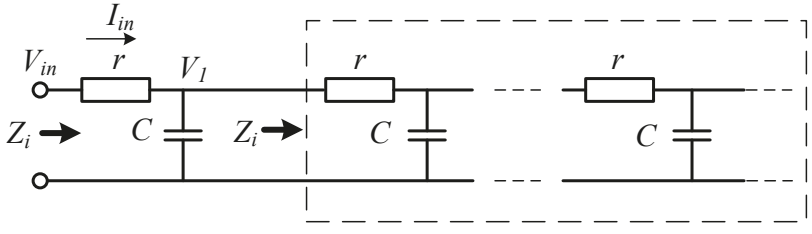

Figure 5. Infinite r–C chains based equivalent circuit of a capacitor (r: resistor, C: capacitor, Zi: input impedance, V_{in}: input voltage, I_{in}: input current).

In our previous work, the infinite r–C chain-based equivalent circuit of the UCs was proposed and discussed [13]. The resistance (R) and reactance (X) of this equivalent circuit can be expressed as:

$$R = \frac{1}{2}\left(r + \sqrt{r^2 + 4X^2}\right). \tag{1}$$

$$X = -\sqrt{\frac{-r^2 + \sqrt{r^4 + \left(\frac{4r}{\omega C}\right)^2}}{8}} = -\frac{r}{2\sqrt{2}}\sqrt{\sqrt{1 + \left(\frac{4}{\omega r C}\right)^2} - 1}. \tag{2}$$

Equations (1) and (2) represent the Fourier transform of internal impedance. If the equivalent capacitance is very large (~100–1000 F), then a relatively small inductivity (~10 nH) of connecting cables and electrodes plays a significant role in the measurement of reactance. Hereafter, the component for the inductivity of cables should be included in the equivalent circuit (Figure 6).

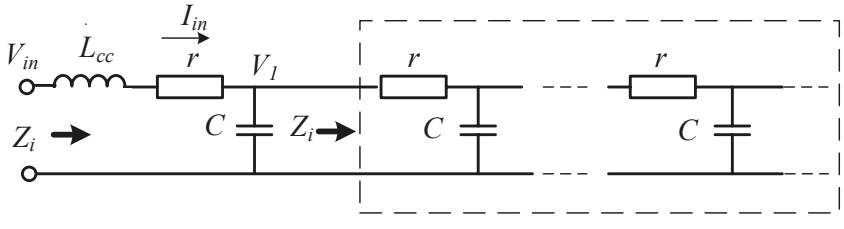

Figure 6. Modified equivalent circuit of the ultracapacitor. The component, *L*cc, represents the inductivity of connection wires.

According to the modified equivalent circuit, the total reactance (X_T) is written as:

$$X_T = \frac{r}{2}\left(\frac{2\omega L_{cc}}{r} - \frac{1}{\sqrt{2}}\sqrt{\sqrt{1+\left(\frac{4}{\omega rC}\right)^2}-1}\right). \quad (3)$$

Inserting Equation (3) into Equation (1) gives the resistance R:

$$R = \frac{r}{2}\left(1+\sqrt{1+\left(\frac{2\omega L_{cc}}{r} - \frac{1}{\sqrt{2}}\sqrt{\sqrt{1+\left(\frac{4}{\omega rC}\right)^2}-1}\right)^2}\right). \quad (4)$$

Figure 7 demonstrates the comparison between experimental and calculated EIS data. Equations (3) and (4) are employed for the simulation, and the least-mean squares approach was applied for the theoretical fitting. The coefficient of determination (χ^2) decides the criterion of the proximity between the theoretical and experimental output. This large value of χ^2 (~0.992) proved the accuracy of the proposed method, although this analysis was performed for the EIS data measured at a temperature of 15 °C, V_{UC} of 2.736 V, and AC current of 1.4 A. However, this model was valid for data measured at different temperatures and voltages (Figure 3).

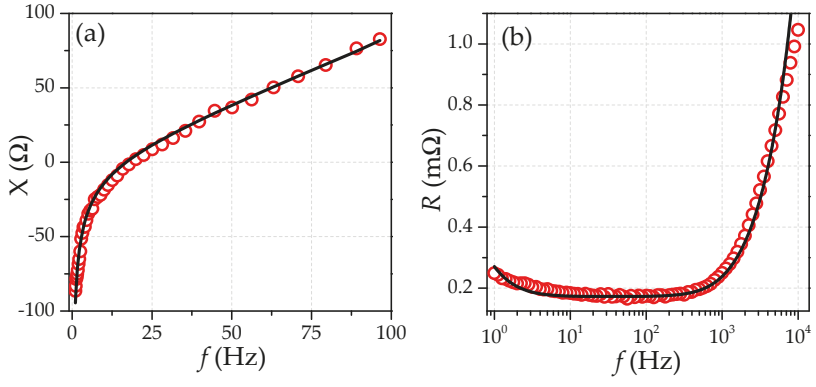

Figure 7. Simulated and measured EIS data of symmetric double-layer UC (**a**) reactance, (**b**) resistance.

The internal resistance and capacitance exhibited relatively small change (±10–15%) for the applicable voltage range (Figure 2). Hence, the constant parameter representation was considered for the calculation of equivalent circuit parameters. The proposed model should be modified accordingly, if the voltage and current parameters are altered significantly.

3.2. Representation of Dynamic UC Parameters Using Reverse Fourier Transform

The equivalent circuit and obtained parameters (r and C) can be utilized to determine the voltage and current parameters of UC for different working conditions. For this purpose, a reverse Fourier transformation was applied. Let us consider that current (I_{in}) is applied as input for the equivalent circuit (Figure 5). Using nodal analysis, the voltage (V_1) is expressed as:

$$V_1\left(j\omega C + \frac{1}{Z}\right) = I_{in} \Rightarrow V_1 = \frac{I_{in}}{j\omega C + \frac{1}{Z}} \quad (5)$$

where V_1 and Z are assumed as complex variables. The solution of the following Fourier integral is needed to restore the capacitor voltage [41]:

$$V_1(t) = \frac{2}{\pi}\int_0^{\infty} \frac{R(\omega)\sin(\omega t)}{\omega} d\omega \tag{6}$$

where $R(\omega)$ is the real part of the Fourier transform of V_1 (Equation (4)). The input voltage (V_{in}) can be calculated:

$$V_{in} = V_1 + \Delta V_r = V_1 + I_{in} r \tag{7}$$

where $\Delta V_r = I_{in} r$ is the voltage drop at the resistance r. The numerical approaches can only solve the integral (6) because of its irrational form. First, the real part of the impedance is obtained using the specific values of r and C following the expression (4). Second, the real part of Z is substituted to the integral (6), which is numerically solved for the required series of time (t_0–t_{max}) and time resolution (Δt). Using the proposed model and EIS data, the equivalent circuit parameters can be calculated as $r = 0.1$ mΩ, C = 800 F. The voltage of UC for charge-discharge processes was simulated for the constant input current of 20 A. The simulated and measured dynamic characteristics of UC for both charge-discharge cycles are demonstrated in Figure 8. The numerical analysis of Fourier integral provides the expected output for charging-discharging processes. The theoretical analysis was consistent with the experimental one, which approves the transverse Fourier transformation for the restoration of UC dynamic behavior.

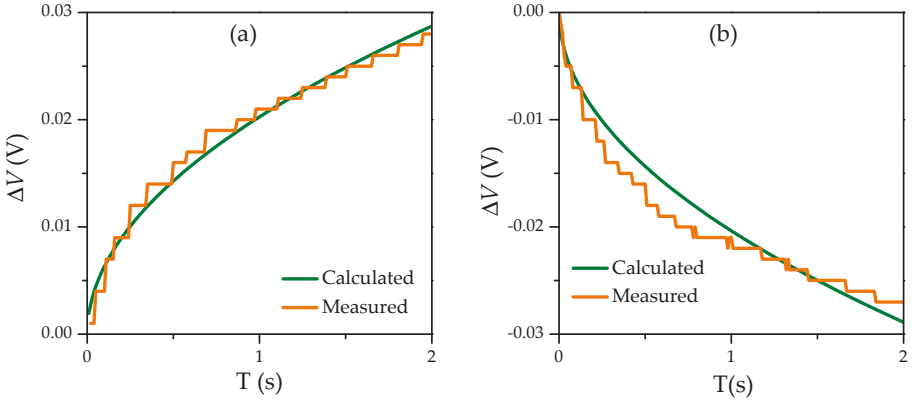

Figure 8. Representation of dynamic behavior of UC voltage using reverse Fourier transform (**a**) charging process, (**b**) discharging process. The UC characteristics are measured at constant input current of 20 A and temperature of 30 °C.

The restoration of parameters can also be achieved by the integral given below:

$$V(t) = \frac{1}{2\pi}\int_{-\infty}^{\infty} F(\omega) e^{j\omega t} d\omega \tag{8}$$

where $F(\omega)$ is the Fourier transform of the input current and can be written as:

$$F(\omega) = \int_{-\infty}^{\infty} V(t) e^{-j\omega t} dt \tag{9}$$

Generally, $F(\omega)$ is a complex variable and contains real and imaginary parts. The rigorous finite analytical representation of the Fourier transform exists for several functions (e.g., step- and

pulse-function). However, an analytical Fourier formulation could not be presented for each mathematical expression.

4. Equivalent Circuit Model with PSIM Software

The previous section stated that the Fourier reverse transformation could be applied only for a restricted class of mathematical expressions. Hence, simulation of the electrical circuit using appropriate software is a convenient and efficient method. For arbitrary functions, one of the most efficient software is the PSIM simulating package [42].

The equivalent circuit model was developed to simulate the periodic charge-discharge process of UC (Figure 9). The model includes a ladder of ten r–C chains and inductivity of connecting cables. This circuit can be applied for any arbitrary current input function. For example, the galvanostatic measurements can be carried out by applying the AC control signal as the input of a current source. Figure 10 shows the measured and simulated (using proposed model) voltage behavior of the symmetric double layer UC for periodic charging-discharging cycles with a constant current of ±100 A, a period of 3 s, and duty-cycle relation of 0.5. The instantaneous deviations of a voltage over its steady-state magnitude were measured. The simulation study yielded an excellent agreement between the experimental and calculated charge-discharge characteristics of UC. The accuracy of such a model lay inside 5–8% of the relative error between the calculated and experimental data.

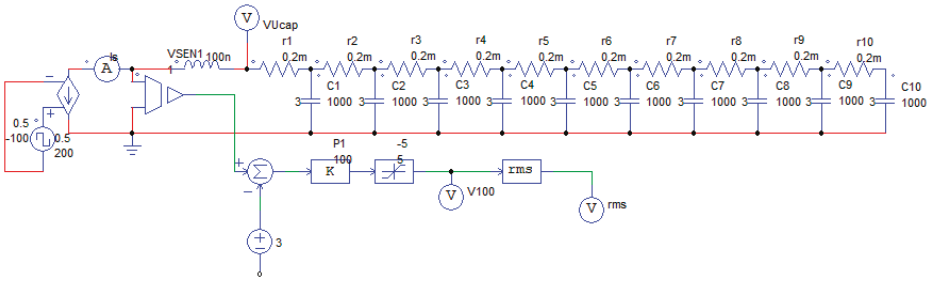

Figure 9. Model of the equivalent electrical circuit for the galvanostatic measurement. This model comprises ten r–C chains and includes the inductivity of connecting cables.

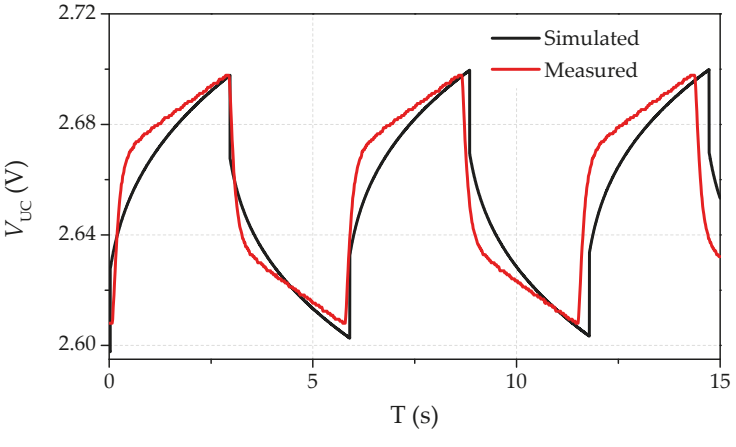

Figure 10. The experimental and simulated characteristics of symmetric double layer UC for periodic charging and discharging cycles.

5. Discussion

The proposed model can effectively describe the dynamic behavior of UC without the usage of PDEs. This model describes the concentration of ions by an electrical potential, charge diffusive motion by electric current, and diffusion coefficient by electrical resistance. Therefore, the exact physical nature of electrolyte is considered in the proposed mathematical model. The infinite r–C chain-based equivalent circuit exactly describes the behavior of ion movement in the electrolyte and porous electrodes. Moreover, we succeeded in finding a rigorous analytical solution of this model in the closed form. The symmetric double layer UCs are purely electrostatic devices. Hence, no electrochemical (Faradaic) reactions occur on electrodes instead of asymmetrical UCs, where the electrochemical reactions occur in the one compartment of UC. Therefore, the voltage-dependent term (pseudo-capacitance related to Faradaic reactions) is not considered in the model. Some previous studies have considered the voltage-dependent capacitance term for the modeling [33,43]. Rafik et al. claimed that consideration of the voltage-dependent term could improve the modeling precision by 10% more than that of constant term approximation [33]. If the voltage and current deviations are significantly large, then the parameters should be adjusted accordingly. Future works will consider the incorporation of voltage-dependent capacitance term in the infinite r–C chain equivalent circuit. More importantly, this study also approved the principle possibility of applying the reverse Fourier transform on the frequency domain for the description of dynamic behavior. We also want to mention that the finite analytical representation of the Fourier transform cannot be applied for every mathematical expression. Hence, the proposed model was analyzed using simulation software to study the dynamic behavior of UC. The experimental and calculated charge-discharge characteristics displayed good agreement with a relative error of 5–8%. During the modeling, it was noted that a higher number of r–C chains led to higher accuracy in the impedance representation. Last but not least, we want to mention that this article strengthens the usefulness and advantages of the infinite r–C chains-based equivalent circuit.

6. Conclusions

The infinite number of r–C chain-based equivalent circuit for a symmetric double-layer UC was evaluated in this work. The dynamic characteristics were studied to authenticate the applicability of the projected equivalent circuit in the practical working conditions. The internal resistance and capacitance values of the ultracapacitor remained relatively constant for the charging-discharging processes despite the current and voltage change in a wide range of parameters. However, the internal resistance is strongly influenced by the working temperature. The possible reason is the decay of the diffusion coefficient at lower temperatures. The EIS studies confirmed that the impedance remained constant for a wide range of applied voltage (0.3376–2.736 V) and temperatures (−30 °C to +30 °C). The reactance was determined by an inductive reactance of a connecting cable, especially for frequencies higher than 100 Hz. Following from the inductive reactance nature, the temperature did not influence it. The UC functionality, periodic, and stochastic phases of the charge-discharge current are recommended to verify using simulation software. An electrical engineer can apply the proposed equivalent circuit to estimate the electrical parameters for the development of energy storage facilities.

Author Contributions: Conceptualization, M.A., A.K., and A.Y.; Methodology, M.A. and S.R.; Software, M.A. and S.R.; Formal analysis, M.A., A.K., and A.Y.; Investigation, S.R.; Resources, M.A. and A.Y.; Data curation, S.R. and M.A.; Writing—original draft preparation, S.R. and M.A.; Writing—review and editing, S.R., A.K., A.Y., and M.A.; Supervision, A.Y. and M.A.; Project administration, M.A. All authors have read and agreed to the published version of the manuscript.

Funding: This research received no external funding.

Acknowledgments: The authors gratefully acknowledge the support of M. Zinigrad (Ariel University), Y. Bernstein (Ariel University), and M. Perl (Wise-Tech. Co.) for the experiments. S. Rajput is thankful to the Israeli Council for Higher Education (CHE) for the fellowship.

Conflicts of Interest: The authors declare no conflict of interest.

References

1. Shtessel, Y.B.; Ghanes, M.; Ashok, R.S. Hydrogen Fuel Cell and Ultracapacitor Based Electric Power System Sliding Mode Control: Electric Vehicle Application. *Energies* **2020**, *13*, 2798. [CrossRef]
2. Karden, E.; Ploumen, S.; Fricke, B.; Miller, T.; Snyder, K. Energy storage devices for future hybrid electric vehicles. *J. Power Sources* **2007**, *168*, 2–11. [CrossRef]
3. Wong, L.A.; Ramachandaramurthy, V.K.; Taylor, P.; Ekanayake, J.B.; Walker, S.L.; Padmanaban, S. Review on the optimal placement, sizing and control of an energy storage system in the distribution network. *J. Energy Storage* **2019**, *21*, 489. [CrossRef]
4. Rajput, S.; Amiel, I.; Sitbon, M.; Aharon, I.; Averbukh, M. Control the Voltage Instabilities of Distribution Lines using Capacitive Reactive Power. *Energies* **2020**, *13*, 875. [CrossRef]
5. Sorkin, O.; Farber, E.; Averbukh, M. Selecting ultracapacitors for smoothing voltage deviations in local grids fed by transformer with tap-changer and distributed PV facilities. *Electronics* **2019**, *8*, 357. [CrossRef]
6. Heard, B.P.; Brook, B.W.; Wigley, T.M.; Bradshaw, C.J. Burden of proof: A comprehensive review of the feasibility of 100% renewable-electricity systems. *Renew. Sustain. Energy Rev.* **2017**, *76*, 1122. [CrossRef]
7. Rajput, S.; Averbukh, M.; Yahalom, A.; Minav, T. An Approval of MPPT Based on PV Cell's Simplified Equivalent Circuit During Fast-Shading Conditions. *Electronics* **2019**, *8*, 1060. [CrossRef]
8. Kumar, G.V.B.; Sarojini, R.K.; Palanisamy, K.; Padmanaban, S.; Holm-Nielsen, J.B. Large Scale Renewable Energy Integration: Issues and Solutions. *Energies* **2019**, *12*, 1996. [CrossRef]
9. Averbukh, M.; Lineykin, S.; Kuperman, A. Portable ultracapacitor based power source for emergency starting of internal combustion engines. *IEEE Trans. Power Electron.* **2015**, *30*, 4283–4290. [CrossRef]
10. Uno, M.; Iwasaki, K.; Hasegawa, K. Series-Parallel Reconfiguration Technique with Voltage Equalization Capability for Electric Double-Layer Capacitor Modules. *Energies* **2019**, *12*, 2741. [CrossRef]
11. Ito, Y.; Yanagisawa, H.; inventors; Panasonic Intellectual Property Management Co Ltd. assignee. Electrolyte Solution for Electric Double Layer Capacitors, and Electric Double Layer Capacitor. U.S. Patent 10,199,179, 5 February 2019.
12. Teuber, M.; Strautmann, M.; Drillkens, J.; Sauer, D.U. Lifetime and Performance Assessment of Commercial Electric Double-Layer Capacitors Based on Cover Layer Formation. *ACS Appl. Mater. Interfaces* **2019**, *11*, 18313. [CrossRef]
13. Abetbool, Y.; Rajput, S.; Yahalom, A.; Averbukh, M. Comprehensive Study on Dynamic Parameters of Symmetric and Asymmetric Ultracapacitors. *Electronics* **2019**, *8*, 891. [CrossRef]
14. Muzaffar, A.; Ahamed, M.B.; Deshmukh, K.; Thirumalai, J. A review on recent advances in hybrid supercapacitors: Design, fabrication and applications. *Renew. Sustain. Energy Rev.* **2019**, *101*, 123. [CrossRef]
15. Jiya, I.N.; Gurusinghe, N.; Gouws, R. Electrical Circuit Modelling of Double Layer Capacitors for Power Electronics and Energy Storage Applications: A Review. *Electronics* **2018**, *7*, 268. [CrossRef]
16. Guo, J.; Liu, W.; Chu, L.; Zhao, J. Fractional-Order Modeling and Parameter Identification for Ultracapacitors with a New Hybrid SOA Method. *Energies* **2019**, *12*, 4251. [CrossRef]
17. Skovranek, T.; Macias, M.; Sierociuk, D.; Malesza, W.; Dzielinski, A.; Podlubny, I.; Pocsova, J.; Petras, I. Anomalous diffusion modeling using ultracapacitors in domino ladder circuit. *Microelectron. J.* **2019**, *84*, 136. [CrossRef]
18. Kang, J.; Wen, J.; Jayaram, S.H.; Yu, A.; Wang, X. Development of an equivalent circuit model for electrochemical double layer capacitors (EDLCs) with distinct electrolytes. *Electrochim. Acta* **2014**, *115*, 587. [CrossRef]
19. Pozo, B.; Garate, J.I.; Ferreiro, S.; Fernandez, I.; de Gorostiza, E.F. Supercapacitor Electro-Mathematical and Machine Learning Modelling for Low Power Applications. *Electronics* **2018**, *7*, 44. [CrossRef]
20. Song, S.; Zhang, X.; Li, C.; Wang, K.; Sun, X.; Huo, Q.; Wei, T.; Ma, Y. Equivalent circuit models and parameter identification methods for lithium-ion capacitors. *J. Energy Storage* **2019**, *24*, 100762. [CrossRef]
21. Buller, S.; Karden, E.; Kok, D.; Doncker, R.W.D. Modeling the dynamic behavior of supercapacitors using impedance spectroscopy. *IEEE Trans. Ind. Appl.* **2002**, *38*, 1622. [CrossRef]
22. Zhang, L.; Hu, X.; Wang, Z.; Sun, F.; Dorrell, D.G. A review of supercapacitor modeling, estimation, and applications: A control/management perspective. *Renew. Sustain. Energy Rev.* **2018**, *81*, 1868–1878. [CrossRef]

23. Drummond, R.; Zhao, S.; Howey, D.A.; Duncan, S.R. Circuit synthesis of electrochemical supercapacitor models. *J. Energy Storage* **2017**, *10*, 48. [CrossRef]
24. Yu, A.; Chabot, V.; Zhang, J. *Electrochemical Supercapacitors for Energy Storage and Delivery: Fundamentals and Applications*; CRC Press: Boca Raton, FL, USA, 2017.
25. Barbero, G.; Lelidis, I. Analysis of Warburg's impedance and its equivalent electric circuits. *Phys. Chem. Chem. Phys.* **2017**, *19*, 24934. [CrossRef] [PubMed]
26. De Pauli, M.; Gomes, A.M.; Cavalcante, R.L.; Serpa, R.B.; Reis, C.P.; Reis, F.T.; Sartorelli, M.L. Capacitance spectra extracted from EIS by a model-free generalized phase element analysis. *Electrochim. Acta* **2019**, *320*, 134366. [CrossRef]
27. Belhachemi, F. *Modélisation et Caractérisation des Supercondensateurs à Couche Double Électrique Utilisés en Électronique de Puissance (Doctoral Dissertation)*; National Polytechnic Institute of Lorraine (INPL): Lorraine, France, 2001.
28. Logerais, P.O.; Camara, M.A.; Riou, O.; Djellad, A.; Omeiri, A.; Delaleux, F.; Durastanti, J.F. Modeling of a supercapacitor with a multibranch circuit. *Int. J. Hydrog. Energy* **2015**, *40*, 13725. [CrossRef]
29. Berrueta, A.; Martin, I.S.; Hernández, A.; Ursúa, A.; Sanchis, P. Electro-thermal modelling of a supercapacitor and experimental validation. *J. Power Sources* **2014**, *259*, 154. [CrossRef]
30. Belhachemi, F.; Rael, S.; Davat, B. A physical based model of power electric double-layer supercapacitors. In Proceedings of the Conference Record of the 2000 IEEE Industry Applications Conference, Rome, Italy, 8–12 October 2000; pp. 3069–3076.
31. Navarro, G.; Nájera, J.; Torres, J.; Blanco, M.; Santos, M.; Lafoz, M. Development and Experimental Validation of a Supercapacitor Frequency Domain Model for Industrial Energy Applications Considering Dynamic Behaviour at High Frequencies. *Energies* **2020**, *13*, 1156. [CrossRef]
32. Musolino, V.; Piegari, L.; Tironi, E. New full-frequency-range supercapacitor model with easy identification procedure. *IEEE Trans. Ind. Electron.* **2012**, *60*, 112. [CrossRef]
33. Rafik, F.; Gualous, H.; Gallay, R.; Crausaz, A.; Berthon, A. Frequency, thermal and voltage supercapacitor characterization and modeling. *J. Power Sources* **2007**, *165*, 928. [CrossRef]
34. K2 ULTRACAPACITORS: 2.85V/3400F. Available online: https://www.maxwell.com/images/documents/K2_2_85V_DS_3000619EN_3_.pdf (accessed on 7 January 2020).
35. Charge/Discharge System Controller, PFX2532. Available online: https://www.kikusui.co.jp/en/product/detail.php?IdFamily=0118 (accessed on 19 January 2020).
36. Variable-Switching MultiRange DC Power Supply PWR 1600W. Available online: https://www.kikusui.co.jp/en/product/detail.php?IdFamily=0064 (accessed on 19 January 2020).
37. Multifunctional DC Electronic Load, PLZ-4W Series. Available online: https://www.kikusui.co.jp/en/product/detail.php?IdFamily=0011 (accessed on 19 January 2020).
38. Midi Logger GL900. Available online: http://www.graphteccorp.com/instruments/gl900/index.html (accessed on 27 January 2020).
39. EchemLab XM Potentiostat Galvanostat. Available online: https://www.ameteksi.com/products/potentiostats/single-channel/apps-xm-series/echemlab-xm-potentiostat-galvanostat (accessed on 1 March 2020).
40. Lunaire Steady State Testing Chamber. Available online: https://www.thermalproductsolutions.com/brands/tenney-lunaire-environmental-test-chambers-and-rooms (accessed on 6 March 2020).
41. Shenkman, A.L.; Zarudi, M. *Circuit Analysis for Power Engineering Handbook*; Springer Science & Business Media: Berlin, Germany, 2012.
42. PSIM-Software for Power Electronics. Available online: https://powersimtech.com/products/psim/ (accessed on 10 May 2020).
43. Zubieta, L.; Bonert, R. Characterization of double-layer capacitors for power electronics applications. *IEEE Trans. Ind. Appl.* **2000**, *36*, 199. [CrossRef]

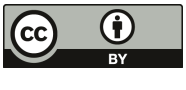

energies

MDPI

Article

An Improved SOC Control Strategy for Electric Vehicle Hybrid Energy Storage Systems

Kai Wang [1,*], Wanli Wang [1], Licheng Wang [2] and Liwei Li [1,*]

[1] School of Electrical Engineering, Qingdao University, Qingdao 266071, China; 2018025373@qdu.edu.cn
[2] College of Information Engineering, Zhejiang University of Technology, Hangzhou 310014, China; wanglicheng@zjut.edu.cn
* Correspondence: wkwj888@163.com or wangkai@qdu.edu.cn (K.W.); llw@qdu.edu.cn (L.L.)

Received: 27 July 2020; Accepted: 2 October 2020; Published: 12 October 2020

Abstract: In this paper, we propose an optimized power distribution method for hybrid electric energy storage systems for electric vehicles (EVs). The hybrid energy storage system (HESS) uses two isolated soft-switching symmetrical half-bridge bidirectional converters connected to the battery and supercapacitor (SC) as a composite structure of the protection structure. The bidirectional converter can precisely control the charge and discharge of the SC and battery. Spiral wound SCs with mesoporous carbon electrodes are used as the energy storage units of EVs. Under the 1050 operating conditions of the EV driving cycle, the SC acts as a "peak load transfer" with a charge and discharge current of $2i_{sc}$~$3i_{bat}$. An improved energy allocation strategy under state of charge (SOC) control is proposed, that enables SC to charge and discharge with a peak current of approximately $4i_{bat}$. Compared with the pure battery mode, the acceleration performance of the EV is improved by approximately 50%, and the energy loss is reduced by approximately 69%. This strategy accommodates different types of load curves, and helps improve the energy utilization rate and reduce the battery aging effect.

Keywords: hybrid energy storage system; supercapacitor; energy allocation

1. Introduction

In recent years, energy shortages and environmental degradation have attracted increasing attention [1–6]. Increasing car ownership has led to an increase in pollution from automobile exhaust emissions, thereby forcing the acceleration of energy transformation in the automotive industry. As a new type of transportation, electric vehicles (EVs) have great advantages in energy saving, emission reduction and reduction of fossil fuel dependence, which has greatly promoted their development.

The power supply system is the core part of the EV and directly affects the overall performance of the vehicle [7–10] and currently, the power supply problem of electric vehicles is a major obstacle to the development of EVs [11]. To promote and use EVs more widely, electric vehicles need higher specific energy, higher specific power, longer cycle life of energy storage system and higher charging efficiency [12–16].

Conventional EV energy storage systems are battery-based storage devices, which have large deficiencies and limitations [17–20]. First, the power density of the battery is low, thereby it cannot meet the peak power demand of EVs under acceleration or climbing conditions. Although the power demand can be satisfied by increasing the number of battery cells, the EV load will be increased considerably. Second, in battery energy storage systems, frequent current changes generate additional heat, reducing efficiency and battery life.

Therefore, we herein study a hybrid energy storage system (HESS) comprising batteries and supercapacitors (SCs). As a new type of environmentally friendly energy storage device, SC has the

advantages of high power density, high efficiency, fast response speed, and long cycle life that can improve energy utilization and dynamic performance to some extent [21–26].

The range of power required for operation under certain operating conditions (such as starting, acceleration, deceleration, stopping, and climbing) is wide. When the SC is directly connected to the battery, stabilizing the output voltage and controlling the energy distribution is difficult. In our research, we adopted the half-bridge of the control topology, wherein a bidirectional DC/DC converter connects the SC to the battery [27–30]. To enhance the discharge persistence of the battery current, the battery current is reduced to a minimum. The entire driving cycle strategy is employed to reduce the power loss in a given load curve. A discrete optimization design is used to improve the control effect of EVs.

This paper analyzes the deficiencies of the topology and control strategies of traditional HESSs, improves the previous topology, and proposes an optimized power allocation strategy based on the current control of EVs, thereby accurately predicting future power requirements. In addition, on the basis of current control, we herein add the SOC control of SCs based on the driving speed of EVs, thereby reducing the overcharge and overdischarge of the battery, improving the climbing performance of the EV, improving the energy utilization rate and reducing the battery aging effect [31–37].

2. Hybrid Energy Storage System

Energy storage devices can be divided into physical energy storage devices, chemical energy storage devices, and electromagnetic energy storage devices. Table 1 lists the main parameters of the common energy storage devices.

Table 1. Main parameters of common energy storage.

Energy Storage Type	Efficiency (%)	Energy Density (Wh/kg)	Power Density (W/kg)	Service Cycle	Cost ($/kW/Year)
Battery	60–80	30–240	100–700	≤2000	25–120
Lithium battery	≥85	250–300	800–1100	10^3–10^4	120
Supercapacitor	≥90	≤10	700–18,000	≥10^5	85
Superconducting energy storage	≥95	≤10	≥10^4	≥10^5	200

Table 1 shows that a single energy storage device cannot unify power density and energy density, and cannot meet the complex and variable power demand of EVs. Combining the advantages of batteries and SCs, it is proposed that batteries and SCs be used as composite energy sources to meet the needs of EV power supply changes. The high energy density of the battery guarantees EV mileage for one charge. SCs can provide instantaneous high current output to meet the peak power (such as for acceleration and climbing) required by EVs, thus ensuring dynamic performance. When the EV decelerates or degrades, the power system is in an energy feedback state; thus, the SC can more efficiently and quickly absorb feedback energy, improve the energy efficiency of the system, and protect the battery from heavy currents. There are four common structures of HESS composed of two energy storage devices and one load device [38–41]:

(1) The SC, battery and load are directly connected in parallel, as shown in Figure 1a. This connection is low cost and fast response, but it also has several limitations: such as the capacity of the energy storage system cannot be fully utilized, and the power allocation is not controlled; the voltage of the SC is not controlled, and it depends on the SOC of the battery, which will affect the optimal utilization of SC.

(2) The SC control structure, as shown in Figure 1b. The SC is connected to the DC/DC bidirectional converter, and the battery is directly connected to the DC bus. This structure can lead to the capacity of the SC being fully utilized, and this is advantageous to the high-power throughput capacity of the SC. However, the charging and discharging and the power of the battery cannot be effectively controlled.

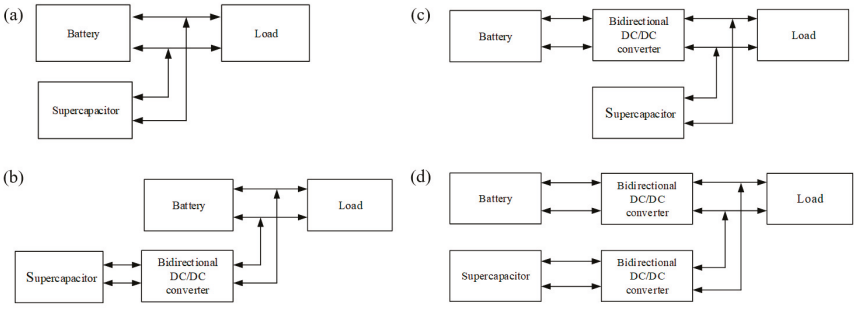

Figure 1. (**a**) Direct parallel structure; (**b**) Structure of SC control; (**c**) Structure of battery control; (**d**) Structure of two power supply control.

(3) The battery control structure, as shown in Figure 1c. The power of the battery can be controlled, and the charging and discharging current of the battery can be optimized that can prolong the service life of the battery. The SC can achieve a fast response speed when the peak power output changes, but obtaining a stable voltage is difficult, resulting in poor system stability.

(4) The dual-power control structure, as shown in Figure 1d. The structure can provide flexible voltage control, and can better allocate power to the battery and the SC. The battery can also prolong the service life, and its energy can be fully utilized. Bidirectional DC/DC can be used for an energy management system with a more flexible configuration. However the existence of bidirectional DC/DC will increase the cost and loss of the system, as well as increase the complexity of the system structure and the mass of EVs [42–44].

Currently, SC control structures are widely used in EV composite power supply systems. In this study, a new power allocation strategy is required to accurately control the charging and discharging of the battery and SC. Figure 1d shows a schematic of the structure. In this study, the bidirectional DC/DC converter adopts half-bridge topology structure. The principle of the bidirectional DC/DC converter in HESS of EVs. When the system is discharged, the bidirectional DC/DC controller operates in the Boost mode, and the energy flows from the low-voltage side to the high-voltage side; when the system is in charge, the bidirectional DC/DC controller operates in the Buck mode, and the energy flows from the high-voltage side to the low-voltage side.

A supercapacitor is a type of energy storage device, that stores electric energy converted from various clean energy sources. It is conventionally divided into two types: stacked and wound. Electrode materials are important factors affecting the energy storage characteristics of SCs. Ordered mesoporous carbon materials not only have the characteristics of uniform pore size distribution, large pore volume and high specific surface area, but also have the advantages good chemical inertness, strength, electrical conductivity and thermal stability. In this study, a spiral wound SC with ordered mesoporous carbon electrodes was used. Figure 2 shows the diagram of the SC structure.

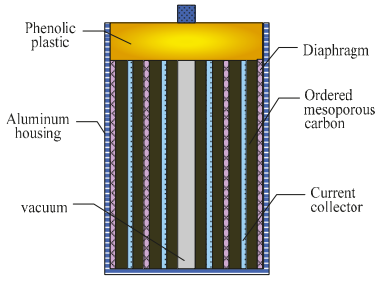

Figure 2. SC structure diagram.

Figure 3 shows the electrochemical properties of the ordered mesoporous carbon (OMC) electrode. According to the X-ray diffraction (XRD) pattern of the ordered mesoporous carbon, it is known that no impurity peak appears, the full width at half maximum is large, and the degree of crystallization is small, indicating it to be a good electrode material. According to the SEM (scanning electron microscope) image of the ordered mesoporous carbon, the basic unit structure is uniform in size. According to the transmission electron microscope (TEM) image of the ordered mesoporous carbon, the pore structure is arranged in order and the conductivity is strong. The charge and discharge curves of the electrode material at 5 mA show good linearity, the self-discharge current is relatively small, and there is no obvious voltage drop at the initial discharge, indicating that the electrode material has a small internal resistance and ideal capacitance performance; moreover, it is suitable as an energy storage system unit for EVs.

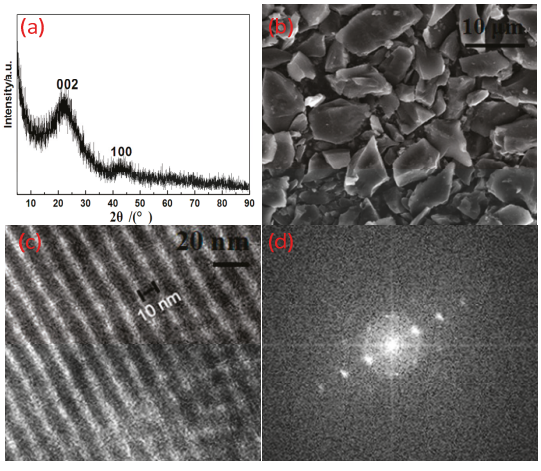

Figure 3. Electrochemical properties: (**a**) =XRD spectrum of the synthesized OMC; (**b**) SEM photograph of the OMC; (**c**) and (**d**) =TEM photographs of the OMC.

To detect the characteristics of SCs, constant current charge and discharge experiments were carried out on the SC cells used herein. The charge and discharge voltage range was set to −1.0–0 V, and the charge and discharge currents were 5, 8 and 10 mA. The single charge and discharge curves have good reversibility, and the two sides of the curve are basically symmetrical. The initial voltage has no significant voltage drop and has ideal capacitive characteristics. As shown in Figure 4b, the half-arc of the high-frequency region is small, indicating that the charge transfer resistance at the interface between the electrode and the electrolyte is small. In the intermediate-frequency region, the slope is close to 45°, which is related to the charge transfer impedance; the straight line in the low-frequency region is similar to the vertical line, demonstrating good capacitance characteristics. As shown in Figure 4c, the curve shows a typical capacitance characteristic. The time constant (the product of capacitance and resistance) determines the steepness of the potential conversion. When the scanning direction changes, the electrode exhibits a fast current response and is rapid in a stable state, indicating that the internal resistance is small, the RC time constant is small, and it is suitable for high current. As shown in Figure 4d, as the number of cycles increases, the attenuation of capacitance weakens. In the initial stage of the cycle, the surface functional groups of the OMC will decompose, thereby consuming part of the capacitance. Second, as the number of cycles increases, the increase in the temperature of the capacitor will decrease the capacitance, causing a partial fragile hole to be broken. Simultaneously, the increase in temperature further exacerbates the decomposition of the surface functional groups. However, the overall fit is good, and it is suitable as an energy storage system unit for EVs.

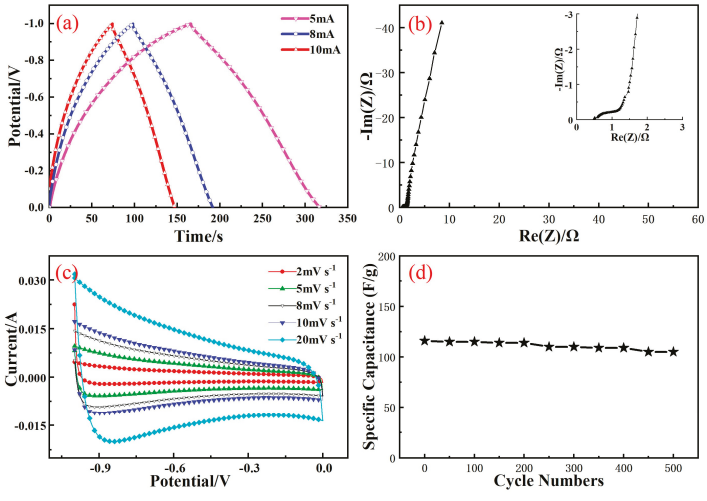

Figure 4. Electrical performance test: **(a)** Charge–discharge curves; (**b**) Impedance characteristic curves; (**c**) CV curves; (**d**) Cycle performance curves.

Figure 5 shows the state of health (SOH) estimation during the supercapacitor cycle. When the number of cycles was less than 6000, the SOH of the supercapacitor was maintained above 80%, and the cycle performance was relatively good.

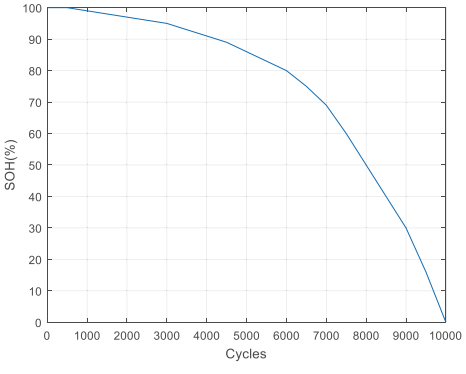

Figure 5. SC cycle performance.

Currently, SC control structures are widely used in EV composite power systems. Based on the dual-power control structure, a new power allocation strategy is proposed to accurately control the charging and discharging of the battery and the SC. The DC converter used herein a composite converter with an isolated soft-switching symmetrical half-bridge bidirectional converter as a protection structure. The principle of bidirectional DC/DC converter in HESS of Ev is as follows: When the system is discharged, the bidirectional DC/DC controller works in the boost mode, and energy flows from the low-voltage side to the high-voltage side. When the system is charged, the bidirectional DC/DC controller operates in the buck mode, and energy flows from the high-voltage end to the low-voltage end. Figure 6 shows a device used in EV testing.

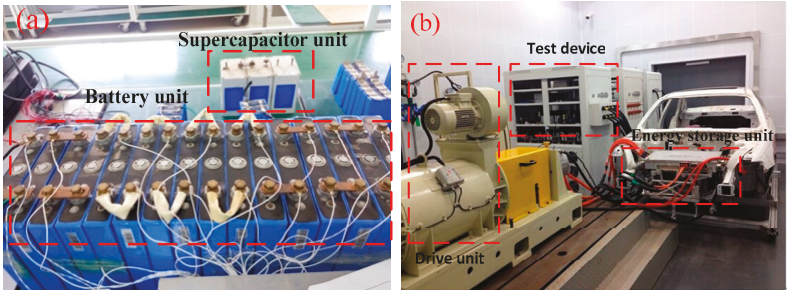

Figure 6. Experimental test device: (**a**) Mixed energy storage unit; (**b**) Vehicle test device.

3. Typical Control Policy

The basic structure of the control strategy in the EV HESSs is shown in Figure 7. The DC/DC converter uses a composite converter with an isolated soft-switching symmetrical half-bridge bidirectional converter as a protection structure when extreme currents occur, as opposed to the non-isolated DC/DC converter used previously. In the event of a sudden increase in current, switching to an isolated converter is possible to avoid damage to the energy storage system due to direct electrical connections. Under normal operating conditions, the DC/DC converter operates in the boost mode during discharge and operates in the buck mode during energy feedback.

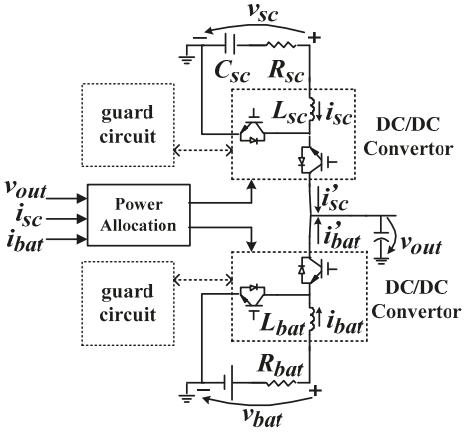

Figure 7. Conventional control structure.

The power distribution method is as follows. When the EV is driven at a constant speed, the battery unit is separately powered in the HESS. At this time, the battery cells were discharged at a constant current. When the EV accelerates or climbs a hill, the remaining peak power is provided by the SC to meet the power demand. When the EV is decelerated, the feedback power generated by the brake is obtained by the battery, reducing energy waste. When the bus current changes abruptly, the battery unit maintains a constant current through the power distribution module, and the remaining peak current is absorbed and released by the SC.

The driving cycle test was performed under the working condition of 1015 as shown in Figure 8. The simulation results of power distribution are shown in Figure 9. It can be concluded that the operating current of the SC is relatively large under this control mode, and *isc* is 2–3 times that of the *ibat*. The SC acts as a "peak load transfer" to help extend battery life. This control method can

effectively play the role of SC's "peak clipping and valley filling", improve the energy utilization rate of the HESS, and limit the peak current of the battery unit to a safe range.

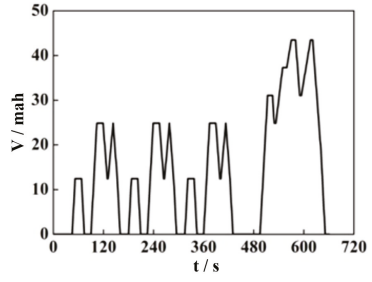

Figure 8. 1015 driving cycle.

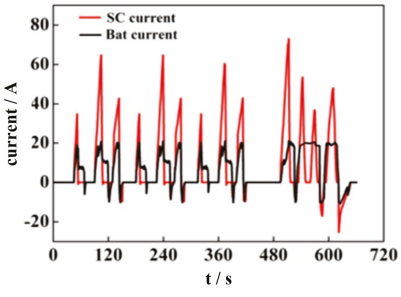

Figure 9. Charge and discharge current distribution of supercapacitors and batteries under the traditional strategy.

As shown in Figure 10, the SOC of the SC demonstrated a large decline at the end of the EV driving cycle and at the lowest point, it dropped to 0.67. This causes the terminal voltage of the SOC of the SC to drop, thereby reducing the transmission efficiency of the DC/DC circuit.

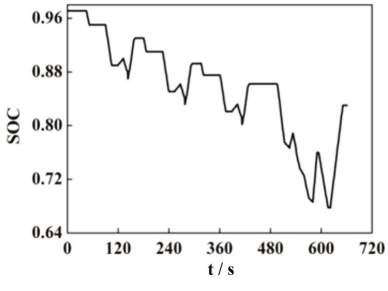

Figure 10. SOC curve of supercapacitors in the typical strategy.

This phenomenon occurs owing to some frequent peak acceleration and deceleration during driving, which result in a large discharge current, but the feedback current is small. During the braking process, most feedback current is absorbed by the battery unit, and the SC cannot recover to a higher SOC value in a short time. In response to this drawback, the feedback object is replaced, and the control SC preferentially absorbs the feedback energy. However, this method allows the SC to charge in a short time. If the remaining large current is still absorbed by the battery, it will reduce the battery life and reduce the energy efficiency.

When an EV operates under extreme acceleration or emergency braking, the energy storage system needs to provide a large peak power or a large peak current. If it is through a non-isolated bidirectional DC/DC converter, direct electrical connections can cause significant damage to the energy storage system. When the peak current exceeds a certain threshold, the current in the DC converter passes through the isolated soft-switching symmetric half-bridge bidirectional converter that protects the safe operation of the energy storage system to some extent. Compared with a full-bridge bidirectional converter, the symmetrical half-bridge bidirectional converter is only half of the latter; therefore, the loss is small and the efficiency is high. The protection circuit topology is shown in Figure 11.

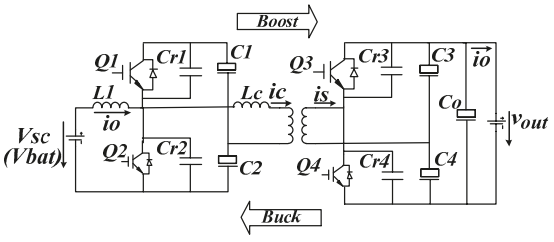

Figure 11. Isolated soft-switching symmetric half-bridge bidirectional converter.

4. Improved SOC Control Strategy

Based on the disadvantages of the traditional control strategy, an improved control strategy is proposed herein based on the compound converter structure with an isolated soft-switching symmetric half-bridge two-way converter as the protection structure. As shown in Figure 12, speed and SC SOC control are added to the controller as influencing factors, thereby forming a four-dimensional space vector control strategy.

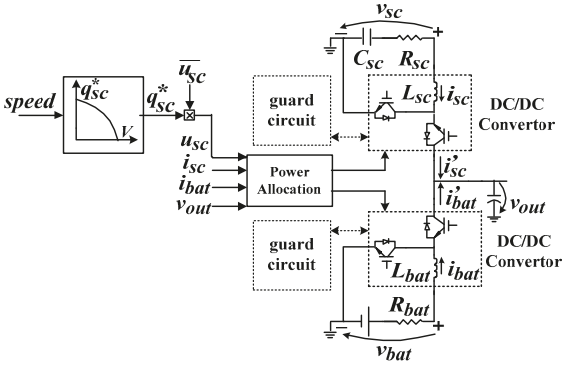

Figure 12. SOC control structure.

According to the above discussion, the driving cycle has an important influence on the control effect. Therefore, the new strategy adjusts SC SOC to the optimal state by analyzing the relationship between SC SOC, speed and power demand. During the electric vehicle is running, the SC provides peak power and the battery provides average power. Considering the kinetic energy theorem, the following relationship can be obtained (excluding power losses):

$$\frac{1}{2}mv_{\max}^2 - \frac{1}{2}mv^2 = \frac{1}{2}cu_{sc}^2 - \frac{1}{2}c(0.5\overline{u_{sc}})^2 + p_{bat}t_0 \quad (1)$$

$$p_{bat} = u_{bat}i_{bat} \quad (2)$$

Here, v is the current vehicle speed, $v_{\max}$ is the maximum vehicle speed, m is the vehicle total mass, c is the SC system capacitance, u_{sc} is the current voltage of the SC end, $\bar{u}_{sc}$ is the rated voltage of the SC, P_{bat} is the rated power of the battery, t_0 is the time for battery to release energy, u_{bat} is the battery nominal voltage, and i_{bat} is the battery nominal current. From (1) and (2), the optimal SC SOC is given by:

$$q_{sc}^{*} = \sqrt{\frac{mv_{\max}^2 - mv^2 - 2u_{bat}i_{bat}t_0}{c\overline{u_{sc}}^2} + 0.25} \tag{3}$$

where, q is the SOC of the ultracapacitor, and q^* is the ideal SOC of the SC. To verify the performance of the optimized power distribution strategy, experimental tests were performed under different conditions. The results of the current distribution are shown in Figure 13. Unlike the traditional control strategy, the battery transfers charge to SC at a constant speed driving and stopping stage, and the current frequency is higher than that of the traditional control strategy. At the end of the acceleration process (380–500 s), the SC provides approximately four times higher i_{bat} peak current than the conventional mode. Based on the comparison between traditional control strategy and the SOC control strategy, the SOC control strategy is concluded to be more conducive to EV acceleration performance. The SOC curve of the SC is shown in Figure 14.

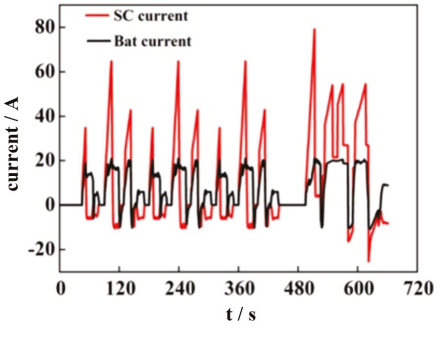

Figure 13. Charge and discharge current distribution of supercapacitors and batteries under SOC control strategy.

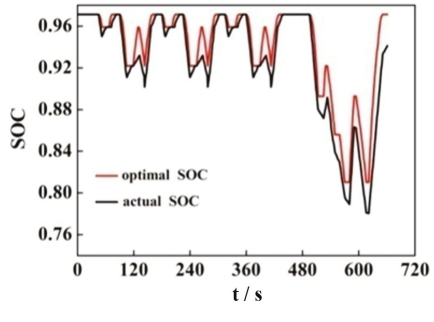

Figure 14. SOC curve of the supercapacitor under the control strategy.

The SOC value of SC is 0.97. In the acceleration and braking stages, the actual SC SOC deviates from the expected value owing to the drastic change in SC charging and discharging current. The SC SOC approaches the optimal curve when EVs continue to operate. Compared with the SOC changes of SC shown in Figure 10, the SOC control strategy is more ideal. Under the optimized control strategy, the SOC of the SC has a small decrease, which can meet the energy output requirement.

The acceleration test of the system is shown in Figure 15a. The acceleration performance under the SOC control is approximately 50% higher than that of the pure battery, and approximately 25% higher than that of the conventional control. The energy loss test under EDUC, NYCC, 1050 and CSHVR is shown in Figure 15b. The energy loss under SOC control is approximately 4%, which is 23% lower than that of conventional control and 69% lower than that of the pure battery. The test parameters of the EV are shown in Table 2. The EV with the SOC control strategy has the shortest acceleration time and the lowest energy consumption. The SOC control strategy proposed herein is superior to the traditional control strategy in terms of acceleration performance and power distribution.

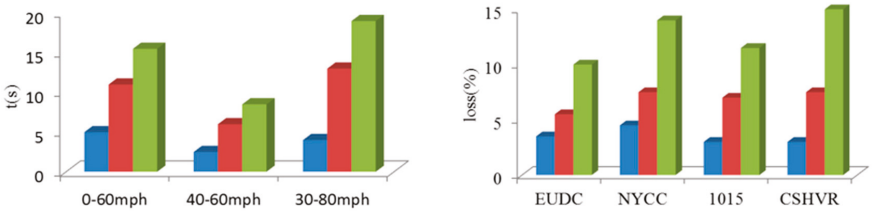

Figure 15. Acceleration and power tests: (**a**) Acceleration tests; (**b**) Power tests.

Table 2. Vehicle, Battery and SC Parameters.

Variable	Symbol	Value	Units
Vehicle total mass	m	1150	[kg]
SC system capacitance	C	5	[F]
SC system nominal voltage	u_{sc}	305	[V]
Battery nominal voltage	u_{bat}	325	[V]
Battery nominal current	i_{bat}	21	[A]
Power assisting time	t_0	9	[s]
Maximum speed	V_{max}	80	[mph]

5. Conclusions

The ordered mesoporous carbon electrode SC prepared herein exhibits good performance under high current conditions through charge and discharge experiments. Using the prepared SC, an optimized hybrid energy distribution method was proposed for the HESS. A hybrid converter with an isolated soft-switching symmetric half-bridge bidirectional converter is used as the protection structure to accurately control the charging/discharging of the SC and battery. Through the optimized power distribution method, the SC energy can be quickly supplemented when stopping and driving at a constant speed; this makes up for the shortcomings of the traditional control strategy. On the other hand, by controlling the SOC of the SC via the speed of EV enables the energy storage system to have better flexibility and adaptability, thereby enhancing the demand for the acceleration performance and energy variation of EVs. The experimental results demonstrate that the optimized SOC control strategy proposed herein can meet the peak power demand and energy loss, shorten the acceleration time of EVs but reduce the energy loss, improve the performance of EVs and extend the service life of the battery.

Author Contributions: Conceptualization, K.W. and L.L.; methodology, K.W.; software, W.W.; validation, W.W. and L.W.; formal analysis, K.W.; investigation, L.W.; resources, L.L.; data curation, L.L.; writing—original draft preparation, K.W.; writing—review and editing, W.W.; visualization, K.W.; supervision, K.W.; project administration, L.L.; funding acquisition, L.L. All authors have read and agree to the published version of the manuscript.

Funding: The work was supported by the Scientific Research Development Plan of Shandong Higher Education Institutions (No. J18KA316), the Development Plan of Shandong Province (No. 2019GGX104019), and Guangdong Basic and Applied Basic Research Foundation (2019A1515110706).

Conflicts of Interest: The authors declare no conflict of interest.

References

1. Yuan, D.; Sun, M.; Zhao, M.; Tang, S.; Qi, J.; Zhang, X.; Wang, K.; Li, B. Persulfate promoted ZnIn2S4 visible light photocatalytic dye decomposition. *Int. J. Electrochem. Sci.* **2020**, *15*, 8761–8770. [CrossRef]
2. Feng, X.; Zhang, Y.; Kang, L.; Wang, L.C.; Duan, C.X.; Yin, K.; Pang, J.B.; Wang, K. Integrated energy storage system based on triboelectric nanogenerator in electronic devices. *Front. Chem. Sci. Eng.* **2020**. [CrossRef]
3. Bu, C.Y.; Li, F.J.; Yin, K.; Pang, J.B.; Wang, L.C.; Wang, K. Research progress and prospect of triboelectric nanogenerators as self-powered human body sensors. *ACS Appl. Electron. Mater.* **2020**, *2*, 863–878. [CrossRef]
4. Xia, G.T.; Huang, Y.N.; Li, F.J.; Wang, L.C.; Pang, J.B.; Li, L.W.; Wang, K. A thermally flexible and multi-site tactile sensor for remote 3D dynamic sensing imaging. *Front. Chem. Sci. Eng.* **2020**. [CrossRef]
5. Wang, K.; Li, L.W.; Xue, W.; Zhou, S.Z.; Lan, Y.; Zhang, H.W.; Sui, Z.Q. Electrodeposition synthesis of PANI/MnO_2/Graphene composite materials and its electrochemical performance. *Int. J. Electrochem. Sci.* **2017**, *12*, 8306–8314.
6. Yuan, D.L.; Zhang, C.; Tang, S.F.; Sun, M.T.; Zhang, Y.T.; Rao, Y.D.; Wang, Z.B.; Ke, J. Fe^{3+}-sulfite complexation enhanced persulfate Fenton-like process for antibiotic degradation based on response surface optimization. *Sci. Total Environ.* **2020**, *727*, 138773. [CrossRef]
7. Jiang, W.; Wu, X.; Zhao, H. Novel bifunctional converter-based supercapacitor energy storage module with active voltage equalizing technology. *IEEJ Trans. Electr. Electron. Eng.* **2017**, *12*, 328–336. [CrossRef]
8. Rizoug, N.; Mesbahi, T.; Sadoun, R.; Bartholomeüs, P.; Le Moigne, P. Development of new improved energy management strategies for electric vehicle battery/supercapacitor hybrid energy storage system. *Energy Effic.* **2018**, *11*, 823–843. [CrossRef]
9. Wang, W.L.; Li, Y.H.; Li, L.W.; Wang, L.C.; Wang, K. Nanoparticle Structure for Flexible Quasi-solid-state Lithium-Ion Batteries. *Int. J. Electrochem. Sci.* **2020**, *15*, 1–14.
10. Samani, H.; Fernando, X. Battery current's fluctuations removal in hybrid energy storage system based on optimized control of supercapacitor voltage. *IEEE Embed. Syst. Lett.* **2016**, *8*, 53–56. [CrossRef]
11. Zhang, T.; Bai, D.; Yang, Z.; Long, Z.; Gao, B. Research of Control Strategy on DC Side of Hybrid Energy Storage in Micro Grid. *Int. J. Grid Distrib. Comput.* **2016**, *9*, 327–336. [CrossRef]
12. Luo, X.; Zhang, F.; Li, Q.; Xia, Q.; Li, Z.; Li, X.; Ye, W.; Li, S.; Ge, C. Reversible control of magnetization in Fe_3O_4 nanoparticles by a supercapacitor. *J. Phys. Condens. Matter* **2020**, *32*, 334001. [CrossRef] [PubMed]
13. Zhang, F.L.; Teng, X.L.; Shi, W.K.; Song, Y.F.; Zhang, J.; Wang, X.; Li, H.S.; Li, Q.; Li, S.D.; Hu, H. SnO_2 nanoflower arrays on an amorphous buffer layer as binder-free electrodes for flexible lithium-ion batteries. *Appl. Surf. Sci.* **2020**, *52*, 146910. [CrossRef]
14. Tang, S.F.; Tang, J.C.; Yuan, D.L.; Wang, Z.T.; Zhang, Y.T.; Rao, Y.D. Elimination of humic acid in water: Comparison of UV/PDS and UV/PMS. *RSC Adv.* **2020**, *10*, 17627–17634. [CrossRef]
15. Muhammad, A.; Du, H.L. Fabrication, structure, and frequency-dependent electrical and dielectric properties of Sr-doped $BaTiO_3$ ceramics. *Ceram. Int.* **2019**, *46*, 2238–2246.
16. Tang, S.F.; Wang, Z.T.; Yuan, D.; Zhang, C.; Rao, Y.D.; Wang, Z.B.; Yin, K. Ferrous ion-tartaric acid chelation promoted calcium peroxide fenton-like reactions for simulated organic wastewater treatment. *J. Clean. Prod.* **2020**, *268*, 122253. [CrossRef]
17. Wang, K.; Zhou, S.Z.; Zhou, Y.T.; Ren, J.; Li, L.W.; Lan, Y. Synthesis of porous carbon by activation method and its electrochemical performance. *Int. J. Electrochem. Sci.* **2018**, *13*, 10766–10773.
18. Wang, X.X.; Song, W.Z.; You, M.H. Bionic single-electrode electronic skin unit based on piezoelectric nanogenerator. *ACS Nano* **2018**, *12*, 8588–8596. [CrossRef]
19. Du, H.L.; Ma, C.Y.; Ma, W.X.; Wang, H.T. Microstructure evolution and dielectric properties of Ce-doped SrBi4Ti4O15 ceramics synthesized via glycine-nitrate process. *Process. Appl. Ceram.* **2018**, *12*, 303–312. [CrossRef]
20. Wang, K.; Pang, J.B.; Li, L.W.; Zhou, S.Z.; Li, Y.H.; Zhang, T.Z. Synthesis of hydrophobic carbon nanotubes/reduced graphene oxide composite films by flash light irradiation. *Front. Chem. Sci. Eng.* **2018**, *12*, 376–382. [CrossRef]
21. Wen, Y.; Dai, Y.; Zhou, X.; Qian, F. Multiple roles coordinated control of battery storage units in a large-scale island microgrid application. *IEEJ Trans. Electr. Electron. Eng.* **2017**, *12*, 527–535. [CrossRef]

22. Wang, K.; Feng, X.; Pang, J.B.; Ren, J.; Duan, C.X.; Li, W. State of Charge (SOC) Estimation of Lithium-ion Battery Based on Adaptive Square Root Unscented Kalman Filter. *Int. J. Electrochem. Sci.* **2020**, *15*, 9499–9516.
23. Zhou, Y.T.; Huang, Y.N.; Pang, J.B.; Wang, K. Remaining useful life prediction for supercapacitor based on long short-term memory neural network. *J. Power Sources* **2019**, *440*, 227149. [CrossRef]
24. Xia, G.T.; Li, C.; Wang, K.; Li, L.W. Structural design and electrochemical performance of PANI/CNTs and MnO_2/CNTs supercapacitor. *Sci. Adv. Mater.* **2019**, *11*, 1079–1086. [CrossRef]
25. Wang, K.; Li, L.; Zhang, T.Z.; Liu, Z.F. Nitrogen-doped graphene for supercapacitor with long-term electrochemical stability. *Energy* **2014**, *70*, 612–617. [CrossRef]
26. Zhou, Y.T.; Wang, Y.N.; Wang, K.; Kang, L.; Peng, F.; Wang, L.C.; Pang, J.B. Hybrid genetic algorithm method for efficient and robust evaluation of remaining useful life of supercapacitors. *Appl. Energy* **2020**, *260*, 114169. [CrossRef]
27. Wang, K.; Li, L.W.; Lan, Y.; Dong, P.; Xia, G.T. Application research of chaotic carrier frequency modulation technology in two-stage matrix converter. *Math. Probl. Eng.* **2019**, *2019*, 2614327. [CrossRef]
28. Zhang, M.; Wang, K.; Zhou, Y. Online state of charge estimation of lithium-ion cells using particle filter-based hybrid filtering approach. *Complexity* **2020**, *2020*, 8231243. [CrossRef]
29. Wang, L.C.; Yan, R.; Bai, F.; Saha, T.K.; Wang, K. A distributed inter-phase coordination algorithm for voltage control with unbalanced PV integration in LV systems. *IEEE Trans. Sustain. Energy* **2020**, *11*, 2687–2697. [CrossRef]
30. Wang, K.; Li, L.W.; Yin, H.X.; Zhang, T.Z.; Wan, W.B. Thermal modelling analysis of spiral wound supercapacitor under constant-current cycling. *PLoS ONE* **2015**, *10*, e0138672. [CrossRef]
31. Kollimalla, S.K.; Ukil, A.; Gooi, H.B.; Manandhar, U.; Tummuru, N.R. Optimization of charge/discharge rates of a battery using a two-stage rate-limit control. *IEEE Trans. Sustain. Energy* **2017**, *8*, 516–529. [CrossRef]
32. Dai, J.; Fu, K.; Palanisamy, R.; Gong, A.; Pastel, G.; Kornfeld, R.; Zhu, H.; Sanghadasa, M.; Bekyarova, E.; Hu, L. A solid state energy storage device with supercapacitor–battery hybrid design. *J. Mater. Chem. A* **2017**, *5*, 15266–15272. [CrossRef]
33. Jiang, W.; Zhang, L.; Zhao, H.; Huang, H.; Hu, R. Research on power sharing strategy of hybrid energy storage system in photovoltaic power station based on multi-objective optimisation. *IET Renew. Power Gener.* **2016**, *10*, 575–583. [CrossRef]
34. Zhang, Q.; Deng, W.; Li, G. Stochastic control of predictive power management for battery/supercapacitor hybrid energy storage systems of electric vehicles. *IEEE Trans. Ind. Inform.* **2018**, *14*, 3023–3030. [CrossRef]
35. Athikkal, S.; Sundaramoorthy, K.; Sankar, A. Development and performance analysis of dual-input DC–DC converters for DC microgrid application. *IEEJ Trans. Electr. Electron. Eng.* **2018**, *13*, 1034–1043. [CrossRef]
36. Hiramatsu, T.; Huang, X.; Kato, M.; Hori, Y. Capacity Design of Supercapacitor-Battery Hybrid Energy System with Repetitive Charging. *Electr. Eng. Japan* **2016**, *197*, 58–66. [CrossRef]
37. Abeywardana, D.B.W.; Hredzak, B.; Agelidis, V.G. A fixed-frequency sliding mode controller for a boost-inverter-based battery-supercapacitor hybrid energy storage system. *IEEE Trans. Power Electron.* **2017**, *32*, 668–680. [CrossRef]
38. Zhang, Q.; Ju, F.; Zhang, S.; Deng, W.; Wu, J.; Gao, C. Power Management for Hybrid Energy Storage System of Electric Vehicles Considering Inaccurate Terrain Information. *IEEE Trans. Autom. Sci. Eng.* **2017**, *14*, 608–618. [CrossRef]
39. Castaings, A.; Lhomme, W.; Trigui, R.; Bouscayrol, A. Practical control schemes of a battery/supercapacitor system for electric vehicle. *IET Electr. Syst. Transp.* **2016**, *6*, 20–26. [CrossRef]
40. Liu, Y.; Du, W.; Xiao, L.; Wang, H.; Bu, S.; Cao, J. Sizing a hybrid energy storage system for maintaining power balance of an isolated system with high penetration of wind generation. *IEEE Trans. Power Syst.* **2016**, *31*, 3267–3275. [CrossRef]
41. Jia, Z.Y.; Liu, M.N.; Zhao, X.L.; Wang, X.S.; Pan, Z.H.; Zhang, Y.G. Lithium Ion Hybrid Supercapacitor Based on Three-Dimensional Flower-Like Nb_2O_5 and Activated Carbon Electrode Materials. *Acta Physico-Chim. Sin.* **2017**, *33*, 2510–2516.
42. Shin, D.; Lee, K.; Chang, N. Fuel economy analysis of fuel cell and supercapacitor hybrid systems. *Int. J. Hydrog. Energy* **2016**, *41*, 1381–1390. [CrossRef]

43. Naseri, F.; Farjah, E.; Ghanbari, T. An efficient regenerative braking system based on battery/supercapacitor for electric, hybrid, and plug-in hybrid electric vehicles with BLDC motor. *IEEE Trans. Veh. Technol.* **2017**, *66*, 3724–3738. [CrossRef]
44. Abeywardana, D.B.; Hredzak, B.; Agelidis, V.G.; Demetriades, G.D. Supercapacitor sizing method for energy-controlled filter-based hybrid energy storage systems. *IEEE Trans. Power Electron.* **2017**, *32*, 1626–1637. [CrossRef]

energies

MDPI

Article

Dimensioning Methodology of an Energy Storage System Based on Supercapacitors for Grid Code Compliance of a Wave Power Plant

Gustavo Navarro [1,*], Marcos Blanco [1], Jorge Torres [1], Jorge Nájera [1], Álvaro Santiago [1], Miguel Santos-Herran [1], Dionisio Ramírez [2] and Marcos Lafoz [1]

[1] Centro de Investigaciones Energéticas, Medioambientales y Tecnológicas (CIEMAT), Government of Spain, 28040 Madrid, Spain; marcos.blanco@ciemat.es (M.B.); jorgejesus.torres@ciemat.es (J.T.); jorge.najera@ciemat.es (J.N.); alvaro.santiago@ciemat.es (Á.S.); miguel.santos@ciemat.es (M.S.-H.); marcos.lafoz@ciemat.es (M.L.)

[2] Centro de Electrónica Industrial (CEI), Universidad Politécnica de Madrid, 28006 Madrid, Spain; dionisio.ramirez@upm.es

* Correspondence: gustavo.navarro@ciemat.es; Tel.: +34-91-335-71-99

Abstract: The aim of this paper is to present a methodology for dimensioning an energy storage system (ESS) to the generation data measured in an operating wave energy generation plant connected to the electric grid in the north of Spain. The selection criterion for the ESS is the compliance of the power injected into the grid with a specific active-power ramp-rate limit. Due to its electrical characteristics, supercapacitor (SC) technology is especially suitable for this application. The ESS dimensioning methodology is based on a mathematical model, which takes into account the power generation system, the chosen ramp-rate limit, the ESS efficiency maps and electrical characteristics. It allows one to evaluate the number of storage cabinets required to satisfy the needs described, considering a compromise between the number of units, which means cost, and the reliability of the storage system to ensure the grid codes compliance. Power and energy parameters for the ESS are obtained from the calculations and some tips regarding the most efficient operation of the SC cabinets, based on a stepped switching strategy, are also given. Finally, some conclusions about the technology selection will be updated after the detailed analysis accomplished.

Keywords: supercapacitor; energy storage; wave energy; dimensioning; efficiency; grid code; renewable energies

Citation: Navarro, G.; Blanco, M.; Torres, J.; Nájera, J.; Santiago, Á.; Santos-Herran, M.; Ramírez, D.; Lafoz, M. Dimensioning Methodology of an Energy Storage System Based on Supercapacitors for Grid Code Compliance of a Wave Power Plant. *Energies* **2021**, *14*, 985. https://doi.org/10.3390/en14040985

Academic Editor: Alon Kuperman
Received: 5 January 2021
Accepted: 6 February 2021
Published: 13 February 2021

1. Introduction

The increased environmental awareness together with the fossil fuel availability reduction, have fostered the development and integration of renewable energy sources (RES) in the last decades [1]. In this sense, hydro, solar, and wind energy sources have been extensively researched and consolidated, whereas other RES as wave energy remain a few steps behind in terms of technology readiness level (TRL). Regarding wave energy, and given the significant potential enclosed in the waves [2], several wave energy farms have been deployed and tested, particularly in areas with high oceanic resource [3]. Thus, the numerous projects developed during the past years in Europe, United States, and Asia have pushed the wave energy technology to a precommercial state (TRL 7), and the first commercial projects are expected to be implemented in niche markets in the near future [2,4–6].

This paper focuses on wave energy converters (WECs) as the device selected for extracting the wave energy and converts it into electricity. For a thorough review of WECs and other wave energy devices, see [7].

The aforementioned integration and connection of wave energy farms, each one composed by a set of WECs, is not exempt of drawbacks. As with other non-dispatchable

RES (wind and solar energy), wave energy farms can have a considerable impact on the stability, quality, and reliability of the power grid [8,9]. Given the intermittent nature of the source, i.e., the waves, the power generated by a WEC also follows an intermittent profile with severe power fluctuations [10]. As a result, the power grid can suffer from sudden frequency deviations, and voltage distortion such as harmonics or flicker [9–11]. These frequency and voltage issues may cause the wave energy farm to not be compliant with the grid codes of the transmission system operators (TSOs) and, hence, make wave energy farms not suitable for being included in the electricity generation mix of a country [8]. In [12,13] an introduction about the study on grid compliance and standardization of renewable generation and other energy systems connected to the power grid is provided. In [13–17] the grid codes of different countries (European and non-European) and the corresponding projects about renewable power are compared and summarized. The impact of grid code regulations on stability is also analyzed. Additionally, these papers provide the information about the future trend of grid code requirements. The main requirements in most of grid codes include reactive power, frequency regulation, fault ride through, power quality, and communication.

Several solutions for solving this issue have been proposed in the literature, including advanced control strategies [18–20] and proper WECs location in the wave energy farm [21]. In [22] an active control for a tidal turbine is developed to grid code requirements in terms of active and reactive powers (P, Q) and, conversely, the voltage at the point of common coupling and reactive power (U, Q). However, the most promising solution for solving power quality issues, which encompass the vast majority of articles of this topic, is the utilization of an energy storage system (ESS) for a combined operation together with the wave energy farm. In this sense, the ESS will store energy when the power generated by the WECs overcomes a certain value, and it will deliver power when required by the control strategy [21].

Different energy storage technologies have been analyzed in the literature for being integrated with WECs, aiming for grid code compliance: battery energy storage system (BESS), flywheel energy storage system (FESS), and supercapacitor energy storage system (SCESS) or a hybrid energy storage system (HESS). All three technologies are able to provide a fast response in the range of 10–50 ms when the control strategy demands it [23,24].

BESSs have been studied in [25] for a combined operation of a wind turbine and a WEC, including a predictive control in order to not overcome the maximum power fluctuations allowed by the Irish grid code and the UK national grid code. The work published in [26] uses a BESS for smoothing the output power of a WEC, in order to have an acceptable power quality for a general grid code defined by the authors.

FESS have been studied together with a wave farm in [27] for controlling the power output of the complete installation, aiming for being compliant with the Nordic grid code. The authors in [27] develop a control based on three stages, achieving a reduction up to 85% in the power output peak. A control strategy is proposed for power smoothing in a hybrid wave energy plant. The control strategy is based on a power filtering process.

Grid code compliance with SCESS has been studied in [28,29], validating control strategies for compensating WEC power oscillations. A finite predictive control is applied to the study proposed in [28], where the SCESS is located in the DC link of the back-to-back power converter. The analysis performed in [30] include an experimental validation in a laboratory test bench of a control that includes a state of charge compensator for the SCESS. In [30] a SCESS is studied to smooth the power extracted from waves by a grid connected linear electric generator. A complete model of the system is developed in Simulink-MATLAB to test the system under varying system conditions (faults with and without the SCESS).

Another possibility is to use a hybrid energy system (HESS) consisting of two different storage technologies. For example, in [29] a power management system for a grid connected OWC wave energy converter with a HESS (battery/SC) is proposed. Performance of the

control system is evaluated in two case studies, fixed and variable operating speed. In [31] an optimization algorithm is aimed at splitting the power required between the battery and SCs of a HESS. This ESS is used to smooth the power oscillations for a wave energy conversion connected to the public grid. The proposed algorithm, among other things, considers minimizing the losses of the storage system and maximizing the battery lifetime.

Apart from those three ESSs, other authors decided not to select a specific ESS, but studied the application of a generic ESS together with a WEC. In this sense, authors in [32] combined a wave farm model with a small ESS for being compliant with the Irish, UK, and Nordic grid code. The study includes a modeling strategy for the wave-to-wire system of WEC arrays. Moreover, the work published in [33] studied the integration of a generic ESS for achieving the grid code requirements at the point of common coupling (PCC), using real location data. The authors also propose a real-time technique for the centralized control of the wave farm, which is validated in critical scenarios such as weak grids. In [34] an adaptive energy filter is proposed to smooth renewable power fluctuations in function of the input power level. The novelty of this paper resides in the robustness of the proposed filter against changes in the level of the generated power (fluctuating in the case of renewable sources). This method is generic and it can be applied to any ESS (BESS, FESS, SCESS, and SMES).

As it has been described above, the combined effects of using a WEC with different ESS has been analyzed, and the benefits for meeting the grid code requirements are clearly stated in the literature. However, from an industrial point of view, knowing that including ESSs is beneficial for integrating wave energy in the grid is as important as knowing the proper size of the ESS, in terms of power and energy. ESSs are expensive equipment, and under or oversizing can result in premature degradation and incompliancy with the grid codes, or unnecessary economic investment, respectively. Hence, ESS dimensioning studies for wave energy become of the utmost importance.

In this regard, the works published in [3,24] propose a dimensioning methodology for a generic ESS integrated with a WEC, without focusing on a specific technology, and based on efficiency and grid code compliancy in terms of frequency. Authors in [24] include a methodology validation for non-regular waves. A further validation with real data from Tenerife is performed in [3]. Moreover, authors in [35] proposed a SCESS dimensioning methodology, which includes an ageing model without temperature dependence, and with no particular focus on grid code compliancy.

For wave energy applications, SCESSs and FESSs perform better that other ESSs in terms of efficiency [36]. Although SCESSs and FESSs present similar characteristics in terms of TRL, power and energy range and number of cycles [23], SCESS is the ESS technology selected by the authors to perform the analysis of this work, since power and energy levels are appropriate, a better economic alternative has been found in terms of €/kW and the system fits better within the available space at the power plant.

A case study is proposed to illustrate the methodology, with the real profile of a wave power generation plant and a real SCESS. To reduce fluctuations in the power delivered to the power grid a specific active power ramp rate (%/min) is set. It is a characteristic parameter of the grid code standards. The proposed methodology allows the establishment of other types of limitations that conform to the existing grid codes in different countries.

The paper is structured as follows: in Section 2 the wave power generation plant on which this study is based is described, in Section 3 the SCESS cabinet on which the complete SCESS (technology, power loss calculation, and efficiency map) is based is described, in Section 4 the results obtained from a simulation model that integrates both the SCESS and the wave generation profile are presented and commented and, finally, in Section 5 some final conclusions are detailed.

2. Wave Power Generation Plant

The study of using supercapacitors (SCs) as a storage solution for systems that harvest energy from waves to comply with the grid code is based on the wave power generation

plant located in the breakwater at the harbor in Mutriku (Spain). The plant was inaugurated in 2011 and has been delivering power into the electric grid ever since. The technology used to extract energy from waves is called the oscillating water column (OWC) with a total installed power of 296 kW, comprising 16 equal turbines of 18.5 kW each [37]. The principle of these oscillating water column converters (OWC-WECs) is based on the pressure variation of the air contained in a chamber when the wave motion enters it. When the wave arrives, the contained air is expelled at high pressure through an orifice located at the upper part of the chamber. The air drives a turbine whose shaft is coupled to an electric generator. When the wave retreats, the water level in the chamber decreases. This causes the pressure inside the chamber to drop and the air to be sucked in through the upper hole. The turbine always rotates in the same direction regardless of the direction of air circulation, so that the rotation in the shaft is more or less continuous. The connection to the local distribution grid of the generation plant is made through a 460 V/13.2 kV power transformer. Figure 1a shows the electrical diagram of the wave power generation plant connected to the grid. Figure 1b shows an aerial image of the power plant.

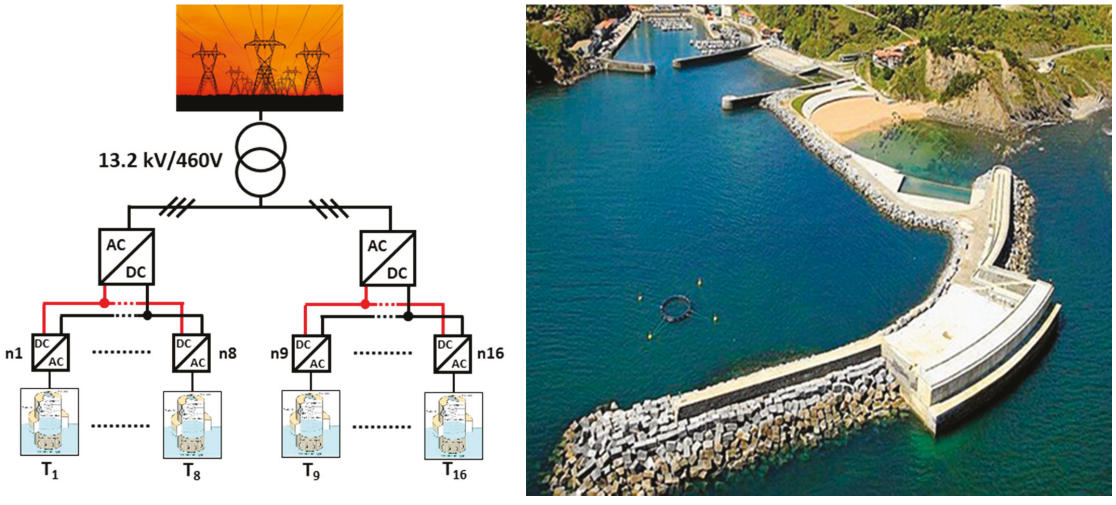

(**a**) (**b**)

Figure 1. (**a**) Electrical diagram of the wave power generation plant and (**b**) aerial photo of the wave power generation plant integrated in the breakwater of Mutriku port.

3. Description of an Energy Storage System Based on SCs

Electric double layer capacitors (EDLCs) [30], commonly known as supercapacitors, are electrochemical capacitors composed of two conductive porous electrodes immersed in an electrolyte, between which a separator is placed. The electrodes are based on a sheet, usually made of aluminum, covered by activated carbon or carbon nanotubes. The electrolyte is the key element in determining internal resistance or equivalent series resistance (ESR). Nonaqueous solutions, such as acetonitrile or propylene carbonate, are often used because they support higher stress. The separator must allow the circulation of ions but avoid contact between the two electrodes. SCs, like conventional capacitors, store charge electrostatically and there is no charge transfer between the electrode and the electrolyte. EDLCs use double electrochemical layers to store energy. When a voltage is applied between the electrodes, the charge accumulates on the surface of the electrodes. Following the natural repulsion of oppositely charged, ions in the electrolyte solution spread through the separator into the pores of the oppositely charged electrode. These

double layers, together with an increase in surface area and a reduction in the distance between electrodes, allow SCs to achieve energy densities much higher than those of conventional capacitors [38]. Since there is no charge transfer between the electrolyte and electrode there are no changes in the chemical composition. For this reason, the storage of charge in EDLCs is reversible and is not associated with a significant loss of capacity with the number of charge and discharge cycles, which is not the case in electrochemical batteries.

SCs are especially suitable devices for high power applications with a relatively low energy capacity compared to batteries [39,40]. It has a lower cost than batteries in terms of power, a complete cycle efficiency of around 95%, the possibility of a high number of charge-discharge cycles (up to a million as per the datasheets) and a useful life of 20–25 years. The operating temperature range is between −40 and 60 °C, much wider than that of batteries, without significant impact on their response. The energy that a capacitor of any type is capable of storing is dependent on its capacitance and its voltage. The capacitance (C) is a constructive parameter related to the electrical charge that the device is capable of storing and that depends on constructive aspects such as the permeability of the dielectric, the area of the metallic plates and the distance between them. On the other hand, the maximum voltage between terminals depends on the insulation conditions of the dielectric that is between the two electrodes that make up the SC.

Regarding capacitance, it should be taken into account that EDLCs are not linear capacitors, but that the capacity depends on the voltage, as shown in Figure 2 [41,42]. In the case of cells, manufacturers provide values for capacitance and ESR. The capacitance value is only a mean value in the voltage operating range. For the basic cell upon which this study was based (BCAP3000 commercialized by Maxwell in the past) the maximum capacity value at the beginning of the operational life was above 3000 F, being 3000 F was the mean value. To model this evolution of the capacitance, an experimental loading process was performed in which measured capacitance was calculated in small voltage increments. Figure 2a shows the evolution of capacitance with voltage. It presents a quadratic relationship with the voltage as indicated in the following equation:

$$C(V) = -95.756 \cdot V^2 + 613.58 \cdot V + 2216.6 \quad (1)$$

V: Voltage measured in the terminals of the SC (V);
C (V): Capacitance as a function of the voltage (F).

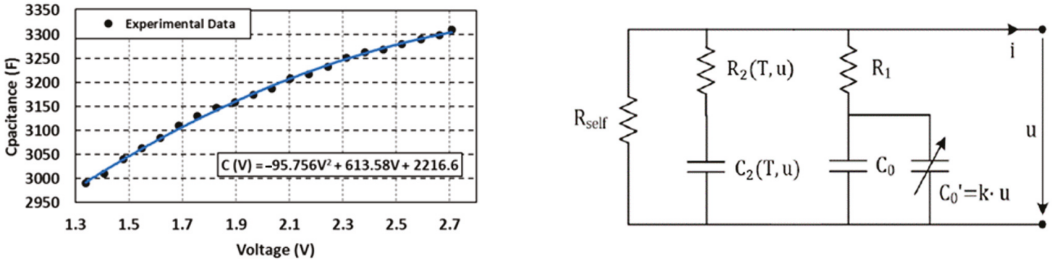

(**a**) (**b**)

Figure 2. (**a**) Evolution of the capacitance value as a function of the voltage in the BCAP3000 cell and (**b**) schematic of the electrical circuit used to model the behavior (voltage) of the supercapacitors (SCs).

An appropriate dimensioning of any storage system must take into account the power losses. The fundamental losses in the SCs are produced in the separator, in the positive and negative current collectors and in the positive and negative porous electrodes [40]. The total resistance of each of these parts is included in the ESR. It must be taken into account that the ESR value is not constant, but depends on the voltage in the cell, the temperature

and the frequency of the current that passes through the cell. To model the losses in the SCs, which will be explained later, an electrical circuit like the one shown in Figure 2b is used [41].

Another difference between batteries and SCs is that, while in batteries the voltage is relatively constant regardless of the state of charge (SoC), in SCs the voltage is more or less linear with the SoC. For this reason, the integration of this type of ESS into industrial applications is usually done through DC/DC power converters. This characteristic means that the SCs cannot be fully discharged, since working at too low of a voltage would greatly penalize the performance of the power converter. For this reason, it is common to define a discharge limit up to half their maximum voltage, which means using $\frac{3}{4}$ parts of their theoretical energy, as can be seen in Equation (2).

$$E_{availablel} = \frac{1}{2} \cdot C \cdot \left(U_{MAX}^2 - U_{MIN}^2 \right) = \frac{1}{2} \cdot C \cdot \left(U_{MAX}^2 - \left(\frac{U_{MAX}}{2} \right)^2 \right) = \frac{1}{2} \cdot C \cdot U_{MAX}^2 \cdot \frac{3}{4} \quad (2)$$

U_{MAX}: Maximum operating voltage measured on the SC (V);
U_{MIN}: Minimum operating voltage measured on the SC (V);
C: Average value of SC capacitance (F).

3.1. Description of the Real SCESS Module on Which this Study Is Based

The unit module of SCs is made up of 8 drawers connected in series as shown in Figure 3. Each of the drawers has, in turn, 30 units of BCAP3000 cells connected in series. The main electrical characteristics of each cell are a nominal voltage of 2.7 V, capacity of 3000 F, and energy of 3 Wh. Therefore, the nominal capacity of the cabinet was 11.7 F and the total energy available was 500 Wh. If each cell is discharged to half its voltage, the total energy available is $\frac{1}{4}$ of the total energy. Despite this fact, and as mentioned in the previous point, the minimum working voltage of each cell was set at half the nominal voltage so that the performance of the DC/DC converter that connects the SCESS with the DC bus does not decrease considerably. Therefore, the theoretical operating voltage range of the cabinet was approximately 381-636 V. The cabinet was provided with 16 electronic boards to measure the voltage evolution of each cell. Another 30 temperature measurement channels were also used to monitor the maximum temperature of the cells and check it did not exceed 65 °C. Analog measurements of voltage and temperature were monitored due to a Concerto F28M35H52C microcontroller commercialized by Texas Instruments (12500 TI Blvd., Dallas, Texas 75243 USA) that was placed inside the same cabinet. This microcontroller acted as a web server to access the temperature and voltage measurements via the internet.

The cabinet had a cooling extractor turbine located in its upper part. The rotation speed of this turbine varied depending on the temperature in the cells. Additionally, each of the cells has a hardware protection system so that the cells did not exceed their maximum voltage. In addition, this system allows the total voltage to be balanced so that it is distributed equally among all the cells. Figure 3a shows the state of the cabinet during a balancing process.

3.2. Operation Limits and Calculation of Power Losses and Performance of the SCESS

As mentioned above, in order to decide which storage system is best suited to a certain application, it is very important to consider its energy efficiency. In general, storage systems are complex non-linear systems and it is not easy to know their performance over the entire operating range. One of the parameters on which efficiency depends is the state of charge (SoC), that is, the operating point at which the system is working. In the case of SCs, efficiency is a function of current and voltage (SoC = f (V)) at each moment. In the present application the ESS, formed by supercapacitors, is connected to a DC bus through a DC/DC converter. Therefore, to calculate the overall efficiency it is necessary to also take into account the performance of this converter. Another parameter on which

the efficiency of the ESS depends is the duty cycle. It is necessary to take into account the frequency with which the SCs are charged/discharged, because, among other parameters (temperature), the value of the series resistance (ESR) depends on this frequency. Therefore, when a performance value is provided, the associated duty cycle must be specified. In the sizing of the storage system for the present application, the overall performance of the set composed by the electronic converter and the SCs for each operating point has been considered. The process followed to calculate these losses is explained in the next points.

(**a**) (**b**)

Figure 3. (**a**) Image of one supercapacitor energy storage system (SCESS) module during a voltage balancing process between cells and (**b**) image of one of the eight drawers that make up the SCs cabinet upon which this study is based.

As has already been commented, the SCESS is connected to a DC bus through a power converter. Another converter, connected between the electrical grid and the DC bus, keeps the voltage value of this bus at 950 V. This DC/DC converter regulates the charge/discharge current according to the received power command. The maximum power and energy available for each SC cabinet (unit module) is 125 kW and 0.5 kWh respectively. These values correspond to the following operating limits for each cell that makes up the SC cabinet:

- $U_{SUPERCAP\_max}$: 2.65 V;
- $U_{SUPERCAP\_max}$: 0.6·U_{MAX};
- $I_{SUPERCAP\_max:}$ 200 A.

The nominal voltage of each cell was 2.7 V (absolute maximum voltage is 2.85 V), but the maximum operating value was set at 2.65 V for two reasons. The higher the voltage in the SCs, the more accelerated their ageing. Reducing the maximum voltage by 0.05 V greatly lengthened the lifetime of the SCs. On the other hand, the ESS was formed by a series connection of cells and the distribution of the total voltage between all of them was not perfect. To ensure that the voltage in any cell was higher than 2.7 V, 2.65 V was set as the maximum value. The total working voltage range of each cabinet will be 382-636 V.

These limits imply an input and output voltage ratio in the DC/DC converter of 1/3-2/3, which did not significantly restrain its performance [43].

3.2.1. Power Losses in the Equivalent Series Resistance (ESR)

In order to calculate the performance of the storage system, in addition to taking into account the efficiency of the storage system (ESR losses) and the converter, the losses in the connection plates, in the cables and in the voltage balancing system were calculated [36]. In this case, the variation of the ESR and capacitance with the temperature in the cell was not considered, since each cabinet had a cooling turbine in the upper part that maintains the temperature of the cells in the working range of 25-40 °C. In this temperature range the variation of both parameters (ESR and C) was very small. Regarding the variation of capacitance with frequency, it was not studied in this paper, only analyzing the variation with voltage.

To calculate the power losses in the ESR, Equation (3) must be taken into account:

$$P_{ESR}(t) = U_{SC}(t) \cdot i_{SC}(t) \tag{3}$$

$P_{ESR}(t)$: Instantaneous power losses;
$U_{SC}(t)$: SC voltage;
$i_{SC}(t)$: Instantaneous current through the SCs.

If the current is considered as a periodic function of period T, it can be written as a Fourier series:

$$i_{SC}(t) = \sum_{i=0}^{+\infty} I_{SC}(i) \cdot \sin(iwt + \vartheta_i) \tag{4}$$

$I_{SC}(i)$: Harmonic component of the current;
w: Angular frequency.

The voltage across the ESR can be expressed as:

$$U_{ESR}(t) = \sum_{i=0}^{+\infty} ESR(iw) \cdot I_{SC}(i) \cdot \sin(iwt + \vartheta_i) \tag{5}$$

$U_{ESR}\ (i)$: Voltage across ESR
$ESR\ (iw)$: ESR value for each frequency

If Equations (4) and (5) are multiplied, the expression for the instantaneous power losses in the ESR is obtained. Applying the Lagrange identity and the orthogonal property of sine and cosine the total power losses can be expressed as [40]:

$$P_{ESR}(t) = I_{RMS}^2 \cdot \left[\sum_{i=0}^{+\infty} ESR(iw) \cdot \frac{I_{SC(i)}^2}{I_{rms}^2} \right] = I_{RMS}^2 \cdot ESR(eq) \tag{6}$$

I_{RMS}: r.m.s value of the current;
$ESR\ (eq)$: Total ESR.

To calculate the equivalent resistance in series for each frequency, it is necessary to complete an analysis of the SCs in the frequency domain. This analysis is based on experimental tests and on the design of a simulation model whose frequency response is adjusted to the results obtained experimentally. A complete analysis of the frequency response of the cell model (BCAP3000) on which the present study is based is presented in [44]. In this way, using Equation (6) the efficiency (η_{ESR}) of the SCESS cabinet can be calculated including the losses in the ESR for a given duty cycle (frequency) as per:

$$\eta_{ESR} = \frac{U_{SC} \cdot I_{rms}}{U_{SC} \cdot I_{rms} + P_{ESR}} \tag{7}$$

U_{SC}: SC voltage;
I_{rms}: r.m.s value of the current through the SC.

Figure 4a,b shows the evolution of the power losses in the ESR and the efficiency of the ESS as a function of the current flowing through the SCs and the voltage measured at the terminals. As expected, the higher the current through the capacitors, the higher the power losses in the ESR.

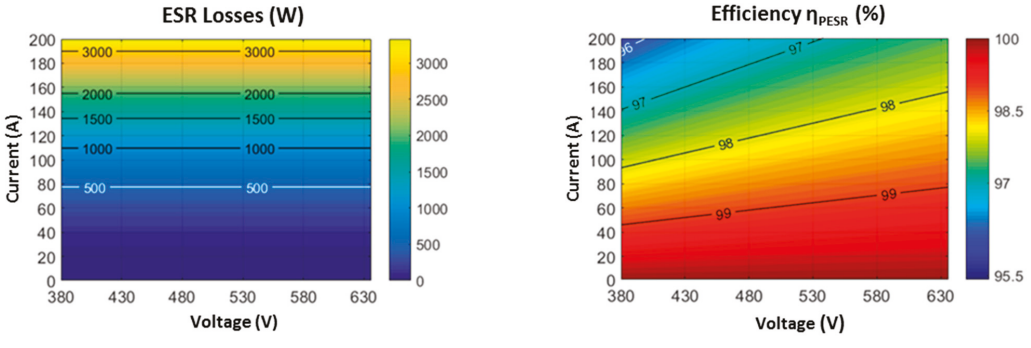

(**a**) (**b**)

Figure 4. (**a**) Power losses in the equivalent series resistance (ESR) as a function of the current and voltage measured in the SC cabinet and (**b**) efficiency map of the module due to ESR losses.

3.2.2. Voltage Balancing System Power Losses

As mentioned above, the ESS was made up of a series connection of cells, whose maximum voltage was 2.65 V, in order to achieve voltage levels more typical of industrial applications. Due to manufacturing tolerances, not every cell has the same capacitance or ESR, which means that the distribution of the total voltage between the different cells is not exactly the same. Therefore, there is a voltage supervisor hardware that prevents any cell from exceeding the voltage limit value (2.7 V) and facilitates the equitable distribution of voltage [45–47]. This system is based on the dissipation of the power in a resistance when the voltage in any of the cells exceeds a predetermined threshold value (approximately 2.6 V). Below this value the protection system does not work. The current and resistance where that current is dissipated is known, so the power losses can be derived from voltage measured in the SCs as follows:

$$P_{V\_Balancing} = R_{DIS} \cdot I^2_{DIS}(U) \quad (8)$$

$P_{V\_Balancing}$: Voltage balancing system power losses;
R_{DIS}: Power dissipation resistance;
$I^2_{DIS}(U)$: Current dissipation as a function of the measured voltage.

Figure 5 shows the power losses map of the voltage balancing system as a function of the current flowing through the ESS and its voltage. Compared to the power losses calculated in the ESR, these losses can be considered negligible.

3.2.3. Cooling System and Electrical Connection Plates Power Losses

Each SCs cabinet has an extractor cooling turbine on top because a natural cooling system is not sufficient for these power requirements. It is a variable speed turbine whose control depends on the temperature measured in the SC cells. The higher the temperature in the cells, the higher the rotation speed. The objective of this refrigeration system is to keep the temperature of the SCs below 40 °C. It is known that SCs age faster the higher the stress to which they are subjected and the higher their temperature [45]. Ageing in this

ESS type causes a decrease in C and an increase in ESR. This results in a loss of available energy in the ESS with respect to its initial value and a loss of efficiency. On the other hand, uneven aging between cells causes an imbalance in the distribution of the total voltage and a limitation in the use of available useful energy. To calculate the losses at the refrigeration system, an equivalent electrical circuit has been implemented using MATLAB-Simulink [48] that models the refrigeration flow. Additionally, a turbine regulation curve has been established to improve its efficiency. Figure 6a shows the map of cooling system losses as a function of current and voltage between terminals. It can be seen that the higher the current, the higher the losses in the cooling system and in the connection bars. As in the previous case, the losses are low compared to the losses in the ESR.

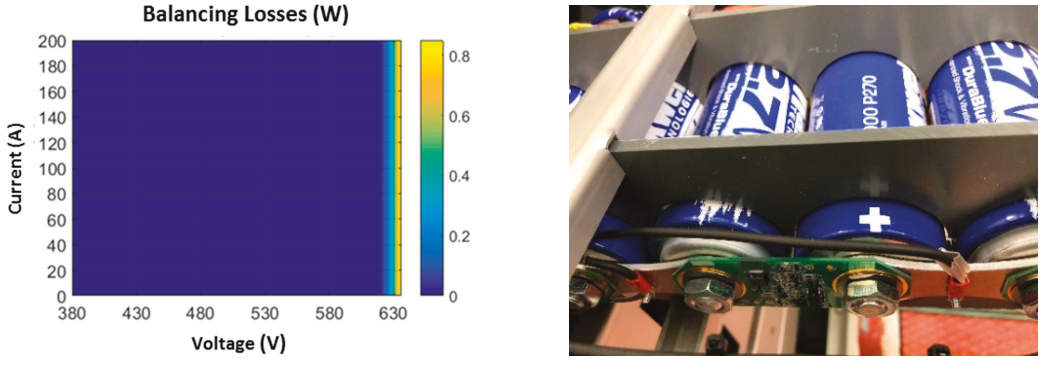

(**a**) (**b**)

Figure 5. (**a**) Power loss map in the voltage balancing system as a function of current and voltage and (**b**) detail of the connection plates between the cells and of the voltage balancing system.

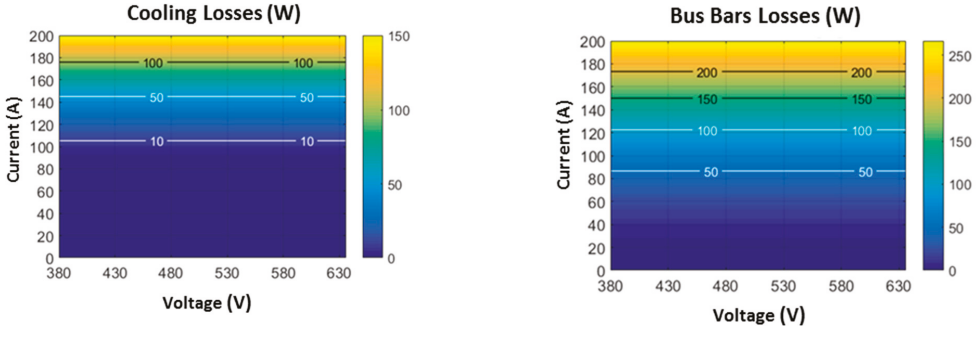

(**a**) (**b**)

Figure 6. (**a**) Power losses map of the cooling system as a function of voltage and current and (**b**) power losses map in the connection bars between cells as a function of current and voltage.

Regarding the losses in the connection plates between cells [49], it must be said that they have a certain resistance and consequently a power loss depending on the current flowing through them. These are 3 mm thick aluminum plates supplied by the manufacturer. The resistance value of each connection plate is given by:

$$R_{CONNEC\_PLATES} = \frac{\rho \cdot l}{S} \quad (9)$$

R_{CONNEC_PLATE}: Resistance of connection bars;
ρ: Aluminum resistivity;
l: Connection plate length;
S: Connection plate section.

Therefore, the power losses in the plates (P_{CONNEC_PLATES}) are calculated as:

$$P_{CONNEC\_PLATES} = I^2_{SUPERCAP} \cdot R_{CONNEC\_PLATES} \cdot No_{SUPERCAP} \quad (10)$$

$I^2_{SUPERCAP}$: Current through the SCs;
$N_{SUPERCAP}$: Number of SCs connected in series.

3.2.4. Power Converter and Total Losses

Each SC cabinet was connected to a DC bus regulated at a voltage of 950 V through a DC/DC converter that regulated the charge/discharge current of the ESS. This current command was the consequence of the reference power value to supply/consume assigned to the SCESS. The generation of this power command and the control of the complete system will be explained in the next point. A 3-branch interleaved DC/DC converter was used to exchange power between the ESS and the mentioned DC bus. This converter was bidirectional in the current to allow both charging and discharging of ESS. Figure 7 shows the topology and the input and output voltage levels of the converter [50,51].

The DC/DC power converter is a voltage source converter that regulates the charge/discharge current of the ESS. The control strategy was designed to operate in the discontinuous driving mode to improve its efficiency. The total current that passes through the SCs was distributed among the three output branches of the converter. The converter was modeled in MATLAB-Simulink to size the power components (filters, semiconductors, cooling system, etc.) and to verify the operation of the converter with the designed control strategy. On the other hand, the model implemented in MATLAB-Simulink allowed calculating the converter losses to obtain, as in the previous cases, the power converter losses as a function of the voltage and current through the SCs. The performance of the converter was calculated according to Equation (11):

$$\eta_{power\_converter} = \frac{U_{SC} \cdot I}{U_{SC} \cdot I + P_{converter\_losses}} \quad (11)$$

U_{SC}: Voltage of the SCs system;
I: Current through the SCs;
$P_{converter\_losses}$: Power converter losses.

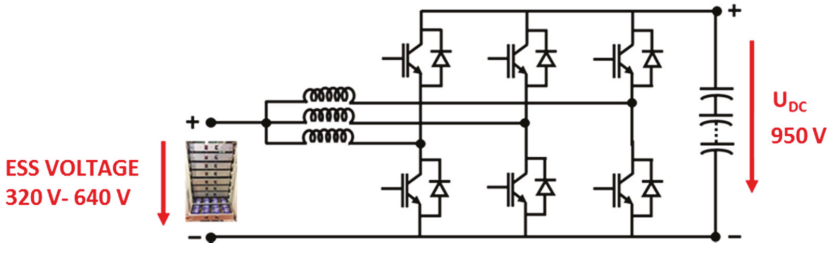

Figure 7. Electrical diagram with the voltage levels at the input and output of the DC/DC converter used.

Figure 8a shows the power converter losses as a function of the voltage and current through the SCs. Figure 8b shows the total efficiency of the power converter. The total losses of the power converter were higher with higher currents. However, the relative efficiency of the converter (with respect to the total power) was higher the higher the current through the SCs.

Figure 9a shows the total power losses of the SC cabinet as a sum of the previously calculated map (ESR, balancing and cooling system, bus bars, and power converter losses). Likewise, Figure 9b shows the total efficiency map of each cabinet as a function of the current and voltage.

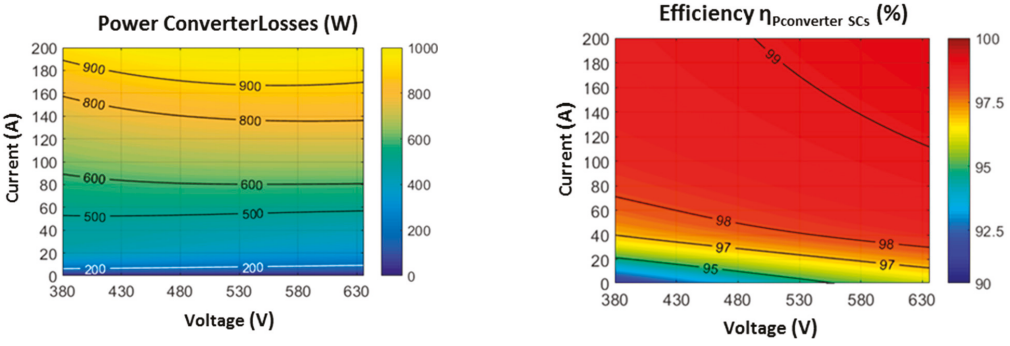

(**a**) (**b**)

Figure 8. (**a**) Power losses map in the DC/DC converter as a function of the current and voltage in the SCESS module and (**b**) efficiency map in the DC/DC converter as a function of the current and voltage in the SCESS module.

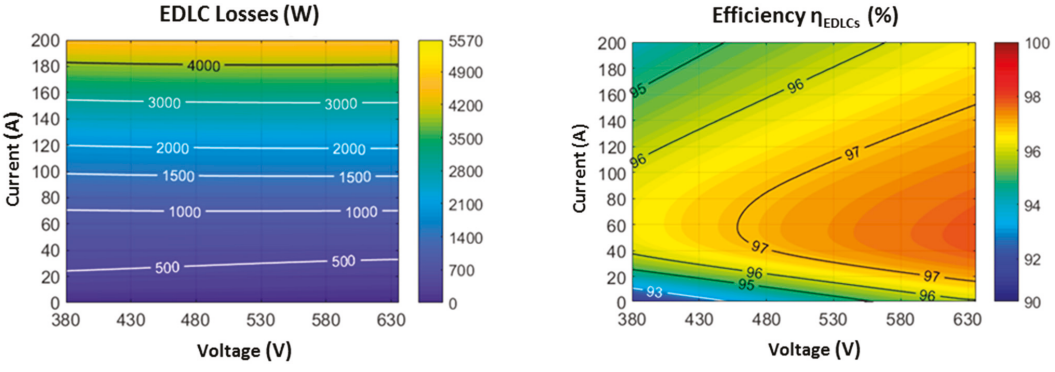

(**a**) (**b**)

Figure 9. (**a**) Total losses map in the energy storage system (ESS) (sum of all commented power losses) as a function of current and voltage and (**b**) total efficiency map of the SC cabinet as a function of current and voltage.

4. Description and Results Obtained from the Simulation Model Developed

This section analyzed the case study chosen for the sizing of a SCESS that allows the power injected into the grid by a wave power generation plant to comply with the grid code standards. The generation profile studied is that of the Mutriku port plant located in Biscay (Spain) and managed by Biscay Marine Energy Platform (BIMEP) [52]. The representative study period is slightly longer than 1 month, from 7 May to 19 June 2020. The sampling time of the power measured during this period was 1 s. Figure 10 shows the wave power generation profile generated by 3 of the 16 water column converters during said period (in blue). The total power generated by the plant (in red) is also displayed (N.B.: criterion: negative sign is generated power). It can be seen how the power generated by the OWCs is highly variable due to the oscillating nature of the wave resource itself [53]. The generation

peaks can reach values of up to 10 times the mean value. Just as a curiosity, the maximum power peak in the generation period occurred on June 11, with a value of 163 kW.

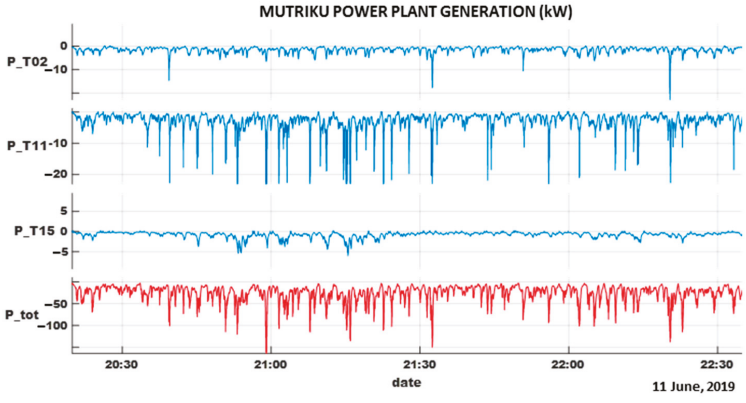

Figure 10. Power profile of three representative turbines of the wave power generation plant and total power in a stretch of time of the period studied.

4.1. Scheme of the Model Elaborated in SIMULINK-MATLAB and Its Input Parameters

For this study, a model has been developed using MATLAB-Simulink that includes the power generation data from the wave power plant for just over a month, the storage system based on several units of a real SC cabinet and the profile of the power that is exchanged with the electrical grid to comply with the different grid codes [54]. The ESS reference power profile is the result of subtracting the power from the generation plant and the target power profile to be injected into the grid [55,56]. The ESS, in addition to the SC cabinets, also integrates the DC/DC power converter. The scheme of the Simulink model is shown in Figure 11.

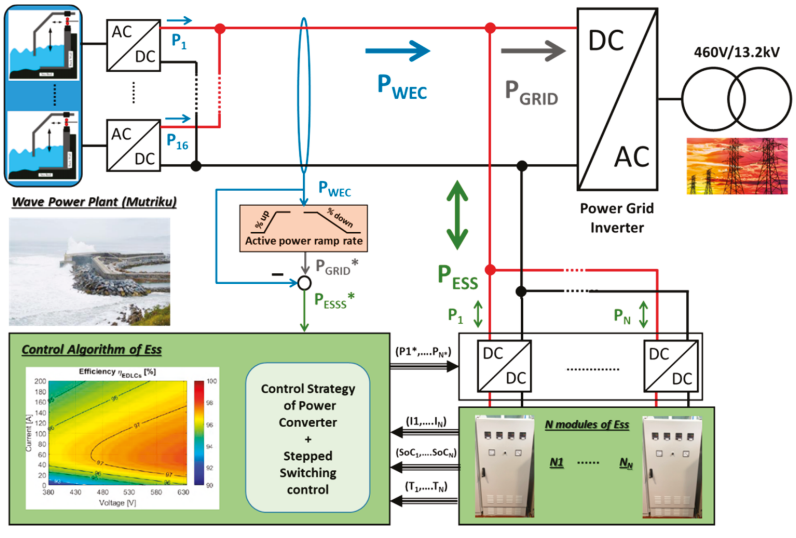

Figure 11. Simplified scheme of the model and control implemented in MATLAB-Simulink.

In order to be able to analyze all the available generation data, the full sample is divided into 15 min sections. It is set as a reference that the energy balance of the complete

storage system (ΔEESS) at the end of the complete generation period is zero. This means that the SoC of the storage system at the end of the analysis is the same as the initial one. In addition to the wave generation power profile, the other input parameters that the model has are: the maximum percentage of the rise ramp of the wave generation profile (% ramp-up/min) that can be injected into the grid, the ESS efficiency maps discussed in the previous section and the electrical parameters of each SC cabinet (maximum power, maximum and minimum voltage, available energy, and initial state of charge). From the limit value of % ramp-up, the value of the maximum percentage of the ramp down of the generation profile that can be injected into the grid was calculated so that the ΔEESS at the end of the generation period is null. In other words, for each allowed value of % ramp-up [57] there will be a value of ramp-down (%/min) that fulfills the previous condition (ΔEESS = 0). On the other hand, the model integrates the instantaneous SoC of each cabinet (voltage/current) to calculate the efficiency and the real instantaneous power that each SCESS module is capable of supplying/storing. Table 1 summarizes the main input parameters of the simulation model:

Table 1. Main input parameters of the simulation model.

Parameter	Meaning	Value
% ramp-up	Maximum ramp-up (%/min)	10
U_{MAX}	Maximum voltage per cell in the SC cabinets	2.65 V
U_{MIN}	Minimum voltage per cell in the SC cabinets	1.59 V
$SoC\_{INITIAL}$	Initial State of charge of the SC cabinets	60%
$Energy\_{USABLE}$	Usable energy respect to the total energy of each SC cabinet	0.5 kWh
P_{ESS_MAX}	Maximum Power provided by one SCESS module	125 kW

4.2. Results Obtained in the Simulation Model

Starting from ramp-up value (%/min) of 10, the value of % ramp-down that fulfilled that at the end of the complete generation period studied the ΔEESS = 0 was 7.22%/min. The ESS energy balance was calculated from the ESS power profile throughout the generation period. The power profile of the ESS was the result of subtracting the wave generation power profile and that same generation profile limited by the maximum ramp-up (%/min) and ramp-down (%/min) allowed (target power injected to the power grid). Figure 12 shows the generation profile throughout the entire period (in blue) and the target power profile that was injected into the grid after applying the aforementioned restrictions.

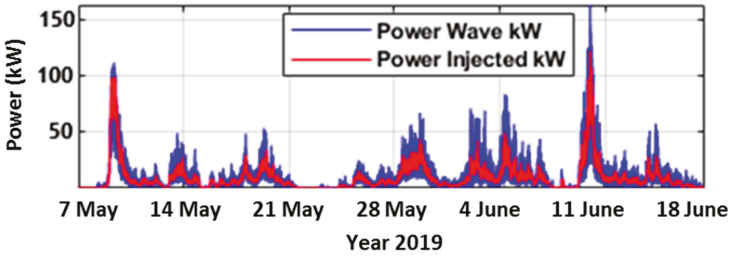

Figure 12. Profile of the generation of the plant (in blue) and theoretical objective profile to be delivered to the grid after applying the power ramp-rate limit.

To evaluate the actual energy required for the storage system, the efficiency maps calculated and introduced in the previous point were integrated, which incorporated the losses in the elements that exist between the SCs and the connection point with the

generation plant. Figure 13a,b shows the target power and energy profiles respectively of the ESS throughout the generation period to comply with the established grid codes. The maximum power requested from the storage system at the connection point was 111 kW (11 June).

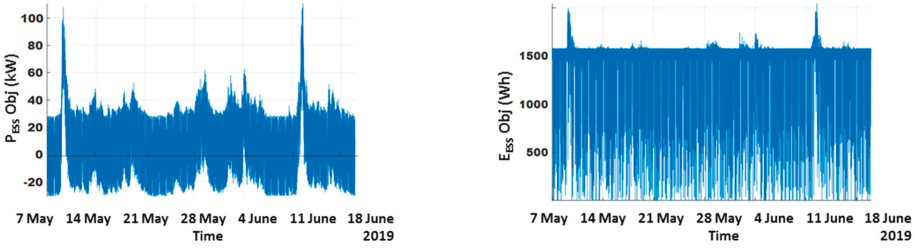

(**a**) (**b**)

Figure 13. (**a**) Power profile that the ESS has to supply to meet the active power ramp-rate limit requirement and (**b**) ESS energy calculated in 15 min periods from required power.

Once the energy and power required from the ESS are known, the optimum number of SC cabinets must be calculated to reduce the oscillations of the power delivered to the grid. To do this, the joint cumulative distribution function of the power and energy required from the ESS was calculated in 15 min steps throughout the entire generation period. This function gives an idea of the percentage of time when the restrictions applied to the power delivered to the grid can be met. Figure 14a shows the values of the normalized cumulative probability of the ESS with respect to power and energy calculated in 15 min steps. Most of the values were found at power figures above 20 kW and energy figures greater than 1400 Wh. On the other hand, areas in Figure 14b represent the areas relative to the percentage of time that the power and energy needs are met as a function of the number of SC cabinets chosen. Considering that each cabinet has a maximum power of 125 kW and an energy of 500 Wh, the resulting black line is shown in black in Figure 14b. If three cabinets are chosen, the percentage of time that the generation curve would be smoothed, complying with the grid codes would be almost 80%. However, if four cabinets were selected, the objective would be met 100% of the generation time on which the study was made. The decision to install three or four cabinets will depend on a further analysis of the particular consequences of the power oscillations in terms of frequency excursions. It can be observed in any case that the ESS would be oversized in terms of required power for the present application while fulfilling the energy requirements, more restricting in this case In other words, the maximum current that each cabinet is capable of giving could be limited to a value lower than the set limit of 200 A, seeking a more optimal ESS point of efficiency complying with the established restrictions for the same percentage of the time.

Considering that 3 o 4 SC cabinets would be required, the most efficient operation would lead to switching between the SC cabinets according to the power and energy needs, the strategy known as “stepped switching”. In this mode, a minimum power value is set, which takes into account the SoC, below which the corresponding SC cabinet is disconnected and another one with a higher SoC takes over and starts up. The maximum power that each cabinet is capable of giving is a function of the SoC and the operating point where it is located (in the efficiency map). What is sought with this strategy is that the efficiency of the cabinets in operation is always above a certain threshold, applying the efficiency maps and knowing the voltage and current that each cabinet is supplying. Another possibility would have been the simultaneous operation of all the chosen cabinets. That is, each cabinet would give the same power and would be working at the same load regime all the time. The total power required would be equally shared among them. However, this strategy known as “all-in, all-out” reduces the efficiency of the ESS as a

whole compared to the efficiency achieved with the previous strategy [58–60]. Figure 15 shows the real power profile delivered to the grid for a 10% ramp-up, a 7.22% ramp-down and an ESS made up of 4 modules of SCs.

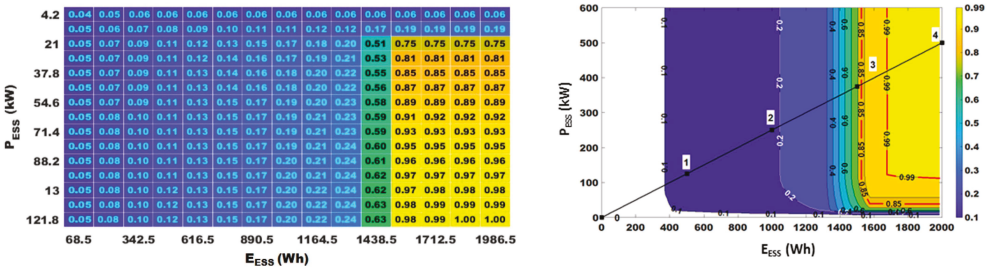

Figure 14. (**a**) Cumulative power and energy distribution function in the ESS and (**b**) cumulated distribution function for selection of the number of cabinets necessary to cover a certain number of cases of the proposed objective.

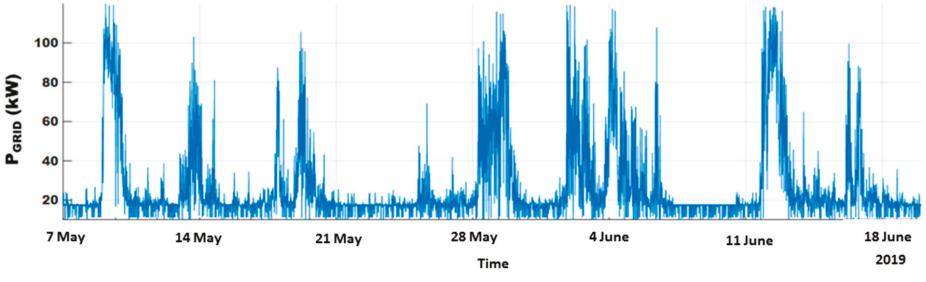

Figure 15. Power profile delivered to the grid throughout the generation period.

Figure 16a shows the percentage of time with respect to the complete generation period that each cabinet would work if 4 units were selected. On the other hand, Figure 16b shows a sensitivity analysis of the mean value of the reference power to be injected into the grid based on different grid codes (% ramp-up). Values from 10% to 23% (p.u./s) were taken. These values will correspond to respective ramp-down values, always complying that at the end of the generation period the energy balance in the ESS was zero. From the box-and-whisker plot it can be extracted that the median (Q2) was very similar in all cases as expected, around 20 kW. On the other hand, the atypical values of power delivered to the grid were below 5 kW and above 40 kW.

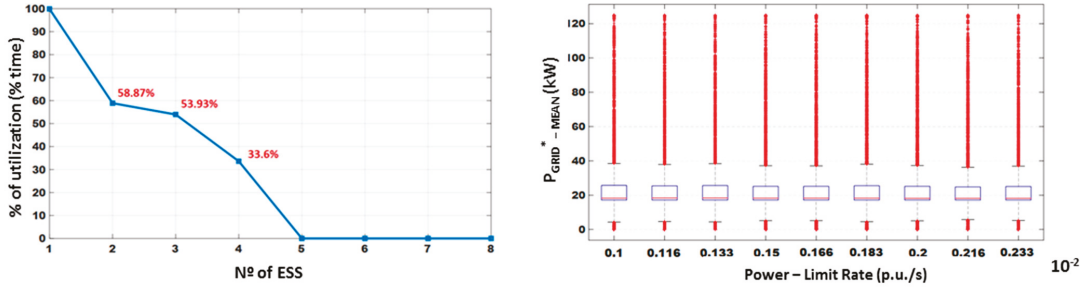

(**a**) (**b**)

Figure 16. (**a**) Percentage of use of each of the four SC cabinets during the entire period studied and (**b**) box and whisker plot showing the average reference power values that will be delivered to the grid based on different active power ramp rate limits per minute (p.u./s).

5. Conclusions

This paper presents the methodology followed in the sizing of a SCESS in order to reduce the power oscillations of a real wave power generation plant connected to the electricity grid. The criterion followed to reduce the oscillations of the power injected into the grid is to limit the ramp-up of the power delivered by 10%/min and the ramp-down by 7.22%/min with respect to the generation profile. This criterion is based on the application of a grid code, which defines the requirements that a facility connected to a public power grid has to meet to ensure a safe, secure, and economic proper functioning. In this case, among all the parameters limited by the grid code standards, the active power ramp rate limit specified by regional transmission system operator (TSO) of each country is studied. For the sizing of the ESS, the calculated efficiency maps calculated of a real SC cabinet (on which this study is based) were drawn up to analyze the real power that the SCESS has to supply based on the measured current and voltage. Unlike other ESSs, such as batteries, the voltage in the SC is more variable and must be properly considered in order to try to operate, as far as possible, at the most optimal point of efficiency when there are several storage modules (cabinets) working in parallel. For the study shown, a model was developed in MATLAB-Simulink that integrated *n* modules of one ESS (SC + power converter), the wave generation profile and the power profile to be delivered to the grid.

Additionally, to select the ESS units that were necessary in this application, the cumulative probability of the ESS power and energy values (calculated in 15 min periods) that satisfy the established criteria were studied. For the dimensioning of any ESS it is necessary to find a compromise between the percentage of cases that the ESS covers and the cost of adding an additional storage module. In this case, SC was considered an appropriate technology for the present application (fast and high number of charge/discharge cycles). It was obtained that four cabinets was the most "optimal" value with a percentage of usage in all of them greater than 33%, although with just three cabinets 80% of power compensation was achieved.

The dimensioning process was more restricting in terms of energy, obtaining, and excess of power capability. By either considering three or four SC cabinets to compensate the power oscillation, there was an excess of power. That was already identified in Figure 14b, where the fact that the line representing the storage technology was quite far from the curves knee. As a consequence, and although in this case it was initially selected SC as technology for available space and economic reasons, it would be interesting to explore other solutions such as flywheels, with a much better ratio energy/power for this application or even a hybrid storage system should not be disregarded.

Finally, it should be highlighted that this methodology can be applied to different renewable generation plants (solar, wind, etc.) connected to the grid that have to comply with grid code standards of different countries or regions.

Author Contributions: Conceptualization, G.N., J.N. and M.B.; methodology, J.T. and M.B.; software, M.B. and Á.S.; validation, G.N. and Á.S.; formal analysis, G.N. and J.T.; investigation, G.N.; data curation, M.B. and M.S.-H.; writing—original draft preparation, G.N. and J.N.; writing—review and editing, M.L., D.R. and G.N.; visualization, G.N. and M.S.-H.; supervision, M.L. and D.R. All authors have read and agreed to the published version of the manuscript.

Funding: This research received no external funding.

Acknowledgments: Special thanks to EVE (Ente Vasco de la Energía) and BIMEP (Biscay Marine Energy Platform) for the real data provided from the wave power generation plant that is operating in Mutriku.

Conflicts of Interest: The authors declare no conflict of interest.

References

1. Robles, E.; Haro-Larrode, M.; Santos-Mugica, M.; Etxegarai, A.; Tedeschi, E. Comparative analysis of European grid codes relevant to offshore renewable energy installations. *Renew. Sustain. Energy Rev.* **2019**, *102*, 171–185. [CrossRef]
2. Cruz, J. *Ocean Wave Energy*; Springer Berlin Heidelberg: Berlin, Germany, 2008.
3. Villalba, I.; Blanco, M.; Pérez-Díaz, J.I.; Fernández, D.; Díaz, F.; Lafoz, M.; Perez-Diaz, J.I.; Fernandez, D.; Díaz, F. Wave farms grid code compliance in isolated small power systems. *IET Renew. Power Gener.* **2019**, *13*, 171–179. [CrossRef]
4. Aderinto, T.; Li, H. Ocean Wave Energy Converters: Status and Challenges. *Energies* **2018**, *11*, 1250. [CrossRef]
5. Lehmann, M.; Karimpour, F.; Goudey, C.A.; Jacobson, P.T.; Alam, M.R. Ocean wave energy in the United States: Current status and future perspectives. *Renew. Sustain. Energy Rev.* **2017**, *74*, 1300–1313. [CrossRef]
6. Khojasteh, D.; Mousavi, S.M.; Glamore, W.; Iglesias, G. Wave energy status in Asia. *Ocean Eng.* **2018**, *169*, 344–358. [CrossRef]
7. Drew, B.; Plummer, A.R.; Sahinkaya, M.N. A review of wave energy converter technology. *Proc. Inst. Mech. Eng. Part A J. Power Energy* **2009**, *223*, 887–902. [CrossRef]
8. Al-Shetwi, A.Q.; Hannan, M.A.; Jern, K.P.; Mansur, M.; Mahlia, T.M.I. Grid-connected renewable energy sources: Review of the recent integration requirements and control methods. *J. Clean. Prod.* **2020**, *253*, 119831. [CrossRef]
9. Eltigani, D.; Masri, S. Challenges of integrating renewable energy sources to smart grids: A review. Renew. Sustain. *Energy Rev.* **2015**, *52*, 770–780.
10. Blanco, M.; Navarro, G.; Lafoz, M.; Perez, J.I. Study of the impact of wave energy generation in the frequency of an island electric grid. In Proceedings of the 12th European Wave and Tidal Energy Conference (EWTEC), Cork, Ireland, 27 August–1 September 2017.
11. Blavette, A.; O'Sullivan, D.L.; Alcorn, R.; Lewis, T.W.; Egan, M.G. Impact of a medium-size wave farm on grids of different strength levels. *IEEE Trans. Power Syst.* **2014**, *29*, 917–923. [CrossRef]
12. Macdowell, J.; Wang, Y.; Quint, R.; Chi, Y.; Ernst, B.; Saylors, S.; Jacobson, D.; Andresen, B.; Sorensen, P.E.; Portales, R.; et al. A journey through energy systems integration: Trending grid codes, standards, and IEC collaboration. *IEEE Power Energy Mag.* **2019**, *17*, 79–88. [CrossRef]
13. Wu, Y.K.; Chang, S.M.; Mandal, P. Grid-connected wind power plants: A survey on the integration requirements in modern grid codes. In Proceedings of the Conference Record—Industrial and Commercial Power Systems Technical Conference, Calgary, AB, Canada, 5–8 May 2019; pp. 1–9. [CrossRef]
14. Karbouj, H.; Rather, Z.H. A Comparative Study on the Impact of Grid Code Regulations on Stability of Wind Integrated Power Systems. In Proceedings of the 2019 IEEE 1st Global Power, Energy and Communication Conference, GPECOM 2019, Nevsehir, Turkey, 12–15 June 2019; Institute of Electrical and Electronics Engineers Inc.: New York, NY, USA, 2019; pp. 342–347.
15. Karray, I.; Ben Kilani, K.; Elleuch, M. Wind Plant Control under Grid Code Requirements. In Proceedings of the 16th International Multi-Conference on Systems, Signals and Devices, SSD 2019, Istanbul, Turkey, 21–24 March 2019; Institute of Electrical and Electronics Engineers Inc.: New York, NY, USA, 2019; pp. 706–711.
16. Attya, A.B. Provision of frequency support by wind power plants: Assessment of compliance with grid codes. In Proceedings of the 2019 IEEE Milan PowerTech, PowerTech 2019, Milan, Italy, 23–27 June 2019; Institute of Electrical and Electronics Engineers Inc.: New York, NY, USA, 2019; p. 8810978.
17. Lin, D.; Li, X.; Ding, S. An Investigation on Cost-effectiveness of Photovoltaic Power Ramp Rate Control by Using the Levelized Cost of Electricity. In Proceedings of the Asia-Pacific Power and Energy Engineering Conference (APPEEC), Nanjing, China, 20–23 September 2020; pp. 1–6. [CrossRef]
18. Coe, R.G.; Bacelli, G.; Wilson, D.G.; Abdelkhalik, O.; Korde, U.A.; Robinett, R.D. A comparison of control strategies for wave energy converters. *Int. J. Mar. Energy* **2017**, *20*, 45–63. [CrossRef]

19. Hong, Y.; Waters, R.; Boström, C.; Eriksson, M.; Engström, J.; Leijon, M. Review on electrical control strategies for wave energy converting systems. *Renew. Sustain. Energy Rev.* **2014**, *31*, 329–342. [CrossRef]
20. Li, L.; Yuan, Z.; Gao, Y.; Zhang, X. Wave Force Prediction Effect on the Energy Absorption of a Wave Energy Converter With Real-Time Control. *IEEE Trans. Sustain. Energy* **2019**, *10*, 615–624. [CrossRef]
21. Göteman, M.; Engström, J.; Eriksson, M.; Isberg, J.; Leijon, M. Methods of reducing power fluctuations in wave energy parks. J. Renew. *Sustain. Energy* **2014**, *6*, 043103.
22. Chabane, S.B.; Alamir, M.; Fiacchini, M.; Riah, R.; Kovaltchouk, T.; Bacha, S. Electricity Grid Connection of a Tidal Farm: An Active Power Control Framework Constrained to Grid Code Requirements. *IEEE Trans. Sustain. Energy* **2018**, *9*, 1948–1956. [CrossRef]
23. Zhou, Z.; Benbouzid, M.; Frédéric Charpentier, J.; Scuiller, F.; Tang, T. A review of energy storage technologies for marine current energy systems. *Renew. Sustain. Energy Rev.* **2013**, *18*, 390–400. [CrossRef]
24. Chauhan, A.; Saini, R.P. A review on Integrated Renewable Energy System based power generation for stand-alone applications: Configurations, storage options, sizing methodologies and control. *Renew. Sustain. Energy Rev.* **2014**, *38*, 99–120. [CrossRef]
25. Anwar, M.B.; El Moursi, M.S.; Xiao, W. Novel Power Smoothing and Generation Scheduling Strategies for a Hybrid Wind and Marine Current Turbine System. *IEEE Trans. Power Syst.* **2017**, *32*, 1315–1326. [CrossRef]
26. Wu, F.; Zhang, X.P.; Ju, P. Application of the Battery Energy Storage in Wave Energy Conversion system. In Proceedings of the 1st International Conference on Sustainable Power Generation and Supply, SUPERGEN 09, Nanjing, China, 6–7 April 2009.
27. Rojas-Delgado, B.; Alonso, M.; Amaris, H.; de Santiago, J. Wave Power Output Smoothing through the Use of a High-Speed Kinetic Buffer. *Energies* **2019**, *12*, 2196. [CrossRef]
28. Rajapakse, G.; Jayasinghe, S.; Fleming, A.; Negnevitsky, M. Grid Integration and Power Smoothing of an Oscillating Water Column Wave Energy Converter. *Energies* **2018**, *11*, 1871. [CrossRef]
29. Rajapakse, G.; Jayasinghe, S.; Fleming, A. Power management of an oscillating water column wave energy converter with battery/supercapacitor hybrid energy storage. In Proceedings of the 2018 8th International Conference on Power and Energy Systems, ICPES 2018, Colombo, Sri Lanka, 21–22 December 2018; Institute of Electrical and Electronics Engineers Inc.: New York, NY, USA, 2019; pp. 246–251.
30. Moreno-Torres, P.; Blanco, M.; Navarro, G.; Lafoz, M. Power smoothing system for wave energy converters by means of a supercapacitor-based energy storage system. In Proceedings of the 2015 17th European Conference on Power Electronics and Applications (EPE'15 ECCE-Europe), Geneva, Switzerland, 8–10 September 2015; Institute of Electrical and Electronics Engineers Inc.: New York, NY, USA, 2015.
31. Agarwal, A.; Iyer, V.M.; Anurag, A.; Bhattacharya, S. Adaptive control of a hybrid energy storage system for wave energy conversion application. In Proceedings of the 2019 IEEE Energy Conversion Congress and Exposition (ECCE), Baltimore, MD, USA, 29 September–3 October 2019; Institute of Electrical and Electronics Engineers Inc.: New York, NY, USA, 2019; pp. 4994–5001.
32. Rasool, S.; Muttaqi, K.M.; Sutanto, D. Modelling of a wave-to-wire system for a wave farm and its response analysis against power quality and grid codes. *Renew. Energy* **2020**, *162*, 2041–2055. [CrossRef]
33. Tedeschi, E.; Santos-Mugica, M. Modeling and control of a wave energy farm including energy storage for power quality enhancement: The bimep case study. *IEEE Trans. Power Syst.* **2014**, *29*, 1489–1497. [CrossRef]
34. Yan, Z.; Zhang, X.P. Adaptive energy filters smoothing renewable power fluctuations at different power levels. In *IET Conference Publications*; Institution of Engineering and Technology: London, UK, 2019; Volume 2019.
35. Kovaltchouk, T.; Multon, B.; Ahmed, H.B.; Aubry, J.; Venet, P. Enhanced aging model for supercapacitors taking into account power cycling: Application to the sizing of an energy storage system in a direct wave energy converter. In Proceedings of the 2014 9th International Conference on Ecological Vehicles and Renewable Energies (EVER), Monte-Carlo, Monaco, 25–27 March 2014; pp. 1–10. [CrossRef]
36. Torres, J.; Moreno-Torres, P.; Navarro, G.; Blanco, M.; Lafoz, M. Fast Energy Storage Systems Comparison in Terms of Energy Efficiency for a Specific Application. *IEEE Access* **2018**, *6*, 40656–40672. [CrossRef]
37. Energías Marinas—EVE. Available online: https://eve.eus/Actuaciones/Marina?lang=es-es (accessed on 4 February 2021).
38. Electric Double Layer Capacitor—An Overview. Electric Double Layer Capacitor—An Overview | ScienceDirect Topics. Available online: https://www.sciencedirect.com/topics/engineering/electric-double-layer-capacitor (accessed on 5 January 2021).
39. *International Electrotechnical Commission Electrical Energy Storage—White Paper*; International Electrotechnical Commission: Geneva, Switzerland, 2011; pp. 1–78.
40. Grbović, P. Ultra-Capacitor Energy Storage Devices. In *Ultra-Capacitors in Power Conversion Systems*; John Wiley & Sons, Ltd.: Hoboken, NJ, USA, 2013; pp. 22–77.
41. Rafik, F.; Gualous, H.; Gallay, R.; Crausaz, A.; Berthon, A. Frequency, thermal and voltage supercapacitor characterization and modeling. *J. Power Sources* **2007**, *165*, 928–934. [CrossRef]
42. Chaoui, H.; Gualous, H. Online Lifetime Estimation of Supercapacitors. *IEEE Trans. Power Electron.* **2017**, *32*, 7199–7206. [CrossRef]
43. Mohan, N.; Undeland, T.; Robbins, R. *Power Electronics Converters, Applications and Design*; John Wiley & Sons: Hoboken, NJ, USA, 1995.
44. Navarro, G.; Nájera, J.; Torres, J.; Blanco, M.; Santos, M.; Lafoz, M. Development and Experimental Validation of a Supercapacitor Frequency Domain Model for Industrial Energy Applications Considering Dynamic Behaviour at High Frequencies. *Energies* **2020**, *13*, 1156. [CrossRef]

45. Maxwell Technologies Maxwell Technologies Ultracapacitors, Supercapacitors, Microelectronics and High Voltage. Available online: https://www.maxwell.com/ (accessed on 10 February 2021).
46. Zuo, X.; Li, G.Z. Isolated voltage balancing in super-capacitor energy storage system. In Proceedings of the 26th Chinese Control and Decision Conference (CCDC), Changsha, China, 31 May–2 June 2014; IEEE Computer Society: Washington, DC, USA, 2014; pp. 5124–5128.
47. Li, L.; Huang, Z.; Liu, W.; Li, H.; Li, H.; Yang, Y. A controllable voltage equalizer with state of charge prediction for supercapacitors in large current applications. In *IFAC Proceedings Volumes (IFAC-PapersOnline)*; IFAC Secretariat: Laxenburg, 2014; Volume 19, pp. 3623–3628.
48. MATLAB - El Lenguaje del Cálculo Técnico—MATLAB & Simulink. Available online: https://es.mathworks.com/products/matlab.html (accessed on 4 January 2021).
49. Castano, S.; Gauchia, L.; Sanz-Feito, J. Effect of packaging on supercapacitors strings modeling: Proposal of functional unit defined around balancing circuit. *IEEE Trans. Compon. Packag. Manuf. Technol.* **2013**, *3*, 1390–1398. [CrossRef]
50. Zhang, S.; Yu, X. A unified analytical modeling of the interleaved pulse width modulation (PWM) DC-DC converter and its applications. *IEEE Trans. Power Electron.* **2013**, *28*, 5147–5158. [CrossRef]
51. Arango, E.; Ramos-Paja, C.; Calvente, J.; Giral, R.; Serna, S. Asymmetrical Interleaved DC/DC Switching Converters for Photovoltaic and Fuel Cell Applications—Part 1: Circuit Generation, Analysis and Design. *Energies* **2012**, *5*, 4590–4623. [CrossRef]
52. BiMEP BiMEP Mutriku. Available online: https://www.bimep.com/area-mutriku/servicios/ (accessed on 10 February 2021).
53. Blanco, M.; Navarro, G.; Lafoz, M.; Pérez, J.I. How harmful is the wave energy penetration in an electric grid? In *Proceedings of the Twelfth European Wave and Tidal Energy Conference*; Lewis, A., Ed.; University College Cork: Cork, Ireland, 2017; p. 942.
54. Lafoz, M.; Blanco, M.; Beloqui, L.; Navarro, G.; Moreno-Torres, P. Dimensioning methodology for energy storage devices and wave energy converters supplying isolated loads. *IET Renew. Power Gener.* **2016**, *10*, 1468–1476. [CrossRef]
55. Moreno-Torres, P.; Lafoz, M.; Navarro, G.; Blanco, M.; García-Tabarés, L. Sistema para el acondicionamiento de la potencia eléctrica generada en un sistema de generación undimotriz. 2016, pp. 1–32. Available online: https://www.patentes-y-marcas.com/fr/brevet/sistema-para-el-acondicionamientode-la-potencia-electrica-generada-en-un-sistema-de-generacion-undimotriz-p201530980 (accessed on 5 January 2021).
56. Lafoz, M.; Blanco, M.; Ramirez, D. Grid connection for wave power farms. In Proceedings of the 2011 14th European Conference on Power Electronics and Applicationsm, Birmingham, UK, 30 August–1 September 2011; IEEE: New York, NY, USA, 2011; pp. 1–10.
57. *ENTSO-E European Network of Transmission System Operators for Electricity (ENTSO-E)*; European Union: Brussels, Belgium, 2016.
58. EASE. *EERA European Energy Storage Technology Development Roadmap - 2017*; EERA: Brussels, Belgium, 2017.
59. Gatta, F.M.; Geri, A.; Lauria, S.; Maccioni, M.; Palone, F. Battery energy storage efficiency calculation including auxiliary losses: Technology comparison and operating strategies. In Proceedings of the 2015 IEEE Eindhoven PowerTech, Eindhoven, The Netherlands, 29 June–2 July 2015.
60. Funaki, T. Evaluating energy storage efficiency by modeling the voltage and temperature dependency in EDLC electrical characteristics. *IEEE Trans. Power Electron.* **2010**, *25*, 1231–1239. [CrossRef]

energies

MDPI

Review

Present and Future of Supercapacitor Technology Applied to Powertrains, Renewable Generation and Grid Connection Applications

Gustavo Navarro *, Jorge Torres, Marcos Blanco, Jorge Nájera, Miguel Santos-Herran and Marcos Lafoz

CIEMAT, Spanish National Research Centre on Energy, Environment and Technology, 28040 Madrid, Spain; jorgejesus.torres@ciemat.es (J.T.); marcos.blanco@ciemat.es (M.B.); Jorge.Najera@ciemat.es (J.N.); miguel.santos@ciemat.es (M.S.-H.); marcos.lafoz@ciemat.es (M.L.)
* Correspondence: gustavo.navarro@ciemat.es

Abstract: Energy storage systems (ESS) are becoming essential as a solution for troublesome industrial systems. This study focuses on the application of a type of ESS, a high-power technology known in the literature as supercapacitors or electric double layer capacitors (EDLC). This technology has had a huge impact during the last decade on research related to the electric traction drives, renewable sources and powergrids. Related to this aspect, this paper summarizes the most relevant scientific publications in the last five years that study the use of supercapacitor technology (SCs) in electric traction applications (drives for rail vehicles and drives for road vehicles), generation systems for renewable energy (wind, solar and wave energy), and connection systems to the electric grid (voltage and frequency regulation and microgrids). The technology based on EDLC and the practical aspects that must be taken into account in the op-eration of these systems in industrial applications are briefly described. For each of the aforementioned applications, it is described how the problems are solved by using the energy storage technology, drawing the solutions proposed by different authors. Special attention is paid to the control strategies when combining SCs with other technologies, such as batteries. As a summary, some conclusions are collected drawn from the publications analyzed, evaluating the aspects in which it is necessary to conduct further research in order to facilitate the integration of EDLC technology.

Keywords: supercapacitors; electric traction drives; electrical vehicle; microgrid; renewable energy; energy storage system

Citation: Navarro, G.; Torres, J.; Blanco, M.; Nájera, J.; Santos-Herran, M.; Lafoz, M. Present and Future of Supercapacitor Technology Applied to Powertrains, Renewable Generation and Grid Connection Applications. *Energies* **2021**, *14*, 3060. https://doi.org/10.3390/en14113060

Academic Editor: Alon Kuperman

Received: 20 April 2021
Accepted: 20 May 2021
Published: 25 May 2021

1. Introduction

Energy storage systems have begun to play a fundamental role in recent years, being one of the most used solutions to improve industrial processes. These devices increase both the production systems performance, improving the energy efficiency, reliability, and flexibility of electrical systems. This topic has nowadays a high relevance due to the expectations of a high integration of renewable energies in electrical grids.

There are different types of energy storage systems (ESSs), divided according to their nature or their operating cycle duration, listed in Tables 1 and 2 respectively. From those tables, the market niches of each ESS could be extracted, considering those technologies with short cycle to applications with fast response, e.g., frequency stability or regenerative braking. Meanwhile, those devices with long cycle could be used in long term applications, as for example massive energy storage or backup system for critical loads.

This paper focuses on a promising energy storage system, supercapacitors (SCs), also known as electrolytic double layer capacitors (EDLC), which have better trend than other competitors. This ESS has a high technology readiness level (TRL), TRL8, and a very promising track record, since it closes the gap between batteries and conventional capacitors, competing with other technologies with similar characteristics such as fly-

wheels, see Figure 1, Tables 1 and 2. SCs are characterized by high power density and low specific energy.

As described before, SCs focus on applications that require charge-discharge cycle times ranging from a few seconds to several minutes. Based on this and considering the objective of improving the performance of the industrial processes and the electrical systems, countless research articles have been published, as well as research & development projects have been developed in recent years. The aim of these studies is to create new industrial products of ESS based on SCs. This great amount of studies related to SCs evidence the current need for this technology, having inter-annual market growth and encouraging impressive expectations for the future [1].

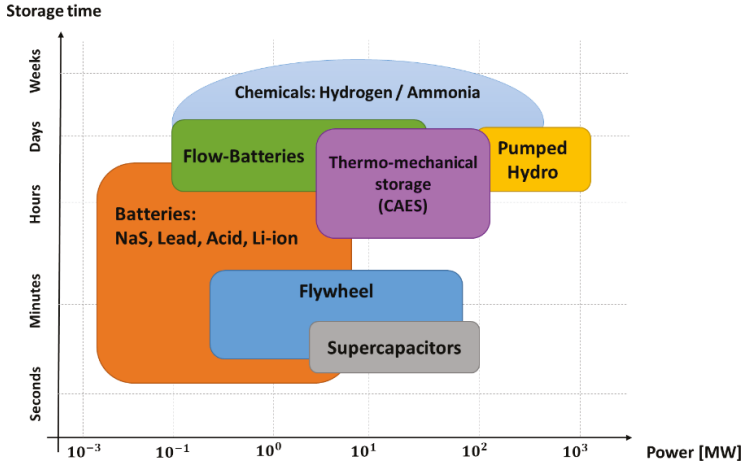

Figure 1. Storage time against the power delivered for electrical energy storage technologies, adapted from [5].

Table 1. ESSs Classification according to their nature, data from [2].

Nature	Electrical Energy Storage Technology
Electromechanical	• Flywheels (FESS) • Compressed Air (CAES) • Hydro Pumped Energy Storage (HPES)
Electromagnetic	Pumped Energy Storage (HPES) Superconducting Magnetic Energy Storage (SMES)
Electrochemical	Batteries (BESS)
Chemical	Fuel Cells (FCs)
Electrostatic	Supercapacitors (SCs)

Table 2. Classification of the ESSs based on their cycle duration (based on [3,4]).

Cycle Duration (Time)	Electrical Energy Storage Technology
Very short (<10 s)	Capacitors, inductors
Short (1 s to 15 min)	SCs, FESS, SMES
Medium (5 min to 24 h)	Batteries
Long (days)	Batteries, CAES, HPES

After showing the operating ranges of some of the most widespread storage technologies in the industry, a comparison between the SCs and their competitors (batteries and

flywheels) is collected in Table 3, where the advantages and disadvantages are described in order to establish criteria to select the most suitable techonology for an application.

Table 3. Comparison based on benefits and drawbacks of the Batteries, flywheels and Supercapacitors.

ESS Technology	Advantages	Drawbacks
Batteries	Low self discharge Narrow range of voltage variation in operation High energy density Low installation cost	Accelerated aging with large power pulses Low recyclability of materials Reduced operating temperature range Low power density Need for a BMS
Supercapacitors	High power density Wide operating temperature range Ageing not dependent on the duty cycle More stable efficiency throughout the operating range	Wide voltage variation in operation Power converter required to operate Voltage balancing system between cells required Low energy densisty Higher cost (€/kWh)
Flywheels	High energy density Power and Energy decoupling Less ageing than batteries and supercapacitors Very wide operating temperature range	High self-discharge High installation cost Lower efficiency than batteries and SCs Power converter required

Regarding the comparison in the above table, the supercapacitors show better performance in some areas, especially regarding cost (specially when cost in terms of power terms, $/W), compared with flywheels, and in the dynamic response and their aging, in applications with short cycle and high power delivered. Supercapacitors will be more preferred than batteries in general for applications where high power, low energy, and large cycling requirements are demanded.

One important aspect when designing and dimensioning SC-based ESS is to define a model of the system which represents its performance under a particular application profile or conditions with high accuracy. Countless SC models for industrial applications have been published in the literature, classified in three main categories: equivalent circuit models, electrochemical models and intelligent models [6]. From these categories, equivalent circuit models are suitable for industry applications, since they describe the SCs behavior using basic common components: capacitors, inductances, and resistors (RLCs) [7]. Within equivalent circuit models, three subcategories can be established, according to their complexity and accuracy: RC models, transmission line models, and frequency domain models [8–11].

Following the SCs model analysis, the next step is to define the main parameters that define the SCs performance:

- The first and main feature is the capacitance. This parameter represents the energy storage behavior of the SCs, being a function of the voltage and the frequency [12]. This variation, shown in Figure 2a, is between 15% and 20% of the rated capacity [13]. This effect is important in ESS applications since the ESS operating voltage impose a capacitance value different to its rated value, which provokes less stored energy. Moreover, the operation frequency of the SCs modifies the capacitance value. Figure 2b shows that there is a cut-off frequency, usually around 1 Hz depending on the materials and manufacturing processes, where the rated capacitance drastically decreases. Therefore, SCs are usually considered for fast charge–discharge cycles, from tens of seconds to minutes.

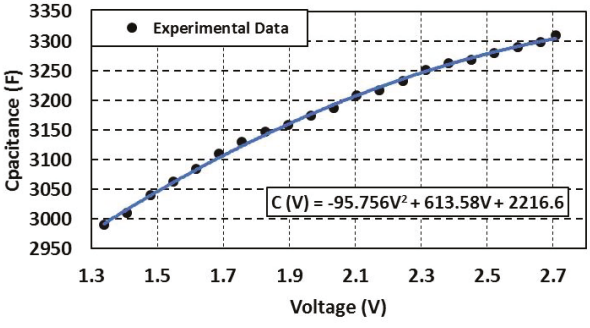

(**a**)

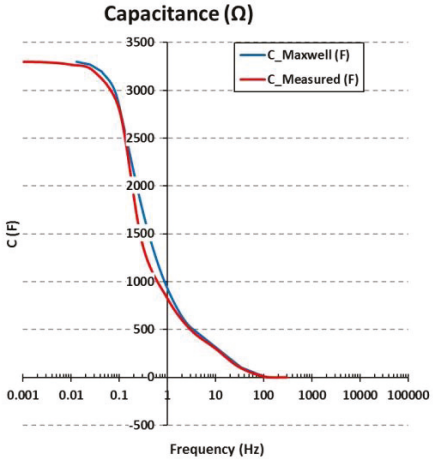

(**b**)

Figure 2. (**a**) Capacitance variation respect to the voltage; (**b**) Capacitance variation as a function of the frequency adapted from [7].

- The second effect is the inner resistance. Joule effect takes place in the positive and negative current collectors, the positive and negative porous electrodes and in the separator [12]. Due to the electron transportation process, their kinetic energy is converted into heat. These effects on the conductors and the electrolyte are grouped in a single term named ohmic phenomena and represented by the equivalent series resistance (ESR). The ESR is not constant and depends on the frequency and the cell temperature in a non-linear form [14], as shown in Figure 3. The ESR value is reltively low compared to other electrochemical ESS such as batteries. However, attention should be paid to the ohmic losses on the SCs in those applications which require high power [15]. Moreover, ESR provokes a voltage drop, decreasing the SCs efficiency, and a temperature rise inside the cells. This heat produced from losses needs to be evacuated in order to avoid accelerated aging due to overtemperature. Therefore, proper operation of cooling systems is always required.
- The third parameter in a SC is the self-discharge, which is a drawback of using SCs for cycles longer in the order of hours [16]. The origin of this effect is the redox reactions at the electrode surface when the electrons cross the double layer [17]. This parameter depends mainly on voltage, temperature and aging. Therefore, it could be modelled

as a voltage-controlled temperature-dependent current source. The self-discharge current value is given by the manufacturer in the datasheet as a constant value [16].

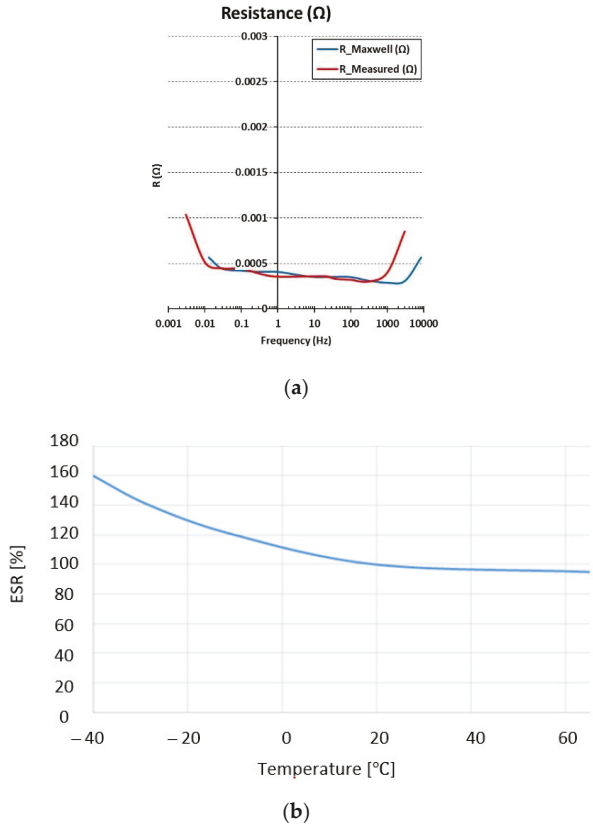

Figure 3. (**a**) ESR variation respect to the voltage, adapted from [7]; (**b**) ESR variation as a function of the frequency.

Navarro G. [18] presents a study in which all these parameters are analyzed and aging and voltage imbalance in a large series connection of SCs are calibrated. Table 4 collects the main parameters of commercial cells for several manufacturers.

With respect to the lifespan of the SCs, several limits are established that imply the SCs replacement. A SC cell is considered to have achieved the end of its useful life when any of the following point are fulfilled:

- ESR current value has doubled from its initial value.
- The current capacitance value has decreased by 20% compared to its nominal value.
- The SC operating cycle number is more than 1 million.

Finally, the last step in the designing and dimensioning process is to evaluate the system losses. A SC-based ESS comprises the SC cells and an interface DC/DC power converter. Power losses take place in both devices, imposing the following issues [15]:

- The ohmic losses in the system located in the SCs, represented by the ESR value, the cell-bars which connects the SCs and the power cables.
- The cooling system to maintain the SCs in an optimum operating temperature range.
- The power electronics (conduction and conmutation) losses.

Considering a literature review, there are many articles focusing on organizing and summarizing the new published research advances of this type of technology, as collected in [26]. This paper collects both small- and large-scale applications. For this purpose, the applications have been classified in four main groups: electric traction applications; renewable generation systems; microgrid and power grid connection applications; and autonomous power systems for energy distribution and ships and aircraft applications.

Table 4. Main parameters of SCs cell for different manufacturers.

Characteristics	Maxwell [19]	Skeleton [20]	Ioxus [21]	EATON [22]	Kamcap [23]	Ls Mtron [24]	Vina Tech [25]	Yunakaso [23]
Rated voltage	2.7 V	2.85 V	2.85 V	2.85 V	2.7 V	2.7 V	2.7 V	2.7 V
Initial rated capacitance	3000 F	3200 F	3000 F	3400 F	3000 F	3000 F	3000 F	3000 F
Initial ESR	0.29 mΩ	0.14 mΩ	0.20 mΩ	0.23 mΩ	0.29 mΩ	0.23 mΩ	0.28 mΩ	0.28 mΩ
Operating temperature range	[−40 °C , 65 °C]							
Maximum current	1900 A	3100 A	2700 A	2700 A	–	–	–	2200 A
Maximum Leakage current	5.2 mA	11 mA	4.5 mA	8 mA	–	–		5 mA

Figure 4 shows the percentage of scientific publications in the last five years related to SCs for the four application groups:

- The most published topic is related to the use of SCs in electric traction applications. This group represents 50% of the published studies. Most of them related to electric vehicles (EV) or hybrid electric vehicles (HEV).
- The second group of the most published topics is related to power grid applications. Most of them are related to the improvement of the control strategy of a microgrid, the voltage and frequency regulation, and the increase of the battery lifespan.
- The third position is for the group of studes related to the renewable generation systems, especially solar PV, wind and wave energy sources. Finally, the last group with 10% of the papers are those applications related to the autonomous power systems, ships and aircrafts.

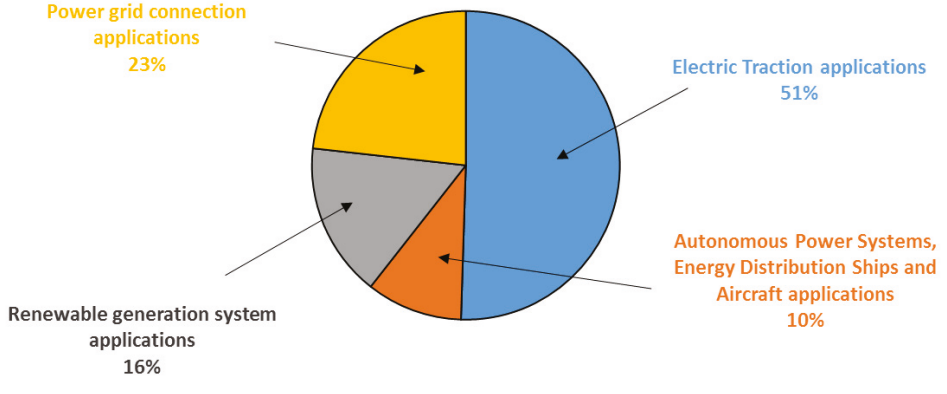

Figure 4. Classification of the research publications related to SCs in the last decade respect to their application.

This paper describes the most important studies done for the three main groups which represent most of the SCs present applications. Those groups collect almost 90% of the whole researches related to SCs.

The information is structured into the following sections. Following this introduction, in Section 2 the applications related to the electric traction are described. This section collects both the railway and the road vehicles. This is followed in Section 3, describing in detail the applications related to the renewable generation systems, which include solar, wind, wave energy and hybrid generation systems. In Section 4, those studies that analyze the electrical systems connected to the grid are detailed; within them, there are topics as frequency regulation, voltage drop problems, etc. Furthermore, this group includes those researches related to microgrids. Finally, the paper concludes with Section 5, which contains a summary of the most important aspects covered, as well as the future prospects of the technology based on the information provided for different applications.

2. Electric Traction Applications

The electric traction drives can be applied to diverse means of transport that use the road or rail transport modes. Regarding the road mode, SCs might be applied in:

- Means of public transport power by catenary
- Hybrid electric vehicles
- Pure electric vehicles

On the other hand, within the vehicles that move on rails, it is possible to distinguish between:

- Heavy-rail catenary supplied vehicles
- Heavy-rail diesel–electric vehicles
- Light-rail rapid transit vehicles

Whether they are vehicles that move on rails or on the road, they have a common structure: a traction drive and control system. Its power stage is formed by the traction motor, the power electronic converter, a braking chopper or dynamic brake and a high impedance/ high power density power supply. This power supply has the capacity to absorb high power consumption peaks, while the power inverter drives the traction motor, and the braking chopper limits the DC voltage during braking dissipating the excess energy into a resistor. Figure 5 shows a general electric scheme of the traction system for this type of vehicles.

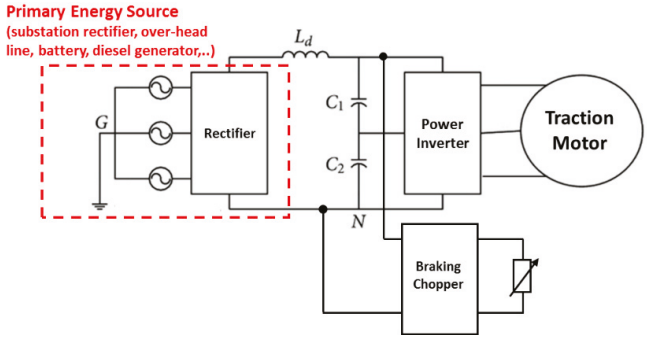

Figure 5. Electrical diagram of a traction converter connected to a high energy/high impedance power source.

Regarding the stages in which the route of a vehicle can usually be divided, the followings are distinguished:

I. Acceleration section (beginning of the route): During this acceleration stage, the vehicle goes from zero speed to nominal speed. Moreover, during this phase, the power consumed begins to increase until it reaches its maximum value when the vehicle reaches its nominal speed.
II. Nominal or cruising speed: At this stage, the power drops till a minimum value required to maintain the vehicle speed at its nominal value.
III. Braking or deceleration phase (end of route): During deceleration, the kinetic energy of the vehicle is transformed into electrical energy by means of a regenerative braking.

As a consequence, the power fluctuations are very high: positive, minimum and finally negative. The problems in the power system derived from this highly irregular power profile are:

- Fluctuations in the supply voltage and instability [27].
- Higher losses in the power system.
- Significant energy consumption due to not being able to take advantage of the braking energy: not reversible power supplies and braking chopper.
- Oversized power system due to the need to fully supply the energy consumed by the vehicle.

A possible solution to the aforementioned problem is the inclusion of a storage system in the vehicle's power train to supply/absorb high power peaks for short periods (acceleration and deceleration section) and to recover braking energy by eliminating or reducing considerably the size of the chopper. When sizing the storage system, it is required to define the maximum power peaks (positive and negative) and the stored energy level. In general, those vehicles use other main power systems and the storage system would usually operate for periods of less than 1 min. Considering the particular characteristics of SCs (high power density and low energy density), they are a highly recommended option for this type of application.

2.1. Electric Drive for Rail Vehicles

2.1.1. Heavy-Rail Catenary Supplied Vehicles

This category mainly includes transport locomotives such as high-speed short-distance passenger and freight trains [28]. In general, the traction system of these vehicles is fed from an overhead line (primary power supply) through a pantograph. The voltage level varies depending on the country, generally 1.5–3 kV DC (short-haul train) or single phase 25–50 Hz (short and long-distance trains). Figure 6 shows a typical block diagram of a common heavy-rail catenary supplied traction drive without any ESS.

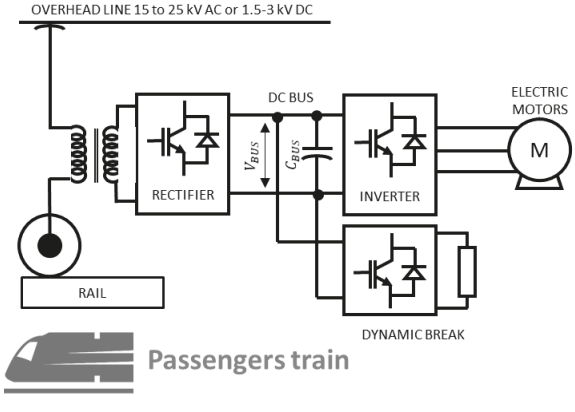

Figure 6. Simplified electrical diagram of the traction drive of a heavy-rail catenary supplied vehicles.

There are several researchers that describe the use of SCs in this type of vehicle. Dutta, O. [29] proposed a mathematical optimization methodology and a model of a stationary storage systemfor a DC rail transportation application, New York City Transit (NYCT). In this study different technologies are compared, including batteries, flywheels and SCs working independently or together. The results of the optimization process are based on the percentage of energy savings because of regenerative braking, voltage regulation, reduction in peak demand, estimated payback period and system re-siliency. The paper concludes that the cheapest storage system to operate autonomously are SCs. On the other hand, it highlights that regarding the the resilience of the system, a hybrid system made up of batteries and SCs is the economic option as long as the percentage of regenerative braking energy recovery is greater than 30%.

Khodaparastan, M. [30] compares two storage technologies (SCs and high-speed flywheels), from an economic point of view, to take advantage of the braking energy of a continuously powered train (650 V rectified voltage from the utility grid AC 13 kV). Two case studies are presented depending on the objective to be achieved: reduce the demand peak or stabilize the supply voltage. A cost analysis of both technologies is also performed for both purposes. It is concluded that the flywheel is the most suitable technology from the economical point of view. However, due to their technical characteristics, both technologies are appropriate for the purpose described.

Chen, J. [31] also proposedthe use of SCs to take advantage of the regenerative braking of a high-speed railway powered by a 27 kV AC catenary. The storage system is connected through a bidirectional DC/DC converter to the intermediate DC stage of a back-to-back converter, whose input and output are connected to two different points on the main power line of the trains. A state machine logic is proposed with four states (charge, discharge, transfer and standby mode) and transitions between them depending on the power line charge level and the maximum state of charge (SoC) of the ESS. One of the back-to-back converters acts as the master converter and the other converter and the DC/DC of the SCs act as slaves. The proposed control coordinates the operation of several converters to stabilize the DC bus voltage, improve the power supplyquality in high-speed railways and take advantage of braking energy. The cost savings will depend on the policy of power utility companies for the returned regenerative braking energy.

Zhong, Z. [32] proposes SCs as an on-board storage system to absorb braking energy and completely replace the brake resitor (see Figure 7). Despite the weight that this implies, it is justified that the storage system is on board and not stationary in order to take advantage of the whole braking energy and to be able to completely replace the on-board brake resistor. A hierarchical optimization energy management strategy is proposed based on an additional power stage in series, connected between the inverter of the traction motor and the main supply voltage (DC). The storage system would be connected to the DC stage through a bidirectional converter. The three benefits extracted from this configuration are:

1. The voltage level of the DC stage is adjusted to its optimal value to extract the maximum torque for each speed.
2. The use of braking energy in any operational scenario.
3. A 10% reduction in system losses is achieved by adjusting the SCs duty cycle in real time.

Xu, C. [33] presented a study related to the use of SCs to extend the service life of the pantographs that feed high-speed trains. The arcing phenomenon due to the irregular movements of the trains and the intermittent line pantograph disconnection reduces its useful life. Morreover, it can even damage onboard equipment and measuring elements. In this study, the SCs based ESS absorbs the inductive energy and reduces the surges in the power line. The strategy to manage the system energy between the storage system, the train and the main power system is analyzed and validated by simulations to compensate the voltage fluctuations and take advantage of braking energy.

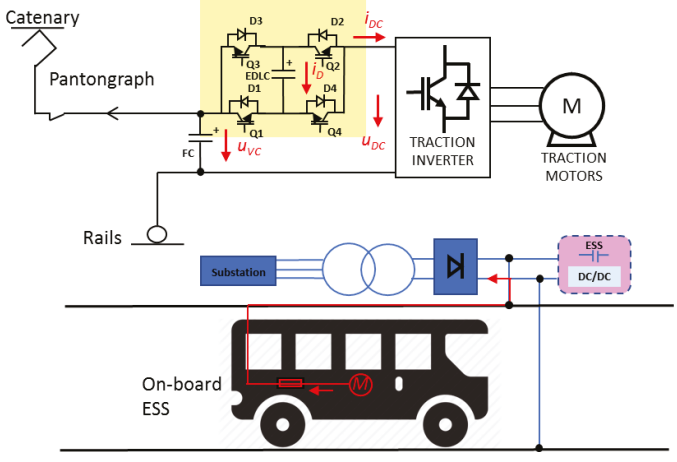

Figure 7. Topology of onboard-wayside supercapacitor hybrid energy storage system extracted adapted from [32].

2.1.2. Heavy-Rail Diesel–Electric Vehicles

This section analyzes the applications of SCs in Heavy-Rail Diesel—Electric Vehicles. These types of vehicles run on fossil fuel and are commonly used in North America and some European countries [34]. The traction scheme of this type of vehicle is composed of an internal combustion engine (ICE) group (gas engine, petrol engine, diesel engine, or gas turbines) coupled to an electric generator that, through two power converters, feed the traction motors. They have also an energy dissipation system to evacuate the braking energy (DC chopper). A typical electrical diagram of this type of vehicle without any ESS is shown Figure 8.

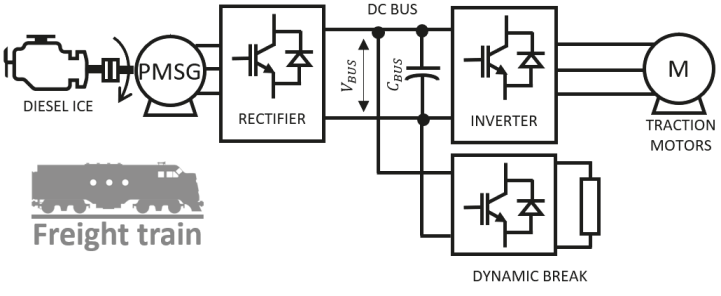

Figure 8. Simplified electrical diagram of the traction drive of diesel-electric vehicles with permanent magnet synchronous generator (PMSG).

Da Silva Moraes, C.G. [35] proposed a hybrid storage system (lithium-ion batteries and SCs) whereby a percentage of the braking energy is used to power auxiliary equipment, while the ICE group remains the main power supply for the traction motor. Thids would reduce the cost and volume of the diesel group. SCs are used as buffers to absorb rapid power fluctuations in a multiport configuration in which each storage system consists of a DC/DC converter.

2.1.3. Light-Rail Rapid Transit Vehicles

Light vehicles powered by a catenary constitute a type of transport that is normally used for moving passengers in urban environment [36]. The locomotive or towing vehicle

is powered by an overhead line through a pantograph. The catenary in turn is fed by a power supply substation. The supply voltage level varies from one country to another, stablishing in most of them in the range of 1.5 kV or 3 kV. Figure 9 shows the most common electrical scheme used by this type of vehicle without any ESS. A three-phase inverter is usually used to power the traction motors from the catenary. On the other hand, it also has a DC/DC converter (DC chopper) to evacuate the braking energy.

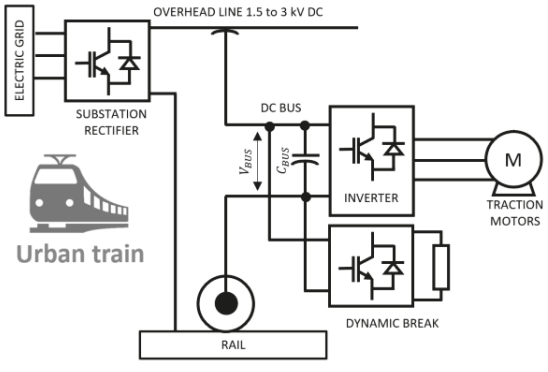

Figure 9. Simplified electrical diagram of the traction drive of light-railupplied vehicles.

In the literature, there are several papers that study the SCs introduction in the feeding scheme of this type of vehicle. Zhang, X. [37] studied the existing problem arises due to the overcurrents suffered by the SCs that feed some light urban transport vehicles during charging from the catenary. This problem is more serious when, due to power needs, it is necessary to connect several chargers in parallel. These overcurrents also cause accelerated aging of the SCs. The authors propose a protocol to coordinate the load of the different storage systems to reduce the current overshoot without hardly increasing the load time.

The study proposed in [38] shows a power management control of wayside lithium-ion capacitor to improve the efficiency of a light railway vehicle. The particularity of this paper is it concludes the SC technology that best suits the present application are Li-ion capacitor and not EDLC due to its higher energy density. The energy stored during regenerative braking is used again during the acceleration section. The energy management strategy is based on monitoring the SCs SoC and the current vehicle speed. Other important conclusions drawn from the study are that the peak power of the power supply is reduced by up to 46% and the maximum energy saved represents 30% of the energy consumed by a system without an ESS.

Zhu, F. [39] suggests a hierarchical control of a stationary supercapacitor-based energy storage system to save energy by taking advantage of braking power. The main power supply for the vehicle is a 750 V or 1500 V voltage catenary. The ESS is connected to this DC bus through a DC/DC converter. A real case study is described and analyzed in which the proposed control strategy is applied with a maximum energy saving of 12%.

Additionally, although no references related to real applications have been found, it is worth mentioning the possibility to use energy storage for ultrafast rail vehicles, mag-netic levitated trains, and the hyperloop, resulting in an especially convenient option in the second one, since the use of a power supply just for the acceleration leads to the use of short-term energy storage [40].

2.2. Electric Drive for Road Vehicles

2.2.1. Public Transportation Catenary-Supplied Vehicles

This section describes the applications of SCs in urban passenger transport vehicles powered by a catenary. This type of vehicle is usually known by the name of trolleybus [41]. The difference respect to light vehicles is the electrical circuit is not closed by the rail,

but the catenary must consist of two poles. The predominant electrical scheme of this type of vehicle is shown in Figure 10. The catenary voltage is usually a direct voltage of 600–900 VDC generated from a three-phase rectifier connected to an electrical substation. The equipment on board the vehicle is made up of the inverter that feeds the traction motor and an electrical braking to avoid overvoltages in the power line (catenary). The trend in this type of transport is to replace the chopper with an ESS to take advantage of regenerative braking energy, save a percentage of energy, and, in a second step for the electrical power system, to place charging points in different sections of the route.

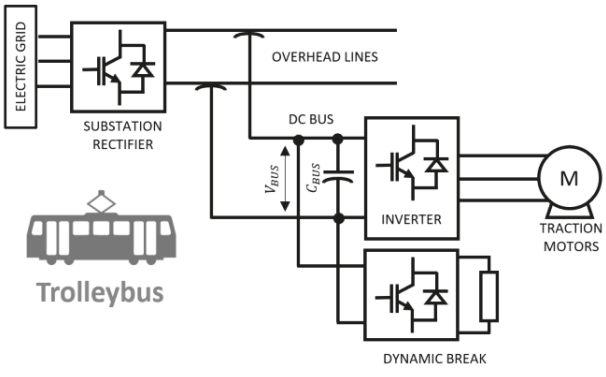

Figure 10. Simplified electrical diagram of the traction drive of public transportation catenary-supplied vehicles.

Cignini, F. [42] made a comparison of four prototypes of electric buses with an on-board storage system to fulfill certain speed requirements in a specific time. The study is carried out from the real data taken from the vehicles (energy consumption, acceleration, and maximum speed) in different scenarios. The four storage technologies being compared are a hybrid energy storage system (HESS) consisting of:

1. SCs and absorbent glass mat (AGM) lead batteries.
2. SCs and lithium-ion batteries.
3. SCs and lead-acid batteries.
4. SCs and lithium-ion iron phosphate batteries.

An economic analysis is also carried out to complement the previous comparison from a life cycle cost point of view. The paper concludes that the best option (lowest cost) is formed by SCs and lithium-ion batteries followed by option 1 (SCs/AGM batteries). On the other hand, from a technical point of view, option 2 is the best because it is the option that supports the highest charging rates.

Soltani, M. [43] proposed a HESS made up of lithium batteries and lithium-ion capacitor (LiC) as the only power source for a city bus. LiCs complement the use of batteries to extend their useful life by reducing the power peaks in the acceleration and decelaration stages, supplying/absorbing that energy in the LiCs. This study proposes an electrical, thermal and aging model of each ESS is presented and a methodology for the distribution of power requirements. The research concludes the HESS, compared to the ESS made up only of batteries, reduces the size of the energy storage required by 30% and the cost by 16%. The reason for this development is the increase of the battery lifetime and an improvement in the dynamic response and efficiency of the system.

2.2.2. Hybrid Electric Vehicles (HEVs)

SCs also have application in hybrid electric vehicles. This type of vehicle combines an ICE group and an electric drive. The aim of the electrical system is to operate at the point of maximum efficiency of the motor at each situation. The main elements are a fossil

combustion engine, an electric traction machine (generally a permanent magnet machine), a power converter and an ESS. According to the arrangement of these elements, four different configurations are distinguished: (1) series based on ICE, (2) parallel based on ICE, (3) series-parallel based on ICE, and (4) plug-in based on ICE.

In the series configuration the heat engine and the electric drive share the traction shaft (see Figure 11a). In the parallel configuration, the thermal motor and the electric drive are connected through a transmission element (see Figure 11b). In ICE based on series-parallel, the hybrid double conversion, the heat engine and the electric drive are interconnected through an electrical link as shown in Figure 11c. The ICE-based plug-in has the same characteristics as the parallel-based ICE, but it allows one to recharge the battery with an external charger (see Figure 11d).

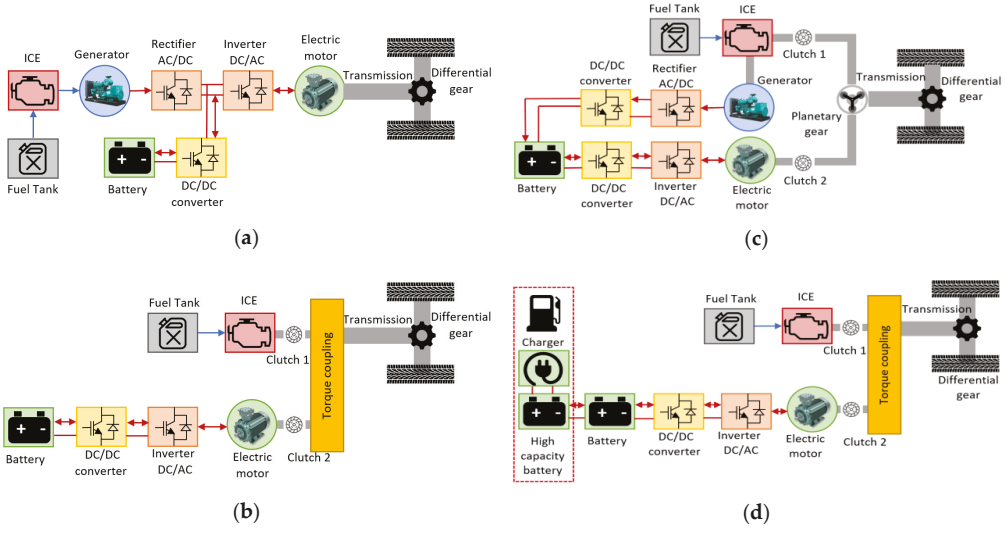

Figure 11. Simplified electrical diagrams of different traction drive configurations in HEV adapted from [44]: (**a**) ICE-based series; (**b**) ICE-based parallel; (**c**) ICE-based series-parallel; (**d**) ICE-based plug-in.

In the literature, there are several studies which propose to include SCs in HEVs to improve their efficiency and reduce the cost of their powertrain. Passalacqua, M. [45] describes the future possible advantages of a serial versus parallel architecture due to the development of the technology of the power elements (power electronics and ESS) that make up the powertrain of a medium size HEV. An SC-based ESS is proposed as a storage system. Results obtained in simulations are presented where fuel consumption is shown for different speed profiles (road missions) and serial vehicle configurations. The vehicle studied is based is equipped with a diesel engine, SiC power converters and SCs in series configuration. The paper concludes that the serial configuration and the proposed energy management system (EMS) achieve an energy saving of 35–48% compared to conventional configurations.

Passalacqua, M. [46] also described and analysed how the sizing of SCs affects engine number of starts (comfort) and the amount of energy that can be stored during braking. A review of the characteristics of a series configuration in HEVs is made and SCs are studied as the only storage system to make series configuration more efficient compared to the parallel configuration in a HEV. An EMS and seven experimentally measured road missions are proposed to calculate the required energy from the ESS to recover all the braking energy. From the point of view of the need for storage energy, mountain mission is the most demanding. The energy needs for the road missions studied are 150–200 Wh with

an approximate weight of 40–50 kg. It is suggested that, if LiCs are used instead of EDLC technology, the storage weight would be reduced to 25–35 kg.

2.2.3. Electric Vehicles (EV)

EVs are vehicles with a pure electric powertrain, i.e., without another power source of a nature other than electric [47]. Figure 12 shows an overall diagram of the traction system in this type of vehicle. In general, the parts that make up the electric drive of an EV are: an ESS (electrochemical battery, fuel cell), a power converter, and an electric traction drive. Depending on the ESS, a braking resistor is necessary (e.g., fuel cells as power source) or not (battery) to dissipate the braking energy.

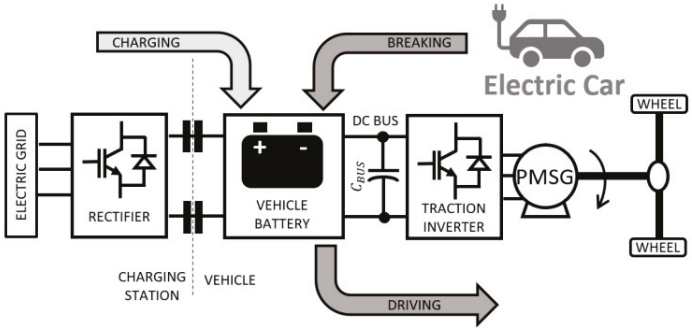

Figure 12. Simplified electrical diagram of the traction drive of EVs.

As in the previous sections, there are studies which analyse the inclusion of SCs in the electric drive of an EV to improve its dynamic response and reduce the cost of the ESS because of the higher battery lifetime. One of these studies is [48], in which a HESS made up of batteries and SCs is analyzed to be used in EVs. Two options of EMSs are proposed, one based on a low pass filter with a fuzzy logic controller and another based on an adaptive proportional integrator. This control distributes the power supplied between the battery and the SCs during acceleration and stores the energy during braking in the SCs considering their SoC. A simulation study has been done for different drive cycles (New York City cycle, Artemis urban cycle, and New York composite cycle). The conclusions of the paper are as follows. The proposed control strategy allows to reduce the variation of the voltage, higher SoC of the battery and efficiency, lower losses in the battery, a reduction of the current ripple through the battery, and a slight increase in temperature. In this case, no economic analysis is performed to compare this configuration to one that uses only batteries.

Sadeq, T. [49] also proposed an EMS for a HESS (battery/SC) to improve the dynamic response of EVs. The proposed topology is a battery/SCs system in semiactive configuration [50]. In order to distribute the power delivered by each ESS, two adaptive algorithms (optimal adaptive and fuzzy adaptive controller) are compared taking into account the profile traveled by the vehicle. Three profiles are simulated in MATLAB-Simulink at three different speeds, demonstrating that the useful life of the batteries is increased due to the reduction of the stress on the battery during high load operations. On the other hand, it is concluded that the response of the vehicle with an optimal adaptive controller is better than with a fuzzy adaptive controller in most cycles.

Additionally, the research described in [51] proposes a traditional topology of a HESS (battery/SC) to improve the drawbacks of using a ESS made up only of batteries (high cost, low power density and short cycle life). For the sizing of the ESS and the power distribution, a bilevel multiobjective design and control framework with the nondominated sorting genetic algorithm (NSGA-II) and fuzzy logic control (FLC) is described. The

authors conclude that a good EMS allows reducing the dimensioning of the SCESS (size and volume), achieving the same dynamic response as with a larger mass of the HESS.

Finally, regarding the most common topologies, Shi, R. [52] proposed a new topology of a HESS comprising batteries and SCs is proposed to distribute the power needed by an open winding motor. This topology connects both ESS to the electric motor through a power converter (dual in-verter drive), which makes it easier for both the batteries and the SCs to deliver the active/reactive power requirements (see Figure 13). This allows the use of machines with a higher voltage level than those that can be used with a traditional configuration. During the periods in which the required power is low, SCs remain in stand-by to improve the efficiency of the set. Experimental tests are carried out with a 10-kW liquid-cooled EV motor.

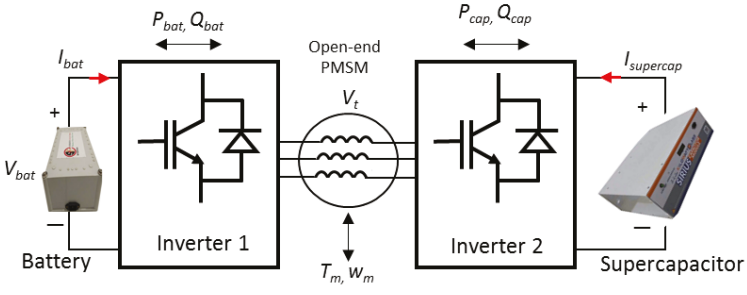

Figure 13. Single stage HESS topology adapted from [52] for its integration in EVs.

2.2.4. Wireless Charging of EVs

This section describes the existing papers in the bibliography that propose the use of SCs in wireless power transfer (WTP) systems for EV recharging. The selected papers have been those considered most relevant in the last three years. In general, the use of an ESS, in this case SCs, is justified to reduce the high fluctuations in power consumption and allow the power flow in the charger to be bidirectional, increasing its versatility. The papers that have been considered most relevant are described below.

Lu, W. and Geng, Y. [53,54] propose the inclusion of a HESS (SCs/lithium-ion batteries) in WTP systems. Lu, W. [53] proposed a methodology for sizing the HESS for recharging a 100kW electric bus during the time the vehicle is at one of the stops on the route. The proposed methodology is applied to a laboratory prototype in which the output power is analyzed based on the power transfer distance, reaching an efficiency of 89.6%. Additionally, Geng, Y. [54] focused on the control strategy from the point of view of the efficiency and cost of the system. The proposed strategy is based on the dynamic distribution of power between both ESS to get the WPT system to work at the optimum power point throughout the entire operating range. The strategy is validated in a 27.8 kW laboratory prototype. The efficiency achieved of the WPT System is 93% with a reduction of the required power of 27.6% compared with non optimal control charging.

Azad, A. [55] proposes the use of SCs as the only ESS to dampen power grid fluctuations that occur in dynamic and wireless power transfer (DWPT) in EVs charging. It seeks to ensure the stability of the network to which the charging point is connected. A complete analysis of the system is carried out through simulation including the design of the regulator and the modeling of the converter, achieving a reduction of grid transients by 75%. Ruddell, S. [56] presents a new topology of a WTP system, also with SCs, for the dynamic recharging of EVs. Experimental tests are carried out on a 3.8 kW prototype highlighting the advantages of the proposed topology over the conventional ones due to its reduced complexity and lower number of required switches. Finally, Wu, Y. [57] also proposes SCs as an energy buffer for dynamic loading in WPT systems. The ESS stores energy when the coupling is strong and discharges when the coupling is weak. To

optimize the dimensioning of the ESS (smallest capacitance) and the pole spacing between two adjacent transmission coils and capacitance of SCs (maximum distance) a genetic algorithm is used. The proposed method is verified by simulations to demonstrate that the WPT system allows for increasing the power density and reducing the construction cost compared with WPT systems without SCs.

3. Renewable Generation Applications

There are two main problems in the operation of generation plants based on renewable energy sources. The first is related to the fluctuating nature of the renewable resource and, as a consequence, the fluctuation of the electrical power generated. Power fluctuation injected into the grid can cause the variation of the point of common coupling (PPC) voltage and affect the system's stability [58]. The second problem is related to the operation and behavior of the renewable generation system when there are disturbances at the grid point where it is connected. In general, this section describes the existing papers in the bibliography that include SCs as a possible solution to the problems discussed. This section is divided into three main points depending on the renewable resource: wind, solar energy, and wave energy.

3.1. Wind Energy

Wind energy is the renewable energy used mostly in the world. The power of wind turbines today can reach up to 3 MW. However, the power generated is highly variable as is the wind speed [59]. A generic electrical scheme used in wind turbines is shown in Figure 14a. It consists of a variable speed wind turbine, an electric generator and a double power conversion stage with two power converters. There are different variants, but normally the converter connected between the generator and the intermediate continuous stage controls the turbine pitch and the generator torque (maximun power in function of the wind speed). On the other hand, the converter connected between the continuous stage and the power grid regulates the DC bus voltage and the reactive power exchanged with the power grid. Although the variation in the power generated can be reduced, it cannot be eliminated due to the dynamic response of the pitch control, which for fast speed variations is not capable of eliminating the fluctuation reflected in the output power. Another effect to take into account is the power fluctuation as a consequence of the tower shadow effect that causes a pulse in the torque and in turn a fluctuation in the output power.

Panhwar, I.H. [60] proposed a HESS (SC/lead-acid battery) to smooth the generated wind power. The wind energy converter consists of a wind turbine mimicking converter (wind turbine generator, rectifier and DC/DC converter), a SCs module, a charge controller and a battery as shown in Figure 14b. The first DC/DC converter charges the SCs and the charge controller control is designed to charge the battery from the energy stored in the SCs. The conclusion of the paper is that the proposed configuration allows smooth charging and extended discharging of the battery. On the other hand, the topology and the proposed mode of operation causes reduced stress on the generator and ancillary components of the circuit.

Liu, J. [61] also proposed a HESS (battery/SC) to smooth out the fluctuations of wind power. The low-frequency components of the generated power are absorbed by the battery and the high-frequency components by the SCs. That makes possible to reduce the charge/discharge times of the batteries and thus extend their useful life. A control strategy is proposed in which the SoC of the storage systems is taken into account to avoid deep discharges, overloads and allow them to work at the optimum efficiency points. Experimental results are presented in which a DC/AC converter controls the HESS to achieve bidirectional active and reactive power exchange. The proposed strategy is validated, demonstrating the optimal response of the HESS to improve power quality and enhance the stability of power systems.

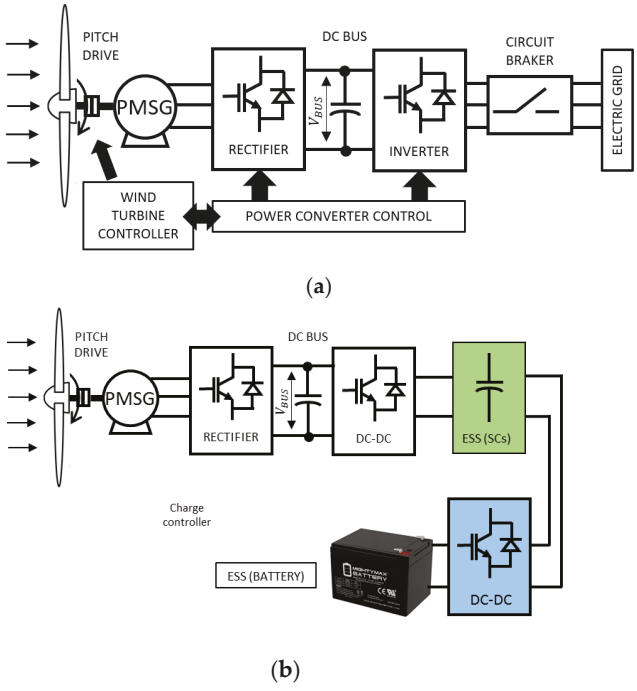

Figure 14. (**a**) Simplified electrical diagram of a variable speed wind turbine with full-scale power converter; (**b**) Wind Energy Conversion System with proposed HESS adapted from [60].

3.2. Solar PV Energy

Solar Photovoltaic (PV) panels are used to convert solar energy into electrical energy. The system that extracts energy from the sun is made up of a solar panel and a power conversion stage that connects the PV panel with the load or the electrical grid. The power conversion stage (power electronic converter) can be single stage (solar PV panel connected directly to the power inverter) or double stage (solar PV panel connected to a power converter with an intermediate direct voltage stage). Figure 15a shows a possible simplified electrical diagram of a double-stage solar PV plant connected to the electrical grid. The problems associated with solar energy are the irregular generation of power, maximum in periods of highest levels of solar irradiation or unregulated in partially cloudy days.

Cabrane, Z. [63] proposed SCs to compensate voltage drops during short periods of time in soalr PV systems connected to the grid. A coordinated control algorithm is described to compensate the effects caused by the variable solar irradiance in PCC and results obtained from simulations are shown. The algorithm applies a two-stage topology with the SCESSS connected to the intermediate DC stage through a DC/DC converter.

Ma, W. [64] proposed a HESS composed of batteries and SCs to smooth out the power fluctuations of solar PV systems. A multi-objective optimization model is established to split the required power between both ESS. The variables that are taken into account in the algorithm to decide how much power each one contributes are: power losses, lifetime aging, cost of batteries and the SoC of the SCs.

Cabrane, Z. [62] proposes an EMS for a HESS (battery/SCs) applied to PV energy in order to stabilize the DC voltage. Different topologies are compared (hybrid passive parallel, semi-active, and multiple converters) for the connection of SCs and batteries in photovoltaic energy systems. The advantages and disadvantages of each of them are listed. The control proposed by the authors applies to the configuration of multiple converters.

For the distribution of the necessary energy between batteries and SCs, a low pass filter is applied. Proportional integral (PI) controllers are used to regulate the DC bus voltage. The output of these regulators is the ESS charge/discharge current reference. Finally, results obtained from simulations are shown and the SoC of batteries is compared for different filter constants.

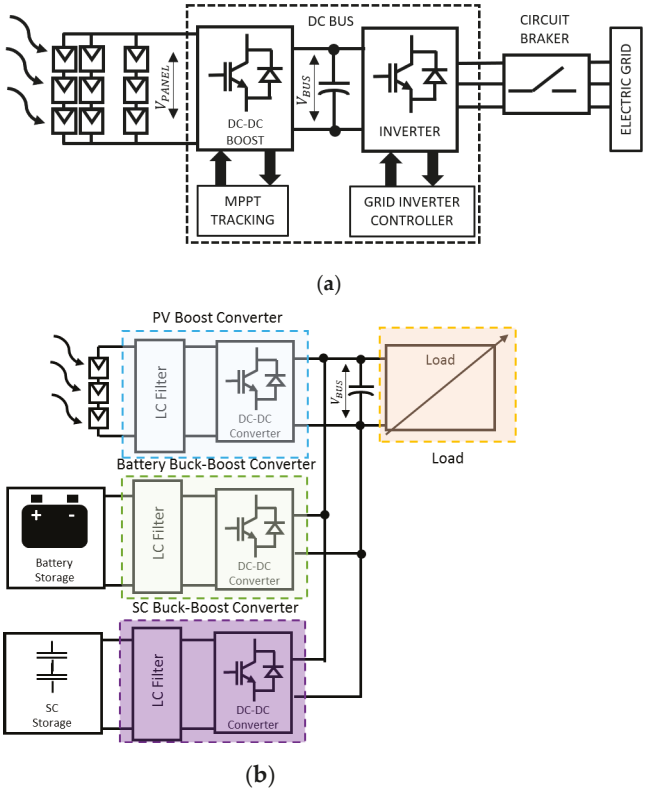

Figure 15. (**a**) Simplified electrical diagramam of grid connected double conversion PV system; (**b**) Structure of a multiple converters configuration with maximum power point tracking (MPPT) adapted from [62].

3.3. Wave Energy

Another source of renewable energy is the energy extracted from waves. Currently there are different systems capable of extracting energy from waves, commonly known as wave nergy converter (WEC). As in the case of other renewable sources, the energy is converted and delivered into the grid by means of a power take-off (PTO). The intermittency associated to the wave energy causes a continuous imbalance between the power generated and the power demanded leading to potential power quality problems, such as voltage and frequency deviations, specially in weak electric grids with high penetration of renewables. The period of the wave energy generated is in the range of 1–10 s, causing frequency variations and voltage distortion, such as flicker and harmonics at the grid connection point [65–68]. Figure 16 shows a general scheme of WEC solution.

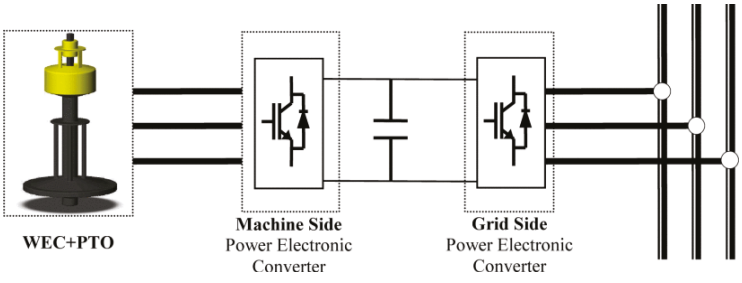

Figure 16. Simplified electrical diagramam of a WEC+PTO with linear generator connected to the grid.

Nunez Forestieri, J. [69] proposes an integrative sizing and EMS based on reinforcement learning (RL) for a HESS (SC/undersea energy storage) applied to grid connected operation of an offsore wave energy source. Different power profiles are used to verify the adaptability of the reinforcement learning-based energy management system (RLEMS). Real-time simulations confirm that the power and energy of the HESS is reduced when EMS is con-sidered in the sizing stage. The number of SC cells and the rate power of the undersea energy storage calculated with the proposed RL-based sizing allows to reduce the required capacity (power and energy) of the HESS to regulate power oscillations. Real-time simulation results are also presented that validate the viability of the proposed method (sizing and EMS) for applications in grid-connected renewable generation systems.

Rajapakse, G. [70] applies a predictive control model to smooth the power delivered to the network of an oscillating water column (OWC) wave energy conversion (WEC). Due to the nature of the resource, as well as the duration of the high-power pulses generated by the air turbine plus permanent magnet synchronous generator (PMSG) on which the study is based, SCs technology is considered the most suitable for this purpose. SCESS is connected to the intermediate DC stage of a back-to-back converter through a bidirectional DC/DC converter. Simulation results are shown in which the model predictive control (MPC) strategy is used, taking as one of the criteria that the SoC of the ESS remains within the limits established to extend the useful life. The THD of the output current obtained in simulations is lower than 5%, below the grid code requirement.

4. Power Grid Connection Applications

In this Section, the applications related to electrical systems, especially in electric grids and microgrids, are collected. Within them, the most published topics have been listed, describing in detail the use of SCs as well as the most relevant bibliography. Those studies are related to the limitations of the renewable energies sources, especially with their oscillatory nature, and the requirement of introducing flexibility in the electrical systems. This entails the integration of an ESS in order to increase the stability of the grid, absorbing or delivering energy, improving the voltage and frequency regulation of the electrical systems.

4.1. Grid Regulation: Voltage and Frequency Compensation

The increasing trend of integrating RES into the electric grids induces in the uncertainty in their operation and control. Their massive penetration into the power systems forces to increase the flexibility of the electric grid, due to the vulnerability of RES towards the unforeseeable variation of meteorological conditions. Related to this issue, ESS are a potential solution to support RES penetration, especially the hybridization of multiple ESS forming a hybrid energy storage system (HESS). This system has ability to fulfil all the requirements of a certain application. However, the limitation of the solution is its complex control strategy, since it plays a key role in optimizing the capabilities of each technology. Related to this scenario, the uses of SCs in the literature are focused on

improving the performance of the RES and the electric grids, collecting those studies in the following topics:

- Smoothing the power generated by renewable energy plants in order to mitigate the harmonics of the power injected to the grid.
- HESS control strategy improvement, especially controlling the power and energy flow between the renewable generation sources and the storage systems, with the aim of improving their capabilities against the frequency and voltage fluctuations.
- Introduce the flexibility required by the electric system to improve the voltage and frequency stability.
- Increasing the lifetime of batteries, using the SCs to suppress the high-frequency oscillations and the batteries to smooth the low-frequency power fluctuations.

Babu, T.S. [71] presents a review of the control strategies proposed in the literature for HESS. The paper classifies the control techniques into interconnection topologies, classical control strategies, advanced control techniques and real cases studies, being briefly discussed with their limitations, see Figure 17. The study collects the challenges faced when an implementation of HESS for standalone microgrid or a grid connected is made. This paper shows a guide to several control techniques implemented for HESS on grid connection applications.

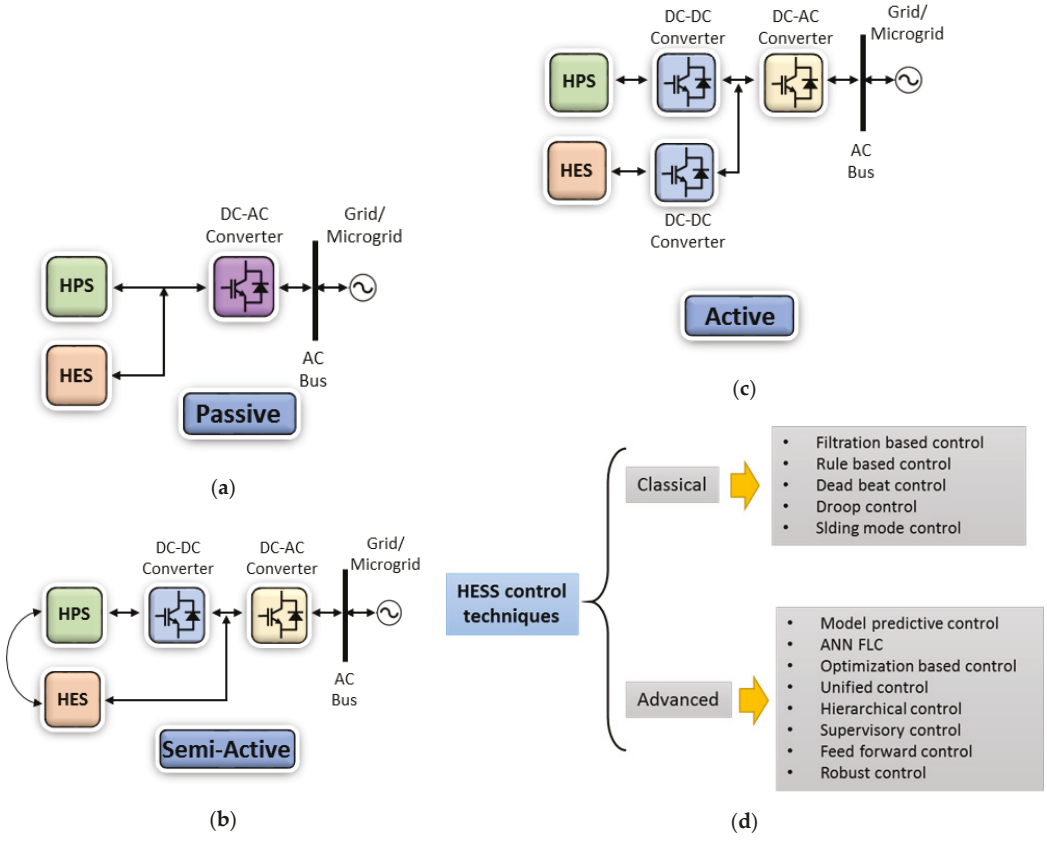

Figure 17. Main interconnection topologies for a HESS, formed by a high power storage (HPS) and a high energy storage (HES): (**a**) passive, (**b**) semi-active and (**c**) active adapted from [71]; (**d**) Classification of HESS control techniques adapted from [71].

The study [72] proposes a strategy to manage a HESS in renewable generation systems which currently require controlling bidirectional power flow. The device is composed by a direct connection of a battery and a SCs unit linked through a dc-dc converter. The proposed strategy includes a power control loop which distributes the power flow through each device, achieving an optimized performance, providing grid-frequency regulation and maximizing the lifespan of the batteries, reducing their number of cycles. As in other researches, the SCs perform the fast response, absorbing the high-frequency term and the batteries provide the long-term power fluctuations. The HESS are controlled using a droop control strategy that considers the converter characteristics, SC voltage levels, and power demand.

Manandhar, U. [73] presents a new energy management scheme proposed for a grid connected HESS, composed of the battery and the SC, under different operating scenarios. The objective of the proposed energy management scheme is to reduce the stress in the battery system, controlling the dynamic power sharing between the battery and grid. The study presents a faster DC link voltage regulation to a generation and load disturbances, a reduced rate cycle on the BESS based on its state of charge. Finally, the SCs are in charge of absorbing the high-frequency power fluctuations, reducing the stress on the BESS, and maintaining the SOC limits of energy storage within the safe operating region.

Akram, U. [74] presents an innovative design and operation framework for a BESS and a HESS used for frequency regulation in the electric grid. The proposed design considers the total system cost, the investment, replacement and maintenance cost, as well as the penalty imposed due to not supplying the required regulation service. Moreover, this study shows a comparison based on cost per unit between two scenarios: a HESS and a BESS used both for frequency regulation. The results show that the HESS is more economical.

Nguyen-Huu, T. [75] proposes a coordinated operating control of a HESS (SCs unit and a battery bank) that provides frequency regulation service. The control, based on a droop control with the state-of-charge (SoC) feedback, includes the power flow scheme between the ESSs considering the coverage of the frequency band for each device, as well as the SoC of the SCs and batteries. Moreover, this study provides a guideline for dimensioning the HESS based on based on the smoothing time constant, droop rate, and renewable energy source power rating. The benefits of this method are improving the lifespan of the battery, estimated using a real-time state-of-health (SOH) method based on the temperature, SOH, and throughput degradation.

Pham, V.L. [76] proposes a triple active bridge converter for what will be DC grid in the future. This system is an isolated bidirectional DC-DC converter, used in DC grids and integrated energy systems, composed by different types of renewable energies and storages, such as the photovoltaic and battery systems in grid connection applications or fuel cells and battery/SC in EVs. The advantages of the triple active bridge converter include multiple interfacing ports with isolation, achievable implementation of centralized controls, and improved flexibility of electric systems.

Georgious, R. [77] presents a control strategy for a buck-boost bidirectional converter used in a HESS for DC microgrids. The HESS connected to the DC bus is formed by a Li-ion battery bank and a SCs unit, combined to achieve the energy and power requirements. The control strategy shows a DC bus short-circuit fault-tolerant scheme which provides a protection to HESS and the converter during a short-circuit fault.

Arkhangelski, J. [78] presents a study of a hybrid renewable energy system (HRES), which includes a HESS formed by SCs and batteries, as a reliable source to connect to the grid. This grid connection imposes restrictions relating to the power delivered and its harmonic content. The aim of SCs is to absorb the high-frequency fluctuations of the power along with smoothing the power of the batteries. This study proposes the use of a low-pass second order filter, which splits the high-frequency component for the SCs and the low-frequency component for the battery system. This solution greatly increases the reliability and durability of the HRES. The results show that the proposed strategy improves the lifetime of the batteries (see Figure 18).

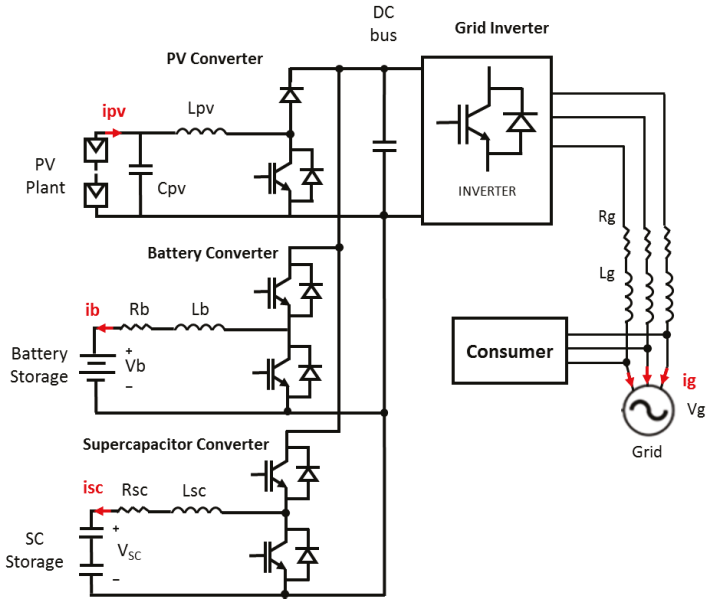

Figure 18. Scheme of model studied adapted from [78].

Malkawi, A.M.A. [79] shows the benefits of using a SCs-based ESS along with batteries in a HESS to mitigate the impact of high and fast current variations on the losses and lifespan of the batteries. The system is used in DC nanogrids and microgrids with distributed renewable sources, see Figure 19. This paper presents a HESS controlled as a single unit or each ESS module independently, since if the SC interface is controlled independently from the battery interface, the SCs are able to produce both high and short current pulses, reducing the voltage variations, improving the voltage regulation.

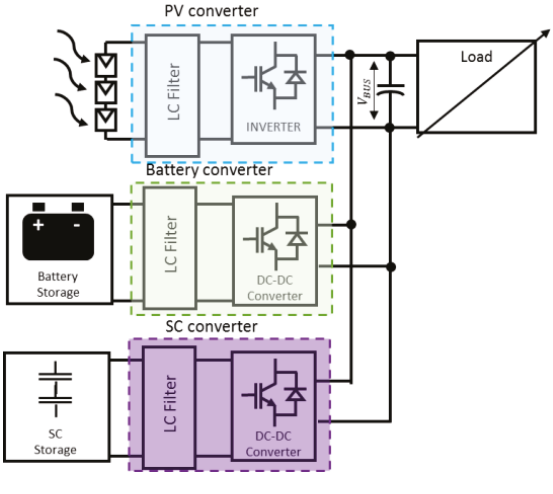

Figure 19. Scheme of the SC nanogrid adapted from [79].

Fang, J. [80] proposed a HESS comprising a battery system and SCs to manage the coordinated control of the ESSs as virtual synchronous generators (VSGs). The study uses

a control where the SCs attendant the fast-changes power modeled as an inertia and the batteries provide the remaining parts of the VSGs, compensating with slow dynamics and a droop control, the long-term power fluctuations.

4.2. Microgrids

The use of SCs in a microgrid is linked to a HESS, i.e., the use together with batteries. Within this approach, researchers are focused on improving the performance of a microgrid, analyzing the following topics:

- Lifespan improvement of the batteries, using the batteries to smooth the low-frequency power fluctuations in the long-term, while the SCs suppress the high-frequency oscillations.
- Capacity and dimensioning optimization of the HESS required to fulfill with the Microgrid restrictions.
- Consumption reduction by diesel groups or fuel cells.
- Control strategy improvement of the microgrid, especially in controlling the power and energy flow between the renewable generation sources and storage systems, with the aim of improving their behavior in transients and faults.
- Voltage and frequency regulation.

Khalid, M. [81] presents a comprehensive review of the research development of the hybrid storage topic over the last two decades. In this paper, each application-focused is thoroughly and independently investigated. The HESS-focused application comprises battery and SC modules, which have complementary characteristics improving their scope in various fields. The review collects research works about regulation of renewable energy sources; grid regulation, especially voltage and frequency compensation; energy storage enhancements, including lifespan improvement, and capacity reduction; and regenerative braking in electric vehicles.

Torkashvand, M. [82] compared a battery ESS and a hybrid energy storage system combining SCs with Li-ion batteries and lead-acid batteries for islanded microgrid applications. This study presents the economical effective of the hybridization, as well as the dimensioning calculation of the ESS to use in the energy management and frequency control of microgrids operating in islanded mode. The results show that the HESS with SC has considerable cost reduction.

Zhu, Y. [83] proposed a strategy based on droop control method for a HESS, comprised of a battery and a SC module, under unbalanced load and nonlinear load conditions. The battery system works in droop mode, providing energy and fundamental active power, i.e., the static performance. Meanwhile, the SC module works in compensation mode, providing the reactive power required, as well as transient changes in the power conditions. This strategy provides better system performance, especially in unbalanced and nonlinear load conditions. Moreover, microgrid stability and the battery lifespan are increased, as well as the power quality.

Oriti, G. [84] presents a novel power flow control system for a remote military microgrid with a HESS, combining batteries and SCs to increase the battery life redirecting the higher frequency current over the SCs. Moreover, this analysis considers several configurations for SCs and filter parameters to achieve the highest cash flow for the overall system, reducing the fuel consumption for the diesel generator. Finally, these results are linked with the sensitivity analysis of the economics of the military microgrid.

Oriti, G. [85] describes an economic analysis combined with a novel power flow control strategy for an energy management system (EMS) involving a HESS. This device is formed by a battery and a SCs module. The aim of the study is increasing the lifetime of the batteries, introducing a SCs module on the EMS to absorb the higher frequency currents, leaving the slow current changes for the batteries. Moreover, the lifetime effect over the economics of the system is analysed.

Akram, U. [86] describes a methodology for the joint capacity optimization of two renewable energy generation system (wind and solar PV) and a HESS, comprised of

batteries and SCs. The optimization problem of the sizing the HESS, solar and wind systems of the microgrid comprises the objective of minimising the cost, improving the reliability and reducing the greenhouse gases emissions. The results show that a microgrid with a HESS is more reliable and has lower greenhouse gases emissions and an economical benefit.

Ghosh, S.K. [87] proposes an energy management system (EMS)-based control scheme for DC microgrids with solar photovoltaic systems as the primary generation and energy storage systems, comprised by a battery ESS and SCs. The main feature of the study is to improve the dynamic performance of the microgrid during severe transients, especially in changes of the load demands and power oscillations of the PV units. Moreover, the EMS aims to increase the lifespan of the battery ESS and improve the voltage stability. The control strategy uses proportional-integral (PI) controllers to regulate the switching control actions based on the decision of the EMS achieving the desired objectives.

Kamel, A. [88] presented in the above studies, a control strategy based on a classic PI controller for an EMS and an isolated microgrid is described. It combines PV panels, FC as power sources and batteries and SCs as ESS. The system includes a maximum power point tracking (MPPT) to maximize the harvested energy from PV units. The aim is to optimize the energy management in the microgrid and the cost savings, using different control strategies, and reduce the hydrogen consumption. The PV array supplies the main power and the FC compensates the transient fluctuation of the solar source. Meanwhile, the battery and SC are used to solve the problems of slow response of the FC during the fast change of the load power and to remove the peak power from the system.

Wu, T. [89] introduces an improved hierarchical control strategy which considers the energy storage status of a distributed hybrid energy storage system, leading to the inconsistency of the remaining capacity of the energy storage system in the process of system operation, improving the stability of the microgrid.

Yu, M. [90] proposes a new control method for a HESS to improve the power quality and the fault ride-through capability of islanded forest microgrids. The system is composed by a wind turbine as source and batteries and SCs as energy storage. The method includes a basic control scheme represented by a mode-based sectional coordinated control, and an improved strategy for the HESS, using the batteries to smooth the low-frequency power fluctuations in the long-term, meanwhile the SCs suppress the high-frequency oscillations. A predictive control of the converters is adopted to reduce control delay and ensure the effectiveness of the energy storage power converters. Moreover, as an additional energy storage unit, a wind turbine is used, analysing its capacity of suppressing the huge power disturbance thanks to its large rotating kinetic energy, improving the fault-ride through capacity of the microgrid.

5. Conclusions

The present manuscript describes the most relevant papers that propose the integration of SCs in electric traction drives, renewable energy sources, and grid connection applications.

Regarding the publications related to electric traction drives, the largest number of them are related to the use of SCs in EVs. Regarding heavy-rail catenary supplied vehicles, most publications focus on the analysis of a DC catenary voltage (1.5–3 kV) against AC (25 kV), because DC voltage levels facilitate the integration of SCs without additional power electronics. SCs in heavy-rail vehicles are used to regenerative braking energy recovery and to stabilize the supply voltage. Energy savings with an ESS is around 12–20% and economic viability will depend on the incentives of each country for the energy returned to the grid. In relation to heavy-rail diesel-electric vehicles, there are hardly any publications because there are few vehicles of this type, due to thatsupply energy is based on fossil fuel sources. In light-rail rapid transit vehicles, SCs are proposed as one of the most appropriate technologies to function as a supplementary power source to the main one, absorbing high power peaks and recovering part of the braking energy. In this application there are also papers that highlight, in terms of cost, Li-ion capacitors (higher energy density) technology compared to EDLC technology.

Regarding electric drive for road vehicles, most of the papers suggest the use of SCs to work in a coordinated manner with batteries as an on-board hybrid storage system (HESS). In the case of public transportation catenary-supplied vehicles, the ultimate goal is to replace the catenary with a HESS with charging points in different sections of the road. Different battery technologies are compared, and strategies are proposed in order to split the required power between SCs and batteries. SCs/lithium-ion batteries combination is the one that offers the best results from a technical point of view. It is also contemplated to replace EDLC technology with Li-ion capacitors due to the latter having a higher energy density (reduction in weight and volume of the ESS), which is an important aspect in on-board systems. The papers related to HEVs study the feasibility of alternative powertrain architectures to the parallel configuration (generally considered the one that offers the best overall efficiency) to reduce fuel consumption when SCs are used as the only ESS. On the other hand, the papers related to EVs study the inclusion of SCs as part of the power system to extend the useful life of the batteries. In both cases (HEVs and EVs), an EMS is necessary to maximize the efficiency of the entire system. Controllers based on fuzzy logic and adaptive algorithm are considered essential tools to optimize the power distribution between SCs and batteries in the case of EVs.

Regarding the papers related to the inclusion of SCs in renewable energy systems (wind and PV solar), most of them consider a HESS (SCs/batteries). In the particular case of wave energy systems, SCs are considered as single and sufficient ESS due to the nature of the resource (high power and low energy peaks) and due to that main requirement is reduction of power oscillations. Solar PV and wind power systems need higher energy density ESS (e.g., batteries) in addition to SCs. The papers related to the inclusion of SCs in solar and wind applications are based on studying the optimal configuration for the connection of the HESS. Multi-objective optimization algorithms are also proposed for dimensioning of energy storage system and control strategies (e.g., low pass filter) to split the required power between both ESS. On the other hand, in wave energy applications the use of reinforcement learning-based energy management system is proposed in the SCESS sizing methodology to reduce and optimize the power and energy required. On the other hand, it is necessary to take into account the SoC of the ESS in the control strategy for the operation of the system.

Regarding the power grids applications, SCs are focused on improve their performance. The results of the studies show that the use of SCs together with batteries as a HESS improves the voltage and frequency stability of the electric grids, as well as the flexibility of the system allowing to introduce a higher number of renewable energy plants. Moreover, the SCs allow to use an advanced control strategy for the HESS, improving their efficiency and their capabilities against frequency and voltage fluctuations. Finally, the use of a HESS, composed by a high energy system and a SC based ESS, allows to dimension the system with high accuracy in order to fulfill the grid codes requirements and minimize its cost and maintenance.

In a nutshell, some generic conclusions of the use of SCs in the mentioned applications are:

- SCs can act as a buffer against large magnitudes and rapid fluctuations in power and for recycling the regenerative braking energy in electric traction vehicles.
- In order to ensure the suitability of SCs in certain applications, it is necessary to define the operating modes of the system, considering the load conditions and taking into account in the control strategy the SoC of ESS. It is also a very important a good dimensioning methodology of energy storage system taking into account the proposed EMS.
- In some cases, HESS can be the best option, but it is necessary to define a control strategy (optimization algorithm) to split the required power between both ESS. This optimization has to take into consideration the cost analysis, the aging of ESS, and weight and volume in the case of on-board systems.

- Remuneration policies for energy returned to the grid and grid code compliance will play a key role in integrating ESS into industrial applications.

Author Contributions: Conceptualization G.N. and J.T.; investigation, G.N., M.B., M.S.-H. and J.T.; writing—original draft preparation, G.N., J.T. and J.N.; writing—review and editing, M.S.-H., M.L. and M.B.; visualization, G.N., J.N. and M.S.-H.; complete review and adding contents, M.L. All authors have read and agreed to the published version of the manuscript.

Funding: This research received no external funding.

Institutional Review Board Statement: Not applicable.

Informed Consent Statement: Not applicable.

Data Availability Statement: Not applicable.

Conflicts of Interest: The authors declare no conflict of interest.

References

1. Faraji, S.; Ani, F.N. The development supercapacitor from activated carbon by electroless plating—A review. *Renew. Sustain. Energy Rev.* **2015**, *42*, 823–834. [CrossRef]
2. EASE. *European Energy Storage Technology Development Roadmap—2017*; EERA: Brussels, Belgium, 2017.
3. International Electrotechnical Commission. *Electrical Energy Storage—White Paper*; International Electrotechnical Commission: Geneva, Switzerland, 2011; pp. 1–78.
4. Beaudin, M.; Zareipour, H.; Schellenberg, A.; Rosehart, W. Energy Storage for Mitigating the Variability of Renewable Electricity Sources. *Energy Storage Smart Grids Plan. Oper. Renew. Var. Energy Resour.* **2014**, *14*, 1–33.
5. FutureBridge Green Ammonia for Energy Storage—FutureBridge. Available online: https://www.futurebridge.com/industry/perspectives-energy/green-ammonia-for-energy-storage/ (accessed on 2 May 2021).
6. Zhang, L.; Hu, X.; Wang, Z.; Sun, F.; Dorrell, D.G. A review of supercapacitor modeling, estimation, and applications: A control/management perspective. *Renew. Sustain. Energy Rev.* **2018**, *81*, 1868–1878. [CrossRef]
7. Navarro, G.; Nájera, J.; Torres, J.; Blanco, M.; Santos, M.; Lafoz, M. Development and experimental validation of a supercapacitor frequency domain model for industrial energy applications considering dynamic behaviour at high frequencies. *Energies* **2020**, *13*, 1156. [CrossRef]
8. Buller, S.; Karden, E.; Kok, D.; De Doncker, R.W. Modeling the dynamic behavior of supercapacitors using impedance spectroscopy. *IEEE Trans. Ind. Appl.* **2002**, *38*, 1622–1626. [CrossRef]
9. Rafik, F.; Gualous, H.; Gallay, R.; Crausaz, A.; Berthon, A. Frequency, thermal and voltage supercapacitor characterization and modeling. *J. Power Sources* **2007**, *165*, 928–934. [CrossRef]
10. Lajnef, W.; Vinassa, J.M.; Briat, O.; Azzopardi, S.; Woirgard, E. Characterization methods and modelling of ultracapacitors for use as peak power sources. *J. Power Sources* **2007**, *168*, 553–560. [CrossRef]
11. Zhang, L.; Wang, Z.; Hu, X.; Sun, F.; Dorrell, D.G. A comparative study of equivalent circuit models of ultracapacitors for electric vehicles. *J. Power Sources* **2015**, *274*, 899–906. [CrossRef]
12. Grbovic, P.J. *Ultra-Capacitors in Power Conversion Systems: Analysis, Modeling and Design in Theory and Practice*; John Wiley and Sons: Chichester, UK, 2014.
13. Berrueta, A.; San Martín, I.; Hernández, A.; Ursúa, A.; Sanchis, P. Electro-thermal modelling of a supercapacitor and experimental validation. *J. Power Sources* **2014**, *259*, 154–165. [CrossRef]
14. Ghodbane, O.; Ataherian, F.; Wu, N.L.; Favier, F. In situ crystallographic investigations of charge storage mechanisms in MnO 2-based electrochemical capacitors. *J. Power Sources* **2012**, *206*, 454–462. [CrossRef]
15. Torres, J.; Moreno-Torres, P.; Navarro, G.; Blanco, M.; Lafoz, M. Fast energy storage systems comparison in terms of energy efficiency for a specific application. *IEEE Access* **2018**, *6*, 40656–40672. [CrossRef]
16. Maxwell Technologies. *Application Note 1007239: Test Procedures for Capacitance, ESR, Leakage Current and Self-Discharge Characterizations of Ultracapacitors*; Maxwell Technologies: San Diego, CA, USA, 2015.
17. Tevi, T.; Takshi, A. Modeling and simulation study of the self-discharge in supercapacitors in presence of a blocking layer. *J. Power Sources* **2015**, *273*, 857–862. [CrossRef]
18. Navarro, G.; Torres, J.; Blanco, M.; González, M.; Lafoz, M. Test Bench Implementation to Calibrate Ageing and Voltage Unbalance in a Large Series Connection of Supercapacitors. In Proceedings of the 2018 20th European Conference on Power Electronics and Applications (EPE'18 ECCE Europe), Riga, Latvia, 17–21 September 2018; IEEE: New York, NY, USA, 2018.
19. Maxwell Technologies. Ultracapacitors, Supercapacitors, Microelectronics and High Voltage. Available online: https://www.maxwell.com/images/documents/K2Series_DS_1015370_5_20141104.pdf (accessed on 21 October 2017).
20. Skeleton Technologies GmbH. *Data Sheet Ultracapacitor SCA0500 to SCA3200 Weldable Cells & SCA0300 PCB-Mountable Cell*; Skeleton Technologies GmbH: Großröhrsdorf, Germany, 2020.
21. IOXUS. *Data Sheet Ultracapacitor*; IOXUS: Oneonta, NY, USA, 2019.

22. EATON. *XL60 Supercapacitors Cylindrical Cells*; EATON: Dublin, Ireland, 2017.
23. KAMCAP Power KAMCAP Supercapacitors. Available online: https://www.kamcappower.com/products/winding-type-2.7-volt-super-capacitors/ (accessed on 27 January 2021).
24. LS Mtron Ultracapacitor Products All View POPUP | LS Mtron. Available online: https://www.lsmtron.com/page/popup/productAllView.asp?divisionCode=D0700 (accessed on 27 January 2021).
25. VINATECH Supercapacitor |PRODUCTS| VINATECH. Available online: https://www.vinatech.com/spn/product/supercapacitor.php (accessed on 16 May 2021).
26. Berrueta, A.; Ursua, A.; Martin, I.S.; Eftekhari, A.; Sanchis, P. Supercapacitors: Electrical Characteristics, Modeling, Applications, and Future Trends. *IEEE Access* **2019**, *7*, 50869–50896. [CrossRef]
27. Rufer, A.; Hotellier, D.; Barrade, P. A supercapacitor-based energy storage substation for voltage compensation in weak transportation networks. *IEEE Trans. Power Deliv.* **2004**, *19*, 629–636. [CrossRef]
28. UIC. *High Speed Rail—Fast Track to Sustainable Mobility*; International Union of Railways: Paris, France, 2012.
29. Dutta, O.; Saleh, M.; Khodaparastan, M.; Mohamed, A. A dual-stage modeling and optimization framework for wayside energy storage in electric rail transit systems. *Energies* **2020**, *13*, 1614. [CrossRef]
30. Khodaparastan, M.; Mohamed, A. Flywheel vs. Supercapacitor as wayside energy storage for electric rail transit systems. *Inventions* **2019**, *4*, 62. [CrossRef]
31. Chen, J.; Hu, H.; Ge, Y.; Wang, K.; Huang, W.; He, Z. An energy storage system for recycling regenerative braking energy in high-speed railway. *IEEE Trans. Power Deliv.* **2021**, *36*, 320–330. [CrossRef]
32. Zhong, Z.; Yang, Z.; Fang, X.; Lin, F.; Tian, Z. Hierarchical Optimization of an On-Board Supercapacitor Energy Storage System Considering Train Electric Braking Characteristics and System Loss. *IEEE Trans. Veh. Technol.* **2020**, *69*, 2576–2587. [CrossRef]
33. Xu, C.; Chen, Z.; Cheng, K.W.E.; Wang, X.; Ho, H.F. A supercapacitor-based method to mitigate overvoltage and recycle the energy of pantograph arcing in the high speed railway. *Energies* **2019**, *12*, 1214. [CrossRef]
34. Diesel Locomotives | The Railway Technical Website | PRC Rail Consulting Ltd. Available online: http://www.railway-technical.com/trains/rolling-stock-index-l/diesel-locomotives/ (accessed on 19 April 2021).
35. Da Silva Moraes, C.G.; Brockveld Junior, S.L.; Heldwein, M.L.; Franca, A.S.; Vaccari, A.S.; Waltrich, G. Power Conversion Technologies for a Hybrid Energy Storage System in Diesel-Electric Locomotives. *IEEE Trans. Ind. Electron.* **2020**, 1. [CrossRef]
36. Tram modernisation in Alexandria/Egypt—Urban Transport Magazine. Available online: https://www.urban-transport-magazine.com/en/tram-modernisation-in-alexandria-egypt/ (accessed on 19 April 2021).
37. Zhang, X.; Zhang, H.; Li, H.; Jiao, Y.; Liao, H.; Peng, J.; Huang, Z. Cooperative Charging of Supercapacitor Trams with Current Overshoot Suppression. *IEEE Trans. Ind. Appl.* **2020**, *56*, 4155–4165.
38. Ciccarelli, F.; Del Pizzo, A.; Iannuzzi, D. Improvement of energy efficiency in light railway vehicles based on power management control of wayside lithium-ion capacitor storage. *IEEE Trans. Power Electron.* **2014**, *29*, 275–286. [CrossRef]
39. Zhu, F.; Yang, Z.; Xia, H.; Lin, F. Hierarchical Control and Full-Range Dynamic Performance Optimization of the Supercapacitor Energy Storage System in Urban Railway. *IEEE Trans. Ind. Electron.* **2018**, *65*, 6646–6656. [CrossRef]
40. Lafoz, M.; Navarro, G.; Torres, J.; Santiago, Á.; Nájera, J.; Santos-Herran, M.; Blanco, M. Power Supply Solution for Ultrahigh Speed Hyperloop Trains. *Smart Cities* **2020**, *3*, 642–656. [CrossRef]
41. First Solaris Trolleybuses Delivered to Norway In Advance of December Launch. Available online: https://www.focustransport.org/2020/10/ (accessed on 19 April 2021).
42. Cignini, F.; Genovese, A.; Ortenzi, F.; Alessandrini, A.; Berzi, L.; Pugi, L.; Barbieri, R. Experimental data comparison of an electric minibus equipped with different energy storage systems. *Batteries* **2020**, *6*, 26. [CrossRef]
43. Soltani, M.; Ronsmans, J.; Kakihara, S.; Jaguemont, J.; Van den Bossche, P.; van Mierlo, J.; Omar, N. Hybrid battery/lithium-ion capacitor energy storage system for a pure electric bus for an urban transportation application. *Appl. Sci.* **2018**, *8*, 1176. [CrossRef]
44. Tran, D.D.; Vafaeipour, M.; El Baghdadi, M.; Barrero, R.; Van Mierlo, J.; Hegazy, O. Thorough state-of-the-art analysis of electric and hybrid vehicle powertrains: Topologies and integrated energy management strategies. *Renew. Sustain. Energy Rev.* **2020**, *119*, 109596. [CrossRef]
45. Passalacqua, M.; Lanzarotto, D.; Repetto, M.; Vaccaro, L.; Bonfiglio, A.; Marchesoni, M. Fuel Economy and EMS for a Series Hybrid Vehicle Based on Supercapacitor Storage. *IEEE Trans. Power Electron.* **2019**, *34*, 9966–9977. [CrossRef]
46. Passalacqua, M.; Carpita, M.; Gavin, S.; Marchesoni, M.; Repetto, M.; Vaccaro, L.; Wasterlain, S. Supercapacitor storage sizing analysis for a series hybrid vehicle. *Energies* **2019**, *12*, 1759. [CrossRef]
47. Blockchain-Based Electric Vehicle Receives $1M from Canadian Government—European Blockchain Convention. Available online: https://eblockchainconvention.com/blockchain-based-electric-vehicle-receives-1m-from-canadian-government/ (accessed on 19 April 2021).
48. Hussain, S.; Ali, M.U.; Park, G.-S.; Nengroo, S.H.; Khan, M.A.; Kim, H.-J. A Real-Time Bi-Adaptive Controller-Based Energy Management System for Battery–Supercapacitor Hybrid Electric Vehicles. *Energies* **2019**, *12*, 4662. [CrossRef]
49. Sadeq, T.; Wai, C.K.; Morris, E.; Tarboosh, Q.A.; Aydogdu, O. Optimal Control Strategy to Maximize the Performance of Hybrid Energy Storage System for Electric Vehicle Considering Topography Information. *IEEE Access* **2020**, *8*, 216994–217007. [CrossRef]

50. Shchur, I.; Biletskyi, Y. Interconnection and damping assignment passivity-based control of semi-active and active battery/supercapacitor hybrid energy storage systems for stand-alone photovoltaic installations. In Proceedings of the 14th International Conference on Advanced Trends in Radioelectronics, Telecommunications and Computer Engineering (TCSET), Slavske, Ukraine, 20–24 February 2018; Institute of Electrical and Electronics Engineers Inc.: Piscataway, NJ, USA, 2018; Volume 2018, pp. 324–329.
51. Yu, H.; Castelli-Dezza, F.; Cheli, F.; Tang, X.; Hu, X.; Lin, X. Dimensioning and Power Management of Hybrid Energy Storage Systems for Electric Vehicles with Multiple Optimization Criteria. *IEEE Trans. Power Electron.* **2021**, *36*, 5545–5556. [CrossRef]
52. Shi, R.; Semsar, S.; Lehn, P.W. Single-Stage Hybrid Energy Storage Integration in Electric Vehicles Using Vector Controlled Power Sharing. *IEEE Trans. Ind. Electron.* **2020**. [CrossRef]
53. Lu, W.; Zhao, J.; Dong, Y.; Wang, B.; Shen, J. 100 kW electric bus wireless charging system with calculating method for hybrid energy storage capacity. In Proceedings of the 8th International Conference on Power Electronics Systems and Applications: Future Mobility and Future Power Transfer (PESA), Hong Kong, China, 7–10 December 2020; Institute of Electrical and Electronics Engineers Inc.: Piscataway, NJ, USA, 2020.
54. Geng, Y.; Yang, Z.; Lin, F. Design and Control for Catenary Charged Light Rail Vehicle Based on Wireless Power Transfer and Hybrid Energy Storage System. *IEEE Trans. Power Electron.* **2020**, *35*, 7894–7903. [CrossRef]
55. Azad, A.; Pantic, Z. A Supercapacitor-based Converter Topology for Grid-Side Power Management in Dynamic Wireless Charging Systems. In Proceedings of the ITEC 2019—2019 IEEE Transportation Electrification Conference and Expo; Institute of Electrical and Electronics Engineers Inc.: Piscataway, NJ, USA, 2019.
56. Ruddell, S.; Madawala, U.K.; Thrimawithana, D.J. A Wireless EV Charging Topology with Integrated Energy Storage. *IEEE Trans. Power Electron.* **2020**, *35*, 8965–8972. [CrossRef]
57. Wu, Y.; Zhang, H.; Liu, M.; Kang, N.; Ma, C. Optimization of super capacitor buffered dynamic wireless power transfer system. In Proceedings of the 2020 IEEE PELS Workshop on Emerging Technologies: Wireless Power Transfer, WoW 2020, Seoul, Korea, 15–19 November 2020; Institute of Electrical and Electronics Engineers Inc.: Piscataway, NJ, USA, 2020; pp. 364–369.
58. Baggini, A. Handbook of Power Quality. Available online: https://www.wiley.com/en-us/Handbook+of+Power+Quality-p-9780470754238 (accessed on 19 April 2021).
59. Ackermann, T. (Ed.) *Wind Power in Power Systems*; John Wiley and Sons, Ltd.: Chichester, UK, 2012.
60. Panhwar, I.H.; Ahmed, K.; Seyedmahmoudian, M.; Stojcevski, A.; Horan, B.; Mekhilef, S.; Aslam, A.; Asghar, M. Mitigating Power Fluctuations for Energy Storage in Wind Energy Conversion System Using Supercapacitors. *IEEE Access* **2020**, *8*, 189747–189760. [CrossRef]
61. Liu, J.; Zhang, L. Strategy design of hybrid energy storage system for smoothing wind power fluctuations. *Energies* **2016**, *9*, 991. [CrossRef]
62. Cabrane, Z.; Kim, J.; Yoo, K.; Ouassaid, M. HESS-based photovoltaic/batteries/supercapacitors: Energy management strategy and DC bus voltage stabilization. *Sol. Energy* **2021**, *216*, 551–563. [CrossRef]
63. Palla, N.; Seshadri Sravan Kumar, V. Coordinated Control of PV-Ultracapacitor System for Enhanced Operation under Variable Solar Irradiance and Short-Term Voltage Dips. *IEEE Access* **2020**, *8*, 211809–211819. [CrossRef]
64. Ma, W.; Wang, W.; Wu, X.; Hu, R.; Tang, F.; Zhang, W.; Han, X.; Ding, L. Optimal Allocation of Hybrid Energy Storage Systems for Smoothing Photovoltaic Power Fluctuations Considering the Active Power Curtailment of Photovoltaic. *IEEE Access* **2019**, *7*, 74787–74799. [CrossRef]
65. Lafoz, M.; Blanco, M.; Ramírez, D. Grid connection for wave power farms. In *Proceedings of the 14th European Conference on Power Electronics and Applications, Birmingham, UK, 30 August–1 September 2011*; IEEE: Birmingham, UK, 2011; pp. 1–10.
66. Blavette, A.; O'Sullivan, D.L.; Alcorn, R.; Lewis, T.W.; Egan, M.G. Impact of a medium-size wave farm on grids of different strength levels. *IEEE Trans. Power Syst.* **2014**, *29*, 917–923. [CrossRef]
67. Eltigani, D.; Masri, S. Challenges of integrating renewable energy sources to smart grids: A review. *Renew. Sustain. Energy Rev.* **2015**, *52*, 770–780. [CrossRef]
68. MaRINET2. MaRINET2 Wave Facilities. Available online: http://www.marinet2.eu/facilities/wave/ (accessed on 19 April 2021).
69. Nunez Forestieri, J.; Farasat, M. Integrative sizing/real-Time energy management of a hybrid supercapacitor/undersea energy storage system for grid integration of wave energy conversion systems. *IEEE J. Emerg. Sel. Top. Power Electron.* **2020**, *8*, 3798–3810. [CrossRef]
70. Rajapakse, G.; Jayasinghe, S.; Fleming, A.; Negnevitsky, M. Grid integration and power smoothing of an oscillatingwater column wave energy converter. *Energies* **2018**, *11*, 1871. [CrossRef]
71. Babu, T.S.; Vasudevan, K.R.; Ramachandaramurthy, V.K.; Sani, S.B.; Chemud, S.; Lajim, R.M. A Comprehensive Review of Hybrid Energy Storage Systems: Converter Topologies, Control Strategies and Future Prospects. *IEEE Access* **2020**, *8*, 148702–148721. [CrossRef]
72. Rocabert, J.; Capo-Misut, R.; Munoz-Aguilar, R.S.; Candela, J.I.; Rodriguez, P. Control of Energy Storage System Integrating Electrochemical Batteries and Supercapacitors for Grid-Connected Applications. *IEEE Trans. Ind. Appl.* **2019**, *55*, 1853–1862. [CrossRef]
73. Manandhar, U.; Ukil, A.; Gooi, H.B.; Tummuru, N.R.; Kollimalla, S.K.; Wang, B.; Chaudhari, K. Energy management and control for grid connected hybrid energy storage system under different operating modes. *IEEE Trans. Smart Grid* **2019**, *10*, 1626–1636. [CrossRef]

74. Akram, U.; Khalid, M. A Coordinated Frequency Regulation Framework Based on Hybrid Battery-Ultracapacitor Energy Storage Technologies. *IEEE Access* **2017**, *6*, 7310–7320. [CrossRef]
75. Nguyen-Huu, T.-A.; Nguyen, V.T.; Hur, K.; Shim, J.W. Coordinated Control of a Hybrid Energy Storage System for Improving the Capability of Frequency Regulation and State-of-Charge Management. *Energies* **2020**, *13*, 6304. [CrossRef]
76. Pham, V.L.; Wada, K. Applications of triple active bridge converter for future grid and integrated energy systems. *Energies* **2020**, *13*, 1577. [CrossRef]
77. Georgious, R.; Garcia, J.; Sumner, M.; Saeed, S.; Garcia, P. Fault Ride-through power electronic topologies for hybrid energy storage systems. *Energies* **2020**, *13*, 257. [CrossRef]
78. Arkhangelski, J.; Roncero-Sánchez, P.; Abdou-Tankari, M.; Vázquez, J.; Lefebvre, G. Control and restrictions of a hybrid renewable energy system connected to the grid: A battery and supercapacitor storage case. *Energies* **2019**, *12*, 2776. [CrossRef]
79. Malkawi, A.M.A.; Lopes, L.A.C. Improved dynamic voltage regulation in a droop controlled DC nanogrid employing independently controlled battery and supercapacitor units. *Appl. Sci.* **2018**, *8*, 1525. [CrossRef]
80. Fang, J.; Tang, Y.; Li, H.; Li, X. A Battery/Ultracapacitor Hybrid Energy Storage System for Implementing the Power Management of Virtual Synchronous Generators. *IEEE Trans. Power Electron.* **2018**, *33*, 2820–2824. [CrossRef]
81. Khalid, M. A review on the selected applications of battery-supercapacitor hybrid energy storage systems for microgrids. *Energies* **2019**, *12*, 4559. [CrossRef]
82. Torkashvand, M.; Khodadadi, A.; Sanjareh, M.B.; Nazary, M.H. A Life Cycle-Cost Analysis of Li-ion and Lead-Acid BESSs and Their Actively Hybridized ESSs with Supercapacitors for Islanded Microgrid Applications. *IEEE Access* **2020**, *8*, 153215–153225. [CrossRef]
83. Zhu, Y.; Fan, Q.; Xiong, L.; Zhang, G.; Qian, X. Coordination control strategy for battery-ultracapacitor hybrid energy storage system in microgrids with unbalanced and nonlinear loads. *IEEE Access* **2019**, *7*, 111577–111591. [CrossRef]
84. Oriti, G.; Anglani, N.; Julian, A.L. Hybrid Energy Storage Control in a Remote Military Microgrid with Improved Supercapacitor Utilization and Sensitivity Analysis. In *IEEE Transactions on Industry Applications*; Institute of Electrical and Electronics Engineers Inc.: Piscataway, NJ, USA, 2019; Volume 55, pp. 5099–5108.
85. Oriti, G.; Julian, A.L.; Anglani, N.; Hernandez, G.D. Novel Economic Analysis to Design the Energy Storage Control System of a Remote Islanded Microgrid. *IEEE Trans. Ind. Appl.* **2018**, *54*, 6332–6342. [CrossRef]
86. Akram, U.; Khalid, M.; Shafiq, S. An innovative hybrid wind-solar and battery-supercapacitor microgrid system—development and optimization. *IEEE Access* **2017**, *5*, 25897–25912. [CrossRef]
87. Ghosh, S.K.; Roy, T.K.; Pramanik, M.A.H.; Sarkar, A.K.; Mahmud, M.A. An energy management system-based control strategy for DC microgrids with dual energy storage systems. *Energies* **2020**, *13*, 2992. [CrossRef]
88. Kamel, A.; Rezk, H.; Shehata, N.; Thomas, J. Energy Management of a DC Microgrid Composed of Photovoltaic/Fuel Cell/Battery/Supercapacitor Systems. *Batteries* **2019**, *5*, 63. [CrossRef]
89. Wu, T.; Yu, W.; Wang, L.; Guo, L.; Tang, Z. Power distribution strategy of microgrid hybrid energy storage system based on improved hierarchical control. *Energies* **2019**, *12*, 3498. [CrossRef]
90. Yu, M.; Zhang, J.; Liu, H. Improved control of forest microgrids with hybrid complementary energy storage. *Appl. Sci.* **2019**, *9*, 2523. [CrossRef]

energies

MDPI

Article

Lactic Acid-Based Solvents for Sustainable EDLC Electrolytes

Massimo Melchiorre [1,2], Roberto Esposito [2], Martino Di Serio [2], Giancarlo Abbate [1], Alessandro Lampasi [3], Andrea Balducci [4] and Francesco Ruffo [2,*]

[1] CapTop S.r.l., 80023 Napoli, Italy; massimo.melchiorre@captop.it (M.M.); abbate@captop.it (G.A.)
[2] Department of Chemical Science, University of Naples Federico II, 80138 Naples, Italy; roberto.esposito@unina.it (R.E.); diserio@unina.it (M.D.S.)
[3] National Agency for New Technologies, Energy and Sustainable Economic Development (ENEA), 00044 Frascati, Italy; alessandro.lampasi@enea.it
[4] Institute of Technical Chemistry and Environmental Chemistry, Center for Energy and Environmental Chemistry (CEEC Jena), Friedrich Schiller University Jena, 07743 Jena, Germany; andrea.balducci@uni-jena.de
* Correspondence: ruffo@unina.it

Abstract: The most relevant electrolytes used in commercial electrical double layer capacitors (EDLCs) are based on non-aqueous solvents as acetonitrile (ACN) and propylene carbonate (PC). However, these solvents are synthesized from non-renewable fossil feedstocks, making it desirable to develop more sustainable alternatives. To address this issue, in this work lactic acid was used to synthesize a panel of substances with small structural variation. The investigated products belong to the chemical family of ketals, and among them the 5-methyl-1,3-dioxolan-4-one (LA-H,H) was found to be the most suitable to prepare electrolytic solutions. Therefore, LA-H,H was combined with triethylmethylammonium tetrafluoroborate ($TEMABF_4$), and analyzed in symmetrical EDLC. This electrolyte was thoroughly characterized by cyclic voltammetry, galvanostatic cycles and electrochemical impedance spectroscopy (EIS), disclosing competitive performances compared to PC-based electrolyte. The EDLC with LA-H,H/$TEMABF_4$ displayed a specific energy and power of 13.4 $Whkg^{-1}$ and 22.5 $kWkg^{-1}$ respectively, with an optimal cycling stability over 5000 cycles at different current densities.

Keywords: EDLCs; sustainable solvents; non-aqueous electrolytes; 5-methyl-1,3-dioxolan-4-one

Citation: Melchiorre, M.; Esposito, R.; Di Serio, M.; Abbate, G.; Lampasi, A.; Balducci, A.; Ruffo, F. Lactic Acid-Based Solvents for Sustainable EDLC Electrolytes. *Energies* **2021**, *14*, 4250. https://doi.org/10.3390/en14144250

Academic Editor: Haolin Tang

Received: 22 June 2021
Accepted: 11 July 2021
Published: 14 July 2021

1. Introduction

The production of sustainable energy is one of the most relevant issues of current times. The increase in polluting emissions and global warming have emphasized the impropriety of fossil fuels, favoring the development of methods to produce clean energy from renewable sources. However, as most of them have a discontinuous nature, storage and management systems are required to secure the generated energy. In this context, the design of efficient and sustainable energy storage devices and systems is therefore a key point to adequately support the energy transition from fossil to renewable sources.

In the field of energy storage, supercapacitors (SCs), and in particular the electrochemical double layer capacitors (EDLCs), have become of great interest thanks to their complementary performance compared to batteries, such as lithium-ion batteries (LIBs). Indeed, EDLCs generally have moderate energy density (generally < 10 $Whkg^{-1}$) but provide high power (up to 10 $kWkg^{-1}$) thanks to a fast charge/discharge mechanism, and they also have a significantly high number of life cycles (>>100,000 cycles).

The properties of an EDLC are defined by its electrostatic energy storage mechanism and by its components. These devices consist of two electrodes with a high surface area electrically isolated by a porous dielectric separator. The electrodes include a metal collector (usually aluminum), on which a layer of high porosity active material (usually activated carbon and carbon black) is cast. The electrodes and the dielectric separator are

soaked with a conductive medium, typically an electrolyte consisting of a solvent and a conducting salt [1].

In EDLC devices, the electrolyte is a key component, as the charges are accumulated at the electrode/electrolyte interface (EEI) and the specific energy (E_{sp}) and the specific power (P_{sp}) can be expressed as [2]:

$$E_{sp} = \frac{C_{sp}V^2}{2} \quad (1)$$

$$P_{sp} = \frac{V^2}{4m_{cell}R_{cell}} \quad (2)$$

In the equations, C_{sp} is the specific capacitance, V is the applied potential, m_{cell} is the mass of electrode active materials, and R_{cell} is the internal resistance of the device [3].

The capacitance is mostly determined by the properties of the electrode (available surface, pore distribution, accessibility of the pores) and by the EEI, while the applicable potential and the internal resistance of the device strongly depend on the nature and characteristics of the electrolyte. Hence, aprotic polar organic solvents are often favored over water, as this is subject to redox activity for potentials between 1.0 V and 1.2 V.

A class of water-containing electrolytes capable of overcoming this limit is that of water-in-salt electrolytes (WiS) [4]. In this type of electrolyte, the water molecules strongly interact with the ions present at very high concentrations, thus increasing the electrochemical stability compared to the classic salt in-water (SiW) solutions [5]. However, WiS with lithium bis(trifluoromethane)sulfonimide (LiTFSI) presents problems related to the internal resistance of the device due to modest conductivity (21 m LiTFSI 8.2 $mScm^{-1}$) and high viscosity (21 m LiTFSI 30.2 mm^2s^{-1}) [6]. Furthermore, a rational design of the active material porosity is essential to achieve high performance [7]. In addition, the development of new technologies should be oriented towards lithium-free devices, given the progressive saturation of its production sites [8], and with cheap and user-friendly electrolytes [9]. To extend the applicable potential window using water as an electrolytic component, Hughson et al. recently reported in a communication the use of water–oil microemulsions in the presence of surfactants at a potential of 2.7 V [10]. However, the high internal resistance recorded (26 Ohm) compromises its concrete application.

Cell voltages of 2.7–3.0 V can be regularly achieved with non-aqueous electrolyte. Moreover, organic solvents can be used in wider temperature ranges than aqueous electrolytes. On the other hand, the electrical conductivity of non-aqueous electrolytes is often significantly lower than that of water, and this contributes to increasing their internal resistance. For these reasons, commercial EDLCs supercapacitors contain acetonitrile (ACN) or propylene carbonate (PC) based electrolytes, but these solvents have limitations for high-voltage applications and risks related to their handling, and are both obtained from fossil feedstock. The need to address these issues represents the driving-force that pushes the scientific community towards the search for new electrolytes.

For a long time, huge efforts have been made to increase the EDLCs performances [11–13], and only more recently to also improve safety and ecotoxicological profiles of the used electrolytes. Previous results and new perspectives towards new electrolytes have been described in recent reviews [14–17].

Among the non-aqueous electrolytes, a category of wide interest consists in aprotic ionic liquids (AILs) [18], and more recently also protic liquids (PILs) [19]. These electrolytes are highly attractive for electrochemical applications due to their stability and safety as non-flammable substances [20,21]. However, their efficiency as electrolytes is strongly affected by the electrodes porosity, resulting in a low energy efficiency in combination with electrodes with a high content of micropores [22]. Furthermore, the high cost of these electrolytes hampered their commercial applications in solvent-free conditions.

A similar approach to that of WiS electrolytes was reported by Stettner et al. [23], using electrolytes based on protic ionic liquids (PILs) with additions of water (1–3.8%).

Despite a considerable improvement of transport properties, the operating voltage of EDLC containing these electrolytes is lower than that of AIL-based EDLCs (from 1.8 V to 2.2 V).

Recent advances regarding electrolytes based on organic solvents concern the study of nitriles, in linear aliphatic chains (glutaronitrile GTN, adiponitrile ADN), branched chains (2-methylglutaronitrile 2MGN) and as functional groups present in methyl esters (3-cyano-propionic acid methyl ester CPAME) [24]. These solvents reach very high operational potentials (3.5 V), making high-voltage applications possibly able to address the need to increase the EDLC's specific energy. However, these substances have high acute toxicity (some even fatal in case of inhalation) and health hazards, and therefore they do not seem suitable for common commercial applications.

To increase the performance of the classic ACN-based electrolytic solutions, binary mixtures with other organic solvents have recently been studied. When mixed with dibutyl carbonate (10%−33% v), a net increase in performance at low temperatures (up to −60 °C) was reported [25], while in combination with ethylisopropylsulfone (75–50%) operational potentials of 3.0 V were reached [26].

Recently investigated nitrile-free organic solvents are 1,2-butylene carbonate (BC) [27], tetramethoxyglyoxal (TMG) and tetraethoxyglyoxal (TEG) [28]. A combination of BC with $Pyr_{14}BF_4$ provided a potential window of 3.1 V, while modest results were achieved with TMG and TEG due to their relatively high viscosity.

From the point of view of the sustainability of EDLCs, many efforts have been made to obtain active carbonaceous materials and binders from biomass [29], but this approach is still lacking for the development of non-aqueous electrolytes. In fact, recent papers do not highlight the origin of the investigated electrolytes despite the design of innovative aprotic polar solvents from renewable sources is a topic of great and current interest [30].

Our research group has long been involved in the study of the catalytic conversion of biomass [31–34] and in the valorizations of bio-based molecules derived from renewable feedstock [35–37] to produce innovative materials that beneficially replace the traditional ones.

This approach has recently been oriented towards the design of innovative solvents, and, in this manuscript, we report the synthesis of different lactic acid ketals and the investigation on their properties as solvents for electrolytes in symmetrical EDLCs. Lactic acid is a bio-based chemical platform industrially prepared through bacterial fermentation of carbohydrates [38] and is widely used to produce biodegradable polymers or as starting feedstock for green routes to bulk chemicals productions [39].

The synthesized solvents have the common structure of 2,2-R,R′-5-methyl-1,3-dioxolan-4-one (DOLOs), which is a chemical platform that allows to selectively evaluate the effect of small structural variations on the electrolyte properties (Figure 1).

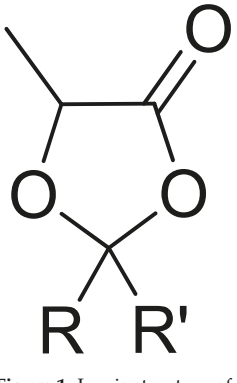

Figure 1. Lewis structure of 2,2-R,R′-5-methyl-1,3-dioxolan-4-one.

These compounds are already used as precursors of sustainable polymers [40,41], but to the best of our knowledge lactic acid derived DOLOs have never been used as solvents in the field of energy storage. The solvent 5-methyl-1,3-dioxolan-4-one displayed performances competitive (C_{sp} 14.2 Fg^{-1}, E_{sp} 13.4 $Whkg^{-1}$ and P_{sp} 22.5 $kWkg^{-1}$) with commercial solvents, such as propylene carbonate, and therefore it represents an example of what can be defined as a "Non-Aqueous Sustainable Electrolyte" (NASE).

2. Materials and Methods

2.1. Materials

All synthesized compounds have been characterized through Nuclear Magnetic Resonance (NMR) with a Bruker Avance Ultrashield 400, operating at proton frequency of 400 MHz (Figures S1–S4). The following abbreviations were used for describing NMR multiplicities: s, singlet; d, doublet; t, triplet; q, quartet; hept, heptet; m, multiplet; dd, doublet of doublets; dt, doublet of triplets; td, triplet of doublets; tt, triplet of triplets.

All electrolytes were prepared and handled in a dry atmosphere using Schlenk line and the appropriate Schlenk line glassware. Lithium tetrafluoroborate ($LiBF_4$) was purchased from Merck KGaA (Darmstadt, Germany). All coin cells were assembled in a dry room. The residual water content in the electrolytes was evaluated through Karl–Fischer titration with a Metrohm 831KF Coulometer.

All electrochemical measurements were recorded using a Gamry Instruments Reference 3000™ potentiostat/galvanostat/FRA, controlled via Gamry Instrument Framework™ software. Data analyses were performed using Gamry Echem Analyst™ software.

The EDLCs electrodes used in this investigation are AC-based, coated on Al-foil, and have been provided as a courtesy by Captop s.r.l. The average mass loading of the electrode was 6 $mgcm^{-2}$, and the thickness of the active material was 55 μm.

2.2. DOLOs and $TEMABF_4$ Synthesis

DL-lactic acid (purity 90%), paraformaldehyde (reagent grade), paraldehyde (purity 98%), acetone (reagent grade), petroleum ether bp 40–60 °C, *p*-toluensulfonic acid monohydrated (*p*TsOH, purity 98%), Amberlite® IR-120 (H^+ form) and other solvents and chemicals used for the synthesis of DOLOs were purchased from Merck KGaA (Darmstadt, Germany).

Triethylmethylammonium chloride (purity $\leq$ 99%), ammonium tetrafluoroborate (purity $\leq$ 97%) and dry acetonitrile to prepare triethylmethylammonium tetrafluoroborate ($TEMABF_4$) were purchased from Merck KGaA (Darmstadt, Germany).

2.2.1. Synthesis of 2,2,5-trimethyl-1,3-dioxolan-4-one (LA-Me,Me)

For the synthesis of LA-Me,Me, we followed the procedure reported by Miyagawa et al. [42] with the following modifications.

We used 45.0 g of DL-lactic acid (0.500 mol), 300 mL of a solution 1:1 v/v acetone (2.00 mol) and petroleum ether (bp: 60–80 °C), and 1.42 g of *p*TsOH (7.50 mmol) as a Brønsted acid catalyst were added in a 500 mL round-bottom flask equipped with a 25 mL Dean–Stark trap and Allihn condenser.

The reaction mixture was refluxed for 24 h under magnetic stirring. After reaction time, the crude mixture was placed in an ice bath and treated with 3.0 g of Na_2CO_3 (35 mmol) for 30 min. The reaction crude was filtered, and volatile solvent evaporated under reduced pressure. The product was isolated by vacuum distillation (15 mbar) at 50–52 °C. ^{1}H NMR (400 MHz, $CDCl_3$) δ 4.46 (q, J = 6.8 Hz, 1H), 1.59 (s, 3H), 1.52 (s, 3H), 1.46 (d, J = 6.8 Hz, 3H).

2.2.2. Synthesis of 2,5-dimetil-1,3-dioxolan-4-one (LA-Me,H)

For the synthesis of LA-Me,H, we followed the procedure reported by Okada et al. [43] with the following modifications.

Here, 45.0 g of DL-lactic acid (0.500 mol), 32.0 mL of paraldehyde (0.250 mol), 650 mL of petroleum ether (bp: 60–80 °C) and 3.65 g of Amberlite® IR-120 (H^+ form) as heterogeneous Brønsted acid catalyst were added in a 1000 mL round-bottom flask equipped with a 25 mL

Dean–Stark trap and Allihn condenser. The reaction was refluxed under magnetic stirring for 5 h. Crude mixture was cooled at room temperature and filtered to remove the catalyst. The volatile solvent was removed, and the product was isolated by vacuum distillation (15 mbar) at 47–49 °C. The product resulted as a mixture of cis-trans stereoisomers in a 70:30 ratio. Major stereoisomer: 1H NMR (400 MHz, $CDCl_3$) δ 5.64 (q, 1H, J = 5.0 Hz), 4.35 (q, 1H, J = 7.0 Hz).1.59 (d, 3H, J = 5.0 Hz), 1.52 (d, 3H, J = 7.0 Hz). Minor stereoisomer: 1H NMR (400 MHz, $CDCl_3$) δ 5.84 (q, 1H, J = 5.0 Hz), 4.50 (q, 1H, J = 7.0 Hz), 1.55 (d, 3H, J = 5.0 Hz), 1.48 (d, 3H, J = 7.0 Hz).

2.2.3. Synthesis of 5-methyl-1,3-dioxolan-4-one (LA-H,H)

For the synthesis of LA-H,H we followed the procedure reported by Cairns et al. [40] with the following modifications.

Here, 45.0 g of DL-lactic acid (0.500 mol), 22.5 g of paraformaldehyde (0.750 mol), 300 mL of petroleum ether (bp: 60–80 °C) and 1.5 g of *p*TsOH (0.0080 mol) as a Brønsted acid catalyst were added in a 500 mL round-bottom flask equipped with a 25 mL Dean-Stark trap and Allihn condenser. The reaction was refluxed under vigorous magnetic stirring for 24 h. After reaction time, the crude mixture was cooled in an ice bath and treated with 3.0 g of Na_2CO_3 (0.035 mol) for 30 min. The reaction crude was then filtered, and volatile solvent evaporated under reduced pressure. The product was isolated by vacuum distillation (15 mbar) at 45–47 °C. ^{1}H NMR (400 MHz, $CDCl_3$) δ 5.51 (s, 1H), 5.38 (s, 1H), 4.27 (q, J = 6.8, 1H), 1.47 (d, J = 6.8, 3H).

2.2.4. Preparation of Triethylmethylammonium Tetrafluoroborate ($TEMABF_4$)

For the synthesis of $TEMABF_4$, a conventional procedure was followed, exploiting the different solubilities of the desired product and the ammonium chloride.

Here, 22.7 g (0.150 mol) of triethylmethylammonium chloride (TEMACl) were added in a 250 mL round-bottom flask and dissolved in 150 mL of dry acetonitrile. After complete solubilization, 18.9 g (0.180 mol) of NH_4BF_4 was added. The resulting suspension was stirred overnight at room temperature. The suspension was filtered to remove the solid, and the mother liquor was concentrated at a reduced pressure and then crystallized with diethyl ether. Purified product was filtered and dried under vacuum at 50 °C overnight, obtaining an almost quantitative yield. ^{1}H NMR (400 MHz, CD_3CN) δ 3.23 (q, J = 7.3 Hz, 6H), 2.84 (s, 3H), 1.47 (d, J = 6.8, 3H), 1.24 (tt, J = 7.3 Hz, $J^{14}N$ = 2.0 Hz, 9H). ^{13}C NMR (101 MHz, $CDCl_3$) δ 56.91 (t, $J^{14}N$ = 3 Hz), 47.48 (t, $J^{14}N$ = 4 Hz) 8.19. ^{19}F NMR (376 MHz, CD3CN) δ −151.29 (^{11}B), −151.34 (^{10}B).

2.3. Electrolyte Characterization

Before preparing the electrolytes, the solvents were stored on molecular sieves (3A) until the water content was reduced to 30–40 ppm, as measured by Karl–Fischer titration. The electrolyte conductivity was measured at 20 °C using platinized Pt electrodes (Crison 254). The conductivity meter was previously calibrated with a 0.1 M KCl standard solution (conductivity 12.89 $mScm^{-1}$ at 25 °C, Hanna Instrument).

The electrochemical stability window (ESW) was evaluated using a Bob's Cell™ electrochemical cell equipped with three electrodes: Au disc electrode (ø 3 mm, embedded in PEEK) as working electrode, Pt wire as counter electrode and an Ag/Ag^+ quasi-reference electrode in a solution of PC ($TEMABF_4$ 0.1 M and $AgNO_3$ 3 mM). The reference electrode was equipped with a bridge tube filled with supporting electrolyte (PC $TEMABF_4$ 1M) and connected to the cell with glass frits (Vycor®). Before each measurement, 5 mL of electrolyte was introduced into the cell and purged with nitrogen under magnetic stirring for 10 min. The magnetic stirring was stopped, and the bubbler was moved from purging to vent position to avoid moisture contamination. Linear Sweep Voltammetry (LSV) measurements were then performed from open circuit potential (OCP) towards both positive and negative potentials with a scan rate of 10 mVs^{-1}.(Figure S5), to evaluate respectively the anodic (E_{ox}) and cathodic limits (E_{red}). The potential limits were explored separately, and each

measurement was made with fresh electrodes and electrolytes. These limits represent the maximum applicable potential in a classic 3-electrode set-up experiment, for which a faradic current density is not negligible due to the electrochemical decomposition of the electrolyte.

2.4. Symmetrical EDLC Assembly

Each coin cell (CR2016) was prepared cutting two circular AC-based electrodes (ø 12 mm). A cellulosic separator (ø 18 mm Celgard® battery separator) was used as the dielectric separator. Before being cut, the activated carbon electrodes were placed in a vacuum oven at 80 °C for 10 h, cooled, and stored in a nitrogen atmosphere.

Before being used, all of the coin cell's components (case, gasket, cap, plate, and spring) were washed and sonicated with detergents, rinsed with ultra-pure water, and dried in a vacuum oven at 80 °C. The cells were assembled in a dry room by placing into the case the first electrode, the dielectric separator, the appropriate electrolytic solution, the second electrode, the plate, the spring and finally the cap. The cells thus prepared were sealed with MSK110 manual hydraulic crimping machine (MTI KJ group™) and tested as symmetrical EDLCs.

2.5. EDLC Characterizations

EDLCs were characterized by cyclic voltammetry (CV), galvanostatic charge-discharge cycles (GCs) and potentiostatic electrochemical impedance spectroscopy (EIS).

The operative voltage (OV) of the investigated electrolytes was defined as the maximum applicable voltage with a Coulombic Efficiency (CE) threshold of 94–95%. CV were recorded with a scan rate of 5 mVs^{-1}, starting from 0 V and gradually increasing to the final voltage (Figure S6). The CE was calculated from the ratio between integration of negative (Q^-) and positive (Q^+) voltammogram areas [44] that represent, respectively, discharge and charge capacitance:

$$CE = |Q^-| / |Q^+| \times 100 \quad (3)$$

The Capacitance Retention (CR) was defined with CV by the ratio of the specific capacitance (SC_{cv}) at different scan rates to that recorded with the scan rate of 5 mVs^{-1} (4). The CV scan rate was increased from 5 to 200 mVs^{-1} in a potential window from 0 V to OV. In the following characterization, $i_{1/2\ Vmax}$ is the current density (Acm^{-2}) referred to half of the OV, s is the applied scan rate (Vs^{-1}) and d is the active materials loading (gcm^{-2}) [45]:

$$CR = SC_{cv(x\ mVs^{-1})} / SC_{cv\ (5\ mVs^{-1})} \times 100 \quad (4)$$

$$SC_{cv} = i_{1/2\ Vmax} / (s \times d) \quad (5)$$

The GC profiles recorded were elaborated to calculate the specific Capacitance (C_{sp}, Fg^{-1}) and maximum specific Energy (E_{sp}, $Whkg^{-1}$) and Power (P_{sp}, $kWkg^{-1}$) according to the following equations [46]:

$$C_{sp} = (dt/dV) \times (i/m_{tot}) \quad (6)$$

$$E_{sp} = (C \times OV^2)/(2 \times 3600 \times m_{tot}) \quad (7)$$

$$P_{sp} = OV^2/(4 \times m_{tot} \times ESR_{GC}) \quad (8)$$

where dt/dV is the slope of the discharging profile, i the applied current, m_{tot} the total mass (in g for C_{sp} and kg for E_{sp} and P_{sp}) of the active materials for the two electrodes, C the capacitance (F), OV the operative voltage (V), 3600 is expressed in second. The ESR_{GC} was calculated according to the following Equation (9), where ΔV_{ohmic} is the ohmic voltage drop at the beginning of discharge and i was the applied current:

$$ESR_{GC} = \Delta V_{ohmic} / (2 \times i) \quad (9)$$

EIS profiles were recorded in the frequency range between 500 kHz and 10 mHz with 5 mVAC perturbation and 10 points per decade. According to analysis reported by Mei et al. [47], from EIS profile we determined the ESR, the Equivalent Diffusive Resistance (EDR), relative to the ions penetration into the electrode pores, and the bulk resistance (R_{bulk}), relative to the bulk resistance of the electrolyte in the cell. The different parameters were defined by the segments obtained from the intersection of the Nyquist plot with the x-axis, also exploiting linear fittings in the diffusive-regime (slope ≈ 1) and capacitive-refine (quasi-vertical line). A clarification of the Nyquist plot analysis is shown in Figure S7. The time constant of the investigated materials was evaluated calculating the imaginary part $C''(\omega)$ of the complex capacitance according to the work of Taberna et al. [48] and the following equation:

$$C''(\omega) = -Z'(\omega)/(\omega \times |Z(\omega)|^2) \quad (10)$$

where ω is the applied frequency, $Z'(\omega)$ is the real part of complex impedance related to the Nyquist plot and $|Z(\omega)|$ is the impedance modulus related to the Bode plot.

3. Results

3.1. Solvent and Electrolyte Characterization

Three dioxolanes with different substituents in position 2 were synthesized performing ketalization reactions between lactic acid (LA) and two different aldehydes (formaldehyde R,R′ = H, acetaldehyde R,R′ = H,Me) or acetone (R,R′ = Me). This panel of substances was chosen to correlate any performance differences to small structural variations. To indicate the different solvents and simplify the discussion, the abbreviation LA-R,R′ will be adopted, where LA indicates the lactic acid fragment and R,R′ explicit the substituents in position 2 (Figure 2).

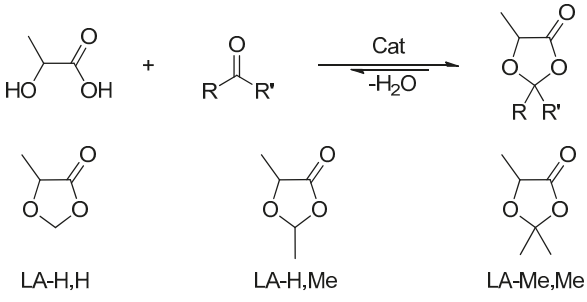

Figure 2. DOLOs synthesis and investigated solvent. 5-methyl-1,3-dioxolan-4-one LA-H,H; 2,5-dimethyl-1,3-dioxolan-4-one LA-H,Me; 2,2,5-trimethyl-1,3-dioxolan-4-one LA-Me,Me.

The ketals synthesis is an equilibrium reaction, and therefore it was necessary to use a Dean-Stark trap to remove water from the reaction mixture and favor the products formation. A synthesis that implies formation of water as a by-product, such as the ketalization reaction, is preferable to other synthetic pathways as water does not contribute to the E-factor of the reaction. Nevertheless, in order to increase the sustainability of the whole process, water-removal technologies that do not involve the use of solvents, such as pervaporation, will be explored in the future [49].

The investigated compounds are potentially obtainable from renewable sources, as there are green industrial routes to lactic acid and the other reactants starting from bio-based feedstocks [50,51].

However, to consider these compounds as sustainable solvents, it is essential to evaluate their intrinsic safety (flammability, toxicological profile), and the environmental impact in case of accidental release (ecological profile). To assess their flammability, the flashpoint was estimated using the method reported by R.W. Prugh [52]. Table 1 reports the calculated flash point of the produced DOLOs, their boiling temperature at atmospheric pressure, and

the stoichiometric concentration in air (CST) expressed as a volume percentage used to estimate the flash points.

Table 1. DOLOs and commercial EDLC solvents flashpoints.

Solvent	Boiling Point (°C)	CST (% *v*/*v*)	Estimated Flashpoint (°C)
LA-H,H	162	4.97	38
LA-H,Me	164	3.67	38
LA-Me,Me	168	2.90	49
ACN	82	-	2 *
PC	242	-	132 *

* Experimental literature data.

DOLOs have an intermediate flash point between those of the two traditional EDLCs solvents (fp_{ACN} = 2 °C; fp_{PC} = 132 °C) and are hence suitable for applications in energy storage devices. The complete evaluation of their ecotoxicological profile is beyond the aim of this study, but it is possible to make some considerations based on their chemical nature. Ketals are a class of substances stable in an alkaline environment but labile in an aqueous and acidic media. Therefore, it is possible to assume that in an atmospheric and physiological environment, these functional groups rapidly hydrolyze, returning the parent reagents [53]. Lactic acid, acetone, acetaldehyde, and formaldehyde are regularly included in the cellular metabolic pathways at physiological concentrations, and have a low persistence in the natural environment. As an example, the human body produces about 50 g of formaldehyde per day [54]; the half-life of blood plasma formaldehyde is 1.5 min [55] and that of atmospheric formaldehyde in daylight is 50 min [56]. Therefore, the investigated solvents are sustainable alternatives also from the point of view of their ecotoxicological profile.

A preliminary evaluation of their electric performance was carried out by measuring the ionic conductivity and the electrochemical stability window of 1M $TEMABF_4$ solutions. The results are reported in Table 2.

Table 2. Electrolyte characterization.

Solvent	Electrolyte	Conductivity ($mScm^{-1}$)	E_{Red} (V vs Ag/Ag^+)	E_{Ox} (V vs Ag/Ag^+)	ΔV
PC	$TEMABF_4$	11.4	−1.75	2.80	4.55
LA-H,H	$TEMABF_4$	8.5	−1.95	2.55	4.50
LA-H,H	$LiBF_4$	2.1	-	-	-
LA-H, Me	$TEMABF_4$	1.5	-	-	-
LA-Me, Me	$TEMABF_4$	0.2	-	-	-

Large variations of ionic conductivity were recorded according to the nature of the substituents in position 2. Indeed, LA-H,H showed a conductivity of 8.5 $mScm^{-1}$, while in presence of additional methyl groups, the conductivity gradually dropped to 1.5 $mScm^{-1}$ (LA-H,Me) and 200 μScm^{-1} (LA-Me,Me). Furthermore, LA-Me,Me and LA-H,Me demonstrated a lower solvent capacity because saturated solutions were obtained at concentrations below 1 M, which are therefore unsuitable for applications in SC. A possible application of LA-H,H in Li-ion based devices was also assessed, as 1M solutions of $LiBF_4$ displayed a conductivity of 2.1 $mScm^{-1}$.

In addition to an adequate conductivity, EDLC applications require that the electrolyte has a wide electrochemical stability window (ESW), that can be preliminary estimated by Linear Sweep Voltammetry (LSW). A large ESW (Figure S5 and Table S1) was obtained for the electrolyte based on LA-H,H (ΔV 4.50 V, cut-off current densities 1 $mAcm^{-2}$), comparable to that recorded for the PC-based electrolyte (ΔV 4.55 V, cut-off current densities 1 $mAcm^{-2}$).

Therefore, LA-H,H was selected to evaluate the performance in a symmetrical EDLC with activated carbon based electrodes using $TEMABF_4$ as conventional conducting salt.

3.2. EDLCs Characterization

Cyclic voltammetries (CVs) at different scan rates were performed to evaluate, respectively, the impact of the investigated electrolytes on the maximum operating voltage (OV) and capacitance retention (CR) of EDLCs. For a homogenous comparative analysis, Figure 3 shows the data with the LA-H,H-based electrolyte, and those of an EDLC prepared with $TEMABF_4$ 1 M in PC.

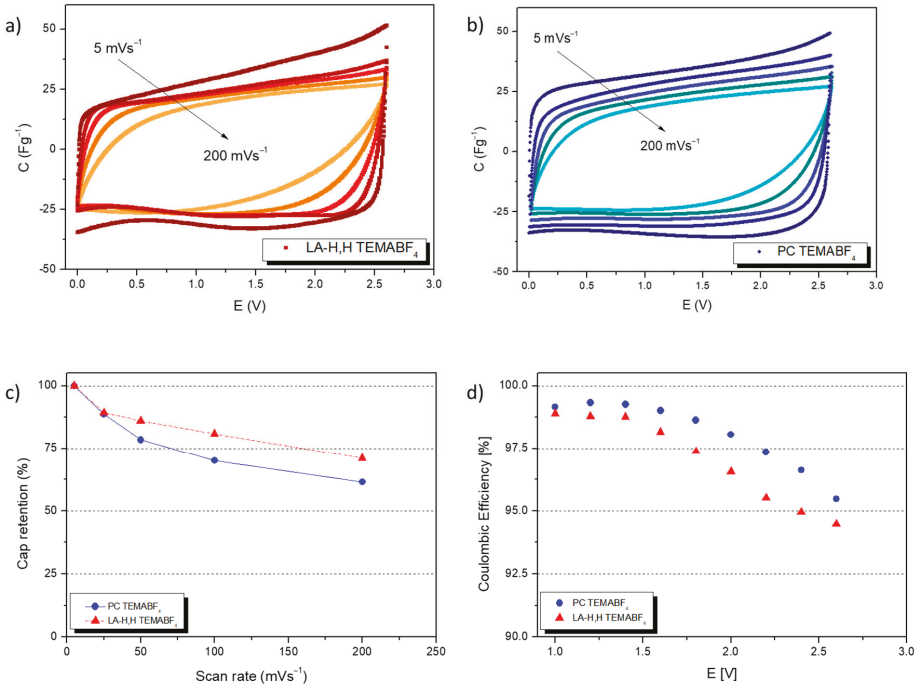

Figure 3. Cyclic voltammetry of LA-H,H and PC based electrolytes EDLC. (**a**) CV of LA-H,H $TEMABF_4$ 1M at different scan rate: 5, 25, 50, 100, 200 mVs^{-1}. (**b**) CV of PC $TEMABF_4$ 1M at different scan rate: 5, 25, 50, 100, 200 mVs^{-1}. (**c**) Capacitance retention at different scan rate of EDLCs containing investigated electrolytes. (**d**) Coulombic efficiency at different cell voltage of EDLCs containing investigated electrolytes.

Initially CVs were recorded at 5 mVs^{-1} from 0 to 1 V, and the final potential was gradually increased by 0.2 V in different cycles and described by a rectangular-like shape typical of SCs devices, which deviates from a perfect rectangle (typical of an ideal capacitor) due to the resistance parameters [46] (Figure S6). The screening was stopped at 2.6 V when a Coulombic Efficiency (CE) close to 95% was achieved, which was chosen as the minimum efficiency threshold. Figure 3d shows the CEs as a function of the applied potentials, and the trend is the same for the electrolytes. The decrease of the EC with the increase of the operating potential is due to a gradual contribution of parasitic and irreversible faradic reactions that interfere in the charging capacitance and are absent in discharge capacitance. At 2.6 V the LA-H,H-based EDLCs provided a CE of almost 94.4%, which was slightly lower than that recorded with the PC-electrolyte (95.4%).

After establishing the OV of 2.6 V for both electrolytes, CVs were performed from 0 to 2.6 V, ranging the scan rate from 5 to 200 mVs^{-1} (Figure 3a,b) to evaluate their capacitance retention (CR). The increase of the scan rate strongly influences the response of the EDLCs

during CVs; in fact, a marked distortion of the rectangular shape was recorded due to the increase of the ESR, while the decrease of the specific capacity is caused by a lower availability of the electrodes surface. Indeed, at high scan rates the formation of the electric double layer is limited by a lower accessibility of the electrolyte ions in the porous structure of the electrode [57]. As reported in Figure 3c, LA-H,H/TEMABF$_4$ resulted in a greater performance than PC/TEMABF$_4$. At 200 mVs^{-1} a CR of 71% was achieved for LA-H,H/TEMABF$_4$, while a CR of 62% were obtained with PC/TEMABF$_4$. Based on these results, the increased performance of LA-H,H/TEMABF$_4$ cannot be justified by its conductivity, as it was slightly lower than the PC-electrolyte. To understand this behavior, the solvent–salt and electrolyte-electrode interactions should be investigated in depth, however this aspect is beyond the scope of this paper and will be the subject of future investigations.

The storage properties and the internal resistance parameters of the investigated EDLCs were assessed through GC and EIS analysis (Figure 4).

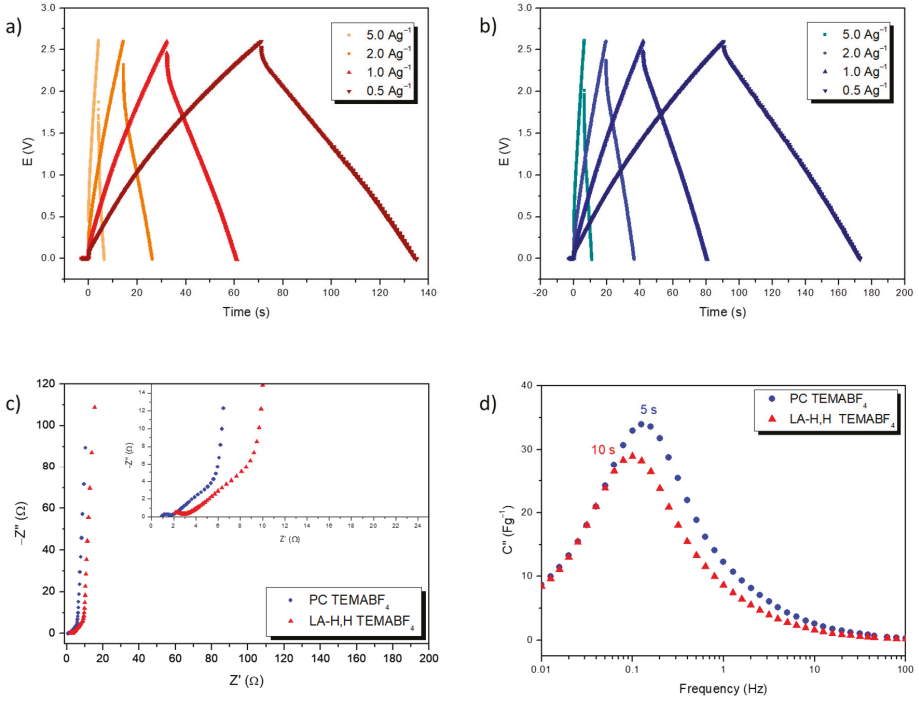

Figure 4. Charge/discharge GC and EIS of LA-H,H and PC based electrolytes EDLCs. (**a**) GC of LA-H,H TEMABF$_4$ 1M at different current densities: 0.5, 1, 2, 5 Ag^{-1}. (**b**) GC of PC TEMABF$_4$ 1M at different current densities: 0.5, 1, 2, 5 Ag^{-1}. (**c**) EIS Nyquist plot of EDLCs containing investigated electrolytes for a frequency range from 500 kHz to 10 mHz. (**d**) Evolution of the imaginary part of the complex capacitance vs frequency of the same EDLCs.

The GCs were performed ranging the current density from 0.5 Ag^{-1} up to 5 Ag^{-1} to test the electrolytes in different conditions (Figure 4a,b). In all applied conditions the GC profile resulted in a symmetrical triangular shape, indicative of a good reversible and capacitive behavior. From the ohmic drop and discharge profile, the ESR$_{GC}$ and specific capacitance of each analysis was estimated, respectively. These results were used to calculate specific maximum power and energy.

The results obtained at low current density are summarized in Table 3.

Table 3. GC results at 0.5 Ag^{-1} normalized with total mass of electrodes active materials.

	Solvent	Electrolyte	ESR_{GC} (Ω)	C_{sp} (Fg^{-1})	E_{sp} ($Whkg^{-1}$)	P_{sp} ($kWkg^{-1}$)	CE_{GC} (%)
Entry 1	PC	$TEMABF_4$	4.3	18	17	29	91.0
Entry 2	LA-H,H	$TEMABF_4$	5.5	14	13	23	90.0

An analysis of the overall performance discloses that LA-H,H is competitive with PC. A modest decrease of capacitance and specific energy was obtained with LA-H,H/$TEMABF_4$ (entries 1 and 2), although the specific power dropped from 29.1 $kWkg^{-1}$ of PC (entry 1) to 22.5 $kWkg^{-1}$ of LA-H,H (entry 2) due to a higher ESR_{GC} of the latter. Moreover, a slight decrease of CE_{GC} was obtained from discharge/charge time ratio. At a high current density (5 Ag^{-1}), the specific energy and power for LA-H,H/$TEMABF_4$ reached 6 $Whkg^{-1}$ and 23 $kWkg^{-1}$, while for PC/$TEMABF_4$ the values were 14 $Whkg^{-1}$ and 29 $kWkg^{-1}$. It is therefore evident that the solvent-salt interaction can significantly affect the performance of the electrolyte, especially the resistance parameters.

To investigate possible variations in resistance parameters, EIS measurements were performed by applying small perturbations (5 mVAC) and spanning the frequency range from 500 kHz to 10 mHz (Figure 4c). The Nyquist plot can be divided into high, medium, and low frequency parts in which the EDLC behavior transits from a completely resistive behavior to a completely capacitive one. This change is highlighted by the time constant $\tau_0 = 1/\nu_0$, where ν_0 is the frequency with the highest imaginary part of the complex capacitance. From the analysis of these profiles, it was possible to separately determine the Equivalent Series Resistance ESR_{EIS}, the Equivalent Distributed Resistance (EDR) relative to the penetration of the ions into the electrode pores, and the bulk resistance of the electrolyte (R_{bulk}) related to electrolyte conductivity.

The resulting profiles of EISs experiments are typical of an EDLC device; in fact, at high frequencies there is a purely resistive behavior, and from the first intersection with the x-axis this can be defined as the ESR. Immediately afterwards, with slightly lower frequencies, a hemicycle shape of a mixed resistive/capacitive behavior begins to be visible due to the accumulation of charge at external electrodes surface and the relative resistance due to the charges transfer from bulk to the electrodes. The segment under the hemicycle has been defined as R_{bulk} due to the preponderant contribution of the electrolyte solution on this parameter. At intermediate frequencies the impedance profile tends to linearize with an almost 45° slope; this property is typical of a diffusive process, and considering the EDLC device is interpreted by the penetration of the ions in the porous structure of the electrodes. At low frequencies the electric double layer is able to structure itself completely, occupying the entire available electrode surface and saturating its internal volume. In this condition, an almost complete capacitive behavior is recorded, highlighted by a quasi-vertical profile. EDR was therefore defined as a segment of resistance between the intercepts with the x-axis by the linear fittings of the diffusive (medium frequencies) and capacitive (low frequencies) behavior.

The parameters obtained were normalized for the surface of the electrodes, and are summarized in Table 4.

Table 4. EIS results normalized for the electrode surface.

	Solvent	Electrolyte	ESR_{EIS} (Ωcm^2)	EDR (Ωcm^2)	R_{bulk} (Ωcm^2)	τ_0 (s)
Entry 1	PC	$TEMABF_4$	1.1	4.6	0.9	5
Entry 2	LA-H,H	$TEMABF_4$	1.4	6.6	2.2	10

According to the previous data obtained from the GC analysis and conductivity evaluations, the resistance parameters obtained with the PC-based electrolyte (entry 1) were lower than those achieved with LA-H,H-based electrolytes (entry 2). Among the

investigated parameters, R_{bulk} and EDR were greater affected by the solvent nature of the electrolytes, while ESR_{EIS} was not particularly sensitive, resulting therefore more highly influenced by the electrode.

The EIS analysis was also used to determine the time constants of the EDLCs. Figure 4d shows the profile of the imaginary part of the complex capacitances as a function of the applied frequency used to determine the time constants. As expected, PC/$TEMAB_4$ displayed a smaller time constant compared to that of LA-H,H/ $TEMAB_4$, respectively 5 s and 10 s.

Finally, the stability over long-cycling of the electrolyte LA-H,H was evaluated by performing 5000 charge/discharge cycles at different current densities (1000 cycles for each current density). The evolution of capacitance, coulombic efficiency and capacitance retention over each cycle are reported in Figure 5.

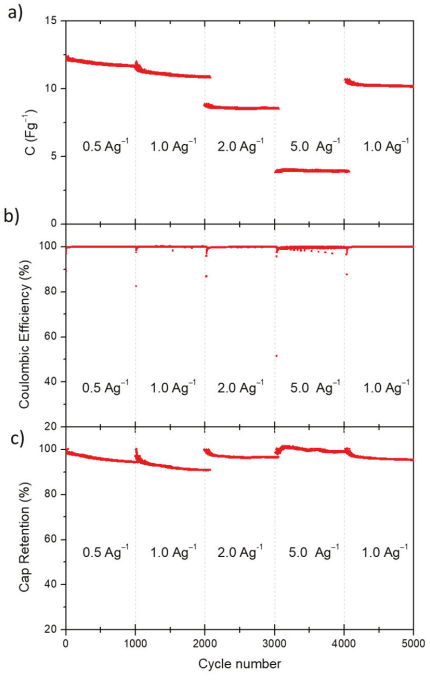

Figure 5. (**a**) Evolution of specific capacitance, (**b**) coulombic efficiency and (**c**) capacitance retention of EDLCs containing LA-H,H/$TEMABF_4$ at different current densities.

As shown in Figure 5a, initial loss of capacitance was observed for the first two groups of cycles, which then stabilized in subsequent cycles. Figure 5c shows the capacitance retention evaluated by the ratio between the specific capacitance of each cycle and the specific capacitance of the first cycle of each group of cycles. A minimum CR of 94% was obtained in the first thousand cycles at 0.5 Ag^{-1}. At 1 Ag^{-1} the efficiency range dropped to a minimum of 90%, while for the further cycles at 2, 5 and again at 0.5 Ag^{-1} the final efficiencies were respectively 96.4%, 98.7% and 95.4%.

Furthermore, Figure 5b shows the coulombic efficiency over all cycling-groups, which was highly stable and close to 100% for all applied current densities, validating the stability of the electrolytes based on LA-H,H. To ensure a prompt comparison between the achieved results with other electrolyte categories, some EDLCs-electrolytes performances reported in literature are collected in Table S2.

4. Discussion

The investigation and individuation of new solvents is a relevant issue that has wide implications in different industrial sectors, and, among them, energy storage represents a driving force for their development. In the field of supercapacitors, the most common solvents used for the electrolytes are acetonitrile (ACN) and propylene carbonate (PC).

The use of ACN has several contraindications due to its high vapor pressure (9.71 kPa at 20 °C) and low flash and boiling points. Indeed, according to Regulation (EC) No. 1272/2008 (Classification, Labeling and Packaging (CLP)) it is classified as a "highly flammable liquid and vapor", and as a volatile organic compound (VOC). Moreover, ACN exhibits acute toxicity for organs and tissues through different types of exposure (skin contact, ingestion, inhalation).

PC is a more user-friendly solvent compared to ACN: it has low vapor pressure (0.006 kPa at 25 °C), high flash and boiling points, and it is classified without hazard statements relative to inhalation or skin exposures. However, the toxicity of organic cyclic carbonates is still under investigation. In recent studies, Strehlau et al. [58] reported that these compounds can penetrate in vitro the simulated blood-cerebrospinal fluid barrier, and it is therefore assumed that they can reach areas of cerebral interest also in physiological conditions.

Concerning their production, ACN is obtained as a by-product from the synthesis of acrylonitrile (SOHIO process, catalytic ammonium oxidation of propylene), which is performed in gas-phase with metal oxide catalysts using ethylene and/or propylene, ammonia and oxygen [59]. The PC is mainly prepared by propylene oxide ring-opening in a CO_2 atmosphere under harsh conditions of pressure and temperature [60,61]. Therefore, both most used solvents to prepare electrolyte are synthesized from non-renewable feedstock.

In this work we have synthesized a panel of substances (LA-H,H; LA-H,Me; LA-Me,Me) obtainable from renewable sources and with a potentially benign ecotoxicological profile, and we used them for the first time as solvent for non-aqueous EDLCs.

Based on preliminary results, the solvent LA-H,H displayed the highest conductivity (8.5 $mScm^{-1}$) and was therefore chosen as the best candidate for subsequent characterizations. Two electrolyte-based LA-H,Hs and PCs were prepared with the same conducting salt ($TEMABF_4$) to investigate any differences related to solvent effect. The prepared electrolytes were used to assemble symmetrical EDLC, which were thoroughly characterized by evaluating:

- the coulombic efficiency and capacitance retentions by cyclic voltammetry;
- the storage performances by charge/discharge GC;
- the resistance parameters by potentiostatic impedance spectroscopy;
- and the cycling stability over 5000 cycles at different current densities.

The ensemble of results provided by the assembled devices highlights the relevance of the solvent-salt interactions to determine the overall performances. Compared to PC based electrolytes, at 2.6 V LA-H,H/$TEMABF_4$ showed approximately the same coulombic efficiency in the range of 94%–95% and a modest increase of capacitance retention with a high scan rate. The overall storage performances achieved with LA-H,H solvent were adequate for EDLC application (E_{sp} > 10 $Whkg^{-1}$ and P_{sp} > 20 $kWkg^{-1}$), and comparable with those achieved with PC/$TEMABF_4$. EIS analysis confirmed small variations among each resistance parameters, and a more prominent difference between the time. Interpreting this behavior with the storage parameters recorded at a high specific current, it is possible to assume that the decrease in specific energy and specific capacity for LA-H,H/$TEMABF_4$ is due to an incomplete formation of the electric double layer, since at high current density the charge time was below the relative time constant. Final stability investigations performed with LA-H,H/$TEMABF_4$ revealed high performance, as capacitance retention (never less than 90% even at high current density) and coulombic efficiency were close to 100% for all the cycles. However, this new electrolyte should be cycled over a longer cycling period (at least 10,000 cycle) to definitively validate its stability in EDLC devices and will be the aim of future developments.

In this work, it was therefore demonstrated that compounds based on the 5-methyl-1,3-dioxolan-4-one scaffold (Figure 6) are sustainable non-aqueous solvents for applications in energy storage devices. In the future, this class of electrolytes will be extended to other modulable and still unexplored solvents by using other common α-hydroxy acids, such as glycolic, mandelic and 2-hydroxyisobutyric acid, as starting material.

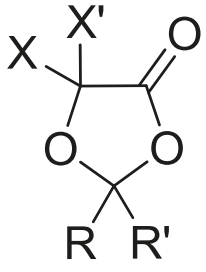

Figure 6. Generic structure of 2,2-R,R′-5,5-X,X′-1,3-dioxolan-4-one compounds.

5. Conclusions

Most of the literature articles on non-aqueous electrolytes aims to uniquely increase the EDLC's performance, often neglecting issues of great importance such as sustainability and safety, and relegating the relevance of these issues only to aqueous electrolytes. In this work we have subverted this concept designing aprotic polar solvents from renewable sources, such as green lactic acid, and investigating their performances.

Within this framework, three dioxolanes with small structural variations in position 2 were synthesized: 2,2,5-trimethyl-1,3-dioxolan-4-one (LA-Me,Me), 2,5-dimethyl-1,3-dioxolan-4-one (LA-H-Me), and 5-methyl-1,3-dioxolan-4-one (LA-H,H). As expected, small structural variations significantly influence their performances, such as conductivity and solvent ability vs $TEMABF_4$, which allowed us to select 5-methyl-1,3-dixolan-4-one for a thorough characterization of the EDLC device. The results demonstrate that the LA-H,H-based electrolyte is suitable for the application, and competitive with the one based on commercial PC. In fact, an operational potential typical of non-aqueous electrolytes (2.6 V, CE ≈ 95%) and adequate storage parameters have been reached (E_{sp} > 10 $Whkg^{-1}$ and P_{sp} > 20 $kWkg^{-1}$). This result paves the way for the use of a wide class of solvents based on α-hydroxyacid ketals as sustainable alternatives to those obtained from non-renewable fossil sources. Moreover, thanks to their structural versatility, the room for improvement is still large and further studies will be aimed at increasing performances by finely tuning the solvent-salt combination.

Supplementary Materials: The following are available online at https://www.mdpi.com/article/10.3390/en14144250/s1, Figure S1: 5-methyl-1,3-dioxolan-4-one (LA-H,H) characterization, Figure S2: 5,2-dimethyl-1,3-dioxolan-4-one (LA-H,Me) characterization, Figure S3: 5,2,3-trimethyl-1,3-dioxolan-4-one (LA-Me,Me) characterization, Figure S4: Triethylmethylammonium tetrafluoroborate ($TEMABF_4$) characterization, Figure S5: ESW investigation, Figure S6: Operative voltage investigation, Figure S7: Nyquist plot analysis and resistances evaluations, Table S1: ESW data at different current densities cut-off, Table S2: Relevant performance from cited literature.

Author Contributions: Conceptualization, M.M. and F.R.; formal analysis, M.M.; investigation, M.M.; data curation, R.E.; funding acquisition, M.D.S., G.A.; supervision, A.L., A.B., F.R.; writing-original draft preparation, M.M., R.E., M.D.S., A.L., A.B., F.R.; writing-review and editing, M.M., R.E., M.D.S., G.A., A.L., A.B., F.R. All authors have read and agreed to the published version of the manuscript.

Funding: This research received no external funding.

Data Availability Statement: Not applicable.

Acknowledgments: Pier Paolo Prosini (ENEA DTE-SPCT, C.R. Casaccia, Santa Maria di Galeria, Rome, Italy) and his research group are acknowledged for their valuable contribution and support on coin cell preparation.

Conflicts of Interest: The authors declare no conflict of interest.

References

1. González, A.; Goikolea, E.; Barrena, J.A.; Mysyk, R. Review on supercapacitors: Technologies and materials. *Renew. Sustain. Energy Rev.* **2016**, *58*, 1189–1206. [CrossRef]
2. Gerlach, P.; Balducci, A. A Critical Analysis about the Underestimated Role of the Electrolyte in Batteries Based on Organic Materials. *ChemElectroChem* **2020**, *7*, 2364–2375. [CrossRef]
3. Nomura, K.; Nishihara, H.; Kobayashi, N.; Asada, T.; Kyotani, T. 4.4 V supercapacitors based on super-stable mesoporous carbon sheet made of edge-free graphene walls. *Energy Environ. Sci.* **2019**, *12*, 1542–1549. [CrossRef]
4. Wang, Y.; Meng, X.; Sun, J.; Liu, Y.; Hou, L. Recent Progress in "Water-in-Salt" Electrolytes Toward Non-lithium Based Rechargeable Batteries. *Front. Chem.* **2020**, *8*, 595. [CrossRef]
5. Martins, V.L.; Torresi, R.M. Water-in-salt electrolytes for high voltage aqueous electrochemical energy storage devices. *Curr. Opin. Electrochem.* **2020**, *21*, 62–68. [CrossRef]
6. Bu, X.; Su, L.; Dou, Q.; Lei, S.; Yan, X. A low-cost "water-in-salt" electrolyte for a 2.3 V high-rate carbon-based supercapacitor. *J. Mater. Chem. A* **2019**, *7*, 7541–7547. [CrossRef]
7. Xu, S.-W.; Zhang, M.-C.; Zhang, G.-Q.; Liu, J.-H.; Liu, X.-Z.; Zhang, X.; Zhao, D.-D.; Xu, C.-L.; Zhao, Y.-Q. Temperature-dependent performance of carbon-based supercapacitors with water-in-salt electrolyte. *J. Power Sources* **2019**, *441*, 227220. [CrossRef]
8. Tabelin, C.B.; Dallas, J.; Casanova, S.; Pelech, T.; Bournival, G.; Saydam, S.; Canbulat, I. Towards a low-carbon society: A review of lithium resource availability, challenges and innovations in mining, extraction and recycling, and future perspectives. *Miner. Eng.* **2021**, *163*, 106743. [CrossRef]
9. El Halimi, M.S.; Poli, F.; Mancuso, N.; Olivieri, A.; Mattioli, E.J.; Calvaresi, M.; Chafik, T.; Zanelli, A.; Soavi, F. Circumneutral concentrated ammonium acetate solution as water-in-salt electrolyte. *Electrochim. Acta* **2021**, *389*, 138653. [CrossRef]
10. Hughson, F.R.; Borah, R.; Nann, T. A 2.7 V Aqueous Supercapacitor Using a Microemulsion Electrolyte. *Batter. Supercaps* **2021**, *4*, 1122–1125. [CrossRef]
11. Ue, M.; Ida, K.; Mori, S. Electrochemical Properties of Organic Liquid Electrolytes Based on Quaternary Onium Salts for Electrical Double Layer Capacitors. *J. Electrochem. Soc.* **1994**, *141*, 2989–2996. [CrossRef]
12. Chiba, K.; Ueda, T.; Yamaguchi, Y.; Oki, Y.; Saiki, F.; Naoi, K. Electrolyte Systems for HighWithstand Voltage and Durability. II. Alkylated Cyclic Carbonates for Electric Double-Layer Capacitors. *J. Electrochem. Soc.* **2011**, *158*, A1320–A1327. [CrossRef]
13. Chiba, K.; Ueda, T.; Yamaguchi, Y.; Oki, Y.; Shimodate, F.; Naoi, K. Electrolyte Systems for High Withstand Voltage and Durability. I Linear Sulfones for Electric Double-Layer Capacitors. *J. Electrochem. Soc.* **2011**, *158*, A872–A882. [CrossRef]
14. Zhong, C.; Deng, Y.; Hu, W.; Qiao, J.; Zhang, L.; Zhang, J. A review of electrolyte materials and compositions for electrochemical supercapacitors. *Chem. Soc. Rev.* **2015**, *44*, 7484–7539. [CrossRef]
15. Wang, Y.; Song, Y.; Xia, Y. Electrochemical capacitors: Mechanism, materials, systems, characterization and applications. *Chem. Soc. Rev.* **2016**, *45*, 5925–5950. [CrossRef]
16. Xia, L.; Yu, L.; Hu, D.; Chen, G.Z. Electrolytes for electrochemical energy storage. *Mater. Chem. Front.* **2017**, *1*, 584–618. [CrossRef]
17. Balducci, A. Electrolytes for high voltage electrochemical double layer capacitors: A perspective article. *J. Power Sources* **2016**, *326*, 534–540. [CrossRef]
18. Ray, A.; Saruhan, B. Application of Ionic Liquids for Batteries and Supercapacitors. *Materials* **2021**, *14*, 2942. [CrossRef]
19. Stettner, T.; Balducci, A. Protic ionic liquids in energy storage devices: Past, present and future perspective. *Energy Storage Mater.* **2021**, *40*, 402–414. [CrossRef]
20. Silvester, D.S.; Jamil, R.; Doblinger, S.; Zhang, Y.; Atkin, R.; Li, H. Electrical Double Layer Structure in Ionic Liquids and Its Importance for Supercapacitor, Battery, Sensing, and Lubrication Applications. *J. Phys. Chem. C* **2021**, *125*, 13707–13720. [CrossRef]
21. Miao, L.; Song, Z.; Zhu, D.; Li, L.; Gan, L.; Liu, M. Ionic Liquids for Supercapacitive Energy Storage: A Mini-Review. *Energy Fuels* **2021**, *35*, 8443–8455. [CrossRef]
22. Santos, M.C.G.; Silva, G.G.; Santamaría, R.; Ortega, P.F.R.; Lavall, R.L. Discussion on Operational Voltage and Efficiencies of Ionic-Liquid-Based Electrochemical Capacitors. *J. Phys. Chem. C* **2019**, *123*, 8541–8549. [CrossRef]
23. Stettner, T.; Gehrke, S.; Ray, P.; Kirchner, B.; Balducci, A. Water in Protic Ionic Liquids: Properties and Use of a New Class of Electrolytes for Energy-Storage Devices. *ChemSusChem* **2019**, *12*, 3827–3836. [CrossRef]
24. Krummacher, J.; Schütter, C.; Hess, L.H.; Balducci, A. Non-aqueous electrolytes for electrochemical capacitors. *Curr. Opin. Electrochem.* **2018**, *9*, 64–69. [CrossRef]
25. Cheng, F.; Yu, X.; Wang, J.; Shi, Z.; Wu, C. A novel supercapacitor electrolyte of spiro-(1,1′)-bipyrolidinium tetrafluoroborate in acetonitrile/dibutyl carbonate mixed solvents for ultra-low temperature applications. *Electrochim. Acta* **2016**, *200*, 106–114. [CrossRef]
26. Schütter, C.; Bothe, A.; Balducci, A. Mixtures of acetonitrile and ethyl isopropyl sulfone as electrolytes for electrochemical double layer capacitors. *Electrochim. Acta* **2020**, *331*, 135421. [CrossRef]
27. Hess, L.H.; Balducci, A. 1,2-butylene carbonate as solvent for EDLCs. *Electrochim. Acta* **2018**, *281*, 437–444. [CrossRef]

28. Hess, L.H.; Balducci, A. Glyoxal-Based Solvents for Electrochemical Energy-Storage Devices. *ChemSusChem* **2018**, *11*, 1919–1926. [CrossRef]
29. Saikia, B.K.; Benoy, S.M.; Bora, M.; Tamuly, J.; Pandey, M.; Bhattacharya, D. A brief review on supercapacitor energy storage devices and utilization of natural carbon resources as their electrode materials. *Fuel* **2020**, *282*, 118796. [CrossRef]
30. Jessop, P.G. Searching for green solvents. *Green Chem.* **2011**, *13*, 1391–1398. [CrossRef]
31. Benessere, V.; Cucciolito, M.E.; Esposito, R.; Lega, M.; Turco, R.; Ruffo, F.; Di Serio, M. A novel and robust homogeneous supported catalyst for biodiesel production. *Fuel* **2016**, *171*, 1–4. [CrossRef]
32. Melchiorre, M.; Benessere, V.; Cucciolito, M.E.; Melchiorre, C.; Ruffo, F.; Esposito, R. Direct and Solvent-Free Oxidative Cleavage of Double Bonds in High-Oleic Vegetable Oils. *ChemistrySelect* **2020**, *5*, 1396–1400. [CrossRef]
33. Esposito, R.; Melchiorre, M.; Annunziata, A.; Cucciolito, M.E.; Ruffo, F. Emerging catalysis in biomass valorisation: Simple Zn(II) catalysts for fatty acids esterification and transesterification. *ChemCatChem* **2020**, *12*, 5858–5879. [CrossRef]
34. Melchiorre, M.; Cucciolito, M.E.; Di Serio, M.; Ruffo, F.; Tarallo, O.; Trifuoggi, M.; Esposito, R. Homogeneous Catalysis and Heterogeneous Recycling: A Simple Zn(II) Catalyst for Green Fatty Acid Esterification. *ACS Sustain. Chem. Eng.* **2021**, *9*, 6001–6011. [CrossRef]
35. Melchiorre, M.; Amendola, R.; Benessere, V.; Cucciolito, M.E.; Ruffo, F.; Esposito, R. Solvent-free transesterification of methyl levulinate and esterification of levulinic acid catalyzed by a homogeneous iron(III) dimer complex. *Mol. Catal.* **2020**, *483*, 110777. [CrossRef]
36. Benessere, V.; Cucciolito, M.E.; De Santis, A.; Di Serio, M.; Esposito, R.; Melchiorre, M.; Nugnes, F.; Paduano, L.; Ruffo, F. A Sustainable Process for the Production of Varnishes Based on Pelargonic Acid Esters. *J. Am. Oil Chem. Soc.* **2019**, *96*, 443. [CrossRef]
37. Esposito, R.; Raucci, U.; Cucciolito, M.E.; Di Guida, R.; Scamardella, C.; Rega, N.; Ruffo, F. Iron(III) Complexes for Highly Efficient and Sustainable Ketalization of Glycerol: A Combined Experimental and Theoretical Study. *ACS Omega* **2019**, *4*, 688–698. [CrossRef]
38. Castillo Martinez, F.A.; Balciunas, E.M.; Salgado, J.M.; Domínguez González, J.M.; Converti, A.; Oliveira, R.P.d.S. Lactic acid properties, applications and production: A review. *Trends Food Sci. Technol.* **2013**, *30*, 70–83. [CrossRef]
39. Pereira, C.S.M.; Silva, V.M.T.M.; Rodrigues, A.E. Ethyl lactate as a solvent: Properties, applications and production processes—A review. *Green Chem.* **2011**, *13*, 2658. [CrossRef]
40. Cairns, S.A.; Schultheiss, A.; Shaver, M.P. A broad scope of aliphatic polyesters prepared by elimination of small molecules from sustainable 1,3-dioxolan-4-ones. *Polym. Chem.* **2017**, *8*, 2990–2996. [CrossRef]
41. Hyoi, K.; Kanazawa, A.; Aoshima, S. Cationic Ring-Opening Co- and Terpolymerizations of Lactic Acid-Derived 1,3-Dioxolan-4-ones with Oxiranes and Vinyl Ethers: Nonhomopolymerizable Monomer for Degradable Co- and Terpolymers. *ACS Macro Lett.* **2019**, *8*, 128–133. [CrossRef]
42. Miyagawa, T.; Sanda, F.; Endo, T. Synthesis and radical polymerization of 5-methylene-2, 2-dimethyl-1, 3-dioxolan-4-one. *J. Polym. Sci. Part A Polym. Chem.* **2000**, *38*, 1861–1865. [CrossRef]
43. Masahiko Okada, H.S.; Atsumi, M. Specific Formation of a Polymer Containing Five-Membered Oxalactone Rings in the Main Chain in the Cationic Ring-Opening Polymerization of 6,8-Dioxabicyclo[3.2.1]octan-7-one. *Macromolecules* **1984**, *17*, 1840–1843. [CrossRef]
44. Xu, K.; Ding, S.P.; Jow, T.R. Toward Reliable Values of Electrochemical Stability Limits for Electrolytes. *J. Electrochem. Soc.* **2019**, *146*, 4172–4178. [CrossRef]
45. Schütter, C.; Husch, T.; Korth, M.; Balducci, A. Toward New Solvents for EDLCs: From Computational Screening to Electrochemical Validation. *J. Phys. Chem. C* **2015**, *119*, 13413–13424. [CrossRef]
46. Noori, A.; El-Kady, M.F.; Rahmanifar, M.S.; Kaner, R.B.; Mousavi, M.F. Towards establishing standard performance metrics for batteries, supercapacitors and beyond. *Chem. Soc. Rev.* **2019**, *48*, 1272–1341. [CrossRef]
47. Mei, B.-A.; Munteshari, O.; Lau, J.; Dunn, B.; Pilon, L. Physical Interpretations of Nyquist Plots for EDLC Electrodes and Devices. *J. Phys. Chem. C* **2017**, *122*, 194–206. [CrossRef]
48. Taberna, P.L.; Simon, P.; Fauvarque, J.F. Electrochemical Characteristics and Impedance Spectroscopy Studies of Carbon-Carbon Supercapacitors. *J. Electrochem. Soc.* **2003**, *150*, A292. [CrossRef]
49. Crespo, J.G.; Brazinha, C. 1—of pervaporation. In *Pervaporation, Vapour Permeation and Membrane Distillation*; Basile, A., Figoli, A., Khayet, M., Eds.; Woodhead Publishing: Oxford, UK, 2015; pp. 3–17.
50. George, A.; Olah, A.G.G.K. Surya Prakash, Production of Methanol: From Fossil Fuels and Bio-Sources to Chemical Carbon Dioxide Recycling. In *Beyond Oil and Gas: The Methanol Economy*; WILEY-VCH Verlag GmbH & Co. KGaA: Weinheim, Germany, 2009; pp. 233–278.
51. Belletante, S.; Montastruc, L.; Negny, S.; Domenech, S. Optimal design of an efficient, profitable and sustainable biorefinery producing acetone, butanol and ethanol: Influence of the in-situ separation on the purification structure. *Biochem. Eng. J.* **2016**, *116*, 195–209. [CrossRef]
52. Prugh, R.W. Estimation of Flash Point Temperature. *J. Chem. Educ.* **1973**, *50*, A85–A88. [CrossRef]
53. Nuhn, L.; Van Herck, S.; Best, A.; Deswarte, K.; Kokkinopoulou, M.; Lieberwirth, I.; Koynov, K.; Lambrecht, B.N.; De Geest, B.G. FRET Monitoring of Intracellular Ketal Hydrolysis in Synthetic Nanoparticles. *Angew. Chem. Int. Ed. Engl.* **2018**, *57*, 10760–10764. [CrossRef] [PubMed]

54. Magnuson, B.A.; Burdock, G.A.; Doull, J.; Kroes, R.M.; Marsh, G.M.; Pariza, M.W.; Spencer, P.S.; Waddell, W.J.; Walker, R.; Williams, G.M. Aspartame: A safety evaluation based on current use levels, regulations, and toxicological and epidemiological studies. *Crit. Rev. Toxicol.* **2007**, *37*, 629–727. [CrossRef] [PubMed]
55. W.H.O. Formaldehyde, Chapter 5.8. In *Air Quality Guidelines*, 2nd ed.; WHO Regional Office for Europe: Copenhagen, Denmark, 2001.
56. United States Environmental Protection Agency (U.S. EPA). Formaldehyde, Toxicity and Exposure Assessment for Children's Health. Available online: https://archive.epa.gov/region5/teach/web/pdf/formaldehyde_summary.pdf (accessed on 15 May 2021).
57. Daraghmeh, A.; Hussain, S.; Saadeddin, I.; Servera, L.; Xuriguera, E.; Cornet, A.; Cirera, A. A Study of Carbon Nanofibers and Active Carbon as Symmetric Supercapacitor in Aqueous Electrolyte: A Comparative Study. *Nanoscale Res. Lett.* **2017**, *12*, 639. [CrossRef] [PubMed]
58. Strehlau, J.; Weber, T.; Lürenbaum, C.; Bornhorst, J.; Galla, H.-J.; Schwerdtle, T.; Winter, M.; Nowak, S. Towards quantification of toxicity of lithium ion battery electrolytes-development and validation of a liquid-liquid extraction GC-MS method for the determination of organic carbonates in cell culture materials. *Anal. Bioanal. Chem.* **2017**, *409*, 6123–6131. [CrossRef] [PubMed]
59. Cavani, F.; Centi, G.; Marion, P. Catalytic ammoxidation of hydrocarbons on mixed oxides. In *Metal Oxide Catalysis*; Jackson, S.D., Hargreaves, J.S.J., Eds.; WILEY-VCH Verlag GmbH & Co. KGaA: Weinheim, Germany, 2008; pp. 771–818.
60. Beckers, J.G.J.; Van Der Heide, E.; Van Kessel, G.M.M.; Lange, J.-P. Process for the Preparation of Propylene Carbonate. US 2005/0148787 A1, 7 July 2005.
61. Lange, J.-P. Process for the Preparation of Propylene Carbonate. US 7,728,164 B2, 1 June 2010.

MDPI
St. Alban-Anlage 66
4052 Basel
Switzerland
Tel. +41 61 683 77 34
Fax +41 61 302 89 18
www.mdpi.com

Energies Editorial Office
E-mail: energies@mdpi.com
www.mdpi.com/journal/energies

MDPI
St. Alban-Anlage 66
4052 Basel
Switzerland

Tel: +41 61 683 77 34
Fax: +41 61 302 89 18

www.mdpi.com

ISBN 978-3-0365-4302-4